

Dissertation  
submitted to the  
Combined Faculties of the Natural Sciences and Mathematics  
of the Ruperto-Carola-University of Heidelberg. Germany  
for the degree of  
Doctor of Natural Sciences

Put forward by

PAZ VICTORIA BLUHM CEBALLOS

born in Santiago, Región Metropolitana, Chile

Oral examination: February 15, 2022



---

DETECTION AND CHARACTERIZATION  
OF EXOPLANETS AROUND M DWARFS IN  
THE PRESENCE OF STELLAR ACTIVITY

---

REFEREES:

PROF. DR. ANDREAS QUIRRENBACH

PD DR. THOMAS HENNING



## Abstract

M dwarfs are the most numerous type of stars in the Universe. Their low masses and their large planet-to-star size ratios offer big advantages to study orbiting exoplanets around these stars. On one hand, the radial velocities signals have greater amplitudes and are easier to identify than in FGK stars. On the other, the small size of M dwarfs leads to transiting planets leaving a stronger imprint in the light curve. Additionally, their low temperatures, places their habitable zone close to the host star, which makes them excellent targets to search for temperate or habitable worlds.

Despite the advantages that M dwarfs offer, these do not come for free. Typically they are active entities, and most of the M-dwarfs have strong magnetic fields, which can heat their stellar chromospheres, creating magnetic activity which drives the occurrence of stellar spots in their photosphere. Consequently, stellar activity can mimic the signal of an orbiting planet which is one of the most problematic sources of noise.

This thesis is focused on the discovery and characterization of exoplanets around M dwarfs, where I highlight the importance of careful modeling of the intrinsic stellar noise present in the data for to avoid false planet claims.

## Zusammenfassung

M Zwerge zählen zu den häufigsten Sterntypen in der Milchstraße. Wegen ihrer niedrigen Massen und den vergleichsweise hohen Größenverhältnissen von Planet zu Stern sind sie gut geeignet, um Exoplaneten um sie herum zu erforschen. Zum Einen führen M Zwerge in Anwesenheit von Exoplaneten größere Reflexbewegungen aus als massenreichere FGK Sterne, was zu höheren und leichter zu detektierenden Amplituden in Radialgeschwindigkeiten führt. Zum Anderen weisen auch ihre Lichtkurven bei Sternbedeckungen durch Planeten höhere Variationen auf. Zudem liegen die bewohnbaren Zonen bei M Zwergen auf Grund ihrer niedrigen Temperaturen näher am Stern, was die Suche nach möglicherweise bewohnbaren erdähnlichen Planeten erleichtert.

Trotz ihrer Vorteile bringen M Zwerge auch Schwierigkeiten bei der Suche nach Exoplaneten mit sich. Die meisten ihrer Art weisen starke Magnetfelder auf, die zur Aufheizung ihrer Chromosphäre und zur Bildung von Sternflecken in der Photosphäre führen können. Sowohl in photometrischen Zeitreihen als auch in solchen von Radialgeschwindigkeiten können Sternflecken dieser Art zu Signaturen führen, die mit denen von Planeten verwechselt werden können. Dieses stellare Rauschen ist höchst problematisch und erfordert ein tiefes Verständnis der physikalischen Prozesse, um die Daten korrekt zu interpretieren.

Die vorliegende Arbeit beschreibt die Entdeckung und Charakterisierung Planeten um M Zwerge. In der Arbeit Ergebnisse unterstreichen die Bedeutung sorgfältiger Modellierung des intrinsischen stellaren Rauschens in photometrischen Daten sowie Radialgeschwindigkeiten um falsche Planetenansprüche zu vermeiden.



|                                                                                                                                |           |
|--------------------------------------------------------------------------------------------------------------------------------|-----------|
| <b>LIST OF FIGURES</b> . . . . .                                                                                               | <b>3</b>  |
| <b>LIST OF TABLES</b> . . . . .                                                                                                | <b>4</b>  |
| <b>1 Introduction</b>                                                                                                          | <b>7</b>  |
| 1.1 Radial velocity technique . . . . .                                                                                        | 9         |
| 1.2 Transit method . . . . .                                                                                                   | 13        |
| 1.2.1 Follow-up efforts for transiting planets . . . . .                                                                       | 14        |
| 1.2.2 The era of space-based exoplanet missions . . . . .                                                                      | 15        |
| 1.3 Exoplanet demographics . . . . .                                                                                           | 17        |
| 1.3.1 Exoplanet statistics: The observed properties and distributions . . . . .                                                | 19        |
| 1.3.2 Planet size distribution . . . . .                                                                                       | 23        |
| 1.3.3 The radius-gap . . . . .                                                                                                 | 23        |
| 1.3.4 Ultra-short-period planets . . . . .                                                                                     | 27        |
| 1.4 M Dwarfs: Challenges and opportunities of planet hosts . . . . .                                                           | 28        |
| 1.4.1 Dealing with stellar activity . . . . .                                                                                  | 29        |
| 1.4.2 CARMENES Instrument . . . . .                                                                                            | 32        |
| 1.4.3 CARMENES M-dwarf survey . . . . .                                                                                        | 33        |
| 1.5 CARMENES–TESS synergy . . . . .                                                                                            | 35        |
| 1.6 Purpose and thesis overview . . . . .                                                                                      | 38        |
| <b>2 Precise mass and radius of a transiting super-Earth planet orbiting the M dwarf TOI-1235: a planet in the radius gap?</b> | <b>41</b> |
| 2.1 Motivation . . . . .                                                                                                       | 41        |
| 2.2 Data . . . . .                                                                                                             | 43        |
| 2.2.1 TESS photometry . . . . .                                                                                                | 43        |
| 2.2.2 High-resolution spectroscopy . . . . .                                                                                   | 45        |
| 2.2.3 High-resolution imaging . . . . .                                                                                        | 46        |
| 2.2.4 Ground-based photometry . . . . .                                                                                        | 47        |
| 2.3 Stellar properties . . . . .                                                                                               | 48        |
| 2.4 Analysis and results . . . . .                                                                                             | 50        |
| 2.4.1 Limits on photometric contamination . . . . .                                                                            | 50        |
| 2.4.2 Stellar rotational period from photometric data . . . . .                                                                | 52        |
| 2.4.3 Signals in spectroscopic data . . . . .                                                                                  | 54        |
| 2.4.4 Joint fit . . . . .                                                                                                      | 58        |
| 2.4.5 Search for transit depth and time variations . . . . .                                                                   | 60        |

|          |                                                                                    |            |
|----------|------------------------------------------------------------------------------------|------------|
| 2.5      | Discussion . . . . .                                                               | 63         |
| 2.6      | Conclusions . . . . .                                                              | 65         |
| <b>3</b> | <b>An ultra-short-period transiting super-Earth orbiting the M3 dwarf TOI-1685</b> | <b>71</b>  |
| 3.1      | Motivation . . . . .                                                               | 71         |
| 3.2      | Data . . . . .                                                                     | 73         |
| 3.2.1    | TESS photometry . . . . .                                                          | 73         |
| 3.2.2    | High-resolution imaging . . . . .                                                  | 75         |
| 3.2.3    | Ground-based seeing-limited photometry . . . . .                                   | 77         |
| 3.2.4    | CARMENES RV measurements . . . . .                                                 | 78         |
| 3.3      | Stellar properties . . . . .                                                       | 79         |
| 3.4      | Analysis and results . . . . .                                                     | 80         |
| 3.4.1    | Periodogram analysis of the RV data . . . . .                                      | 80         |
| 3.4.2    | Searching for the rotation period . . . . .                                        | 81         |
| 3.4.3    | Modeling results . . . . .                                                         | 83         |
| 3.4.4    | Only RV data . . . . .                                                             | 86         |
| 3.4.5    | Joint fit . . . . .                                                                | 89         |
| 3.5      | Discussion . . . . .                                                               | 93         |
| 3.5.1    | Ultra-short-period planet: TOI-1685 b . . . . .                                    | 93         |
| 3.5.2    | The planet candidate TOI-1685 [c] . . . . .                                        | 95         |
| 3.6      | Conclusion . . . . .                                                               | 98         |
| <b>4</b> | <b>Gliese 617 an M-dwarf binary system in TESS Continuous View Zone</b>            | <b>101</b> |
| 4.1      | Gliese 617 system . . . . .                                                        | 101        |
| 4.1.1    | New available CARMENES and TESS data . . . . .                                     | 102        |
| 4.2      | Preliminary photometric analysis – How to work with TESS data? . . . . .           | 102        |
| 4.2.1    | Creating a Design Matrix . . . . .                                                 | 104        |
| 4.2.2    | Cotrending Basis Vectors (CBVs) . . . . .                                          | 107        |
| 4.2.3    | Optimizing the fit . . . . .                                                       | 107        |
| 4.3      | Photometric analysis of GJ 617 A . . . . .                                         | 111        |
| 4.3.1    | Stellar rotational period from TESS data . . . . .                                 | 112        |
| 4.4      | Spectroscopic analysis of GJ 617 A . . . . .                                       | 117        |
| 4.4.1    | Radial velocity exploration and modeling . . . . .                                 | 117        |
| 4.4.2    | Conclusions . . . . .                                                              | 124        |
| 4.5      | Photometric analysis of GJ 617 B . . . . .                                         | 125        |
| 4.5.1    | Identifying the stellar rotational period from TESS data . . . . .                 | 126        |
| 4.6      | Radial velocity analysis of GJ 617 B . . . . .                                     | 129        |
| 4.6.1    | Discussion . . . . .                                                               | 131        |
| <b>5</b> | <b>Conclusions and future work</b>                                                 | <b>135</b> |
| 5.1      | Future work . . . . .                                                              | 138        |
|          | <b>Bibliography</b>                                                                | <b>142</b> |

## List of Figures

---

|      |                                                                                                                                  |    |
|------|----------------------------------------------------------------------------------------------------------------------------------|----|
| 1.1  | Cumulative histogram of exoplanet discoveries per year . . . . .                                                                 | 9  |
| 1.2  | Schematic of the radial velocity method . . . . .                                                                                | 10 |
| 1.3  | Illustration of the planet's orbital elements . . . . .                                                                          | 11 |
| 1.4  | Schematic light curves for the first five planet discovered by <i>Kepler</i> . . . . .                                           | 14 |
| 1.5  | Illustration of an exoplanet transit . . . . .                                                                                   | 15 |
| 1.6  | Illustration of <i>TESS</i> sky coverage map . . . . .                                                                           | 16 |
| 1.7  | Exoplanet population as function of stellar mass and metallicity . . . . .                                                       | 18 |
| 1.8  | Planetary mass distribution as a function of the orbital period . . . . .                                                        | 20 |
| 1.9  | Distribution of confirmed planets with radius $\leq 30 R_{\oplus}$ , and periods $\leq 400$ days . . . . .                       | 24 |
| 1.10 | Histogram distribution of detected <i>Kepler</i> planets with radii $\leq 4 R_{\oplus}$ and periods less than 100 days . . . . . | 25 |
| 1.11 | The radius gap as function of incident bolometric flux and host stellar mass . . . . .                                           | 26 |
| 1.12 | Diagram illustrating how flux blocked by a spot moving across on the rotating disk . . . . .                                     | 30 |
| 1.13 | Planets discoveries around different stellar masses, determined with RVs . . . . .                                               | 34 |
| 1.14 | Mass-radius diagram for all transiting planets around nearby M dwarfs with measured mass . . . . .                               | 36 |
| 2.1  | <i>TESS</i> transit photometry data for TOI-1235 b . . . . .                                                                     | 44 |
| 2.2  | Target pixel files of TOI-1235 . . . . .                                                                                         | 51 |
| 2.3  | Contrast curves of TOI-1235 from AstraLux and NESSI . . . . .                                                                    | 53 |
| 2.4  | Photometric data from ASAS-SN and NSVS for TOI-1235 . . . . .                                                                    | 55 |
| 2.5  | GLS periodograms of CARMENES RV data and activity indicators of TOI-1235 . . . . .                                               | 56 |
| 2.6  | S-BGLS periodogram of the CARMENES and HARPS-N RV data of TOI-1235 . . . . .                                                     | 57 |
| 2.7  | Joint fit results for TOI-1235 . . . . .                                                                                         | 61 |
| 2.8  | Mass-radius and insolation-radius diagrams for TOI-1235 b . . . . .                                                              | 64 |
| 3.1  | <i>TESS</i> and ground-based photometry light curves of TOI-1685 . . . . .                                                       | 72 |
| 3.2  | Target pixel files of TOI-1685 in <i>TESS</i> sector 19 . . . . .                                                                | 74 |
| 3.3  | Sensitivity curve for the AstraLux high-spatial-resolution observation of TOI-1685 in the SDSS $z'$ filter . . . . .             | 75 |
| 3.4  | GLS periodograms of RV CARMENES data and activity indicators of TOI-1685 . . . . .                                               | 78 |
| 3.5  | False alarm probability (FAP) versus window size for RV of TOI-1685 . . . . .                                                    | 81 |

List of Figures

|      |                                                                                                                                 |     |
|------|---------------------------------------------------------------------------------------------------------------------------------|-----|
| 3.6  | S-BGLS periodogram of the RV data of TOI-1685 . . . . .                                                                         | 83  |
| 3.7  | GLS periodogram of the joint V-band LCOGT Teide and Haleakalā light curve of TOI-1685 . . . . .                                 | 84  |
| 3.8  | Posterior distribution of the GP fit to the RV data in the $\alpha$ versus $P_{\text{rot}}$ plane for TOI-1685 . . . . .        | 85  |
| 3.9  | RV data from CARMENES with the best-fit Keplerian <code>juliet</code> model for TOI-1685 . . . . .                              | 87  |
| 3.10 | Phase-folded RV curves and their residuals of the USP TOI-1685 b . . . . .                                                      | 87  |
| 3.11 | Posterior distribution for the joint model parameters (1cp+GP) derived with <code>juliet</code> for TOI-1685 . . . . .          | 90  |
| 3.12 | Density-radius diagram for TOI-1685 b . . . . .                                                                                 | 94  |
| 3.13 | Mass-radius diagram in Earth units for TOI-1685 b . . . . .                                                                     | 95  |
| 3.14 | ESM and TSM metrics for TOI-1685 b . . . . .                                                                                    | 96  |
| 3.15 | Density-equilibrium temperature diagram for TOI-1685 b . . . . .                                                                | 97  |
|      |                                                                                                                                 |     |
| 4.1  | <i>TESS</i> SAP and PDCSAP light curves for GJ 617 A . . . . .                                                                  | 103 |
| 4.2  | Background variation of <i>TESS</i> Sector 15 . . . . .                                                                         | 104 |
| 4.3  | Principal component analysis (PCA) for a given dataset . . . . .                                                                | 105 |
| 4.4  | <i>TESS</i> SAP and Pixel-DM light curve of GJ 617 A . . . . .                                                                  | 106 |
| 4.5  | <i>TESS</i> Co-detrending basis vectors . . . . .                                                                               | 108 |
| 4.6  | Comparison between SAP and Pixel-DM light curves obtained through an optimal reduction for GJ 617 A . . . . .                   | 109 |
| 4.7  | Goodness Metrics . . . . .                                                                                                      | 110 |
| 4.8  | Comparison between corrected light curve Pixel-DM and the light curve using a regularization factor Pixel_CBV-DM . . . . .      | 111 |
| 4.9  | <i>TESS</i> PDCSAP, SAP, and corrected Pixel-DM light curves of GJ 617 A . . . . .                                              | 112 |
| 4.10 | Target Pixel Files for GJ 617 A . . . . .                                                                                       | 113 |
| 4.11 | <i>TESS</i> photometric GLS periodogram of GJ 617 A . . . . .                                                                   | 115 |
| 4.12 | Binned <i>TESS</i> light curve with the best <code>juliet</code> dSHO-GP fit for GJ 617 A. . . . .                              | 115 |
| 4.13 | Posterior distribution for the dSHO GP model parameter derived with <code>juliet</code> . . . . .                               | 116 |
| 4.14 | GLS periodograms of the RV data and the residuals for GJ 617 A . . . . .                                                        | 118 |
| 4.15 | GLS periodograms of set of activity indicators of GJ 617 A . . . . .                                                            | 119 |
| 4.16 | CARMENES RV data for GJ 617 A with the best <code>juliet</code> fit model . . . . .                                             | 120 |
| 4.17 | Posterior distribution for the planet parameters GJ 617 A b . . . . .                                                           | 121 |
| 4.18 | Posterior distribution for the QP-GP RV model parameters for GJ 617 A . . . . .                                                 | 122 |
| 4.19 | S-BGLS periodogram and $\log_{\alpha}$ versus $P_{\text{rot}}$ diagram of the RV data for GJ 617 A . . . . .                    | 124 |
| 4.20 | <i>TESS</i> SAP and Pixel-DM light curves for GJ 617 B . . . . .                                                                | 125 |
| 4.21 | GLS periodogram of the binned <i>TESS</i> light curve of GJ 617 B . . . . .                                                     | 126 |
| 4.22 | Target Pixel Files for GJ 617 B . . . . .                                                                                       | 127 |
| 4.23 | Binned <i>TESS</i> light curve with the best <code>juliet</code> dSHO-GP fit and posterior distributions for GJ 617 B . . . . . | 128 |
| 4.24 | GLS periodograms of the RV data and the residuals for GJ 617 B . . . . .                                                        | 129 |
| 4.25 | GLS periodograms of set of activity indicators of GJ 617 A . . . . .                                                            | 130 |
| 4.26 | S-BGLS periodogram for GJ 617 B . . . . .                                                                                       | 131 |
| 4.27 | Posterior distribution for the QP-GP RV model parameters for GJ 617 B . . . . .                                                 | 132 |

## List of Tables

---

|      |                                                                                                                         |     |
|------|-------------------------------------------------------------------------------------------------------------------------|-----|
| 2.1  | <i>TESS</i> observations of TOI-1235 . . . . .                                                                          | 43  |
| 2.2  | Descriptions of data from public ground-based surveys of TOI-1235 . . . . .                                             | 47  |
| 2.3  | Stellar parameters of TOI-1235 . . . . .                                                                                | 50  |
| 2.4  | Priors used for TOI-1235 b in the joint fit with <code>juliet</code> . . . . .                                          | 59  |
| 2.5  | Posterior parameters of the <code>juliet</code> joint fit for TOI-1235 b . . . . .                                      | 62  |
| 2.6  | Derived planetary parameters for TOI-1235 b . . . . .                                                                   | 63  |
| 2.7  | Radial velocity measurements and spectroscopic activity indicators for TOI-1235 from HARPS-N optical spectra . . . . .  | 66  |
| 2.8  | Radial velocity measurements for TOI-1235 from iSHELL spectra . . . . .                                                 | 66  |
| 2.9  | Radial velocity measurements and spectroscopic activity indicators for TOI-1235 from NIR spectra . . . . .              | 67  |
| 2.10 | Radial velocity measurements and spectroscopic activity indicators for TOI-1235 from CARMENES optical spectra . . . . . | 68  |
| 3.1  | <i>TESS</i> observations of TOI-1685 . . . . .                                                                          | 74  |
| 3.2  | Ground-based transit follow-up observations of TOI-1685 . . . . .                                                       | 77  |
| 3.3  | Stellar parameters of TOI-1685 . . . . .                                                                                | 80  |
| 3.4  | RV model selection of TOI-1685 . . . . .                                                                                | 85  |
| 3.5  | Priors used for TOI-1235 b and TOI-1685 c in the joint fit with <code>juliet</code> . . . . .                           | 88  |
| 3.6  | Posterior distributions of the <code>juliet</code> joint fit for the instrumental parameters of TOI-1685 . . . . .      | 91  |
| 3.7  | Derived planetary parameters for TOI-1685 b and TOI-1685 c . . . . .                                                    | 92  |
| 3.8  | RV measurements and spectroscopic activity indicators for TOI-1685 from CARMENES VIS spectra . . . . .                  | 99  |
| 4.1  | RV model selection for GJ 617 A . . . . .                                                                               | 119 |
| 4.2  | Prior and Posterior parameters of the <code>juliet</code> RV fit for GJ 617 A b . . . . .                               | 123 |
| 4.3  | RV model selection for GJ 617 B . . . . .                                                                               | 131 |



# 1

## Introduction

---

*“Whenever I saw the sun, I reminded myself that I was looking at a star. One of over a hundred billion in our galaxy. A galaxy that was just one of billions of other galaxies in the observable universe. This helped me keep things in perspective.”*

*by Ernest Cline*

---

Ever since the ancient times, man has been fascinated at observing the night sky. The vast curiosity to understand what is beyond the planet Earth has moved him to attempt to study the cosmos, both theoretically and practically. To achieve this, the building of larger and more sophisticated telescopes over time has allowed us to reach a point today where we can observe very faint and tiny, blurred distant objects.

Questions as, “Are we alone in the vast Universe?”, or “Exist life in other worlds?” remain unanswered, until we find probes of life in other worlds.

In the search for life beyond Solar System, our collection of planets has expanded, reaching in the present-day to an impressive amount of 4569<sup>1</sup> planets discoveries. Most of them have been identified in a relatively small region of the Milky Way, revealing to be a common phenomena. Currently, we know that the so called “exoplanet zoo” is composed by a large variety of objects, covering a broad range of masses and sizes, on which these planets can be found as single objects or in multi-planetary configurations, around single or binary systems, and across different spectral-type stars. However, only few of them were found in their habitable zones, defined as the orbital region around a star in which an planet can possess liquid water on its surface. Just recently the discovery of the unique TRAPPIST-1 system has offered, for the first time, the opportunity to directly compare their exoplanetology with the Earth. This finding has boosted the exoplanet field into a new era, crossing from detection to fully characterization of exoplanets, and gradually moving towards the compositional studies of exoplanet atmospheres. The latter is a fundamental step in our quest to find evidence of life in extra solar planets, and it is one of the main science goal of the new generations of ground- and space-based astronomical instruments.

---

<sup>1</sup>According to the NASA Exoplanet Archive (<https://exoplanetarchive.ipac.caltech.edu>), accessed November 19, 2021

## 1 Introduction

In order to detect exoplanets, several methods have been developed, namely in order of number of planet discoveries, the transit method, radial velocity (RV) technique, microlensing, direct imaging, transit timing variations, eclipse timing variations, pulsar timing, disk kinematics, astrometry, among others. Particularly, the transit method is responsible for 75.5% of all exoplanet detections, whereas the RV method comes in second with 19.6%<sup>2</sup>. The first of these two methods is based on measuring the dimming in the starlight flux when the star has a planet that passes in front of it, while the second is basically based on monitoring a star and measuring the shifts in the position of the stellar spectral features induced by the gravitational pull of a substellar companion.

In fact, during the 90's until the first decade of 2000's, the RV technique, was the most successful way to detect substellar companions. The discovery of a planetary system around the pulsar PSR 1257+12 (Wolszczan & Frail, 1992) and then, the discovery of the giant planet 51 Pegasi b around a solar-like star (Mayor & Queloz, 1995), totally revolutionized modern astronomy, marking the beginning of the exoplanets era and leading Michel Mayor & Didier Queloz to win the Nobel Prize in 2019. However, the RV technique by itself only provides constraints for the period and the minimum mass of the planet. To obtain other valuable planetary parameters (e.g., planet radius, eccentricity), additional method is required.

Therefore, the discovery of 51 Pegasi b, prompted new studies in detecting transiting systems from ground-based photometry. One of these studies was made by David Charbonneau, when, in 2000, he applied the transit method to the star HD 2019458 and, thus, could successfully measure the mass and radius of HD 2019458 b (Charbonneau et al., 2000) confirming the existence of an exoplanet for the first time. The advantage to combine these two methods is being able to determine the density of the planet. Therefore by comparing with theoretical models is possible to derive the planet atmospheric composition (Seager & Deming, 2010), and finally distinguish between a gaseous-type or a rocky-type world.

The revelation of the huge potential when combining these two techniques triggered the development of high-resolution spectrographs, and constructing larger ground-based telescopes. However, it was only with the development of dedicated space missions that it became possible to efficiently detect transiting exoplanets, through the continuous monitoring of large sky regions.

In Figure 1.1, we can see how the exoplanet field has growth during nearly the last three decades. It seems clear that the exoplanet occurrence rates have been experiencing an exponential development since space missions were launched. With more than the 2000 confirmed exoplanets by *Kepler* mission, and, more than 4000 additional planet candidates from *TESS* (Günther et al., 2020), this sample is expected to keep growing at giant steps, thanks to ongoing and future missions such as the upcoming *PLATO* (Rauer et al., 2014) and *ARIEL* (Tinetti et al., 2021) missions utilizing the transit method and even the next *GAIA* (DR3; Gaia Collaboration et al., 2021) data release, applying the astrometric technique.

---

<sup>2</sup><https://exoplanets.nasa.gov/discovery/discoveries-dashboard/>

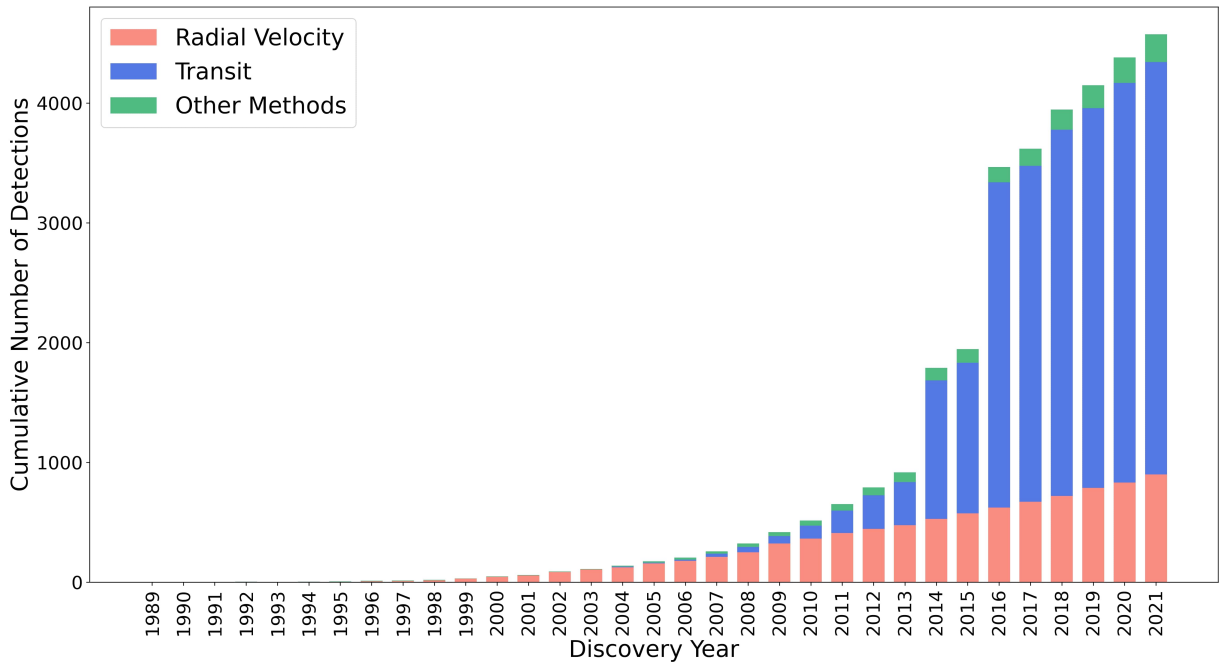


**Figure 1.1:** Cumulative histogram of exoplanet discoveries per year. According to the NASA Exoplanet Archive, accessed December 3, 2021.

## 1.1 Radial velocity technique

The **radial velocity (RV) technique** is based on the effect described in the 19<sup>th</sup> by Christian Doppler, who discovered that waves, like sound or light, change frequency according to the object’s speed emitting the waves. In the case of a planet orbiting a star, we can measure this effect by measuring the movement in the stellar spectral lines due to the gravitational influence on its host star. In planetary systems, all bodies orbit around the common center of mass, the presence of a planet induces a “wobbling” effect, moving the star away or towards us over time; the movement can be represented as a wave that can be stretched (i.e., red-shifted) or compressed (i.e., blue-shifted) the stellar spectral lines depending on if the star is moving approaching or moving away from us. A schematic representation of the RV method is shown in Figure 1.2.

By measuring the wavelength shift ( $\Delta\lambda$ ) in the position of the stellar lines, we can compute the RV, or in other words, the relative speed between the observer and the star ( $v_r$ ). For velocities much lower than the speed of light ( $c$ ), this is given by:

$$\frac{v_r}{c} = \frac{\Delta\lambda}{\lambda} \quad (1.1)$$

From the periodic variations in the RV curve, represented in the right panel of Fig. 1.2, the planet orbital period ( $P$ ) is directly measured. By using Kepler’s third law is possible

## 1 Introduction

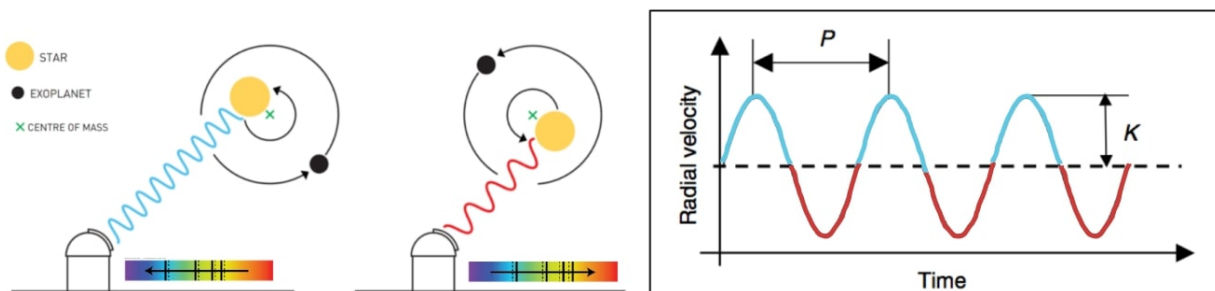


**Figure 1.2:** Schematic of the RV method. The plot shows the RV vs. time for the host star indicating how the period,  $P$ , and the semi amplitude,  $K$ , can be determined from the data

to determine the planet's distance to the star,  $a$ ,

$$\frac{a^3}{P^2} = \frac{G(M_\star + M_p)}{4\pi^2} \quad (1.2)$$

where  $G$  is the gravitational constant,  $M_\star$  is the mass of the star, and  $M_p$  is the mass of the planet.

To obtain the remaining planetary parameters, we need to keep in mind that for this method, the planetary mass and the inclination of the orbit,  $i$ , (angle between the plane-of-orbit and the plane-of-sky, which is defined as perpendicular to the line-of-sight) are degenerate, for larger inclination angles, such that the RV method can only give a lower limit on the mass,  $M_p \sin(i)$ .

Since the velocity of the star along its orbital motion around the star-planet center of mass varies with time, the RVs follow a periodical movement, which is modeled by a Keplerian orbit. Figure 1.3 shows a schematic diagram with the orbital elements of the planet. The gray plane represents the plane-of-sky, and the tilted plane is the plane-of-orbit in which the planet revolves around its host star. The ascending and descending nodes are the points at which the planet's orbit passes through the plane-of-sky. The angle  $\nu$  is known as the true anomaly and is defined as the position of the orbiting planet along its orbit at a specific time (corresponds to the planet's angular distance with respect to the periastron point<sup>3</sup>), the angle  $\omega$  is referred to as the argument of periastron, and is the angular distance from the ascending node to the periastron point.

If we designate the plane-of-sky to be the  $x$ - $y$  plane, then the direction to the observer along the line-of-sight is the  $z$ -direction. In terms of  $\omega$ ,  $\nu$ , and  $i$ ,  $z$  can be expressed as:

$$z = r \sin(\nu + \omega) \sin i \quad (1.3)$$

Since  $z$  is the direction along the observer's line-of-sight, the derivative of  $z$  with respect

---

<sup>3</sup>periastron correspond to the closest point between an object moving in an elliptical orbit around another celestial body

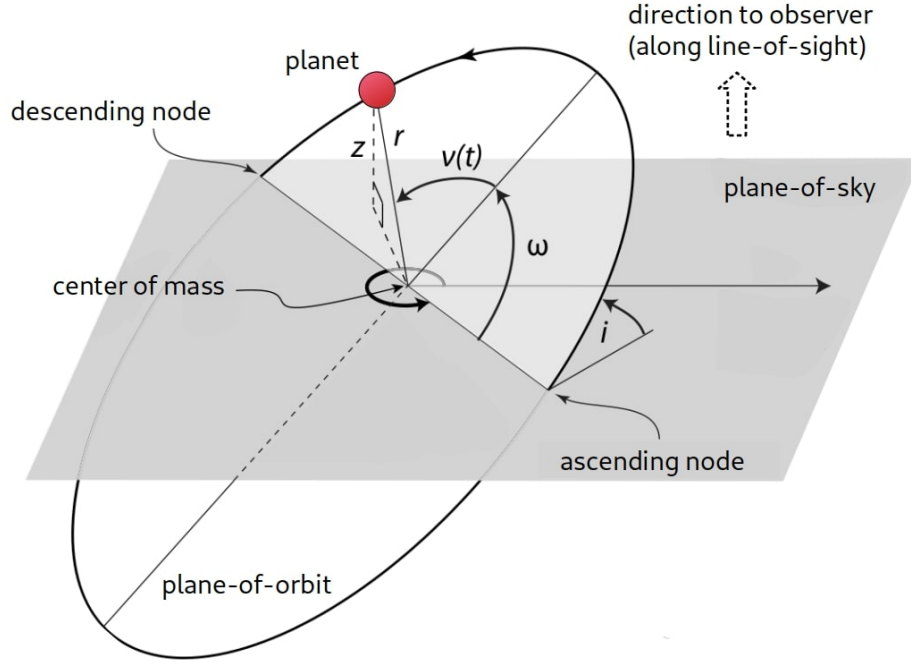


**Figure 1.3:** Illustration of the planet's orbital elements.

to time provides us an expression for RV ( $\dot{z} = v_r$ ). Therefore,

$$v_r = [r\dot{\nu} \cos(\nu + \omega) + \dot{r} \sin(\nu + \omega)] \sin i \quad (1.4)$$

Considering the orbit shape as an ellipse, we can use the general equation for an ellipse and its derivative to find  $\dot{r}$ . Additionally, we know that the ellipse area is defined as:  $A = \pi ab$ , and the eccentricity as:  $e^2 = 1 - b^2/a^2$ . Combining these two equations, we can get:  $A = \pi a^2 \sqrt{1 - e^2}$ , where  $a$  and  $b$  the semi-major and semi-minor axis of the ellipse,

$$r(\nu) = \frac{a(1 - e^2)}{1 + e \cos \nu}, \quad \Rightarrow \quad \dot{r} = \frac{re\dot{\nu} \sin \nu}{1 + e \cos \nu} \quad (1.5)$$

Using Kepler's second law and integrating the left-hand side over the time it takes the planet to make one complete revolution around its host star ( $P$ ), we can get,

$$\frac{dA}{dt} = \frac{1}{2} r^2 \dot{\nu}, \quad \Rightarrow \quad \frac{A}{P} = \frac{1}{2} r^2 \dot{\nu}, \quad \Rightarrow \quad r\dot{\nu} = \frac{1}{r} \left[ \frac{2\pi a^2 \sqrt{1 - e^2}}{P} \right] \quad (1.6)$$

and using Eq. 1.5, we can find  $\dot{\nu}$ ,

$$r\dot{\nu} = \left[ \frac{1 + e \cos \nu}{a(1 - e^2)} \right] \left[ \frac{2\pi a^2 \sqrt{1 - e^2}}{P} \right], \quad \Rightarrow \quad \dot{r} = \frac{2\pi a e \sin \nu}{P \sqrt{1 - e^2}} \quad (1.7)$$

Finally, substituting Eq. 1.6 and Eq. 1.7 in Eq. 1.4 and using some trigonometric identities,

## 1 Introduction

we finally derived the fundamental equation of RV,

$$v_r = K(\cos(\nu + \omega) + e \cos(\omega)), \quad \text{with} \quad K = \frac{2\pi a^2 \sin i}{P \sqrt{1 - e^2}} \quad (1.8)$$

where  $K$  is known as the RV semi-amplitude.

Alternatively, one can use the Kepler's third law (Eq. 1.2) to replace the semi-major axis  $a$  with the orbital period  $P$ , and assuming that  $M_\star \gg M_p \Rightarrow M_\star + M_p = M_\star$ , we can write the RV semi-amplitude of the star as,

$$K = \left(\frac{2\pi G}{P}\right)^{\frac{1}{3}} \frac{M_p \sin i}{M_\star^{2/3}} \frac{1}{\sqrt{1 - e^2}} \quad (1.9)$$

Finally, it is helpful to express this formula in more practical units:

$$K = \frac{28.433 \text{ m s}^{-1}}{\sqrt{1 - e^2}} \frac{M_p \sin i}{M_{Jup}} \left(\frac{M_\star}{M_\odot}\right)^{-2/3} \left(\frac{P}{1 \text{ yr}}\right)^{-1/3} \quad (1.10)$$

From the previous formula, we can see that to detect giant planets around a solar-like star through the RV technique requires precision of at least  $30 \text{ m s}^{-1}$ . To put this statement into context, in the case of Solar System planets, the RV signal that induces Jupiter to the Sun has a semi-amplitude of  $12.5 \text{ m s}^{-1}$ , the effect in Saturn is  $2.7 \text{ m s}^{-1}$ , and in the case of Earth, the signal is only  $\sim 0.1 \text{ m s}^{-1}$ .

With current instrumentation, searching planets with similar mass and distances to Jupiter or Saturn can easily be detected. On the other hand, to achieve a precision below than one meter per second, instruments must be able to resolve drifts in the wavelength space of the order of  $10^{-5} \text{ \AA}$ , which, for a  $\mathcal{R}=100.000$  high-resolution instrument, represent  $\sim 1/3000$  of the line width or about  $1/1000$  of a CCD pixel on the detector (Lovis & Fischer, 2010). To reach this high precision, it is necessary to have stable spectrographs during the full acquisition time, which means that the instrument needs to be under highly controlled environmental conditions. Otherwise temperature and pressure variations can induce noise in the RV measurements.

To track the noise variations in the spectrograph, as well as to subtract the nightly drift (so-called nightly zero point), a simultaneous calibration source such as hollow-cathode lamps (e.g., Th-Ne U-Ne, U-Ar), laser frequency combs (Murphy et al., 2007), Fabry-Pérot interferometer (Bauer et al., 2015) or a molecular iodine gas cell (Marcy & Butler, 1992) is required.

Currently, state-of-the-art high-resolution spectrographs can reach (or even break) the  $1 \text{ m s}^{-1}$  precision frontier. Examples of such instruments are HARPS (Queloz et al., 2001), CRIRES+ (Follert et al., 2014), CARMENES (Quirrenbach et al., 2014), MAROON-X (Seifahrt et al., 2018), and ESPRESSO (Pepe et al., 2010), the latter has already shown a long-term stability, which leads to RV precision of the order of  $\sim 25\text{-}50 \text{ cm s}^{-1}$  (Pepe et al., 2021).

## 1.2 Transit method

More than 3.400 exoplanets have been discovered by detecting signals from periodic planetary transits, making it the most effective and sensitive method for detecting extrasolar planets.

A **transit** occurs when a planet passes directly between an observer and the star it orbits, blocking some of that star's light. When the passage of the planet is behind to their host star is called an **occultation** or **secondary transit**. During the transit, the resulting dip in the stellar flux is called transit depth and it is directly proportional to the size ratio of star and planet. Thus, the ratio of the observed change in flux,  $\Delta F$ , to that of the stellar flux  $F$  can be expressed as:

$$\delta = \frac{\Delta F}{F} = \left(\frac{R_p}{R_\star}\right)^2 \quad (1.11)$$

Where  $R_\star$  is the radius of the star, and  $R_p$  is the radius of the planet. The effect measured during transit is relatively small. For example, for a Sun-like star, the transit of a Jupiter-size planet will cause a decrease in the apparent luminosity of about 1%, while this decrease will be of about 0.001% for an Earth-size planet.

To observe a transit, the inclination angle of the orbit must be almost exactly edge-on to the observer ( $i \approx 90^\circ$ ). Under the assumption that planetary orbits are randomly space-distributed, detecting a transit is only possible for a small fraction of planetary systems. Using the equation of the ellipse described Eq. 1.5, the probability of such transit can be calculated as

$$p = \frac{R_\star + R_p}{a} \left(\frac{1 + e \cos \nu}{1 - e^2}\right), \text{ where } R_\star \gg R_p, \text{ and } e = 0 \Rightarrow p \approx \frac{R_\star}{a} \quad (1.12)$$

Therefore, the probability of finding a planet at 1 AU distance orbiting a Sun-like star in a circular orbit is 0.5%. In the case of longer orbits, the probability of having a transit decreases linearly with the orbital distance. So the transit technique is most sensitive to short-period planets with large planet-to-star radius ratios.

In Figure 1.4 a schematic diagram of five confirmed transiting planets in the Kepler's field is shown. As mentioned above, in all cases, the amount of flux blocked by the transiting planets is below 1%. Also, an inspection of the transit light curve reveals that the transit shape is round-bottomed. This is because stars are not uniformly bright over their surfaces, instead, stars are brighter at their centers (of their 2D projection from our perspective) and fainter towards their edges. This effect is called limb darkening, and it is stronger at shorter wavelengths (leading to highly rounded transits in bluer bands) and less severe at longer wavelengths (producing a flatter transit shape in redder bands). Another interesting feature is that the decrease in brightness into transit is not instantaneous. Figure 1.5 shows an illustration of a transit. The total transit duration ( $t_T$ ) is the time between the first and the last planet-star contact ( $t_T = t_4 - t_1$ , ingress-egress), while the transit full duration ( $t_F$ ) measures the time that the planet is fully in front of the stellar disk ( $t_F = t_3 - t_2$ ). Based on the periodicity at which the transit occurs, we can derive the orbital period of the planet, and from the former observables ( $\delta$ ,  $t_T$ , and  $t_F$ ), it is possible to obtain the planet-radius, semi-major axis, and inclination (Seager & Mallén-Ornelas, 2003).

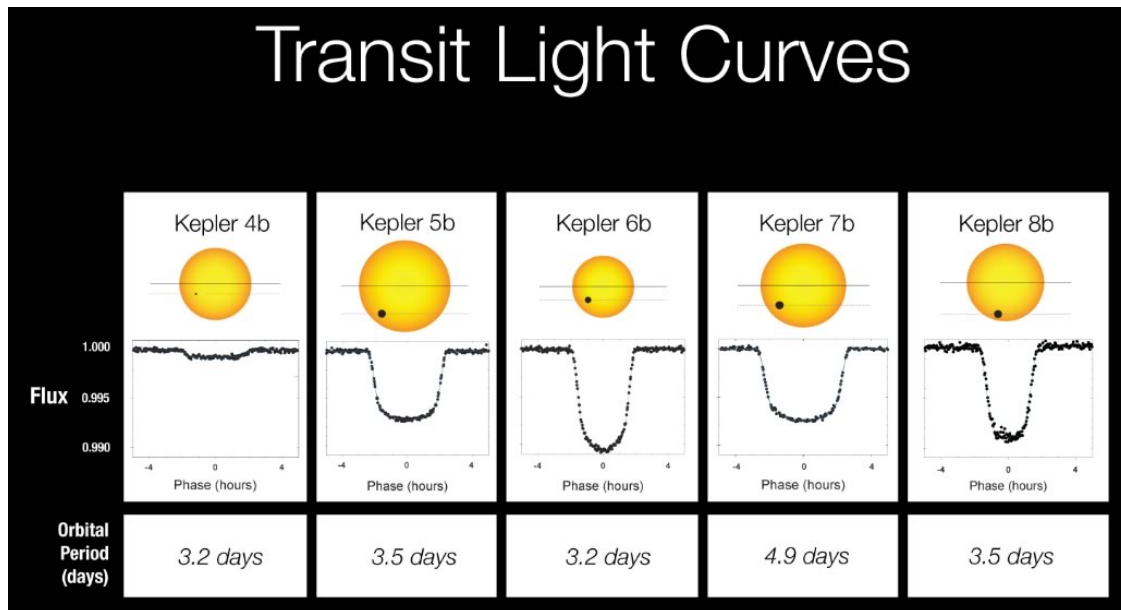


**Figure 1.4:** Schematic light curves for the first five planets discovered by *Kepler*. Image credit: NASA/*Kepler*

### 1.2.1 Follow-up efforts for transiting planets

During the transit, it is also possible to study the atmosphere of the planet through transit spectroscopy. When the planet crosses the star disk (transit), some light from the star will pass through the planet's atmosphere. By measuring the fraction of stellar light able to penetrate the atmosphere at different wavelengths during the transit, the atmosphere's chemical composition can be inferred, this technique is called **transmission spectroscopy** (Seager & Sasselov, 2000) and is the most frequently-used technique for the observation of exoatmospheres. Using the same concept explained for transmission spectroscopy, it is possible to measure the thermal emission and reflection from the planet during the occultation through **emission spectroscopy** (Kreidberg, 2018). In this case, a measure of the flux of the system that spans from moments before the occultation to moments after can be immediately converted into the relative contribution of the light coming from the exoplanet..

If a transiting planetary system hosts additional non-transiting planets, in some cases, it is possible to constrain their masses based on **transit timing variations** (TTV) (Agol et al., 2005; Holman & Murray, 2005). The basic idea of this technique is to measure variations in the predicted central time of the transit, which is attributed to the presence of other planets or exomoons that are gravitationally pulling the orbit of the transiting planet. Planetary systems with TTVs can be verified without requiring extensive ground-based observations, accelerating confirmation of planet candidates.

The transit method also allows us to learn about the orbital alignment with respect to the rotation axis of the star using the **Rossiter-McLaughlin effect** (RM, Rossiter, 1924; McLaughlin, 1924). The effect appears as an anomalous RV variation during the transit. In

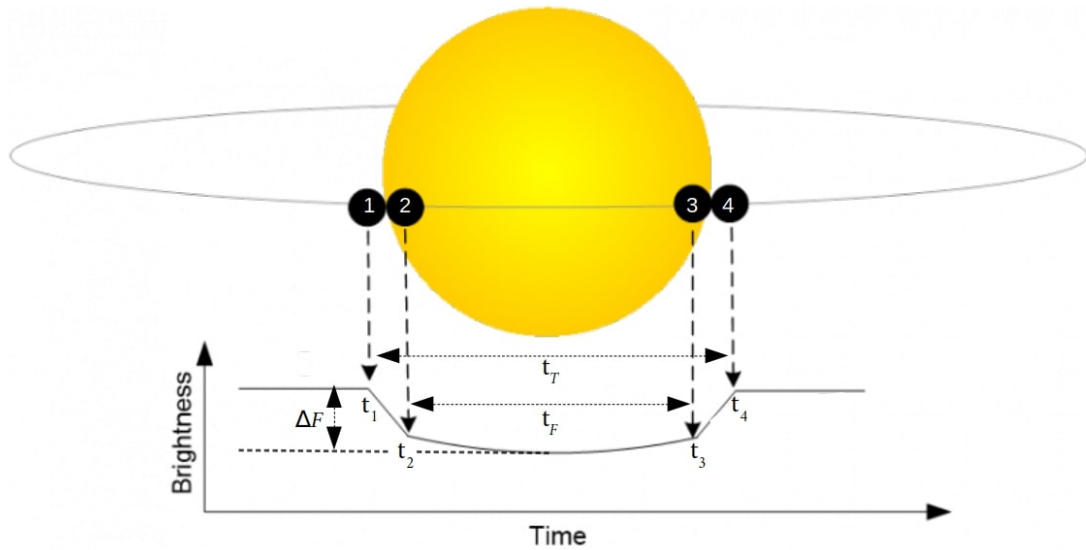


**Figure 1.5:** Illustration of an exoplanet transit. The total transit duration ( $t_T$ ) is the time between the first and the last planet-star contact ( $t_T = t_4 - t_1$ ), while the transit full duration ( $t_F$ ) measures the time that the planet is fully in front of the stellar disk ( $t_F = t_3 - t_2$ ).  $\Delta F$  correspond to observed change in flux.

a rotating star, one of its sides is approaching the observer while the other recedes. Thus, while the planet transits, it will cover different star sections sequentially, perturbing the relative light contribution of the different hemispheres. For example, if the planet blocks the light from the approaching side of the star, the average flux received by the observer will appear offset rewards, creating a positive shift in the RV measured for the star, deviating from the standard Keplerian RV curve (Triaud, 2018).

## 1.2.2 The era of space-based exoplanet missions

The first space mission to look for exoplanets using the transit method was *CoRoT* (Convection, Rotation, and planetary Transits: Barge et al., 2008). The mission's main objective was to continuously observe stars in the field of the Milky Way to search for large-terrestrial sizes exoplanets with short orbital periods. As a result, the first rocky exoplanet was discovered in 2009 (CoRoT-7 b; Léger et al., 2009). During its active operations between 2007 to 2012, *CoRoT* revealed several hundred extrasolar planets candidates, 34 of which were successfully confirmed by RV measurements.

In 2009, the *Kepler* mission (Borucki et al., 2010a) was launched. The principal goal was to survey a portion of the galaxy to determine what fraction of stars might harbor potentially habitable, Earth-sized planets. During the mission, *Kepler* detected thousands of transiting planets and contributing to other areas of Astronomy such as asteroseismology. Finally, in 2018, after nine years of operations, the *Kepler* mission ended, and left behind a rich legacy and valuable lessons about planetary formation and evolution. For example, the mission detected a variety of transiting planets, including hot- and warm-Jupiters, Neptune-sized planets, and Earth-sized planets. It also showed us that there are more

# 1 Introduction

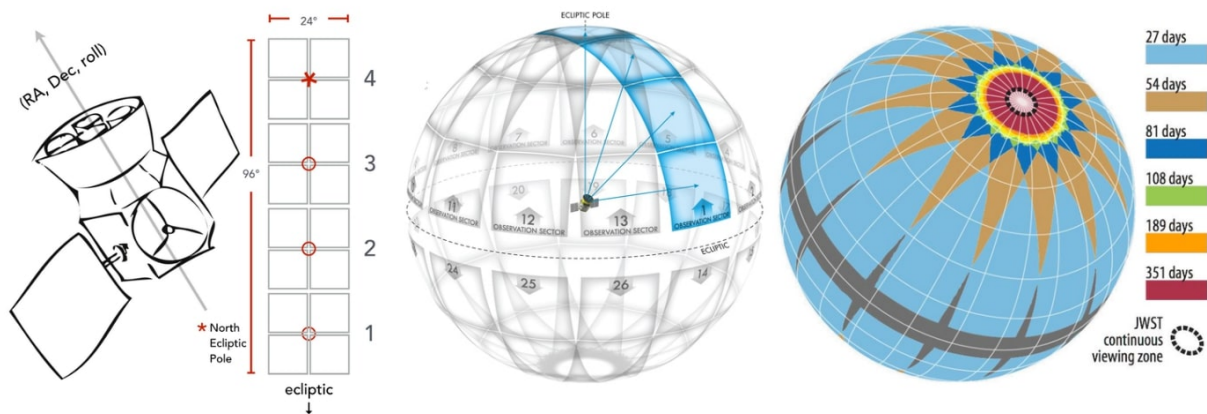


**Figure 1.6:** Illustration of *TESS* sky coverage map. The survey is spitted into 26 observation sectors, each sector being  $24\text{deg} \times 96\text{deg}$ , with an overlap of sectors at the ecliptic poles to allow additional sensitivity toward smaller and longer-period exoplanets in that region of the celestial sphere. The spacecraft spend two 13.7-day orbits observing each sector, mapping the southern hemisphere of sky in its first and then the northern hemisphere. credits: NASA/*TESS*.

planets than stars in our Galaxy, opening new horizons in the field of the extrasolar planets.

Subsequently in 2018, the *TESS* mission (Transiting Exoplanet Survey Satellite; [Ricker et al., 2014](#)) was launched. The mission was designed to survey over 85% of the sky (an area of sky 400 times larger than that covered by *Kepler*) with the principal goal to detect small planets with bright host stars in the solar neighborhood, which the aim was to provide precise planetary mass for 50 planets with radii  $<4 R_{\oplus}$ .

Planets detected around bright stars are suitable for further characterization with follow-up observations, allowing us to perform a detailed and accurate characterization of the planet physical properties (mass, radius, density, orbital misalignment, atmospheric composition, etc.), using high cadence photometric and high-resolution spectroscopic observations from the ground. During the past two-year primary mission, *TESS* monitored over 200.000 main-sequence dwarf stars and mapped the whole sky in pointings of 27 days each (Fig. 1.6), producing a large stellar catalog with transiting planets (e.g., [Bluhm et al., 2020, 2021](#)). After the huge success of the primary mission, the mission is ongoing and will be extended until September 2022. Currently, *TESS* has confirmed 167 planets<sup>4</sup>, in addition, more than 4000 planets candidates are waiting for confirmation.

The combination of this information with the valuable astrometry from *GAIA* ([Gaia Collaboration et al., 2020](#)) will help characterize a vast sample of stars, improving our understanding of planet-star connections, emphasizing that stellar knowledge is a fundamental key to better understanding exoplanets formation, evolution, and habitability.

Additionally, the *CHEOPS* mission (CHAracterising ExOPlanets Satellite; [Benz et al., 2021](#)), will further improve the determination of the physical properties of low-mass planets

<sup>4</sup>November 1, 2021, according to the NASA Exoplanet Archive

detected by *TESS*, and potentially detect additional planets and exomoons in these planetary systems. Future space missions like *PLATO* (PLANetary Transits and Oscillations of star; [Rauer et al., 2014](#)) focusing on detecting terrestrial exoplanets in the habitable zone of solar-type host stars, will help us to characterize their bulk properties and therefore will provide the information needed to determine their habitability. Finally, the launch of *JWST* (James Webb Space Telescope; [Gardner et al., 2006](#)) will characterize the atmospheres of many exciting extrasolar systems, which will shed light on the building blocks of life in planets beyond the Earth.

### 1.3 Exoplanet demographics

The study of exoplanets demographics comprises the study of occurrence rates and physical parameters of planetary systems, and how these quantities depend on the physical properties of the host star. Mathematically, the distribution of a given set of physical properties can be defined as:

$$\frac{d^k N}{d\vec{\alpha}}, \text{ where } \vec{\alpha} = \{\alpha_1, \alpha_2, \alpha_3, \dots, \alpha_k\} \quad (1.13)$$

Where  $\vec{\alpha}$  represents physical planetary parameters as radius ( $R_p$ ), mass ( $M_p$ ), semi major axis ( $a$ ), period ( $P$ ), eccentricity ( $e$ ), inclination angle ( $i$ ), multiplicity, etc.

$$\vec{\alpha} = \{M_p, R_p, P, a, e, i, \text{multiplicity}, \dots\} \quad (1.14)$$

The distributions of the planetary parameters depend on the properties of the host stars, and this connection is key to understand the planet formation, migration mechanisms, dynamical interactions, and orbital evolution of planetary systems. However, understanding the host stars is not an as simple endeavor, as it requires a good understanding of the galaxy itself. Stars are not located randomly across the Galactic disk. Spiral arms host younger stellar populations, which tend to be more metal-rich, as they form from the recycled intergalactic medium ([Sánchez-Menguiano et al., 2020](#)). As they also host a larger gas and dust reservoir, sight-lines that pass through spiral arms are subject to higher extinction values than those that do not pass through these structures. Therefore, in simple words, “a better understanding of the host star implies that we can better understand the planet”, so developing highly accurate instruments which can provide detailed physical stellar properties are mandatory to achieve this goal.

One of the first results regarding exoplanet demographics was the called giant **planet-metallicity correlation** ([Fischer & Valenti, 2005](#)), where the frequency of giant planets ( $R_p \gtrsim 8 R_\oplus$  or  $M_p \gtrsim 0.3 M_J$ ) increases with the stellar mass and have a positive correlation at super-solar metallicities ( $[\text{Fe}/\text{H}] > 0$ ). In contrast, planets smaller than Neptune or sub-Neptunes ( $R_p \gtrsim 1\text{--}4 R_\oplus$ ) form around stars with a wide range of metallicities ([Udry et al., 2006](#); [Sousa et al., 2008](#); [Buchhave et al., 2012](#)), and occur more frequently around lower-mass stars ([Howard et al., 2012](#); [Mulders et al., 2015](#)). Additionally, several studies have shown that the planet occurrence rate of sub-Neptunes steeply increases towards low mass stars, being systematically higher around M dwarfs than in -F,-G, and -K stars. A schematic representation of the distribution of exoplanets frequency as a function of stellar mass and

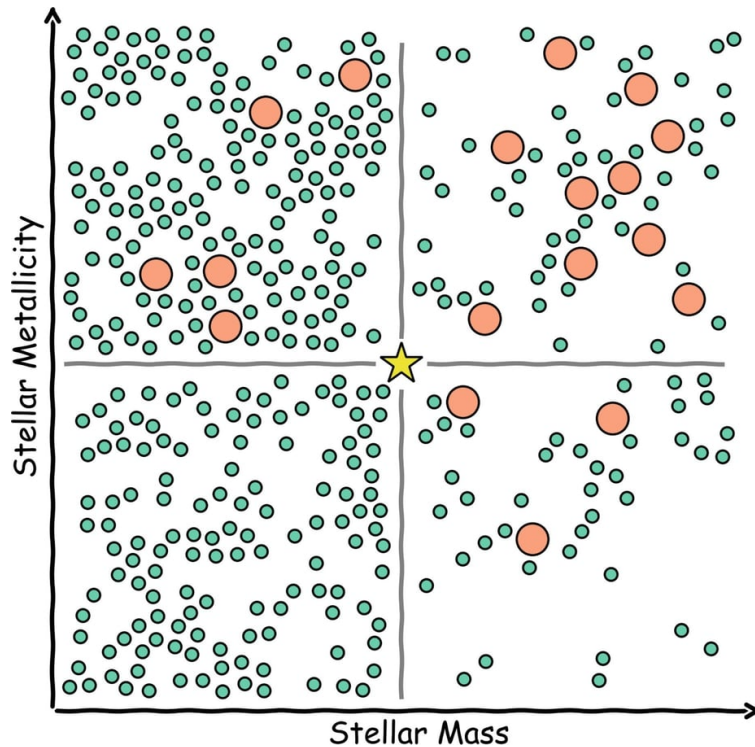


**Figure 1.7:** The diagram illustrates the different behavior of the giant planet population (pink circles) and planets smaller than Neptune (cyan circles) in the exoplanet population as a function of stellar mass and metallicity. The location of the Sun is indicated with a yellow star. Credits: [Mulders \(2018\)](#)

metallicity is shown in Figure 1.7, but “What does this entail?”. From the **planet formation theory**, it is expected that more massive stars host more massive exoplanets compared with less massive stars. This could be explained as massive stars host more massive protoplanetary disks, resulting in a higher giant-planet occurrence rate.

Under the general assumption that protoplanetary disks have the same metallicity from the parental molecular cloud, it is reasonable to believe that the planetary occurrence rate and planet properties may be correlated with the host star metallicity. Due to the fact that giant planets only form in protoplanetary disk with sufficient amount of material, the **core accretion** scenario is highly supported by the giant planet-metallicity correlation, in which the time scale for core growth depends on the amount of material locally available in the disk (e.g., [Pollack et al., 1996](#); [Ida & Lin, 2004](#)). Here, the rocky protoplanet core accretes planetesimals (many times its mass in gas) from the protoplanetary disk, yielding eventually the accretion of a surrounding H-He envelope ([Chabrier et al., 2014](#)).

In contrast with the core accretion theory, the different scaling relations between mass and metallicity for sub-Neptunes seems to indicate a different formation process. Several planet formation mechanisms have been proposed to explain the presence of small planets at short orbital periods. The two most relevant here are **in-situ formation** and **planet migration**.

The first scenario is based on the terrestrial planet formation in the Solar System, where the final total planet mass depends on the local surface density of the protoplanetary disk, so it is necessary to have a protoplanetary disk massive enough that allows to planetary embryos

can grow to a fraction of the final planet mass. On the other hand, the planet migration hypothesis is supported by theoretical simulations where the planets are formed farther out in the disk and, during or after formation, migrated inward to their present positions through interactions with the protoplanetary disks. However, until today, the formation location of sub-Neptunes planets is not well established.

### 1.3.1 Exoplanet statistics: The observed properties and distributions

Since the *Kepler*, *K2*, and *TESS* transiting missions were launched, the discovery of thousands of exoplanets of all sizes around a variety of star types has been revealed that our system appears to not be as much of a common configuration when compared to those of other, detected multi-planetary systems. Furthermore, thanks to the combination of multiple detection techniques, the exoplanet field has rapidly transitioned in the last years from discovering exoplanets to characterizing them, further allowing us to study the properties of exoplanet demographics.

One of the exciting features from Fig. 1.8 is to notice how the detection techniques are more sensitive to different planets populations. While the transit method seems to be more sensitive to detect planets with short orbital periods, the RV technique appears to be capable of detecting both kinds of planet populations, those that have shorter periods and those that have longer ones. However, it is not surprising that the methods for detecting exoplanets can be biased. Most of them are more sensitive to the size or the planet’s mass, resulting in a combining total sample principally biased to larger objects with short orbits. Therefore, it is imperative for observational biases to be taken into account in order to make a bonafide interpretation of the distribution of different planet parameters.

Despite these multiple biases, several groups of planets can be identified in Fig. 1.8. Below, I summarize some of the most important planet populations:

- There is a large population of massive planets (gas giants; GP)  $\gtrsim 100 M_{\oplus}$  which is separated of sub-stellar **brown dwarfs** (BD) close to  $\sim 13 M_J$ , the mass limit where objects are able to fuse deuterium<sup>5</sup>.

It is widely recognized that GPs and BDs arise from two different formation mechanisms. While BDs appear to form from the fragmentation of a molecular cloud, GPs arguably formed either by core accretion or **gravitational instability**, in which part of the protoplanetary disk become gravitationally unstable and lead eventually to the formation of giant planets (e.g., [Boss, 1997](#); [Durisen et al., 2007](#)). Also, according to the distinct formation scenarios, planets should have a substantial enrichment in heavy elements compared with their parent star, whereas BDs of the same mass should have the same composition as their parent cloud.

- The GP planet population is split into two sub-populations, the **hot Jupiters**, with periods  $\lesssim 10$  d, and the **cold Jupiters** with periods longer than  $\gtrsim 300$  d.

Investigations of the origins of hot Jupiters orbiting in close-in orbits, reveals that they can form either by in-situ formation (e.g., [Lee et al., 2014](#)), or planet migration

---

<sup>5</sup>According to the International Astronomical Union (IAU)

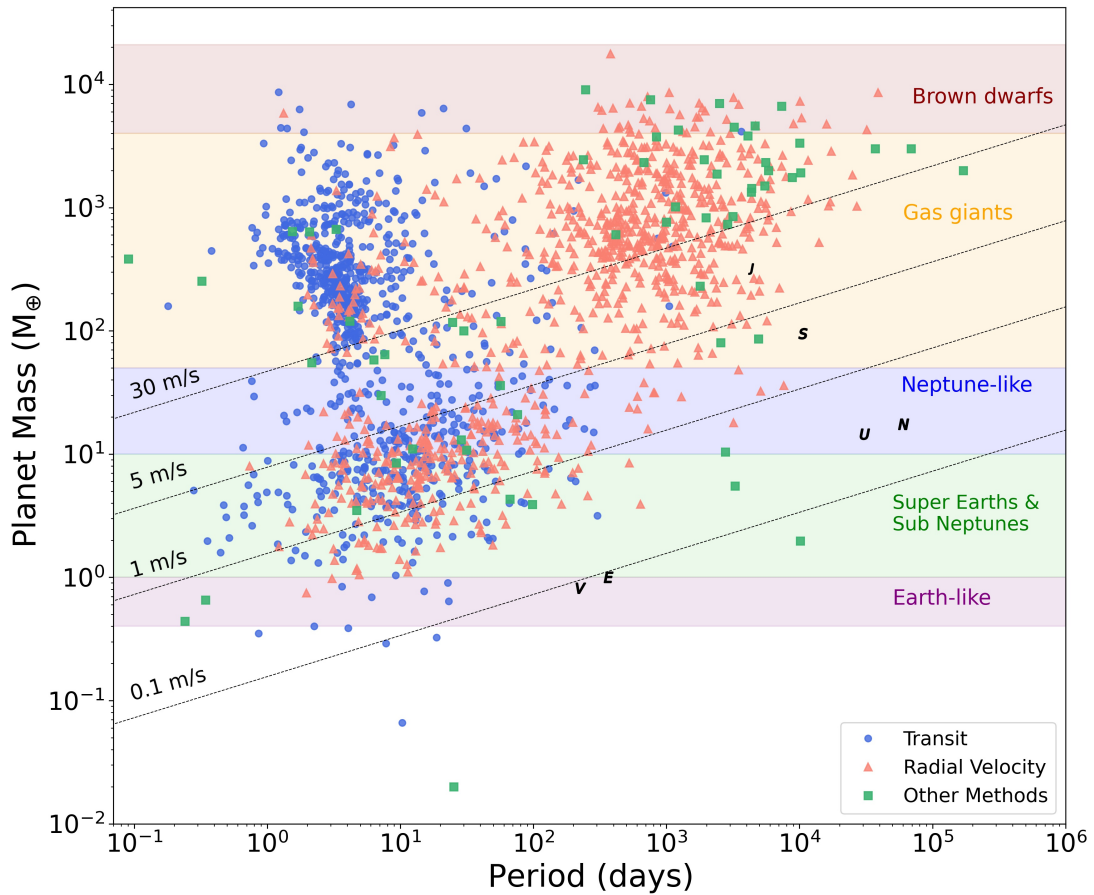


**Figure 1.8:** Planetary mass distribution as a function of the orbital period for planets detected by transit method (blue circles), the RV technique (red triangles) and other methods (green squares). The four dashed lines represent the RV semi-amplitude ( $K$ ) following Eq. 1.10 assuming a  $1 M_{\odot}$  and zero eccentricity. Solar system planets are shown for reference, and the colored zones mark the limit between different planet populations. The data was taken from the NASA exoplanet archive, November 19, 2021.

mechanism (Baruteau et al., 2014). However, from the in-situ formation theory it is unclear how exactly the large cores could form so close to the host star, not only because the growing zones are small, and the locally available solids are insufficient (e.g., Schlichting, 2014), but also because at these conditions the accretion stalls at a much lower mass.

Due to the large planet-to-star mass ratio, hot Jupiters are the easiest planets to detect. Ground-based RV and photometric surveys have deeply explored this population, and today we count with hundreds of detections.

- The **cold Jupiters** population is located at a much larger separation than hot-Jupiters, starting at about 300 days to several astronomical units (AU). It is composed of temperate to cold giants and includes planets like Jupiter (shown as reference). Here, it is essential to highlight that most of these planets were found by RV measurements. Not only because follow-up transiting planets from the ground with long-time baselines is expensive, but also due to in-space surveys like *Kepler* or *TESS*, which can detect giant planets at a few hundred days, this population has a lower transit geometric probability (Eq. 1.12) (Santerne et al., 2016) difficulting their detection.
- Also, it can be noticed that there is a lack of GP planets orbiting between  $\geq 10$  to 100 days. This transition is known as the **period valley**, was first identified by Udry et al. (2003) based on RV detections. The origin of this valley could be explained by **type II migration**, where giant planets open gaps in their protoplanetary disks, separating the inner from the outer disk (Lin & Papaloizou, 1986). Once the gap is open, the planet is repelled inwards by the outer disk and outwards by the inner disk. Thus, the final location of the planet would be where the torques from the inner and outer disks cancel out. However, because the gas on both sides of the gap moves towards the star, and as long as the disc remains viscous, the planet is also will be pushed in.

However, after the *Kepler* mission, this valley turns less pronounced. One explanation for this behavior could be that the extrasolar giant planets with orbital periods between 20-100 days detected by the *Kepler* mission, belong to multiple planetary systems. These additional planets might have stopped their migration in the period valley and did not end as hot Jupiters; this mechanism is believed to play a role in the mutual interaction of Jupiter and Saturn in the Solar System. (Morbidelli & Crida, 2007).

- Additionally, from Fig. 1.8 and moving to lower masses, we found the **Neptune-like** planets, ice giants, which are similar in size to Neptune or Uranus. Neptunian-like planets typically have hydrogen and helium-dominated atmospheres with cores of rock and heavier metals.

Observational surveys show that most of these planets were found in shorter orbits. However, this result might be interpreted as an observational bias caused by the current insensitivity of the detection techniques at long orbital periods.

- Also, there is a paucity of very short period ( $P \lesssim 3$  days) giant and Neptune-like planets. This desert is fully described in Mazeh et al. (2016) and in this case, an observational bias cannot explain this behavior since these systems should be easily detected by transit and RV techniques. Two main hypotheses that have been proposed to explain

this desert. The first could be due to the strong stellar radiation that receives low mass giant planets, thus the outer planets layers are evaporated, losing a significant fraction of its atmosphere. As a consequence, the remnants of photo-evaporated hot Jupiters could be short-period super-Earths.

A second hypothesis proposes that the distance at which planets stop their migration depends on the planet mass (Chang et al., 2010). In this case, the migration driven by the interaction between planet and disk is stopped in the disk’s inner edge. This could be explained because, at that point, the disk is not dense enough to continue pushing the planets inward. One possible explanation might be due to the creation of a central hole in the accretion disk induced, e.g., by the stellar magnetic field. However, the absence of planets is currently under debate.

- Moving to masses between 2 and 10  $M_{\oplus}$  we found a population of **sub-Neptunes** and **super-Earths**. Those are larger than Earth but smaller than Neptune. The main differences between them depend on their bulk densities, while the sub-Neptunes still have a substantial atmosphere and may have a significant contribution of water. The super-Earths are predominantly rocky and have a small or no atmosphere. In this case, the super-Earths name only references an exoplanet’s size and does not suggest they are necessarily similar to our planet.

Observations have revealed that super-Earths are the most abundant type of planets in the inner systems. Their formation is strongly linked to the structure of the protoplanetary disc, which determines growth and migration. Current theories of planet formation, suggests that these planets are formed by planetary embryos which by oligarchic growth collide with one another to complete planets (Lambrechts et al., 2019). They are typically formed exterior to the water ice-line<sup>6</sup> and migrated in into the inner region close to the central star. However, whether this migration covered several AU or only a factor of a few of their current locations remains to be established (Bitsch et al., 2019). More about sub-Neptunes and super-Earths will be detailed discussed in the next Sec 1.3.2.

- **Terrestrial planets** (Earth-sized and smaller) are rocky worlds, composed of rock, silicate, water, and/or carbon, and have very thin or no atmospheres. Today, only  $\sim 168$  of terrestrial planets has been discovered<sup>7</sup>, where seven of them orbit the famous M dwarf star TRAPPIST-1 (Gillon et al., 2017). In this case, TRAPPIST-1 e, f, and g are located in their star’s habitable zone. However, these seven planets are tidally locked<sup>8</sup>. As a result, they likely have weather patterns totally unlike those on Earth, such as strong winds and extreme temperature changes. Thus, despite TRAPPIST-1 hosting some exciting prospects, its planets are not Earth’s twins. However, the TRAPPIST-1 system provides one of the best opportunities to study the planet’s atmospheres using the upcoming *JWST*.

---

<sup>6</sup>Correspond to the distance from a central protostar at which ice grains can form

<sup>7</sup>November 22, 2021, according to the NASA Exoplanet Archive

<sup>8</sup>The equal time it takes for an astronomical body to rotate around its axis as it revolves around its host star, showing the same face toward the object it is orbiting.

Finally, size and mass play a crucial role in determining planet classification. Each planet type varies in interior and exterior appearance depending on its composition, which is directly related to the physical characteristics of their host star.

### 1.3.2 Planet size distribution

One of the first revelations made by *Kepler* mission was the large amount of planets with radii smaller than Neptune but larger than Earth ( $R_p = 1 - 3.9 R_\oplus$ , Batalha et al. (2013)). Our Solar System has no example of these intermediate planets; nevertheless they are by far the most common sample in the confirmed exoplanet reported up today. This fact reflects that we are just beginning to reveal the diversity of exoplanets outside our solar system. The large number of exoplanets discovered, will help us puzzle out the current questions regarding their formation and evolution.

Figure 1.9 shows the distribution of confirmed planets with radius less than  $30 R_\oplus$ , and periods less than 400 days<sup>9</sup>. If we focus the attention on planets with  $R \leq 4 R_\oplus$ , is clear to see that intrinsic radius distribution is dependent on the orbital period (Foreman-Mackey et al., 2014; Hsu et al., 2018), where the planet frequencies tend to increase from planets with large radii and small period (upper left) toward the small radii and large period (lower right).

### 1.3.3 The radius-gap

An important discovery revealed by *Kepler* mission, was that the bimodality in the frequency of small and close-in planet sizes ( $R \leq 4 R_\oplus$ ) (Fulton et al., 2017). This bimodality is marked by a paucity of planets with sizes between  $\sim 1.6 - 2 R_\oplus$  and is called “**radius gap**” or “**radius valley**”, and would marks the transition from a large population of sub-Neptunes with significant H-He envelopes a to a small population of rocky super-Earths. The gap was theoretically predicted by several groups (e.g., Owen & Wu, 2013a; López & Fortney, 2013; Chen & Rogers, 2016), and recently observed by the California-Kepler Survey (CKS) team.

Figure 1.10 shows the radius distribution of a sample of 1305 F, G, and K host stars with measurements in star radius better than 10%, derived by CKS team. While sub-Neptunes has typically radii between  $2 - 4 R_\oplus$ , super-Earths have their peak at  $1 - 2 R_\oplus$ . The radius gap is easily visible between this two populations.

After this discovery, Van Eylen et al. (2018), also observed the radius gap using a smaller but better constrained sample of 117 stars, confirming the results found by the CKS team. More recently and thanks to precise parallaxes from *GAIA* mission, uncertainties in stellar radii of CKS team was improved, followed by more detailed investigations of the gap, which was extended and related it as a function of stellar mass (Fulton & Petigura, 2018), metallicity (Owen & Murray-Clay, 2018), planet orbital period, and stellar incident flux (Berger et al., 2018).

The location and depth of the gap are important signatures of the physical processes that form and sculpt planets. In particular, planets residing in the radius gap are valuable probes of these processes as they may undergo the final envelope loss stages. Several studies explore

---

<sup>9</sup>According to NASA exoplanet archive, November 19, 2021.

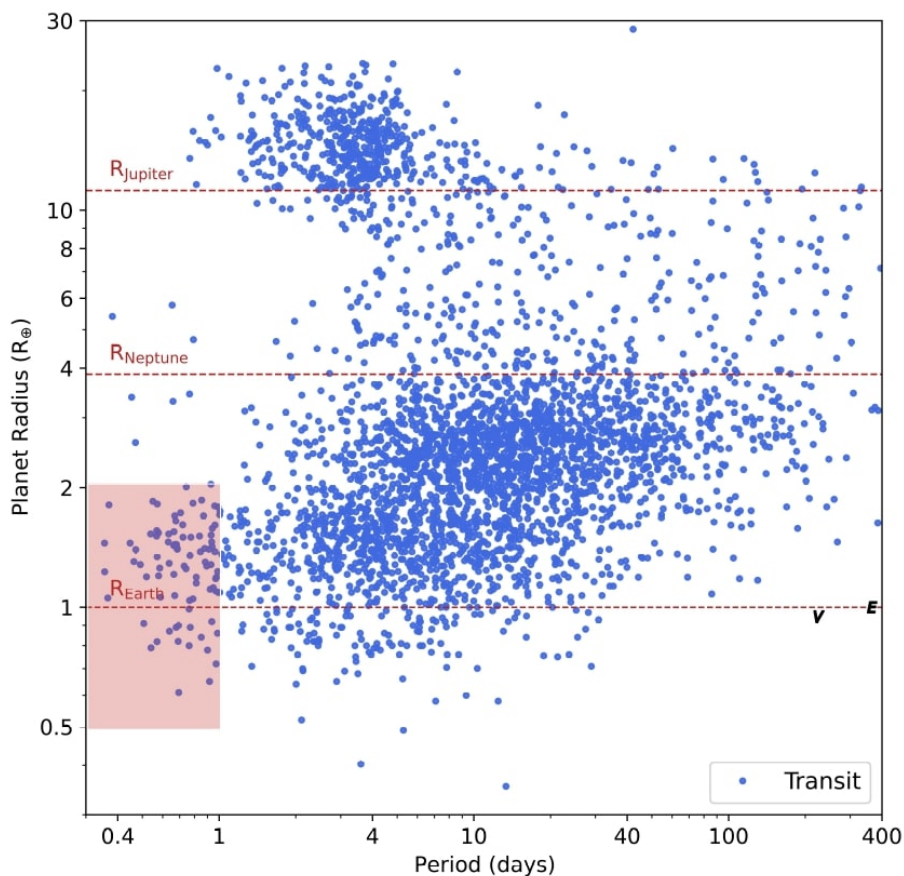


**Figure 1.9:** Distribution of confirmed planets with radius  $\leq 30 R_{\oplus}$ , and periods  $\leq 400$  days. Horizontal dashed lines marking the radius of Jupiter, Neptune, and Earth. Venus and Earth are included for reference. The red area encloses the ultra-short-period planets (USPs).

the radius gap dependence on host star properties, and are two leading theories that can effectively explain the dependence of the gap with stellar mass, orbital period, incident flux, and age. These theories are: **photoevaporation** and **core-powered mass loss**. In the first case, the atmospheric evaporation is driven by high-energy photons from the host star (Owen & Wu, 2013a, 2017; Lopez & Rice, 2018; Wu, 2019a), and predicts that higher mass stars will strip larger planetary envelopes at fixed incident flux. The second mechanism, the planet’s internal luminosity is which drives the loss of its atmosphere (Ginzburg et al., 2016, 2018), where the source of this luminosity would be the planet’s primordial energy from formation (Gupta & Schlichting, 2019, 2020). In this case, the theory doesn’t predict a trend in stellar mass at constant incident flux, providing a useful difference in demographic predictions.

Despite the difference of energy source for each mechanism, the two models predict very similar observable signatures in the exoplanet demographics and predict similar slopes to the radius valley as a function of host stellar mass and incident flux. Figure 1.11 shows the predicted radius gap for photoevaporation and core-powered mass loss models, for a set of modeled planets, as a function of these two physical parameters. As can be seen, both models are capable of reproducing the observed general demographics of close-in exoplanets and are essentially indistinguishable.

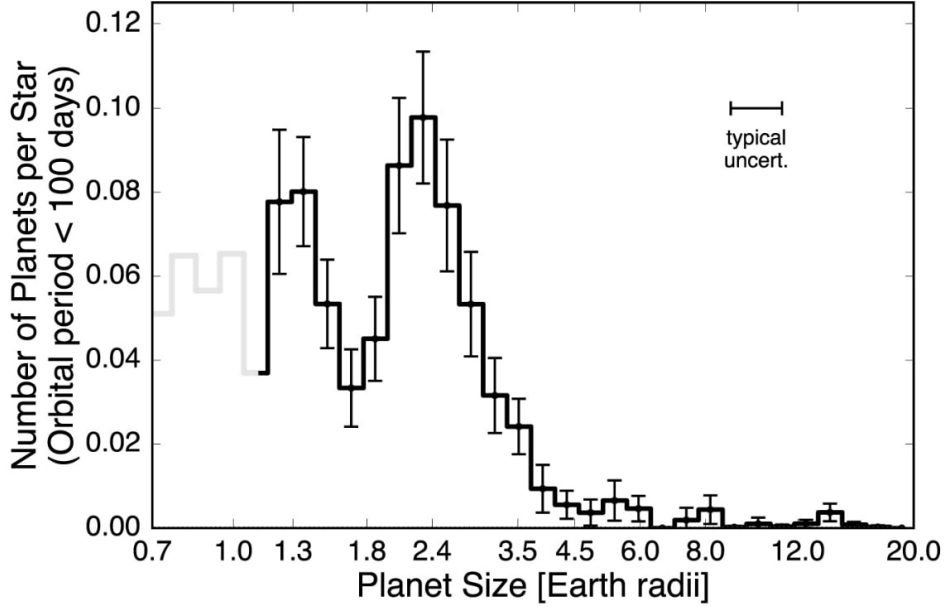


**Figure 1.10:** Histogram distribution of detected *Kepler* planets with radii  $\leq 4 R_{\oplus}$  and periods less than 100 days. Credits: [Fulton et al. \(2017\)](#)

In a very recent study, [Rogers et al. \(2021\)](#) propose a new method to compare the photoevaporation versus the core-powered mass-loss models through a 3D radius gap, and they compare their predictions with available CKS data. As discussed earlier, the comparing models need to be in to disagree on how the radius gap behaves as a function of stellar mass ( $M_{\star}$ ) at fixed incident bolometric flux ( $S$ ). Therefore, making a 3D comparison would reveal which of the models will better describes between this two planet populations. With this purpose, the authors define a new parametrization which describes the position of the radius gap as a joint power law as follow:

$$R_{val} \propto S^{\alpha} M_{\star}^{\beta}, \text{ with } \alpha \equiv \left( \frac{\partial \log R_{val}}{\partial \log S} \right)_{M_{\star}}, \text{ and } \beta \equiv \left( \frac{\partial \log R_{val}}{\partial \log M_{\star}} \right)_{S}, \quad (1.15)$$

where  $\alpha$  and  $\beta$  are key mass-loss parameters and can be used to distinguish between photoevaporation and core-powered mass-loss. From theoretical predictions,  $\alpha$  is expected to be similar for both models. On the other hand,  $\beta$  is expected to vary significantly between the two models, taking negative values for scenarios where the mass loss is driven by photoevaporation, and close to zero when it is driven by core-powered mass-loss.

However and despite their efforts, their results were not conclusive, as the data does not significantly favor one model over the other. Based on simulations, the author propose to increasing the number of well-characterized planets to  $\sim 5000$  would be needed in order to discern between both models. Additionally, to truly understand which mechanism is responsible for this bimodal behavior, a higher number of planets extended to M dwarfs is required.

Currently, observational studies have not yet been able to differentiate between these two theories. To distinguish between them, a sizable sample of systems hosting planets with

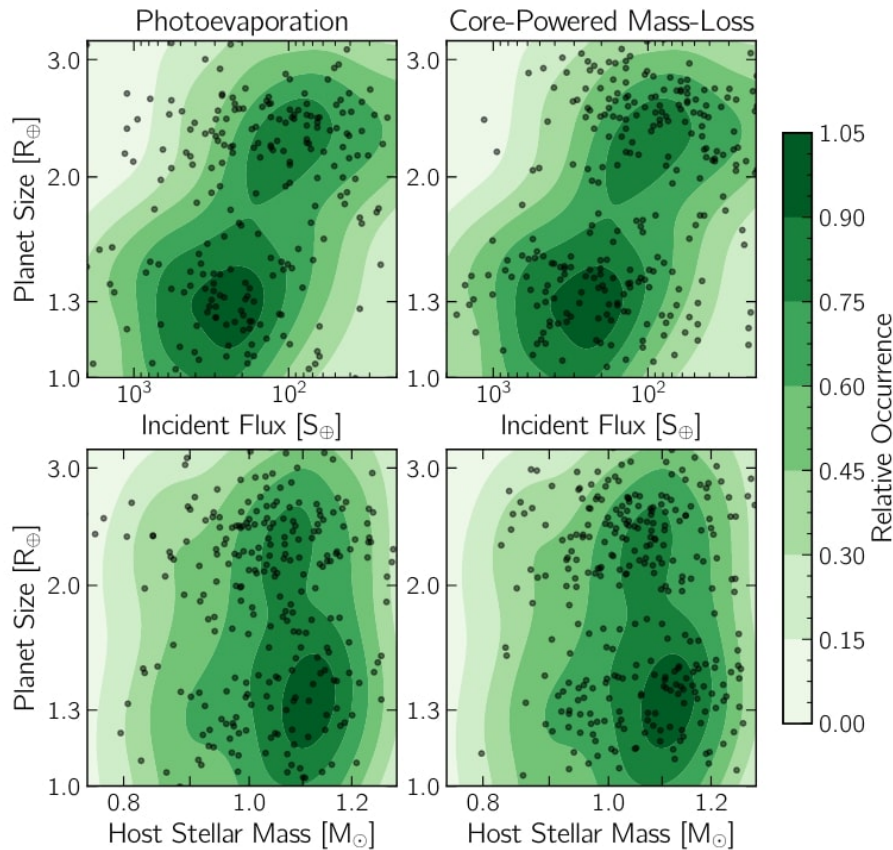


**Figure 1.11:** The radius gap is shown as function of incident bolometric flux (top row) and host stellar mass (bottom row). Where green contours represent relative occurrence of the observed CKS planets (Fulton et al., 2017). Black points represent forward modelled planets from the photoevaporation model (Owen & Wu, 2013a)(left) and core-powered mass loss model (Ginzburg et al., 2016) (right). Clearly both models can reproduce the distribution of observed planets with the radius gap in the correct location and similar slopes. Credits: Rogers et al. (2021).

radii above and below of the radius gap are needed. Unfortunately, only a few systems with these characteristics are currently available (Dumusque et al., 2019; Cloutier et al., 2020a; Nowak et al., 2020a; Van Eylen et al., 2021).

However, thanks to the *TESS* mission, recent studies started to extend the sample of well-characterized planets around low-mass stars. For example, Van Eylen et al. (2021) compared the current properties of radius gap with planets orbiting M dwarfs. In their previous work he determined that the location of the radius valley as a function of orbital period has a slope of  $m = -0.09_{-0.04}^{+0.02}$ , and  $a = 0.37_{-0.02}^{+0.04}$  for  $\log m = m \log P + a$  (Van Eylen et al., 2018), and now the slope would have a value of  $m = -0.11_{-0.05}^{+0.04}$  and a intercept of  $a = 0.30_{-0.03}^{+0.05}$ . Additionally, he found that the gap is located at slightly smaller planet radii for the same orbital period. Thus, the predictions from the models start to slightly diverge towards low-mass stars.

In Chapter 2, I present TOI-1235 b and interesting planet which period and radius place it inside of the radius gap. The rocky composition determined for TOI-1235 b makes it

consistent with thermally-driven atmospheric mass loss scenarios (i.e. photoevaporation or core-powered mass loss).

To remark the impact that this discovery has in the exoplanet community. Following the announcement of the TOI-1235, multiple teams began pursuing its mass characterization through the *TESS* Follow-up Observing Program (TFOP), where another collaboration has also submitted a paper presenting their own RV time series and analysis (Cloutier et al., 2020b). Although the submissions of these complementary studies were coordinated between the two groups, their respective data, analyses, and write-ups, were intentionally conducted independently.

### 1.3.4 Ultra-short-period planets

Besides the planets population described in Section 1.3, one interesting feature in the radius-period plane are the planets with radii between  $0.5\text{--}2 R_{\oplus}$  and periods  $P \leq 1$  day. These planets are marker in Fig. 1.9 with a red rectangle, and are known as **ultra-short-period** planets (USPs). However, the defining criterion of one day is arbitrary, and was chosen by Winn et al. (2018) mostly because, at one day corresponds to an equilibrium temperature  $\sim 2000$  K (for a Sun-like host star), which is hot enough to sublimate dust grains, and also due to this is relatively unexplored planet population. Currently, a number of 114<sup>10</sup> of these planets have been discovered mostly by transiting missions. Statistical analysis based on *Kepler* data, reveals that about one out of 200 Sun-like stars (G dwarfs) has an USP planet, where the occurrence rate for planets larger than  $0.84 R_{\oplus}$  and periods shorter than one day was found to be  $(0.51 \pm 0.07)\%$  (Sanchis-Ojeda et al., 2014), a recent study also based in *Kepler* sample derived a occurrence rate of  $(0.39 \pm 0.04)\%$  (Zhu & Dong, 2021), which was in good agreement with previous results.

Several formation models have been proposed to explain the origin of these planets. One theory is that they are the remnant cores of giant planets, which may be attributed to photoevaporation as the planets are intensely irradiated. There are some observational parallels between USP planets and hot Jupiters (for details see Sec 1.3.1). First, hot Jupiters occur about  $\sim 1\%$  compared with  $\sim 0.5\%$  of USP on F, G, K stars, making them slightly less abundant. Second, both have a lack of close neighbors, and some studies have shown that either seem to have outer companions (e.g., Knutson et al., 2014; Steffen & Coughlin, 2016). Nevertheless, the true multiplicity for USPs rate is probably much higher, since USPs can be largely misaligned relative to the outer planetary companion (Dai et al., 2018; Petrovich et al., 2019). However, while hot Jupiters preferentially orbit around metal-rich stars, the USPs have not a direct association with stellar metallicity.

Another scenario proposes that USP planets may be the exposed cores of sub-Neptunes that have arrived at their current locations without losing much of their initial mass (Lundkvist et al., 2016). Lee & Chiang (2017) proposed a model that reproduced planet occurrence as a function of the period in which proto-USP planets are brought to their observed locations by the gradual decay of the orbit due to the tidal dissipation within the host star. Other models do not rely on tidal dissipation within host stars to explain the formation of USP planets and instead appeal to tidal dissipation within other planets.

---

<sup>10</sup>November 9, 2021, according to the NASA Exoplanet Archive

Here the proto-USP planet may reach an eccentric (and misaligned) orbit by dynamical interactions in multiple-planet systems, and then the undergo orbital circularization due to tidal effects (Schlaufman et al., 2010; Petrovich et al., 2019; Pu & Lai, 2019). However, how the planets get so close to the stars remains without an answer.

More details about this interesting planet population is presented in Chapter 3, where I presented an unusual transiting USP discovered as a transiting in *TESS* data, with an outer non-transiting planet candidate with a longer period.

### 1.4 M Dwarfs: Challenges and opportunities of planet hosts

M dwarfs are the most abundant class of stars in the solar-neighborhood (Chabrier & Baraffe, 2000; Winters et al., 2015), as it is estimated that they constitute more than a 70% of the stars in our galaxy (Henry et al., 2006, 2018). Their effective temperatures, sizes, and luminosities are within the ranges of 2300 – 4000 K, 0.1 – 0.6  $R_{\odot}$ , and 0.0002 – 0.08  $L_{\odot}$ , respectively (Cifuentes et al., 2020).

Their convective interiors make the fusion process slower compared to larger stars such as the Sun. Therefore, their lifespan is extremely long, and can remain in the main-sequence for tens of billions of years (Adams & Laughlin, 1997). Their cooler temperatures allow the formation of simple molecules such as water, methane, titanium oxide, and many others, which leaves prominent spectral features, hindering the accurate determination of atmospheric parameters in these stars (for details see; Passegger et al., 2018).

However, M dwarfs offer clear observational advantages. Due to their smaller masses and radii, compared to Sun-like stars, small planets are more accessible to detect via transit and RV techniques. Due to the relatively low temperatures, their habitable zones (Kasting et al., 1993) are much closer to the stars than those of Sun-like stars, increasing the geometric probability of observing a transit, as well as the frequency of transits of habitable-zone planets during a given observational time. Small planets orbiting M dwarfs are also better suited for atmosphere characterization through transmission spectroscopy technique (e.g., Kreidberg et al., 2014).

On the side of RV technique, since the Doppler signal increases as  $1/\sqrt{M_{\star}}$  at constant semi-major axis (Lovis & Fischer, 2010) searching planets towards lower-mass stars increases the chances of finding Earth analogs by factor 3 (compared to a Sun-like star). Additionally, M-dwarfs exhibit thousands of absorption lines in their spectra, produced by all kinds of chemical elements, which permit a statistically robust measurement of the RV, as the RV uncertainty scales with the inverse of the square root of the number of lines of the star measured. Therefore, it is beneficial to have as many lines as possible. However, not all the absorption lines are suitable to increase the RV precision. If we assume approximately Gaussian shapes for spectral lines, non-saturated lines, or narrow and depth absorption lines, like Fe lines, would be the best choice for the RV computation, as the center of these lines (centroids) is better defined. Unfortunately, the strong molecular bands present in the spectra produce forests of spectral features, making the determination of spectral continuum one of the challenging tasks to do.

Also, M dwarfs have their emission-peak in the near-infrared (NIR), which brings two main problems. Firstly, to archive high-SNR spectra, longer exposures times are needed. Secondly, ground-based collected NIR spectra suffer a strong contamination from telluric absorption lines compared with optical observations, hindering even more the selection of the spectral lines to compute the RVs.

Since the RV technique is based on the precise determination of the centroid of the spectral lines, stellar phenomena pose one of the main obstacles to detect and characterize small exoplanets, as stellar noise can produce an effect in the RV curve similar to the Doppler shift induced by an orbiting planet, mimicking the signal.

Finally, M dwarfs can show strong signs of stellar activity, which can also impact not only the exoplanet detection (e.g., stellar spots), but also impact the habitability of planets. For example, has long been debated how stellar flare can impact the surface of planets, mostly because the planet's climate is primarily determined by the incoming stellar radiation it receives from its host star, and an intense stellar activity (especially early star lifetimes) can significantly affect the atmospheric chemistry and evolution of planet's life.

### 1.4.1 Dealing with stellar activity

Magnetically active M dwarfs are those with a persistent chromosphere, and often are diagnosed by  $H_\alpha$ , Ca ii H&K, and the Ca ii triplet lines (Dorren & Guinan, 1994; Cincunegui et al., 2007). These lines also known as spectroscopic activity indicators, and are good tracers of stellar active regions, which can be especially attributed to stars with a strong magnetic fields. Activity indicators are discussed further in Section 1.4.2.

In active stellar regions, several mechanisms can create sources of stellar noise, which can affect the observed photometric and the RV measurements, and thus, limit the exoplanet detection. The most common sources of photometric variability and RV jitter, are granulation, stellar oscillation, flares, rotational modulation, and magnetic cycles:

- **Granulation:** Granules are originated from the convective motions in the stellar photosphere. Convection creates hot fluid cells that rise up from the convective zone to the surface, forming large and bright areas, called granules. On the surface, granules cool down and become dense enough for gravity to pull them back down. These movements can be seen as, vertical motions, which produce RV variations of the order of around  $\text{m s}^{-1}$ . The effect of granulation can be significantly reduced by taking several RV measurements on each night (Dumusque, 2010).
- **Oscillations:** Stellar acoustic waves or p-modes, are pressure waves that radially move in the star. They are caused by pressure fluctuations which take place in the surface of the convection zone. The individual amplitudes of p-modes are typically from a few to tens of  $\text{cm s}^{-1}$ , but the interference of many close frequencies p-modes can introduce RV variations of several  $\text{cm s}^{-1}$ , depending on the star's spectral type and evolutionary stage (Schrijver & Zwaan, 2000; Bedding & Kjeldsen, 2003, 2007; Dumusque et al., 2011). The amplitude and period of the oscillation modes increase with mass along the main sequence. For M dwarfs, p-modes, have predicted periods on timescales between 20 minutes to 3 hours and empirically estimated amplitudes of a few  $\mu\text{mag}$ . Until now, a clear detection of a pulsating M dwarf has not yet been achieved

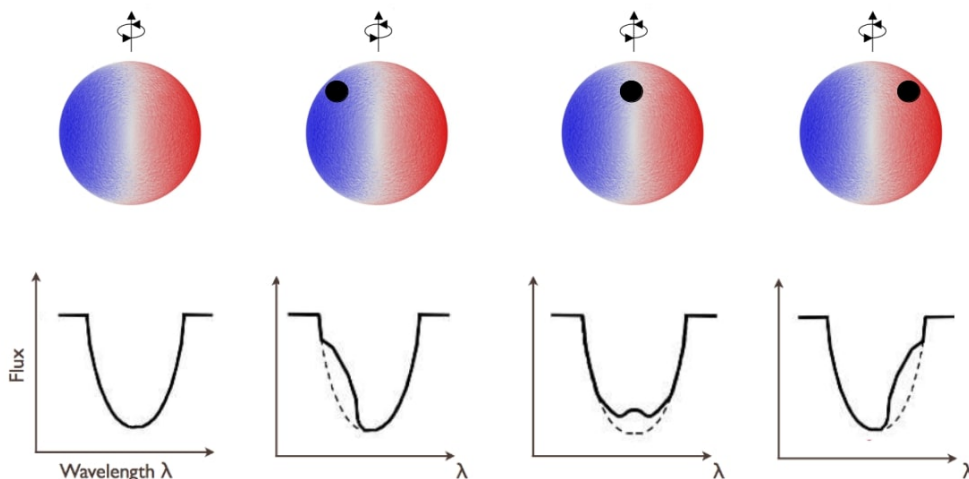


**Figure 1.12:** Diagram illustrating how flux blocked by a spot moving across on the rotating disk. The second row shows the corresponding stellar absorption line profiles, assuming rotation to be the dominant broadening mechanism.

(Rodríguez-López, 2019) despite the observational efforts made with high-precision spectroscopy, and ground- and space- based photometry.

- **Flares:** Stellar flares are dramatic increases in the stellar brightness, originated by powerful magnetic reconnection events on the star. Flares often come accompanied by coronal mass ejections, which are a massive release of plasma from the stellar corona.

Flares take place in active regions of the the stellar atmosphere, and usually occurs in short timescales, from minutes to a few hours. In M dwarfs, flares produce intense white-light continuum emission from near-ultraviolet to optical wavelengths, and appear with high contrast against the quiescent flux level (Kowalski et al., 2013). The contrast of the flare emission against the quiescent background is known as the “flare visibility” (Gershberg, 1972), and increases towards bluer spectral passbands, making the Johnson U-band filter preferred for flare studies (Moffett, 1974). In 2020, from a sample of 1228 flaring stars observed during the beginning of the *TESS* mission, Günther et al. (2020) found that  $\sim 55\%$  of them were mid- to late-type M dwarfs. In their work, it solidified that fast-rotating M dwarfs are the most likely to flare and that their flare amplitude is independent of the rotation period.

- **Rotational Modulation:** Stellar surface features such as **spots**, **faculae**, and **plage** are known as active regions, and can induce photometric and spectroscopic variations that are modulated by the rotation period of the star (Solanki, 2003).

Spots are seen as dark areas where strong magnetic field emerge from the star surface as magnetic flux loops. Their lifetime ranges from a few days up to several weeks (Allen & Youse, 1973; Schrijver, 2002; Hussain, 2002), and in general, their lifetime is proportional to its size (Berdyugina, 2005). Spots are caused because the magnetic

fields inhibit part of the outgoing convective heat flux, resulting in areas of reduced brightness and temperature. Given that spots grow and decay, they induce variations in the spectral lines profile that are modulated by the star’s rotation. As the star rotates, one half of the disc is moving towards us, while the other half is moving away. As a result, the flux emitted by the approaching half is blue shifted, while the receding half is red shifted. When the spot is passing in the front of the region that is approaching the observer it blocks some of the blue shifted emission (as shown in Fig. 1.12), producing an asymmetry in the spectral lines. A similar effect is caused by the spot after it moved toward the red shifted side of the disk, which translates into an RV modulation in the order of  $\text{cm s}^{-1}$  to  $\text{m s}^{-1}$  (Lagrange et al., 2011; Makarov et al., 2009). When the spot remains stable during several rotational periods, the RV curve of the star will show a similar variation as the one caused by the presence of a planet.

Faculae and plage usually surround spots. While faculae are bright granular structures on the stellar photosphere, plage are bright regions of the chromosphere; the two phenomena are associated with strong magnetic fields. Faculae have lifetimes of a couple of hours (Hirayama, 1978), but groups of faculae can remain on the stellar surface for several weeks and will last for several stellar cycles. In the case of plage, lifetimes are shorter and commonly with a duration of 15 to 30 minutes.

- **Magnetic Cycles:** Long-term magnetic cycles are present in magnetically active stars such as the Sun, but are also observed on stars with external convection envelopes like M dwarfs (Suárez Mascareño et al., 2016, and references therein), showing a multiple and variable cycles on different timescales with varying amplitudes.

In the case of the Sun, the cyclic pattern is roughly every 11 years, where the magnetic field completely flips, inverting its polarity. The most famous and useful technique to determine where the Sun is on its cycle is observing the modulation in the average number of spots on its disk. This technique has been used for more than four centuries (Galilei et al., 1613), reaching up-to-date more than two dozen of observed cycles (Hathaway, 2015, and references therein). Stellar magnetic cycles can produce significant RV variations, which in the case of the Sun are of approximately  $10 \text{ m s}^{-1}$  (Meunier et al. (2010)), but in some cases can reach up to  $25 \text{ m s}^{-1}$  (Lovis et al., 2011). Caution is therefore mandatory when searching for long-period exoplanets.

To observe magnetic cycles in stars other than our Sun, ground-based automatic photometric telescopes have been running for decades (e.g., ASAS, WASP-South, ASAS-SN; Pojmanski, 1997; Pollacco et al., 2006; Kochanek et al., 2017), providing the photometric precision and time coverage to explore rotation periods and activity cycles for sufficiently bright stars with a low activity level.

### 1.4.2 CARMENES Instrument

CARMENES (Calar Alto high-Resolution search for M dwarfs with Exoearths with Near-infrared and optical Echelle Spectrographs) is an instrument, a survey, and also a consortium (Quirrenbach et al., 2018). The Consortium is composed of more than 200 scientists and engineers of 11 institutions in Spain and Germany that have participated in the instrument design, construction, and science exploration<sup>11</sup>.

The instrument was built for the 3.5 m telescope at the Calar Alto Observatory in Almería, Spain. It is composed by two high-resolution spectrographs which are optimized for measuring RVs in the wavelength range from 0.53 to 1.71  $\mu\text{m}$ , with spectral resolutions of  $R = 80.000 - 100.000$ , and achieve a  $\sim 1 \text{ m s}^{-1}$  in the blue arm and  $\sim 3-4 \text{ m s}^{-1}$  in the red arm, both with long-term stability. The main motivation of constructing an optical and near-infrared spectrograph is to measure RVs in very cool stars (e.g., Martín et al., 2006) and to understand the amount of RV information and stellar RV jitter as a function of wavelength.

The blue and red arm of the CARMENES spectrograph use hollow-cathode emission line lamps (HCLs) and Fabry-Pérot etalons (FPs) for spectral calibration. For the wavelength calibration, Th-Ne, U-Ar, and U-Ne lamps provide optimal coverage in all wavelength regimes. Additionally, the instrument has incorporated two thermally stabilized FPs with more than 10.000 emission lines covering the whole CARMENES wavelength range. By comparing the FPs and the HCL data taken before and after science observations, observations can monitor the long-term stability and follow short-term spectrograph drifts.

The data reduction is made by CARACAL pipeline (Zechmeister et al., 2014) and applies standard bias, dark, and flat corrections, tracing the échelle orders, and wavelength calibration. The computation of RVs is carried out by a second pipeline called SERVAL (SpEctrum Radial Velocity AnaLyser; Zechmeister et al., 2018). In this case, SERVAL creates a high signal to noise ratio template by co-adding all observed spectra and computing the RVs using the least-squares fitting (Anglada-Escudé & Butler, 2012). The final RVs are corrected by barycentric motion, instrumental drift, secular acceleration, and nightly zero-points (Kaminski et al., 2018; Tal-Or et al., 2019; Trifonov et al., 2020). At this precision, a  $10 M_{\oplus}$  planet can be discovered on a 1 yr orbit in the liquid-water habitable zone around a  $1 M_{\odot}$  star (Reiners et al., 2018b).

As mentioned in Section 1.4.1 RV jitter can be caused by variations in active regions, granulation, magnetic cycles, flares, etc. In contrast with RVs from Keplerian signals related to exoplanets, the RV amplitude caused by stellar activity is expected to be wavelength-dependent (Reiners et al., 2010; Marchwinski et al., 2015).

For example, by studying how the slope of the RVs change in each échelle order versus the wavelength, so-called **chromatic index** (CRX; Tal-Or et al., 2018; Zechmeister et al., 2018), we can distinguish between a planetary signal or an activity induced one. Two examples of this behaviour are the active star YZCMi (Zechmeister et al., 2018) and the interesting case of AD Leonis (Kossakowski, in prep.).

Furthermore, by studying the periodograms of the **activity indicators** that SERVAL provides

---

<sup>11</sup><https://carmenes.caha.es/index.html>

such as, such as  $H_\alpha$ , Na i D lines, Ca ii infrared triplet, and the photospheric titanium oxide bands (TiO) bands (Schöfer et al., 2019) we can extract information of the highest peaks which usually related to the stellar rotational period. Activity indicators are also a good tracers of fake RV planetary signals. For example, if we see a RV signal at the same period or harmonic in the periodograms of the activity indicators, we can very likely attributed to stellar activity instead an planetary companion.

By studying the presence or absence of  $H_\alpha$  emission line in M dwarfs, we can also differentiate if the star is an early-M dwarf with high or significant rotational velocity or inactive late-M dwarf with low rotational velocity (Jeffers et al., 2018a).

Other activity indicators such as parametrisations of the cross-correlation function (CCF) full-width-at-half-maximum (FWHM), CCF contrast, asymmetry measurements of the CCF bisector inverse slope (BIS), differential line width (dLW, an indicator that measures changes in the width of the absorption lines) can give important information about instrumental effects such as changes in the instrument profile, sky background, or an artificial broadening of the lines due to barycentric motion during a long exposures (for details see e.g; Lafarga et al., 2020a). Recently, Lafarga et al. (2021) analyzed the temporal behavior of RVs on most of the former activity indicators and concluded that it is critical to take into account as many sets of indicators as possible, or at least the most effective ones (considering the characteristics of the star) to not fall in false planet claims.

### 1.4.3 CARMENES M-dwarf survey

CARMENES survey began operations on first of January in 2016, and regularly observe about 350 M dwarfs across all M-spectral sub-types during guaranteed time observations (GTO). The main scientific objective of the survey is to detect low-mass planets in their habitable zones, where the conditions might be favorable for the existence of liquid water and perhaps life. The success of CARMENES, have been reflected in the large number of discoveries, contributing in more than 40% of new exoplanets in the low-end mass parameter space  $\leq 0.2 M_\oplus$ , reaching areas that were previously was not possible to cover as is shown in the pink panel in Fig. 1.13. Additionally, CARMENES has proven to be very successful not only in detecting interesting planets but also in understanding stellar activity and astrophysical processes in low-mass stars. Also, the near-infrared arm of the instrument has opened a new field in exoplanet atmospheres with the detection of chemical elements like He and  $H_2O$  in giant planets (e.g., Nortmann et al., 2018; Casasayas-Barris et al., 2021; Khalafinejad et al., 2021).

Since 2018, part of the CARMENES success has come from follow-up transiting systems detected by the *TESS* mission, and up today, about 30% of transiting exoplanets around M dwarfs have been confirmed by the team. Figure 1.14 shows the mass-radius diagram for transiting planets around nearby M dwarfs with measured mass-based in the latest version of the catalog of physical properties of transiting planetary systems (TEPCat; Southworth, 2011), and Martínez-Rodríguez et al. (2019). Published and submitted works by CARMENES-TESS are marked with red circles. The two stars correspond to TOI-1235 b and TOI-1685 b, which will be discuss in detail on Chapter 2, and Chapter 3, respectively. The two inverted

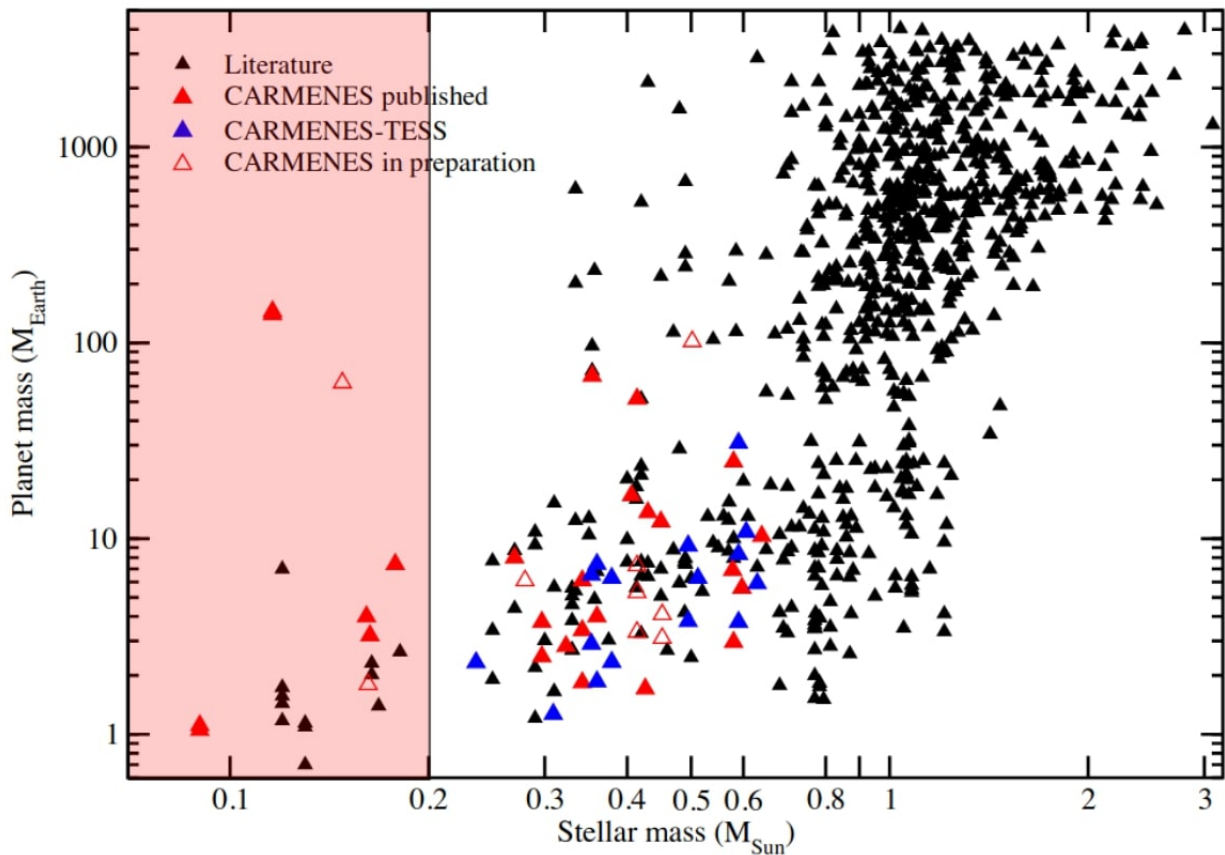


**Figure 1.13:** Planets discoveries around different stellar masses, determined with RVs. Planet from literature are showed with black-triangles, Planets from CARMENES survey are showed in red (published) and open (in preparation works) triangles, and planets discovered by CARMENES-TESS synergy are showed with blue triangles. Credit: 15<sup>th</sup> CARMENES scientific meeting (November 23, 2021).

triangles are TOI-1468 b, and TOI-1468 b, the square is TOI-1201 b, and the cross represents Gliese 486 b, the latter planets will be discussed in Sec. 1.5. Additionally, from the figure, it is easy to see the big contribution that CARMENES has made since starting its operations. This “zoo” of small exoplanets cover large ranges of radius and masses going from planets composed fully be iron, passing through a big amount of Earth-like planets, to pure water with H-H<sub>e</sub> envelopes.

## 1.5 CARMENES–TESS synergy

CARMENES has proven to be a novel astronomical instrument specifically designed to detect Earth-like planets. At the same time, the *TESS* mission has been monitoring the brightest and closer stars across the whole sky to discover hundred of transiting planets. Since both instruments were mainly designed to meet the same goal, the natural synergy between them makes this team particularly well suited to detect and characterize small planets orbiting M dwarfs.

To achieve this goal, CARMENES has been dedicating an essential fraction of their observing time to follow-up *TESS* candidates, where this synergy is further complimented, as more than 70% of targets from the CARMENES-GTO survey are also observed by *TESS*.

Today, the success of the CARMENES–TESS synergy has revealed a vast sample of exoplanets with precise planetary parameters, and it will continue to do so, providing valuable information that will allow us to understand the composition and the planet formation mechanisms as a function of stellar host properties.

As an active member of CARMENES consortium, I participated in more than ten scientific articles. In all of them, I have provided feedback and carefully reviewed the manuscripts. For the publications that I will briefly summarize below, I have been involved in data analysis closely, such as modeling the photometric and RV data, selecting the final model, analyzing the activity indices, making figures, and directly writing some paper sub-sections.

- **Gliese 486 b:** The planet Gliese 486 b is one of the GTO targets in the CARMENES survey and was published during this year by [Trifonov et al. \(2021\)](#). This discovery has a big impact in the exoplanets community due the combination of physical and orbital characteristics of this planet makes it the “Rosetta Stone” for atmospheric investigations of rocky exoplanets.

Gliese 486 b is a transiting rocky planet with a mass of  $\sim 2.81 M_{\oplus}$ , and a radius of  $\sim 1.31 M_{\oplus}$  as is shown with a red-cross in Fig. 1.14. At a distance of 8.1 pc, Gliese 486 b is one of the closest transiting exoplanets around a M dwarf with a measured mass. It is expected that planets with radius size and distance as Gliese 486 b have lost their primordial H-He atmospheres owing to photoevaporation processes. However, its equilibrium temperature of  $\sim 700$  K, which roughly corresponds to the surface temperature of Venus, harbor the possibility of a tenuous layer atmosphere, making this discovery suitable for thermal emission spectroscopy ([Kempton et al., 2018](#)). Futures observations with the next *JWST* and *ELT*<sup>12</sup> telescopes will give us valuable information on the bright, and hot surface of Gliese 486 b what would help to answer questions such as How well rocky planets can hold their atmospheres? What are these atmospheres made of?, and How they influence the energy distribution on the planets?.

- **TOI-1201 b:** M dwarfs are the most numerous star in our Galaxy ([Chabrier, 2003](#)), which about 40% of them are in binary systems ([Fischer & Marcy, 1992](#)). However, only a few exoplanets have been found in binary systems where the primary is an M dwarf (<10%)<sup>13</sup>. Such low number would related to close M-dwarf systems were

---

<sup>12</sup>European Extremely Large Telescope (ELT) is planned to start operations as an integrated part of the Paranal Observatory in 2025. <https://www.eso.org/sci/facilities/eelt/>

<sup>13</sup>According to NASA exoplanet archive, accessed on November 17, 2021

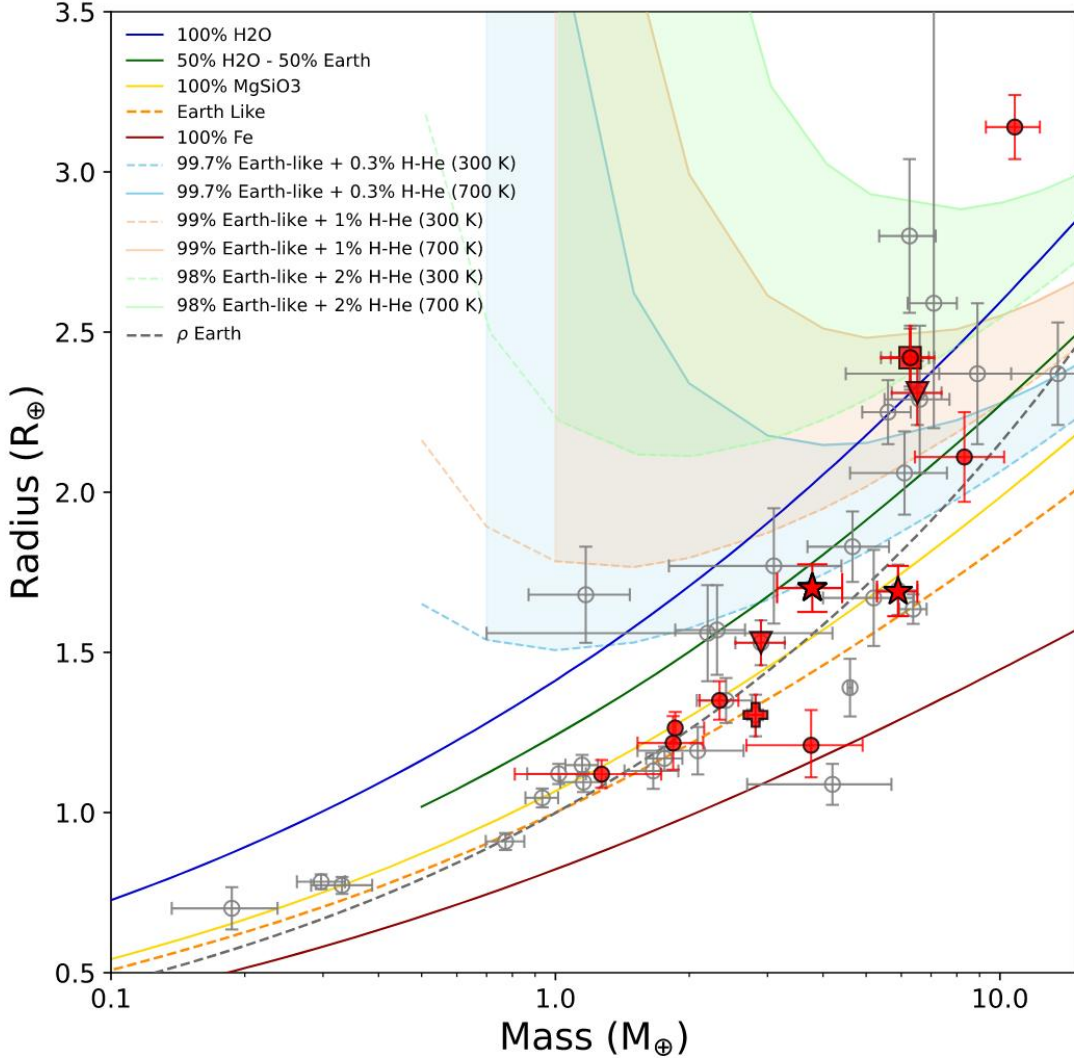


**Figure 1.14:** Mass-radius diagram for all transiting planets around nearby M dwarfs with measured mass. Planets discovered by CARMENES are marked with red symbols. Red circles are the already published and submitted planets. The two red stars are TOI-1235 b, and TOI-1685 b, of which I am first-author and will further discuss in Chapter 2 and Chapter 3, respectively. The two inverted-triangles are TOI-1468 b, and TOI-1468 b, the square represent to TOI.1201 b, and the cross is Gliese 486 b (for all of them see Sec. 1.5). All theoretical composition models were taken from (Zeng et al., 2019). The lines represent models for cores composed of pure Iron (100% Fe, dark red), Earth-like rocky (32.5% Fe+67.5% MgSiO<sub>3</sub>, dashed-orange), pure Rock (100% MgSiO<sub>3</sub>, yellow), 50% H<sub>2</sub>O+50% Earth-like (green), and pure water (100% H<sub>2</sub>O, blue), and the Earth density (dashed-gray). The dashed areas represents 0.3% (light blue), 1% (light orange), and 3% (light green) of H-He atmosphere envelopes for Earth-like rocky cores between 300–700 K.

typically discarded from dedicated detection surveys due the high risk of potential light contamination in transits (Cortés-Contreras et al., 2017). However, observations of planets in multiple-star systems can help us to understand about the connection between planet-host star formation (see e.g., Goodwin et al., 2007, 2008).

TOI-1201 b is an interesting transiting mini-Neptune with a period of 2.5 d and orbits the a relatively bright and young companion of the M-dwarf wide binary system PM J02489-1432. The mini-Neptune is shown with a red-square in Fig. 1.14. From the RV data besides the planetary signal, two additional prominent signals around  $\sim 19$ -23 d are popped-up. One of them related to rotational period based on long-term photometry and stellar activity indicators, and the other a long-term unknown signal  $\sim 100$  d where, that would need further monitoring to determine its origin is related to an extra planet on the system.

One attractive characteristic of this system would be the study Rossiter-McLaughlin effect, described in Sec. 1.2 with extremely precise spectrographs with  $\text{cm s}^{-1}$  precision such as *ESPRESSO* or *MAROON-X*. Study the obliquity of TOI-1201 b would can help to understand orbital architectures of planetary systems, specifically around low-mass.

Additionally, TOI-1201 b is ranked as one of the more promising target for further atmospheric studies using both, transmission and emission spectroscopy. Determining the atmospheric composition of mini-Neptunes will allow for a better understanding of the formation histories of these planets studies with the upcoming *JWST* telescope could add light into this topic.

The publication was recently accepted and was written under the leadership of Kosakowski et al. (2021), of which I am the third co-author.

- **TOI-1468 b, c:** TOI-1468 is the perfect example of a planetary system system with two transiting planets in the opposite sides of the radius gap (see Sec. 1.3.2 for details). TOI-1468 b and TOI-1468 c orbits the early type M dwarf, LSPM J0106+1913 with periods of 1.88 d and 15.54 d, respectively. Both planets the inner and outer one lie on the opposite sides of the radius gap making this system a prefect laboratory for planet formation and migrations theories.

The density of the inner planet is consistent with a mostly rocky composition whereas the outer one possess an outer envelope as is shown with red-inverted-trinagles in Fig. 1.14. Two planets that orbit the same host star with different densities suggest that both planets would be formed in different environments. It is possible that TOI-1468 b formed at its current location whereas TOI-1468 c could have formed further out and eventually migrated inwards be keeping its H-He envelope (Ida & Lin, 2010). Another explanation is that both planets could be formed in similar environments, but the extreme ultra-violet (XUV) radiation from its host star could have stripped off a substantial portion of the outer envelope (López & Fortney, 2013). Currently, only a few planets around M dwarfs with this condition was found (e.g., LTT 3780 (Nowak et al., 2020a), LP 961-53 (Van Eylen et al., 2021) and TOI-1749 (Fukui et al., 2021)), and since most of the planets found in the in the two sides of the radius was around -F,-G,-K stars increasing the sample towards late-type stars could help us to discriminate between planet formations scenarios.

The publication is currently circulated in draft-mode. Is written under the leadership of [Chaturvedi \(in prep.\)](#), of which I am the third co-author.

## 1.6 Purpose and thesis overview

As previously discussed, exoplanets orbiting M dwarf stars are a prime target in searching for life in the Universe. The relative sizes between the host stars and their planets make these perfect systems targets follow-up through ground-based and space telescopes. It also has been proved that the synergy between the transit and RV techniques is the most successful approach to detect small exoplanets with unprecedented precision, which will be the first step towards a comprehensive characterization of exoplanets.

However, M dwarf stars are active entities, where strong sources of stellar noise, such as powerful flares, magnetic cycles, spots, among others, can highly influence the photometric and RV measurements, making the planet detection challenging. In this thesis, I will present how to deal with stellar noise to correctly characterize planetary parameters by first identifying all the signals shown in the data, recognizing which of them are planets, alias, harmonics, or potentially caused by stellar activity, to model each one of them appropriately.

My thesis is divided into four parts. First, I presented the introduction, providing an overview of how the field of exoplanets has progressed from discovery to characterization. Also, I explained how the synergy between CARMENES spectrograph and *TESS* space telescope is a perfect team to find small exoplanets around M dwarfs. Finally, the introduction was made from the point of view of the transit method and the RV technique, methods which I used during my investigation.

- **Chapter 2** reports the discovery of TOI-1235 b a transiting super-Earth planet around an M0.5 V star with mass of  $\sim 5.90 M_{\oplus}$ , radius of  $\sim 1.69 R_{\oplus}$ , and its irradiation level of  $\sim 60 S_{\oplus}$ . According to the location of the radius gap, TOI-1235 b would be placed near the lower edge of this. Its rocky composition, derived from comparison with compositional models, is indeed consistent with a planet having lost its atmosphere, as expected for planets below the radius valley. If the gap exists for M-dwarfs, these findings would help to better constrain the dependence of the gap location on stellar type and irradiation, and thus to understand its origin. Finally, the brightness of TOI-1235 ( $V \approx 11.5$  mag) makes this planet a very interesting object for further studies of planet formation and atmospheric evolution.
- **Chapter 3** presents the discovery of a possible multi-planetary system around the M3.0 V star TOI-1685. The system has one transiting planet with an ultra-short orbital period (USP) TOI-1685 b with a period  $\sim 0.669$  d plus another planet candidate at a wider orbit found in RV data only TOI-1685 [c]. The USP was detected by the *TESS* mission and confirmed by CARMENES RV data, as well as ground-based photometric observations. The USP has a mass of  $\sim 3.78 M_{\oplus}$ , and a radius of  $\sim 1.70 R_{\oplus}$ . The derived bulk density of about  $\sim 4.21 \text{ g cm}^{-3}$  makes TOI-1685 b the least dense USP around an M dwarf known to date.

It is expected that small exoplanets at higher temperatures have higher bulk densities. However, TOI-1685 b does not follow such a prediction, suggesting that TOI-1685 b

might maintain a substantial atmosphere, unlike other hot small planets, making this USP a rather unusual and interesting laboratory.

Finally, the measured values of the emission and transmission spectroscopy metrics make this planet a suitable candidate for atmospheric characterization by *JWST* which will help us to understand the evolution and atmosphere escape processes.

- **Chapter 4** is presented Gliese 617 a binary system observed in 12 of the 13 sectors of the northern continuous viewing zone (CVZ) of *TESS* mission. Additionally, more than 100 RVs measurements were taken with CARMENES between 2016 to 2021. This large amount of data, will provide a unique opportunity to search exoplanets, analyzing long orbital period baselines, and also investigate the rotational period for both stars. Also in this chapter I study how to reduce *TESS* raw data in order to study stellar variability. Since *TESS* is an exoplanet finding mission, most of the *TESS* data products are focused on providing corrected light curves. In this case, the corrected light curves or Pre-search Data Conditioning SAP flux (PDCSAP) are subject to an extensive treatment to remove most of the systematics while keeping planetary transits (if there are) intact. However, these light curves are not suitable to study stellar variability, as the PDCSAP often removes astrophysical features and long-term trends from the data. Unfortunately, a standard post-processing of the data that allows to the user removes the common systematics while preserving stellar variability currently does not exist. In this chapter I also presented a method that optimizes the reduction of the *TESS* raw data, by finding a balance between maximizing the removal of systematics and minimizing the removal of real astrophysics components.
- **Chapter 5** summarizes the results and conclusions of this thesis. Future work related to the contents of this thesis are also presented here.



# 2

## Precise mass and radius of a transiting super-Earth planet orbiting the M dwarf TOI-1235: a planet in the radius gap?

---

*“Absence of evidence is not evidence of absence.”*

by Carl Sagan

---

The content of this chapter is based in the published article *“Precise mass and radius of a transiting super-Earth planet orbiting the M dwarf TOI-1235: a planet in the radius gap?”*, (Bluhm et al., 2020), from which I am the first author from a team effort of 83 co-authors. I have done the scientific work, analysis, and reached the conclusions. I was under the supervision of Prof. Andreas Quirrenbach with collaboration with Rafael Luque, Néstor Espinoza, and Enric Pallé. The stellar parameters were computed by Vera Passegger, Andreas Schweitzer, and Carlos Cifuentes. The Galactic velocities UVW were computed by Carlos Cardona. Since this was a competitive article, most of the text was written by me but also was a team effort working side by side with the co-authors.

### 2.1 Motivation

Currently, over 4000 exoplanetary systems have been discovered orbiting stars other than the Sun<sup>14</sup>, with the majority of the planets having sizes between that of the Earth and Neptune (Batalha et al., 2013). Most of these systems were discovered by the *Kepler* mission (Borucki et al., 2010a; Borucki, 2016), which by design focused its transit survey on stars of spectral types F, G, and K. In order to understand the processes involved in the formation and evolution of planets, it is useful to compare the variations in the outcomes in different environments, for instance, by considering planetary demographics in a range of host star contexts. No picture of exoplanet populations can be complete without a sizable and representative sample of planetary systems around M dwarfs, which are the most common type of stars in our Galaxy (Chabrier, 2003; Henry et al., 2006).

The occurrence rate of small planets orbiting M dwarfs indeed appears to increase toward late spectral subtypes at all orbital periods (Bonfils et al., 2013; Dressing & Charbonneau,

---

<sup>14</sup><https://exoplanetarchive.ipac.caltech.edu/>,  
<http://exoplanet.eu/>

## 2 Precise mass and radius of a transiting super-Earth planet orbiting the M dwarf TOI-1235: a planet in the radius gap?

2015; Mulders et al., 2015; Gaidos et al., 2016). In spite of this abundance, the number of exoplanets with M-star hosts whose radii and masses are precisely known is still small because these stars are intrinsically faint, and only the closest ones are well suited for detailed follow-up and characterization.

One of the most interesting features observed in the distribution of sizes of small ( $R < 4 R_{\oplus}$ ) exoplanets has been the bimodal nature of this distribution, which is commonly referred to as the “radius gap”. It separates planets with radii slightly smaller than that of Neptune ( $2\text{--}4 R_{\oplus}$ ) from those with radii slightly larger than Earth ( $1\text{--}2 R_{\oplus}$ ). While the former are believed to bear a significant contribution of water (Morbidei, 2018), the latter are thought to be predominantly rocky. Although it was theoretically predicted (e.g., Owen & Wu, 2013a; Jin et al., 2014; López & Fortney, 2014; Chen & Rogers, 2016), the radius gap was observationally characterized only relatively recently (e.g., Fulton et al., 2017; Zeng et al., 2017; Van Eylen et al., 2018; Berger et al., 2018; Fulton & Petigura, 2018) owing to an improvement in the planetary radius determination through more accurate models and stellar radii. This was possible through new high-resolution stellar spectroscopy (Schweitzer et al., 2019), asteroseismology (García & Ballot, 2019), and precise parallactic distances from the *Gaia* mission (Gaia Collaboration et al., 2018).

Two classes of models are currently accepted to explain this radius gap: photoevaporation models, which posit that planets that finally lie below the radius gap lost their atmospheres due to X-ray and ultraviolet radiation from the star (XUV; e.g., Owen & Wu, 2013a; López & Fortney, 2013; Jin et al., 2014; Chen & Rogers, 2016; Owen & Wu, 2017), and core-powered mass-loss models, which also propose that close-in planets below the radius gap have lost their atmospheres, but conjecture that mass loss is powered by heat from the planetary core (Ginzburg et al., 2016, 2018; Gupta & Schlichting, 2019). These two mechanisms have different dependences on the stellar type of the host stars and the total irradiation that the planets receive (Wu, 2019b; Gupta & Schlichting, 2020), which means that the actual location of the radius gap can indeed change with these parameters. Because most of the existing studies are based on *Kepler* samples or subsamples, which are samples that are heavily focused on F, G and K-type stars, transiting exoplanetary systems around M-type stars have a huge potential to help constrain the most important mechanism(s) producing this bimodal distribution (see, e.g., Hirano et al., 2018a). Measuring the planetary mass in turn allows us to gain some insight into the bulk composition of the exoplanets, which delivers a clearer picture of the underlying nature of the radius gap. The *Transiting Exoplanet Survey Satellite* (*TESS*; Ricker et al., 2015) has proven to be a prime instrument for detecting and characterizing small planets orbiting bright stellar hosts. Having completed its first year of monitoring, it has contributed to the detection and confirmation of more than 40 new transiting exoplanetary systems, many of which consist of small planets orbiting low-mass M stars (e.g., Luque et al., 2019; Crossfield et al., 2019; Günther et al., 2019; Astudillo-Defru et al., 2020; Cloutier et al., 2020a; Gilbert et al., 2020; Nowak et al., 2020b). Here we report on a very interesting addition to this growing sample of *TESS* transiting exoplanet discoveries around M dwarfs: a transiting super-Earth that appears to be right in the radius gap for low-mass stars orbiting the early M dwarf TOI-1235 (see also the coordinated, but intentionally independent, announcement by Cloutier et al. 2020b). The paper is organized as follows. Section 2.2 presents the *TESS* photometry we used, along with ground-based observations of the star, including high-resolution spectroscopy, lucky and speckle imaging,

and photometric variability monitoring. Section 2.3 presents the stellar properties of the host star, newly derived and collected from the literature. In Section 2.4 we present our analysis of the available data to constrain the planetary properties of the system. In Section 2.5 we discuss our results, with an emphasis on the location of the planet in the mass-radius diagram and its composition, and, finally, Section 2.6 shows our conclusions.

## 2.2 Data

Radius and mass are key physical properties of a planet. Together, they inform the planetary density, bulk composition, internal structure, and ability to retain an atmosphere. The combination of a transit and radial velocity (RV) detection is the most straightforward way to measure both the planetary radius and mass. In this work, we used the CARMENES<sup>15</sup>, HARPS-N<sup>16</sup>, and iSHELL<sup>17</sup> high-resolution spectrographs for the RV follow-up (Sect. 2.2.2).

Moreover, given the intrinsic faintness of M dwarfs in general and the large photometric apertures of wide-field surveys such as *TESS* in particular, many light curves with transit candidates are susceptible to contamination by nearby sources. Blends with stars other than the target star are frequent, especially at low Galactic latitudes, while many stars are unresolved multiples. In some cases, other stars in the aperture mask are variable and bright enough to affect the photometric, and even RV, measurements. A particularly difficult type of false positives are background-eclipsing binaries near the target star, which can mimic planet transits. High-resolution imaging follow-up is therefore needed to identify nearby potential contaminants, and ground-based photometric monitoring is helpful in discarding false positives, such as nearby eclipsing binaries. For this second follow-up stage, we used the lucky and speckle imagers AstraLux and NESSI and collected light curves complementary to those of *TESS*, either measured by us with 1 m class telescopes (LCOGT, TJO) or compiled from public data bases (Sects. 2.2.3 and 2.2.4).

### 2.2.1 TESS photometry

The goal of *TESS* is to search for planets transiting bright and nearby stars. It was designed to observe 26 sectors of  $24 \times 96 \text{ deg}^2$  split into 13 partially overlapping sectors in the north and south ecliptic hemispheres, each of which observed for 27–28 d. The Mikulski Archive

| Sector | Camera | CCD | Start date       | End date         |
|--------|--------|-----|------------------|------------------|
| 14     | 4      | 3   | 18 July 2019     | 15 August 2019   |
| 20     | 2      | 1   | 24 December 2019 | 21 January 2020  |
| 21     | 2      | 2   | 21 January 2020  | 18 February 2020 |

**Table 2.1:** *TESS* observations of TOI-1235.

<sup>15</sup>Calar Alto high-Resolution search for M dwarfs with Exoearths with Near-infrared and optical Echelle Spectrographs: <http://carmenes.caha.es>

<sup>16</sup> High Accuracy Radial velocity Planet Searcher for the Northern hemisphere: <https://plone.unige.ch/HARPS-N/>

<sup>17</sup>Immersion Grating Echelle Spectrograph: <http://irtfweb.ifa.hawaii.edu/~ishell/>

## 2 Precise mass and radius of a transiting super-Earth planet orbiting the M dwarf TOI-1235: a planet in the radius gap?

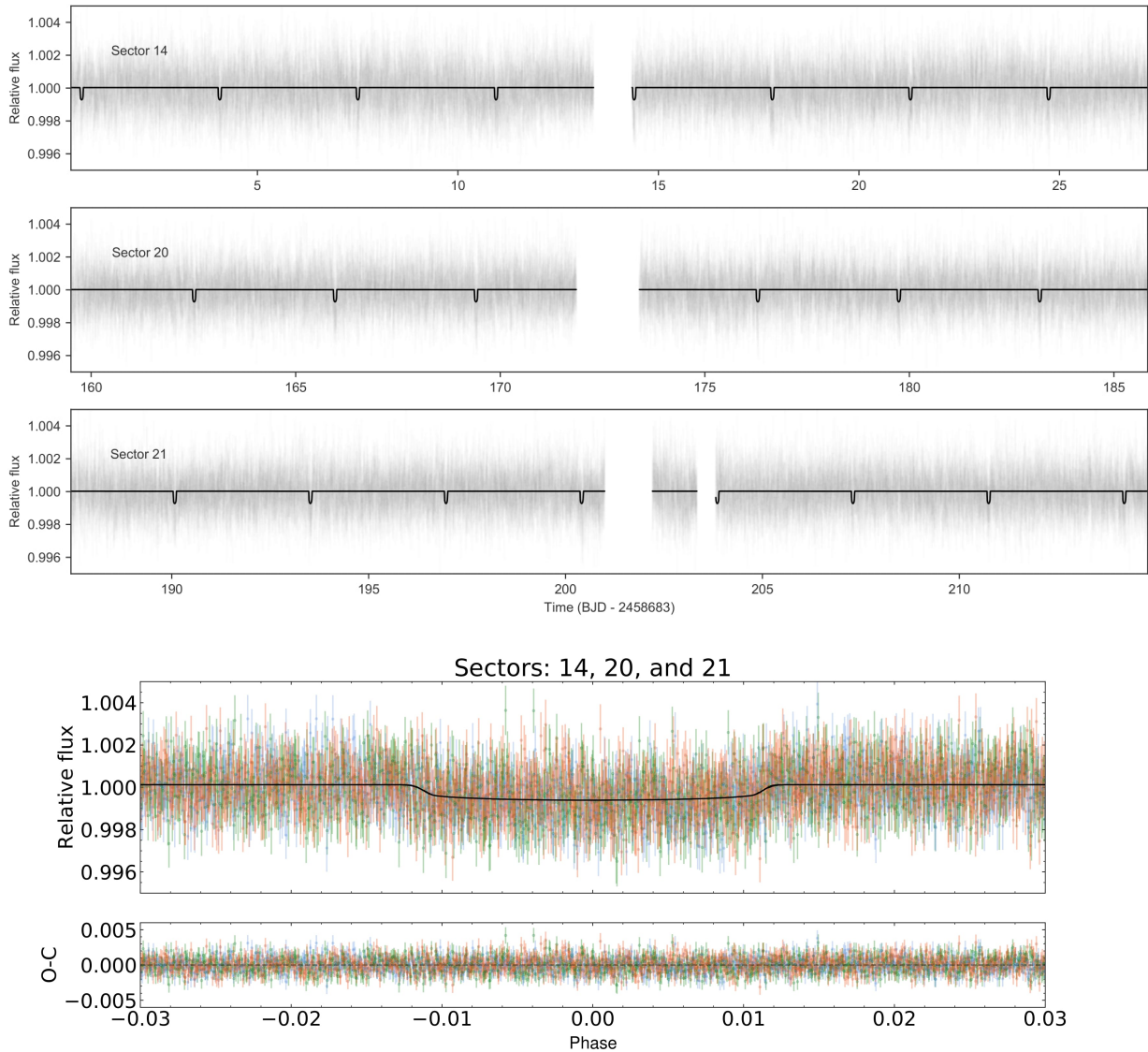


**Figure 2.1:** *Top panel:* TESS transit photometry for the three sectors (gray points) with the best-fit juliet model (black line; see Sect. 2.4.4 for details on the modeling). *Bottom panel:* Phase-folded transit light curve of TOI-1235 b. The three sectors (14, 20, and 21) are color-coded in red, green, and blue, respectively. The best-fit model is depicted by the black curve.

for Space Telescopes<sup>18</sup> (MAST) stores the light curves of stars in the *TESS* Input Catalog (TIC; [Stassun et al., 2018](#)). About 200,000 bright main-sequence F, G, K, and M-type stars, small enough to enable the detection of transiting planets smaller than Neptune ( $R \leq 4 R_{\oplus}$ ), are observed with a 2 min cadence (cf. [Stassun et al., 2018](#)), while fainter stars ( $V \gtrsim 13$  mag) or with earlier spectral types (and, thus, high masses and large radii) are observed with a 30 min cadence. TOI-1235 (TIC 103633434) was observed by *TESS* in 2 min short-cadence integrations in sectors 14, 20, and 21 during the *TESS* primary mission (see Table 2.1). The transiting-planet signature was detected when the Science Processing Operations Center (SPOC; [Jenkins et al., 2016](#)) processed the data from sector 14 and searched the light curve for transits with the transiting planet search module ([Jenkins, 2002](#); [Jenkins et al., 2017](#)). The transit signature passed all the diagnostic tests performed by the data validation module ([Twicken et al., 2018](#)), which also provided the initial limb-darkened transit model fit ([Li et al., 2019](#)). After these steps, TOI-1235 was announced on 16 September 2019 as a *TESS* object of interest (TOI) through the dedicated MIT *TESS* data alerts public website<sup>19</sup>. The transit signal had a period of  $3.4431 \pm 0.0008$  d and a depth of  $0.91 \pm 0.08$  mmag, corresponding to a planet radius of about  $2 R_{\oplus}$ , well in the super-Earth domain.

Soon after, we downloaded the corresponding light curve produced by the SPOC at the NASA Ames Research Center from MAST. SPOC provides simple aperture photometry (SAP) and photometry corrected for systematics (PDC, [Smith et al., 2012](#); [Stumpe et al., 2012, 2014](#)), which is optimized for *TESS* transit searches. Figure 2.1 shows the PDC data for the three *TESS* sectors with the best-fit model (see Sect. 2.4.4 for details).

## 2.2.2 High-resolution spectroscopy

### CARMENES

CARMENES ([Quirrenbach et al., 2014, 2018](#)) is a high-resolution spectrograph mounted on the 3.5 m telescope at the Observatorio de Calar Alto in Almería, Spain. It splits the incoming light into two channels, one that operates in the optical (VIS: 0.52–0.96  $\mu\text{m}$ ,  $\mathcal{R} = 94600$ ) and the other in the near-infrared (NIR: 0.96–1.71  $\mu\text{m}$ ,  $\mathcal{R} = 80400$ ). TOI-1235 was observed 40 times with CARMENES between 09 November 2019 and 18 February 2020, overlapping with the *TESS* sector 20 and 21 observations. We used the maximum exposure time of 1800 s and followed the standard data flow of the CARMENES guaranteed time observations. In particular, we reduced the VIS spectra with CARACAL ([Zechmeister et al., 2014](#)) and determined the corresponding RVs and spectral activity indices (see Sect. 2.4.3) with SERVAL ([Zechmeister et al., 2018](#)). We corrected the RV's for barycentric motion, instrumental drift, secular acceleration, and nightly zero-points (see [Kaminski et al. 2018](#), [Tal-Or et al. 2019](#), and, especially, [Trifonov et al. 2020](#) for details). For exposure times shorter than 1800 s, the CARMENES standard integrations are automatically limited by signal-to-noise (S/N) ratio to 150 by an exposure-meter per channel that collects the light of the zeroth order of the respective échelle grating during the exposure ([Caballero et al., 2016](#)). However, the median S/N of our CARMENES VIS spectra was slightly lower ( $\sim 97$ ). Correspondingly, the weighted root-mean-square (wrms) and median uncertainty ( $\hat{\sigma}$ ) of the

<sup>18</sup><https://mast.stsci.edu>, <https://archive.stsci.edu/>

<sup>19</sup><https://tess.mit.edu/toi-releases/>

## 2 Precise mass and radius of a transiting super-Earth planet orbiting the M dwarf TOI-1235: a planet in the radius gap?

CARMENES VIS data were  $3.7 \text{ m s}^{-1}$  and  $1.9 \text{ m s}^{-1}$ , respectively. These RVs and their uncertainties are listed in the top part of Table 2.10.

As expected from the results presented by Bauer et al. (2020), the RV precision of the CARMENES NIR observations of TOI-1235 was lower than that of the VIS observations:  $\text{wrms} = 9.1 \text{ m s}^{-1}$  and  $\hat{\sigma} = 7.4 \text{ m s}^{-1}$ . The expected RV amplitude of the planet of about  $3\text{--}4 \text{ m s}^{-1}$  was lower than the data radial precision of the CARMENES NIR data. The RVs, CRX, and dLW of CARMENES NIR spectra are displayed in the top part of Table 2.9.

### HARPS-N

HARPS-N (Cosentino et al., 2012) is a high-resolution spectrograph mounted on the Italian 3.58 m Telescopio Nazionale Galileo at the Observatorio del Roque de los Muchachos, La Palma, Spain. HARPS-N covers the optical wavelength regime between  $0.38 \mu\text{m}$  and  $0.69 \mu\text{m}$  with a spectral resolution of  $\mathcal{R} = 115\,000$ . The precision and stability of HARPS-N is comparable to its sister instrument HARPS on the ESO 3.6 m telescope and therefore to CARMENES (Trifonov et al., 2018; Perger et al., 2019). TOI-1235 was observed 21 times between 14 January 2020 and 26 February 2020 with HARPS-N<sup>20</sup>, also overlapping with *TESS* sectors 20 and 21. Just as with the CARMENES data, we determined the RVs and  $\text{H}\alpha$  spectral activity index with SERVAL. They are listed in the bottom part of Table 2.10. The typical S/N per exposure was 100, while the wrms and  $\hat{\sigma}$  of the HARPS-N data were  $4.5 \text{ m s}^{-1}$  and  $1.0 \text{ m s}^{-1}$ , respectively.

### iSHELL

We obtained 49 spectra during five nights for TOI 1235 spanning 26 days in January–February 2020 with iSHELL mounted on the 3.2 m NASA Infrared Telescope Facility (IRTF) on Maunakea, Hawaii (Rayner et al., 2016). We used the silicon immersion grating optimized for the *K* band with the  $0.375$  arcsec slit, which resulted in a spectral resolution of 80 000. The spectra were wavelength calibrated with a methane isotopolog gas cell in the calibration unit. The exposure times were 300 s, repeated 9–11 times within a night to reach a cumulative photon S/N per spectral pixel at about  $2.4 \mu\text{m}$  (at the approximate center of the blaze for the middle order) varying from 77 to 98 to achieve a per-night precision of  $4\text{--}11 \text{ m s}^{-1}$ . Spectra were reduced and RVs extracted using the methods outlined by Cale et al. (2019). The resulting wrms and  $\hat{\sigma}$  of the iSHELL data were  $7.2 \text{ m s}^{-1}$  and  $6.1 \text{ m s}^{-1}$ , slightly better than the CARMENES NIR data, but still twice higher than the expected planet semiamplitude. The RVs are displayed in the bottom part of Table 2.9.

## 2.2.3 High-resolution imaging

### AstraLux

We observed TOI-1235 with the high spatial resolution camera and lucky imager AstraLux (Hormuth et al., 2008) on the 2.2 m telescope at the Observatorio de Calar Alto in Almería, Spain. The observations were carried out in the  $z'$  band on 30 October 2019 under good

---

<sup>20</sup>HARPS-N data: 15 RVs were obtained from the Spanish CAT19A-162 program (PI: Nowak) and 6 RVs from ITP 19-1 program (PI: Pallé).

| Survey                | Band  | Start date   | End date     | $N$              | $\Delta t$<br>(d) | $\bar{m}$<br>(mag) | $\sigma_m$<br>(mag) | $\overline{\delta m}$<br>(mag) |
|-----------------------|-------|--------------|--------------|------------------|-------------------|--------------------|---------------------|--------------------------------|
| ASAS-SN               | $g'$  | 29 Oct. 2017 | 24 Mar. 2020 | 603 <sup>b</sup> | 877               | 12.255             | 0.026               | 0.010                          |
|                       | $V$   | 28 Jan. 2012 | 26 Nov. 2018 | 713 <sup>b</sup> | 2494              | 11.572             | 0.018               | 0.009                          |
| NSVS                  | Clear | 04 June 2018 | 20 May 2019  | 111              | 359               | 11.027             | 0.024               | 0.011                          |
| Catalina <sup>c</sup> | Clear | 02 Feb. 2006 | 18 Apr. 2013 | 43               | 2632              | 10.761             | 0.089               | 0.050                          |

**Table 2.2:** Descriptions of data from public ground-based surveys<sup>a</sup>. **Notes.** <sup>(a)</sup> Number of collected data points. <sup>(b)</sup> After discarding 20  $g'$  and 10  $V$  dubious data points (with poor quality flags). <sup>(c)</sup> Data set eventually not used.

weather conditions with a mean seeing of 1.0 arcsec. We obtained 96 000 frames of 10 ms in a  $6.0 \times 6.0$  arcsec<sup>2</sup> window. With the observatory pipeline, we selected the 5 % frames with the highest Strehl ratio (Strehl, 1902), aligned them, and stacked them for a final high-spatial resolution image.

## NESSI

On 14 October of 2019, we observed TOI-1235 with the NASA Exoplanet Star and Speckle Imager (NESSI; Scott et al., 2018; Scott & Howell, 2018) on the 3.5 m WIYN telescope at the Kitt Peak National Observatory in Arizona, USA. We observed nearby point-source calibrator stars and reduced the data following Howell et al. (2011). The high-speed electron-multiplying CCDs of NESSI capture images at 25 Hz simultaneously in two bands centered at 562 nm and 832 nm. Finally, we obtained two  $4.6 \times 4.6$  arcsec<sup>2</sup> reconstructed images, one for each passband.

### 2.2.4 Ground-based photometry

Additional photometric data for TOI-1235 were taken on 31 December 2019 with one of the 1 m telescopes of the Las Cumbres Observatory Global Telescope (LCOGT; Brown et al., 2013) Network at the McDonald Observatory in Texas, USA. We used the TESS Transit Finder, which is a customized version of the Tapir software package (Jensen, 2013), to schedule a full transit observation. We used the  $zs$  (short  $z'$ ) band and an aperture radius of 7.0 arcsec for the photometry extraction. A total of 358 photometric measurements were obtained with a cadence of 56 s and a median precision of 1.1 mmag per point. The images were calibrated using the standard LCOGT Banzai pipeline (McCully et al., 2018), and the photometric data were extracted using the AstroImageJ software package (Collins et al., 2017a).

We also observed a TOI-1235 transit on 29 March 2020 with the 0.8 m Telescopi Joan Oró (TJO) at the Observatori Astronòmic del Montsec in Lleida, Spain. We obtained a total of 221 images with the Johnson  $R$  filter using the LAIA imager, a  $4k \times 4k$  CCD with a field of view of 30 arcmin and a scale of  $0.4$  arcsec pixel<sup>-1</sup>. The observations were affected by poor weather conditions, and the photometry was extracted and analyzed with AstroImageJ. Although we did not use this photometry in the joint modeling due to the relatively poor photometric precision, of about 2 mmag, and an observational gap in the middle of the tran-

## 2 Precise mass and radius of a transiting super-Earth planet orbiting the M dwarf TOI-1235: a planet in the radius gap?

sit, it was still useful as an independent confirmation that the transit event indeed occurred on the target star, as the TJO photometry for all *Gaia* DR2 sources within 2.5 arcmin of the target ruled out the possibility that the *TESS* transit signal was produced by any of these stars being short-period eclipsing binary contaminants.

Finally, we searched for public time-series data of wide-area photometric surveys and databases exactly as in [Díez Alonso et al. \(2019\)](#). In particular, we retrieved light curves from the All-Sky Automated Survey for SuperNovae (ASAS-SN; [Shappee et al., 2014](#); [Kochanek et al., 2017](#)) in the  $g'$  and  $V$  bands, and the Northern Sky Variability Survey (NSVS; [Woźniak et al., 2004](#)), and the Catalina Sky Survey ([Drake et al., 2009](#)) in white light. Table 2.2 summarizes the three public data sets, including the standard deviation of the magnitudes and mean of the magnitude errors. The Catalina data set is much noisier, sparser, and shorter than the others, therefore we did not use it in our analysis. In addition, we did not find data on TOI-1235 in the public archives of other photometric surveys, such as MEarth ([Irwin et al., 2011](#)), SuperWASP ([Pollacco et al., 2006](#), including unpublished data), ASAS ([Pojmanski, 1997](#)), and HATNet ([Bakos et al., 2004](#)). Finally, TOI-1235 was not labeled as a variable star in the ATLAS survey ([Heinze et al., 2018](#)).

### 2.3 Stellar properties

The star TOI-1235 (TYC 4384–1735–1) has been included in only a few proper-motion surveys ([Høg et al., 2000](#); [Lépine & Shara, 2005](#); [Kirkpatrick et al., 2016](#)) and catalogs of nearby M dwarfs that could host exoplanets ([Lépine & Gaidos, 2011](#); [Frith et al., 2013](#); [Gaidos et al., 2014](#)). As indicated by its Tycho-2 identifier, TOI-1235 is a relatively nearby ( $d \approx 39.6$  pc) bright ( $V \approx 11.5$  mag) star. [Lépine et al. \(2013\)](#) and [Gaidos et al. \(2014\)](#) reported spectral types M0.5 V and M1.0 V and effective temperatures  $T_{\text{eff}}$  of 3660 K and 4060 K. [Gaidos et al. \(2014\)](#) also derived stellar radius  $R_{\star}$  and bolometric luminosity  $L_{\star}$ , which are consistent with the determinations by [Gaia Collaboration et al. \(2018\)](#), mass  $M_{\star}$ , and pseudo-equivalent width of the  $H\alpha$  line,  $\text{pEW}(H\alpha)$ .

We redetermined all stellar parameters for this early-M dwarf. In particular, we measured  $T_{\text{eff}}$ , surface gravity  $\log g$ , and iron abundance  $[\text{Fe}/\text{H}]$  from the stacked CARMENES VIS spectra by fitting them with a grid of PHOENIX-SESAM models as in [Passegger et al. \(2019\)](#), the rotational velocity  $v \sin i$  with the cross-correlation method as in [Reiners et al. \(2018b\)](#), and the stellar luminosity  $L_{\star}$  by integrating the spectral energy distribution as in [Cifuentes et al. \(2020\)](#). To do this, we used photometric data in 17 passbands from the optical blue Tycho-2  $B_T$  ([Høg et al., 2000](#)) to the mid-infrared AllWISE  $W4$  ([Cutri & et al., 2014](#)), the Virtual Observatory Spectral energy distribution Analyzer (VOSA; [Bayo et al., 2008](#)), and the BT-Settl CIFIST theoretical models, which were used to extrapolate the spectral energy distribution at ranges bluer than  $B_T$  and redder than  $W4$ . The full photometric data set including  $u'$  is made available by [Cifuentes et al. \(2020\)](#). The photospheric contributions to the total stellar flux of an M0.5 V star in these ranges are  $<0.5\%$  and  $<0.004\%$ , which means that the  $L_{\star}$  determination was model independent at the  $>99.5\%$  level at fixed metallicity. Next, we determined  $R_{\star}$  through the Stefan-Boltzmann law,  $L_{\star} = 4\pi R_{\star}^2 \sigma T_{\text{eff}}^4$ , and  $M_{\star}$  with the mass-radius relation derived from main-sequence eclipsing binaries by [Schweitzer et al. \(2019\)](#). All redetermined parameters ( $T_{\text{eff}}$ ,  $L_{\star}$ ,  $R_{\star}$ , and  $M_{\star}$ ) match the values published by [Gaidos et al. \(2014\)](#) and [Gaia Collaboration et al. \(2018\)](#) within  $1\sigma$ . Furthermore, we used the

precise astrometric data of *Gaia* DR2, the absolute RV measured on the stacked CARMENES spectra as in Lafarga et al. (2020b), and the prescription of Johnson & Soderblom (1987) for measuring the Galactocentric space velocities  $UVW$ . Using this kinematic information with the BANYAN  $\Sigma$  tool (Gagné et al., 2018), we classified TOI-1235 as a field star in the Galactic thin disk not associated with any young stellar kinematic group.

Finally, we determined key indicators of stellar activity. First, we measured the Mount Wilson  $S$  index,  $S_{\text{MWO}}$ , with the Yabi data environment on the HARPS-N spectra (Hunter et al., 2012; Borsa et al., 2015), from which we derived  $\log R'_{\text{HK}}$  using the formulae of Astudillo-Defru et al. (2017) and  $V - K_s = 3.602 \pm 0.059$  mag. Next, we measured  $\text{pEW}(\text{H}\alpha)$  on the CARMENES stacked spectrum following Schöfer et al. (2019), which was in agreement within  $2\sigma$  to the  $\text{pEW}(\text{H}\alpha) = +0.74 \pm 0.11 \text{ \AA}$  measured by Gaidos et al. (2014) in April 2009. This means that the activity level of the star (as determined by  $\text{H}\alpha$ ) has not substantially changed for over a decade. These three indicators make TOI-1235 one of the least active stars for its spectral type (Wright et al., 2004; Astudillo-Defru et al., 2017; Boro Saikia et al., 2018). See Sect. 2.4.3 for a search for periodic signals in other spectroscopic activity indicators.

We also searched for soft X-ray and ultraviolet data of TOI-1235, but the star was not covered by any pointing (*XMM-Newton*, *Chandra*, or *EUVE*), or was too faint and far from axis to be detected (*ROSAT* and *GALEX*). As an inactive member of the thin disk without further clear evidence to support a very young or very old age, TOI-1235 is likely between 0.6 Ga (older than the Hyades) and 10 Ga (younger than low-metallicity thick-disk stars).

Table 2.3 summarizes the stellar properties of TOI-1235. We provide the average values, their uncertainties, and corresponding reference.

2 Precise mass and radius of a transiting super-Earth planet orbiting the M dwarf  
TOI-1235: a planet in the radius gap?

| Parameter                             | Value                    | Reference | Parameter                                       | Value                      | Reference |
|---------------------------------------|--------------------------|-----------|-------------------------------------------------|----------------------------|-----------|
|                                       | <i>Name/identifiers</i>  |           |                                                 | <i>Parallax/kinematics</i> |           |
| Name                                  | TYC 4384-1735-1          | Høg00     | $\varpi$ [mas]                                  | $25.202 \pm 0.030$         | Gaia DR2  |
| Karmn                                 | J10088+692               | AF15      | $d$ [pc]                                        | $39.680 \pm 0.048$         | Gaia DR2  |
| TOI                                   | 1235                     | ExoFOP    | $\mu_\alpha \cos \delta$ [mas a <sup>-1</sup> ] | $+196.631 \pm 0.040$       | Gaia DR2  |
| TIC                                   | 103633434                | Sta18     | $\mu_\delta$ [mas a <sup>-1</sup> ]             | $+17.369 \pm 0.047$        | Gaia DR2  |
|                                       | <i>Phot. parameters</i>  |           | $\gamma$ [kms <sup>-1</sup> ]                   | $-27.512 \pm 0.018$        | This work |
| $T_{\text{eff}}$ [K]                  | $3997 \pm 51$            | This work | $U$ [kms <sup>-1</sup> ]                        | $+45.98 \pm 0.04$          | This work |
| $\log g$                              | $4.64 \pm 0.04$          | This work | $V$ [kms <sup>-1</sup> ]                        | $-4.29 \pm 0.01$           | This work |
| [Fe/H]                                | $+0.33 \pm 0.16$         | This work | $W$ [kms <sup>-1</sup> ]                        | $+1.732.384 \pm 0.03$      | This work |
| $v \sin i_\star$ [kms <sup>-1</sup> ] | $< 2.0$                  | This work | Gal. population                                 | Thin disk                  | This work |
|                                       | <i>Coords/Spec. type</i> |           |                                                 | <i>Physical parameters</i> |           |
| $\alpha$ (J2000)                      | 10:08:52.38              | Gaia DR2  | $L_\star$ [ $10^{-4} L_\odot$ ]                 | $883 \pm 3$                | This work |
| $\delta$ (J2000)                      | +69:16:35.8              | Gaia DR2  | $M_\star$ [ $M_\odot$ ]                         | $0.630 \pm 0.024$          | This work |
| Sp. type                              | M0.5 V                   | Lep13     | $R_\star$ [ $R_\odot$ ]                         | $0.619 \pm 0.019$          | This work |
| $G$ [mag]                             | $10.8492 \pm 0.0005$     | Gaia DR2  |                                                 | <i>Activity and age</i>    |           |
| $T$ [mag]                             | $9.9192 \pm 0.0072$      | Sta19     | pEW(H $\alpha$ ) [Å]                            | $+0.97 \pm 0.06$           | This work |
| $J$ [mag]                             | $8.711 \pm 0.020$        | Skr06     | $\log R'_{\text{HK}}$                           | $-4.728 \pm 0.015$         | This work |
|                                       |                          |           | $S_{\text{MWO}}$                                | $1.005 \pm 0.029$          | This work |
|                                       |                          |           | Age (Ga)                                        | 0.6–10                     | This work |

**Table 2.3:** Stellar parameters of TOI-1235. **References.** Høg00: Høg et al. (2000); AF15: Alonso-Floriano et al. (2015); Gaia DR2: Gaia Collaboration et al. (2018); Lep13: Lépine et al. (2013); Skr06: Skrutskie et al. (2006); Sta19: Stassun et al. (2019)

## 2.4 Analysis and results

### 2.4.1 Limits on photometric contamination

The presence of an unresolved companion could have a strong effect on our results. This is particularly relevant for *TESS* photometry because of its large pixel size ( $\sim 21$  arcsec). For comparison, the CARMENES and HARPS-N optical fiber apertures projected on the sky have sizes of only 1.5 arcsec and 1.0 arcsec, respectively. Even so, they are not immune to contamination from sub-arcsecond blends. Here, we place limits on the dilution factor and the presence of contaminant sources that can affect our photometric and RV measurements of TOI-1235. First, we verified that the sources in the selection apertures in the *TESS* pixel file (TPF) did not affect the depth of the transits significantly. The TPFs shown in Fig. 2.2 were created with `tpfplotter`<sup>21</sup> (Aller et al., 2020). In particular, *Gaia* DR2 sources 2 and 3 in sectors 14, source 4 in sector 20, and source 8 in sector 21 all have *G*-band fluxes lower by 0.5% than that of TOI-1235 (*Gaia* and the *TESS* photometric bands are very similar). Similar results were found for the apertures of the ground-based surveys ASAS-SN and NSVS.

For subarcsecond separations, we used our lucky imaging AstraLux and speckle NESSI

<sup>21</sup><https://github.com/jlillo/tpfplotter>

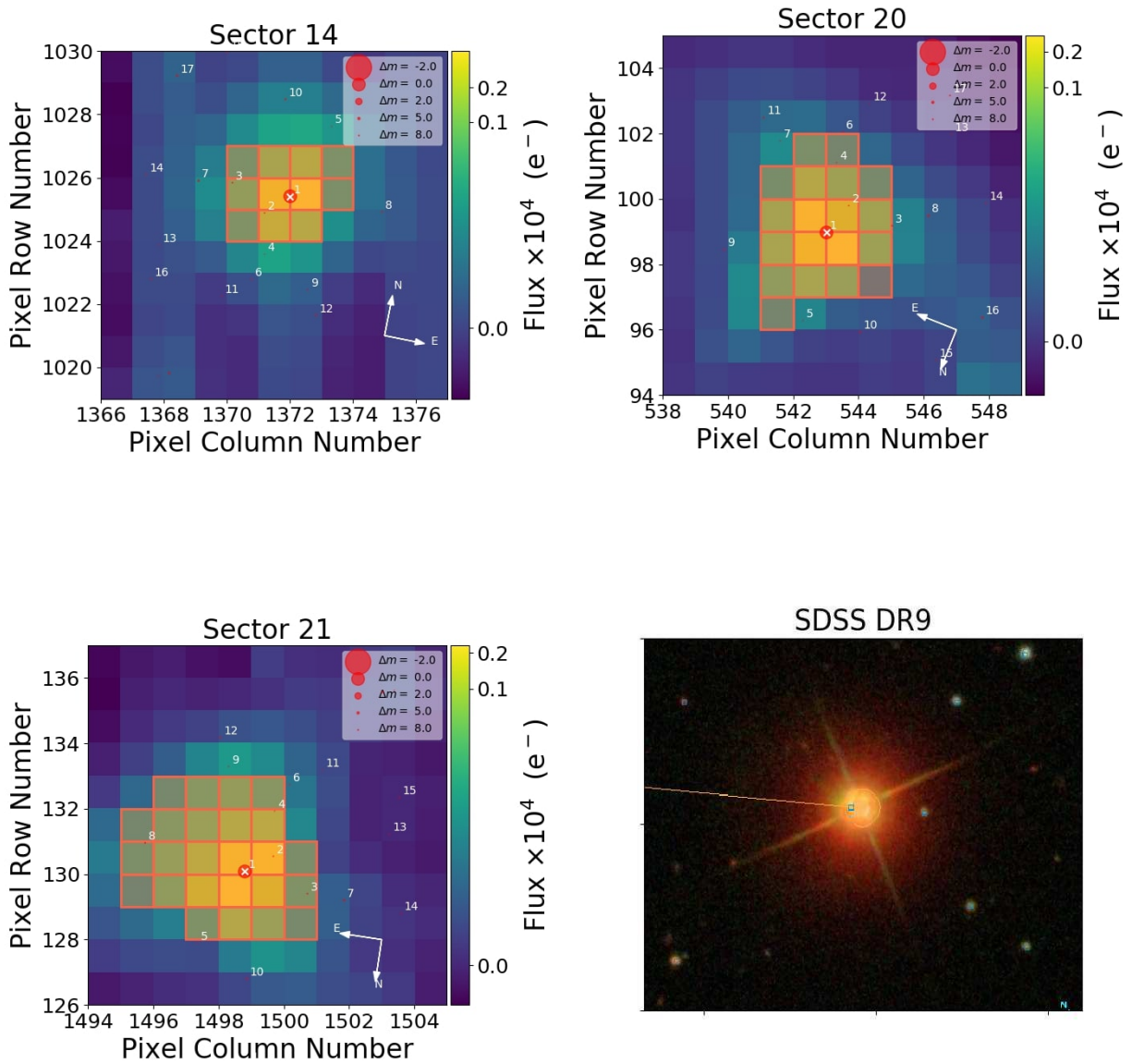


**Figure 2.2:** Target pixel files of TOI-1235 in *TESS* sectors 14, 20, and 21. The electron counts are color-coded. The red bordered pixels are used in the SAP. The size of the red circles indicates the *TESS* magnitudes of all nearby stars and TOI-1235 (circle 1 is marked with a cross). *Bottom right:* False-color,  $2 \times 2$  arcmin<sup>2</sup> Sloan Digital Sky Survey DR9 image centered on TOI-1235 (north is up, east is left).

data sets described in Sect. 2.2.3 and illustrated by Fig. 2.3. We computed  $5\sigma$  contrast curves as described by Lillo-Box et al. (2012) with the `astrasens` package<sup>22</sup> for AstraLux, and as reported by Livingston et al. (2018) for NESSI. From both data sets, we confirmed the absence of any close companion 4–6 mag fainter than TOI-1235, and derived an upper limit to the contamination of around 2% between 0.15 arcsec and 1.5 arcsec (6.0–60 au if physically bound).

A further constraint came from the *Gaia* DR2 renormalized unit weight error (RUWE) value, which for TOI-1235 is 1.03, below the critical value of 1.40 that “indicates that a source is non-single or otherwise problematic for the astrometric solution” (Arenou et al., 2018; Lindegren et al., 2018). We also searched for wide common proper motion companions with similar *Gaia* DR2 parallax, as in Montes et al. (2018), and found none within 30 arcmin of our star. Following these results, we conclude that TOI-1235 is a single star. We estimated the *TESS* and LCOGT dilution factors at  $D = 1.0$  with Eq. 2 in Espinoza et al. (2019), and fixed this value for all our model fits in the next sections.

## 2.4.2 Stellar rotational period from photometric data

The low activity levels of TOI-1235 probably imply a slow rotation and that there may not be enough spot coverage to measure a rotation period. Empirically, the measured limit on rotational velocity ( $v \sin i < 2 \text{ km s}^{-1}$ ) places a lower limit on  $P_{\text{rot}}/\sin i > 15.7 \text{ d}$ . Given the estimate of the stellar radius in Table 2.3, the short-period transiting planet around such a low-mass stars indicates a low obliquity (Winn et al., 2017), so that most probably,  $\sin i \sim 1$  and therefore  $P_{\text{rot}} \gtrsim 16 \text{ d}$ . On the other hand, from the  $\log R'_{\text{HK}}-P_{\text{rot}}$  relation of Astudillo-Defru et al. (2017), TOI-1235 has a most likely  $P_{\text{rot}}$  between 22 d and 38 d. However, from Jeffers et al. (2018b), the range of rotation periods that M dwarfs with  $v \sin i < 2 \text{ km s}^{-1}$  can have is between 10 d and 150 d.

To determine the actual rotational period of the star, we carried out different analyses of the available photometric data for TOI-1235. First, we employed the traditional periodogram analysis to search for significant peaks from the ASAS-SN  $g'$ - and  $V$ -band light curves. With the generalized Lomb-Scargle periodogram (GLS) of Zechmeister & Kürster (2009a), we obtained a peak at  $48.63 \pm 0.08 \text{ d}$  above the 10% false-alarm probability (FAP) threshold for the combined light curve after subtracting an independent zero-point from each band. We explored the time parameter space between 10 d and 1000 d. Because the ASAS-SN light curves contained a significant number (15%) of outlying data points because of flares and low S/Ns that might bias the previous GLS analysis, we repeated the GLS analysis after removing these deviant data from the two light curves in two steps: we first applied a  $2\sigma$  and then a  $1\sigma$  clipping algorithm. The new GLS periodogram of the resulting combined  $g'$  and  $V$  data looked different to the one of the original ASAS-SN data, as there were no significant peaks in the studied parameter space. The highest peak near the 10% FAP level was located, but at a longer period of  $136.9 \pm 1.4 \text{ d}$ . The marginal amplitude of the cleaned ASAS-SN  $g'$ - and  $V$ -band light curve folded in phase with this long period was only 1.4 mmag.

Next, we used a more sophisticated model and fit the ASAS-SN and NSVS photometry with a quasi-periodic Gaussian process (GP). In particular, we used the GP kernel introduced

---

<sup>22</sup><https://github.com/jlillo/astrasens>

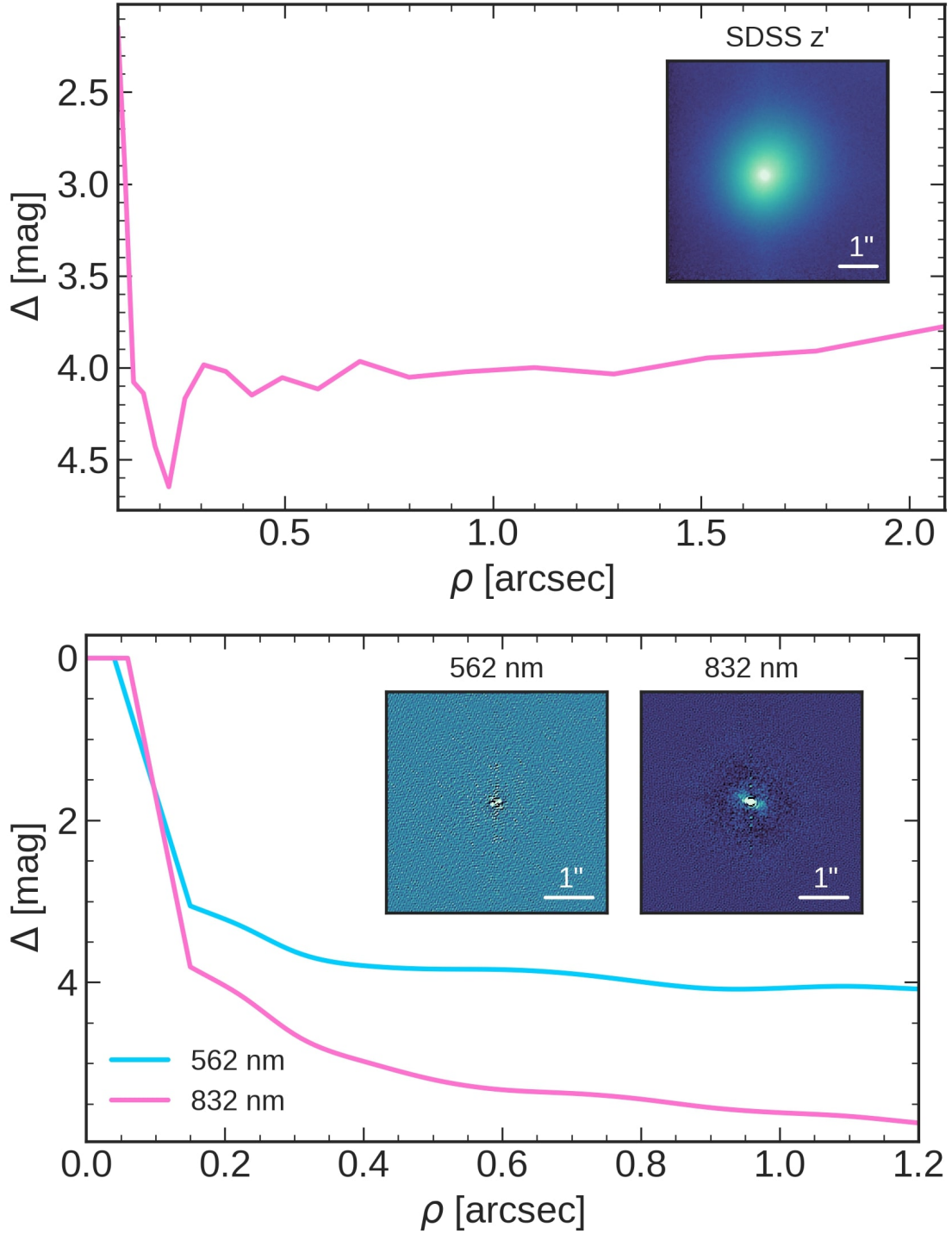


**Figure 2.3:** Contrast curves ( $5\sigma$ ) of TOI-1235 from AstraLux (*top*) and NESSI (*bottom*) observations. Inset images are  $6.0 \times 6.0$  arcsec<sup>2</sup> stacked in  $z'$  band and  $4.6 \times 4.6$  arcsec<sup>2</sup> reconstructed at 562 nm and 832 nm, respectively.

## 2 Precise mass and radius of a transiting super-Earth planet orbiting the M dwarf TOI-1235: a planet in the radius gap?

by Foreman-Mackey et al. (2017) of the form

$$k_{i,j}(\tau) = \frac{B}{2+C} e^{-\tau/L} \left[ \cos\left(\frac{2\pi\tau}{P_{\text{rot}}}\right) + (1+C) \right],$$

where  $\tau = |t_i - t_j|$  is the time lag,  $B$  and  $C$  define the amplitude of the GP,  $L$  is a timescale for the amplitude-modulation of the GP, and  $P_{\text{rot}}$  is the period of the quasi-periodic modulations. For the fit, we considered that each instrument and passband could have different values of  $B$  and  $C$ , while  $L$  and  $P_{\text{rot}}$  were left as common parameters. We considered wide uninformative priors for  $B$ ,  $C$  (log-uniform between  $10^{-3}$  ppm and  $10^8$  ppm),  $L$  (log-uniform between  $10^2$  d and  $10^8$  d),  $P_{\text{rot}}$  (uniform between 10 d and 300 d), and instrumental jitter (log-uniform between 10 ppm and  $10^6$  ppm). The fit was performed using *juliet* (Espinoza et al., 2019, see the next section for a full description of the algorithm), and the resulting fit is presented in Fig. 2.4. The rotational period from the quasi-periodic GP analysis was found to be  $P_{\text{rot}} = 41.2_{-1.2}^{+1.1}$  d, with an amplitude of about 10 mmag during the time of highest stellar variability.

Finally, we took advantage of the *TESS* observations of TOI-1235 in three sectors spanning almost 210 d. We analyzed the light curve described in Sect 2.2.1 and two light curves obtained from an optimized aperture (González-Cuesta et al. in prep.), in which we selected pixels with integrated flux above thresholds of  $10 e^- s^{-1}$  and  $20 e^- s^{-1}$ , respectively. We then corrected the light curves for outliers and jumps, filled the gaps, concatenated the three sectors following García et al. (2011, 2014a), and removed the transits to make sure that they did not bias the results. Last, we applied our rotation pipeline (Mathur et al., 2010; García et al., 2014b; Santos et al., 2019) with three different methods to search for a periodicity in the data: time-frequency analysis with wavelets (Torrence & Compo, 1998), autocorrelation function (McQuillan et al., 2014), and a composite spectrum that is a combination of the two previous methods (Ceillier et al., 2017). While different combinations of methods and light curves generally yielded somewhat different periodicities, signals in the range 32–42 d were present in the time-frequency and composite spectrum analysis of the last two sectors. The significance of the peaks in the autocorrelation function and composite spectrum was slightly below the criteria of in Section 3.3 of Ceillier et al. (2017) for establishing a reliable period (i.e., height of the peaks in the autocorrelation functions and composite function greater than or equal than 0.30 and 0.15, respectively). To summarize, the GLS periodogram of the raw ASAS-SN data (although with a low significance), the quasi-periodic GP modeling of the combined ASAS-SN and NSVS data, and the s-BGLS analysis of the spectroscopic data (see Sect 2.4.3) all indicate a stellar origin of the  $\sim 41.2$  d photometric signal, which suggests that this value might be the true rotation period of TOI-1235.

### 2.4.3 Signals in spectroscopic data

We searched for periodic signals in the combined CARMENES VIS and HARPS-N RV data, which had the lowest median RV uncertainties, by computing GLS periodograms, as illustrated by Fig. 2.5. A signal corresponding to the transits in the *TESS* light curve was significantly detected in the RVs at  $P_b = 3.44$  d (FAP  $\sim 1\%$ ; panel *a*) and its aliases at 1.41 d, 0.96 d, and 0.77 d. However, we also found an additional signal at  $P \approx 20.6$  d, at about half the most likely stellar rotation period. After removing the planetary signal, the 20.6 d signal

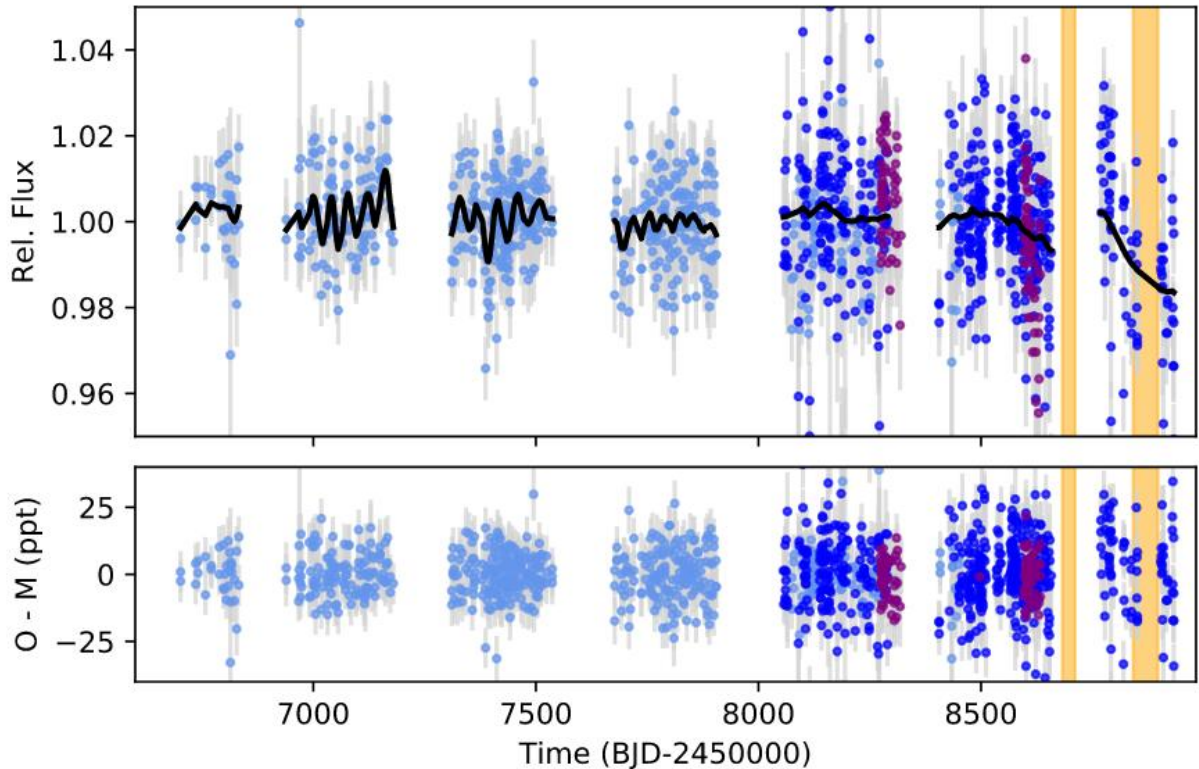


**Figure 2.4:** ASAS-SN ( $V$  passband in light blue,  $g'$  passband in dark blue) and NSVS (purple) long-term photometric monitoring modeled with a quasi-periodic GP kernel defined as in Foreman-Mackey et al. (2017). The time span of the *TESS* observations is shown in gold. ASAS-SN and NSVS fluxes were computed from the original magnitudes and normalized with their respective median.

and its aliases still remained with an FAP  $\gtrsim 0.1\%$  (panel *b*).

To understand the origin of the 20.6 d signal, we searched for additional peaks in the periodograms of the activity indicators CRX, dLW, and  $H\alpha$  derived from the individual CARMENES and HARPS-N spectra (panels *c-e*), and Ca IRTa (panel *f*), and the titanium oxide indices that quantify the strengths of the TiO  $\gamma$ ,  $\epsilon$ , and  $\delta$  absorption band heads at 7050 Å, 8430 Å, and 8860 Å (panels *g-i*), respectively, from the CARMENES spectra alone (Zechmeister et al., 2018; Schöfer et al., 2019). The activity indices and their uncertainties are listed in Table 2.10. Except for daily aliases, the highest peaks in the dLW,  $H\alpha$ , Ca IRTa, and TiO7050 periodograms are at about  $P \approx 32\text{--}47$  d, which adds further credence to  $P_{\text{rot}} \approx 41.2$  d as inferred in Section 2.4.2. All these indicators track different features in the stellar atmosphere, and our spectra cover only slightly more than two periods, therefore it is plausible that they do not yield exactly the same periods. We also detected the 20.6 d signal in the dLW series, which supports the notion that this signal is also related to stellar activity. As expected for an early-type M dwarf, the TiO8430 and TiO8860 indices showed no significant signals.

We used the stacked Bayesian generalized Lomb-Scargle periodogram (s-BGLS; Mortier et al., 2015) with the normalization of Mortier & Collier Cameron (2017) to verify whether

2 Precise mass and radius of a transiting super-Earth planet orbiting the M dwarf TOI-1235: a planet in the radius gap?

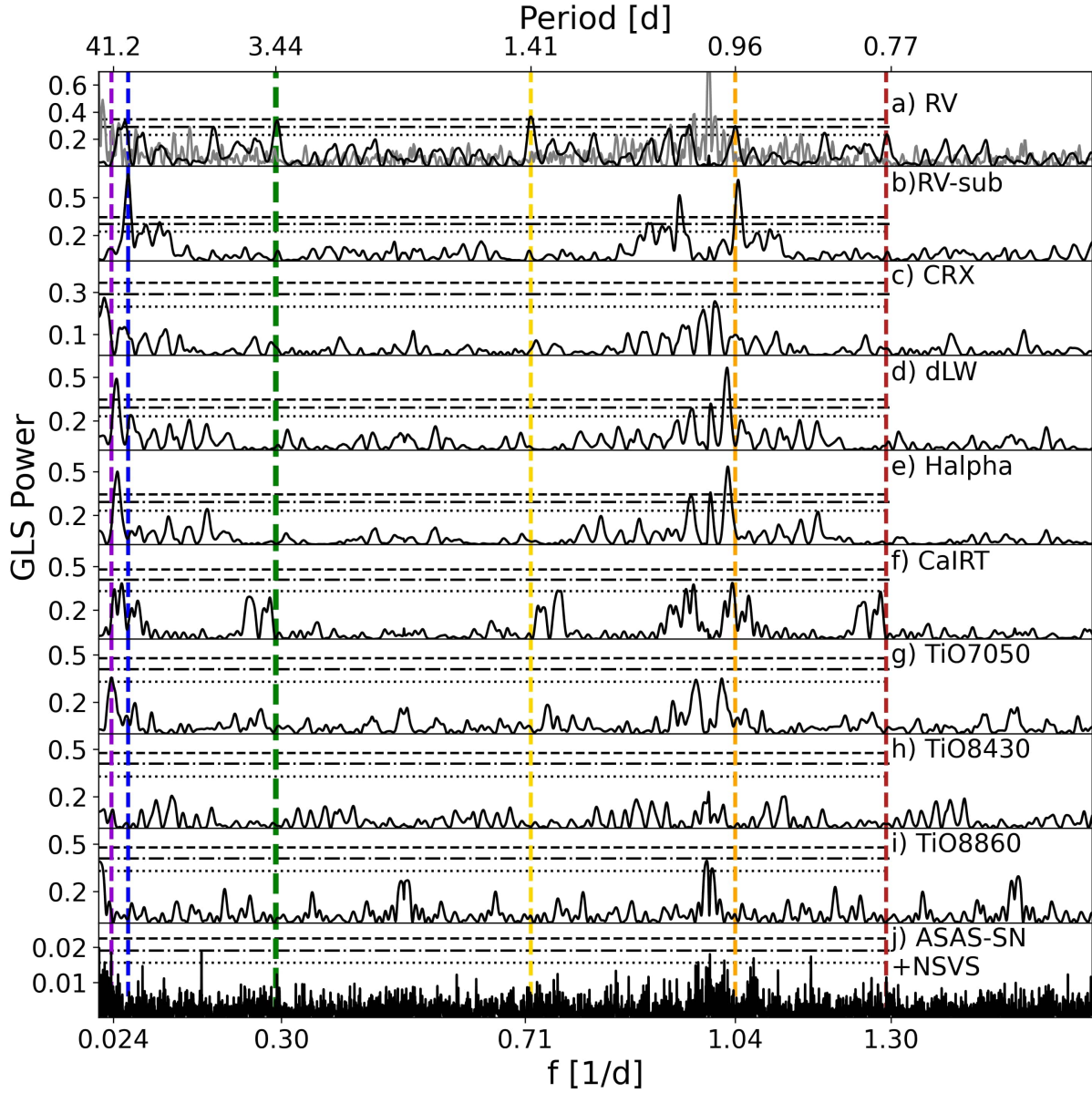


**Figure 2.5:** GLS periodograms of: (a) combined RVs from CARMENES VIS and HARPS-N (black) and the respective spectral window function (gray), (b) RV residuals after subtracting the planet signal, (c-e) combined CRX, dLW, and  $H\alpha$  index from CARMENES VIS and HARPS-N, and (f-i) Ca IRT, TiO7050, TiO8430, and TiO8860 indices from CARMENES VIS alone, (j) combined ASAS-SN ( $V$  and  $g'$  bands), and NSVS data photometry. In all panels the vertical dashed lines indicate the periods of 3.44 d (thick green, planet) and the aliases of the orbital period (yellow, orange, and red), 41.2 d (violet,  $P_{\text{rot}}$  from the quasi-periodic GP analysis of the combined photometric data), 20.6 d (blue,  $\sim P_{\text{rot}}/2$ ). The horizontal lines mark the theoretical FAP levels of 0.1% (dashed), 1% (dash-dotted), and 10% (dotted).

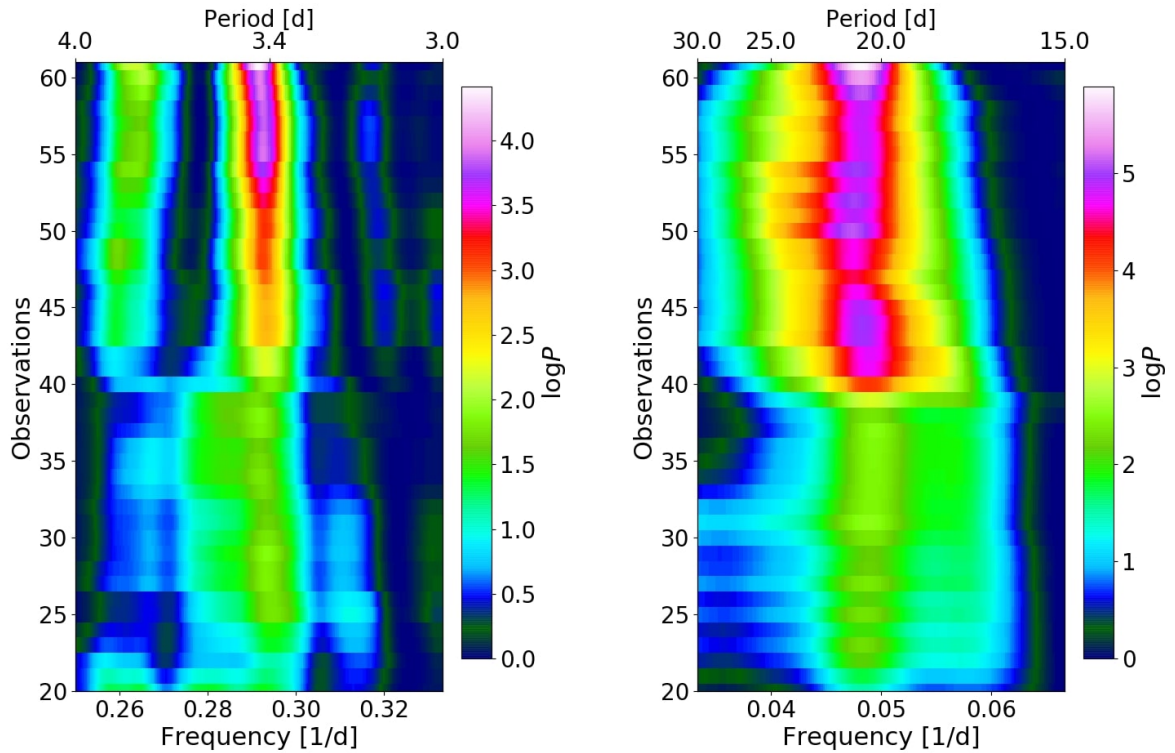


**Figure 2.6:** Evolution of the s-BGLS periodogram of the CARMENES and HARPS-N RV data of TOI-1235 around the 3.44 d signal of the transiting planet (*left*) and around the 20.6 d activity signal after subtracting the planet signal (*right*). The number of data points included in the computation of the periodogram increases from bottom to top.

the 20.6 d signal was coherent over the whole observational time baseline of CARMENES VIS and HARPS-N. In Fig. 2.6 we display s-BGLS periodograms of the raw RV data around 3.44 d, and of the RV data, after subtracting a sinusoid at the transiting planet period, around the 20.6 d signal.

This signal showed a first probability maximum after around 44 observations (BJD  $\sim$  2458663) and thereafter decreased for some time. This incoherence is characteristic of a nonplanetary origin of the signal (Mortier & Collier Cameron, 2017). The s-BGLS of the 3.44 d signal, on the other hand, showed a monotonically increasing probability, as expected for a Keplerian signal. Last, we measured the Pearson  $r$ , Student  $t$ , and Fisher  $z$  correlation coefficients between the temporal series of RV and the activity indicators CRX, dLW,  $H\alpha$ , Ca IRTa, TIO7050, and  $S_{MWO}$ , and we did not see any intrinsic correlation between RV and activity as in Gan et al. (2020). In particular, we determined absolute values of  $r$  and  $z$  below 0.006 and of  $t$  above 0.7, respectively, for all relations except for RV versus dLW, which was in any case weakly anticorrelated.

#### 2.4.4 Joint fit

To obtain precise parameters of the TOI-1235 system, we performed a joint analysis of the *TESS* and LCOGT photometry and CARMENES VIS and HARPS-N RV data using *juliet*. The model that we selected for our RV joint fit analysis was one composed of a circular Keplerian orbit for the transiting planet plus a quasi-periodic GP that we used to model the 20.6 d signal observed in the RVs; we have discussed this in previous sections. However, we also computed models of a circular orbit, an eccentric orbit, a circular orbit plus a sinusoid, an eccentric orbit plus a sinusoid, an eccentric orbit plus a GP, and two circular orbits. The two best-fit models, judged by their log-evidences, were a two-planet model and a one-circular-planet model combined with a GP to fit the 20.6 d signal. The star-planet tidal locking and consequent circularization of the planet orbit following the theoretical predictions of [Barnes \(2017\)](#), for instance, support both models with eccentricity fixed to zero (see also Fig. 2 in [Martínez-Rodríguez et al. 2019](#)). However, the difference between their log-evidence was  $\Delta \ln \mathcal{Z} < 2$ , which made the two models indistinguishable if they were equally likely a priori. The two models gave almost identical constraints on the properties of the transiting exoplanet. The analyses of the activity indices and photometric data, however, gave a higher prior weight to the stellar activity model, and we therefore decided to use a GP, which is typically better at modeling stellar activity than a simple sinusoid, as our final model to account for the 20.6 d signal. In our analysis we used the exp-sine-squared kernel for the GP, which is a very common kernel to model stellar activity signatures in the literature (see, e.g., [Nava et al., 2020](#), and references therein), and which is of the form

$$k_{i,j}(\tau) = \sigma_{\text{GP}}^2 \exp\left(-\alpha\tau^2 - \Gamma \sin^2\left[\frac{\pi\tau}{P_{\text{rot}}}\right]\right).$$

For the transit modeling, *juliet* uses the *batman* package ([Kreidberg, 2015](#)). To parameterize the limb-darkening effect in the *TESS* photometry, we employed the efficient, uninformative sampling scheme of [Kipping \(2013\)](#) and a quadratic law. We used a common set of limb-darkening coefficients across the three *TESS* sectors. In the LCOGT light-curve analysis, we instead used a linear law to parameterize the limb-darkening effect, as a more complex law was not warranted given the precision of the data, as explained by [Espinoza & Jordán \(2016\)](#). We used the [Espinoza \(2018\)](#) parameterization to explore the full physically plausible parameter space for the planet-to-star radius ratio,  $R_p/R_*$ , and impact parameter,  $b$ . Finally, we used a white-noise-only fit for the *TESS* photometry, as an analysis using a GP on the photometry returned a log-evidence that was indistinguishable from the one of a white-noise model. For the LCOGT photometry, on the other hand, we used a linear model to detrend the data, with airmass and pixel position of the target as regressors. The selected priors for our joint fit are presented in Table 2.4.

As illustrated by the posterior parameters of our joint fit presented in Table 2.5 and the resulting RV model presented in Fig. 2.7, the maximum a posteriori of the GP periodic component,  $P_{\text{rot;GP,RV}}$ , is about 20.9 d, in agreement with the signal observed in the GLS periodogram of the RVs (Fig. 2.5). This is almost exactly half the period derived from the long-term photometric monitoring discussed in previous sections, which means that a rotating spotted stellar surface is the most plausible cause of these variations. Consequently,

| Parameter <sup>a</sup>       | Prior                           | Unit               | Description                                         |
|------------------------------|---------------------------------|--------------------|-----------------------------------------------------|
| <i>Stellar parameters</i>    |                                 |                    |                                                     |
| $\rho_{\star}$               | $\mathcal{N}(3.7, 3.8)$         | $\text{g cm}^{-3}$ | Stellar density                                     |
| <i>Planet parameters</i>     |                                 |                    |                                                     |
| $P_b$                        | $\mathcal{U}(3, 4)$             | d                  | Period of planet b                                  |
| $t_{0,b}$                    | $\mathcal{U}(2458683, 2458687)$ | d                  | Time of transit center of planet b                  |
| $r_{1,b}$                    | $\mathcal{U}(0, 1)$             | ...                | Param. for $p$ and $b$                              |
| $r_{2,b}$                    | $\mathcal{U}(0, 1)$             | ...                | Param. for $p$ and $b$                              |
| $K_b$                        | $\mathcal{N}(0, 100)$           | $\text{ms}^{-1}$   | RV semi-amplitude of planet b                       |
| $e_b$                        | 0.0 (fixed)                     | ...                | Orbital eccentricity of planet b                    |
| $\omega_b$                   | 90.0 (fixed)                    | deg                | Periastron angle of planet b                        |
| <i>Photometry parameters</i> |                                 |                    |                                                     |
| $D_{\text{TESS}}$            | 1.0 (fixed)                     | ...                | Dilution factor for <i>TESS</i> Sec. 14, 20, and 21 |
| $M_{\text{TESS},S14}$        | $\mathcal{N}(0, 0.1)$           | ...                | Relative flux offset for <i>TESS</i> Sec. 14        |
| $M_{\text{TESS},S20}$        | $\mathcal{N}(0, 0.1)$           | ...                | Relative flux offset for <i>TESS</i> Sec. 20        |
| $M_{\text{TESS},S21}$        | $\mathcal{N}(0, 0.1)$           | ...                | Relative flux offset for <i>TESS</i> Sec. 21        |
| $\sigma_{\text{TESS},S14}$   | $\mathcal{LU}(1, 10^4)$         | ppm                | Extra jitter term for <i>TESS</i> Sect. 14          |
| $\sigma_{\text{TESS},S20}$   | $\mathcal{LU}(1, 10^4)$         | ppm                | Extra jitter term for <i>TESS</i> Sec. 20           |
| $\sigma_{\text{TESS},S21}$   | $\mathcal{LU}(1, 10^4)$         | ppm                | Extra jitter term <i>TESS</i> Sec. 21               |
| $q_{1,\text{TESS}}$          | $\mathcal{U}(0, 1)$             | ...                | Limb-dark. param. for <i>TESS</i> Sec. 14, 20, 21   |
| $q_{2,\text{TESS}}$          | $\mathcal{U}(0, 1)$             | ...                | Limb-dark. param. for <i>TESS</i> Sec. 14, 20, 21   |
| $D_{\text{LCO}}$             | 1.0 (fixed)                     | ...                | Dilution factor for LCOGT                           |
| $q_{1,\text{LCO}}$           | $\mathcal{U}(0, 1)$             | ...                | Limb-dark.param. for LCOGT                          |
| $M_{\text{LCO}}$             | $\mathcal{N}(0, 0.1)$           | ...                | Relative flux offset for LCOGT                      |
| $\sigma_{\text{LCO}}$        | $\mathcal{LU}(1, 10000)$        | ppm                | Extra jitter term for LCOGT                         |
| $\theta_{0,\text{LCO}}$      | $\mathcal{U}(-100, 100)$        | ...                | Extra jitter term for LCOGT                         |
| $\theta_{1,\text{LCO}}$      | $\mathcal{U}(-100, 100)$        | ...                | Extra jitter term for LCOGT                         |
| <i>RV parameters</i>         |                                 |                    |                                                     |
| $\gamma_{\text{HARPS-N}}$    | $\mathcal{N}(0, 10)$            | $\text{ms}^{-1}$   | RV zero-point for HARPS-N                           |
| $\sigma_{\text{HARPS-N}}$    | $\mathcal{LU}(0.01, 10)$        | $\text{ms}^{-1}$   | Extra jitter term for HARPS-N                       |
| $\gamma_{\text{CARMENES}}$   | $\mathcal{N}(0, 10)$            | $\text{ms}^{-1}$   | RV zero point for CARMENES                          |
| $\sigma_{\text{CARMENES}}$   | $\mathcal{LU}(0.01, 10)$        | $\text{ms}^{-1}$   | Extra jitter term for CARMENES                      |
| <i>GP hyperparameters</i>    |                                 |                    |                                                     |
| $\sigma_{\text{GP,RV}}$      | $\mathcal{LU}(10^{-10}, 100)$   | $\text{ms}^{-1}$   | Amp. of GP comp. for the RVs                        |
| $\alpha_{\text{GP,RV}}$      | $\mathcal{LU}(10^{-10}, 100)$   | $\text{d}^{-2}$    | Inv.length-scale of GP exp. comp. for the RVs       |
| $\Gamma_{\text{GP,RV}}$      | $\mathcal{LU}(10^{-10}, 100)$   | ...                | Amp. of GP sine-squared comp. for the RVs           |
| $P_{\text{rot;GP,RV}}$       | $\mathcal{U}(1, 100)$           | d                  | Period of the GP-QP comp. for the RVs               |

**Table 2.4:** Priors used for TOI-1235 b in the joint fit with *juliet*.

**Notes.** <sup>(a)</sup> The parameterization for  $(p, b)$  was made with  $(r_1, r_2)$  as in [Espinoza \(2018\)](#). The prior labels of  $\mathcal{N}$ ,  $\mathcal{U}$ , and  $\mathcal{LU}$  represent normal, uniform, and log-uniform distributions, respectively, where  $\mathcal{N}(\mu, \sigma^2)$  is a normal distribution of the mean  $\mu$  and variance  $\sigma^2$  and  $\mathcal{U}(a, b)$  and  $\mathcal{LU}(a, b)$  are uniform and log-uniform distributions between  $a$  and  $b$ .

## 2 Precise mass and radius of a transiting super-Earth planet orbiting the M dwarf TOI-1235: a planet in the radius gap?

we performed joint fits using the period observed in the photometry of  $P_{\text{rot}} = 41.2_{-1.5}^{+1.2}$  d as a prior, and the results were almost identical regarding the properties of the transiting planet to the ones presented in Table 2.5. Therefore our model is marginalized properly over the possible different scenarios on the stellar surface in terms of stellar activity. As shown in Fig. 2.7 and Table 2.5, we attained a  $10\sigma$  detection of the planetary RV semi-amplitude.

We also performed two additional fits of the the lower-precision CARMENES NIR and iSHELL RVs (Sects. 2.2.2 and 2.2.2). We set all the ephemeris priors to those found in the joint fit, including the planet  $P$  and  $t_0$ , with and without stellar rotation period and timescale of the GP. All other parameters were free to vary around the entire parameter space. The two models, with and without GP, were indistinguishable based on their log-evidences ( $\Delta \ln \mathcal{Z} < 1$ ). Interestingly, the GP amplitude in the first model was consistent with zero, which supports the nonplanetary origin of the  $\sim 41.2$  d period, as argued above. The new NIR RV analysis yielded a lower statistical precision in model parameter recovery than VIS RVs, but the new recovered planet-semi-amplitude  $K_{\text{NIR}} = 2.8 \pm 1.4 \text{ m s}^{-1}$  was consistent within  $1\sigma$  with that listed in Table 2.5. In addition, the NIR RVs, taken at independent wavelengths and in the case of iSHELL with a different facility, help validate the system and instrument performance.

To summarize, the TOI-1235 system consists of a relatively weakly active M dwarf with at least one super-Earth-like planet, namely TOI-1235 b (see Table 2.6), with a mass of  $M_{\text{p}} = 5.9_{-0.6}^{+0.6} M_{\oplus}$  and radius of  $R_{\text{p}} = 1.69_{-0.08}^{+0.08} R_{\oplus}$  on a circular orbit with a period of 3.44 d. We also derived a bulk density of  $\rho_{\text{p}} = 6.7_{-1.1}^{+1.3} \text{ g cm}^{-3}$  and an equilibrium temperature, assuming a zero albedo, of  $T_{\text{eq}} = 776 \pm 13 \text{ K}$ , which is slightly hotter than the mean surface temperature of Venus.

### 2.4.5 Search for transit depth and time variations

*TESS* observed TOI-1235 in three sectors and covered 22 transits of TOI-1235 b. This allowed us to assess the presence of transit-timing variations (TTVs) and transit depth variations. We carried out a search for TTVs using the `batman` package and fit each transit individually. We only left transit times and transit depth as free parameters, and fixed the remaining parameters to the values obtained in the joint analysis in Sect. 2.4.4. The best-fit parameters and associated uncertainties in our fitting procedure were derived using a Markov chain Monte Carlo analysis implemented in the `emcee` python package (Foreman-Mackey et al., 2013). We found an indication of a periodic TTV signal with a semi-amplitude of about 4 min. Using the GLS of the observed TTV signal, we found that the observed TTVs had a periodicity of  $25.3 \pm 0.2$  d, which might indicate the presence of a second nontransiting planet in the system (Holman & Murray, 2005). However, a TTV signal with this amplitude might also easily be generated by the stellar activity (e.g., Oshagh et al., 2013), and the period was consistent with our previous analyses of the stellar rotation. We also searched for trends in the derived transit depths, and found that individual depths agreed within  $1\sigma$  with the depth derived from the combined analysis.

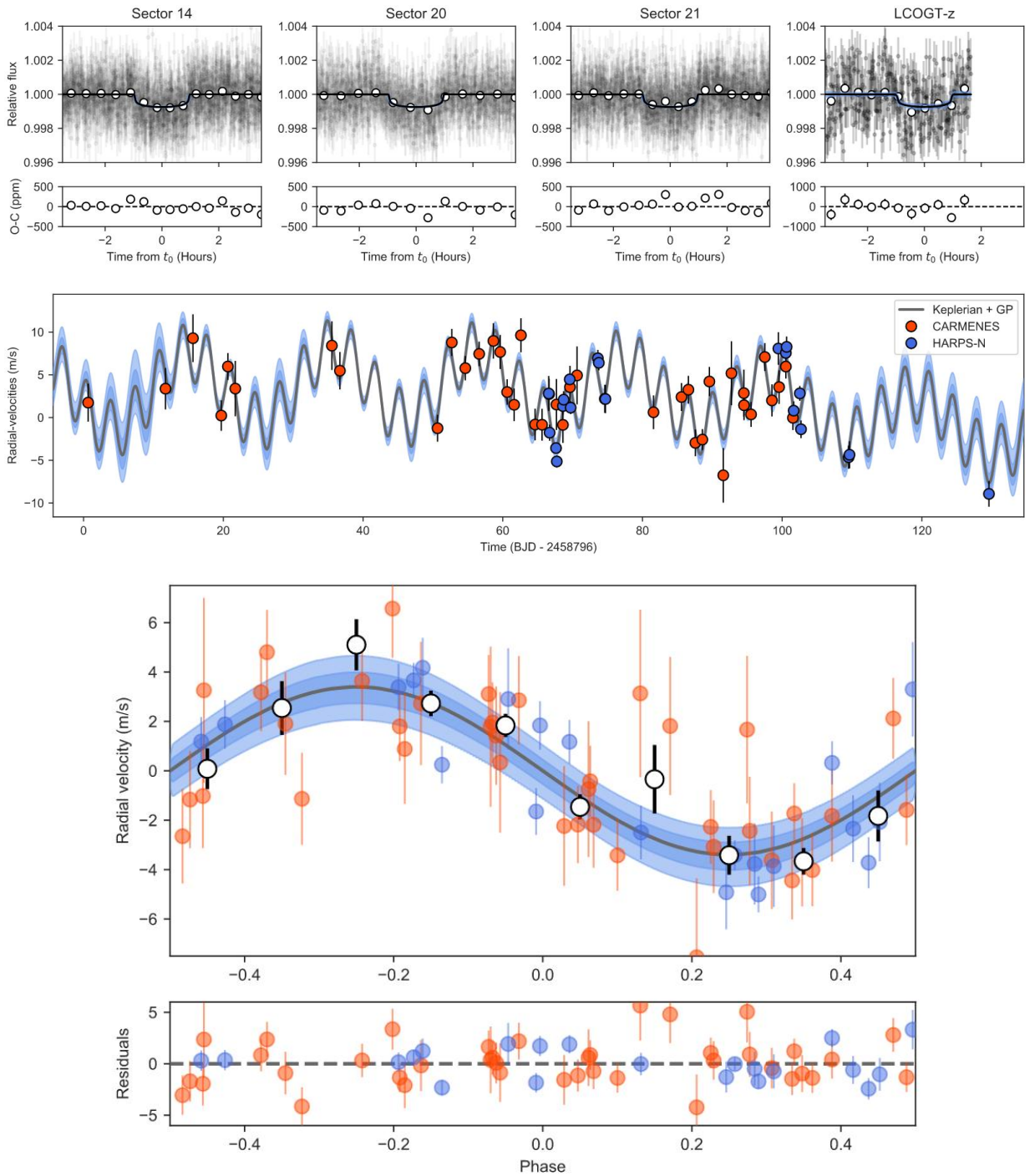


**Figure 2.7:** Joint fit results. *Top panels:* Phase-folded light curves of *TESS*, sectors 14, 20, and 21, and LCOGT, from left to right, and their residuals. White circles are binned data (shown only for reference; data used to fit the model were the unbinned points), black curves are the best-fit models, and blue areas are the 68% credibility bands. *Middle panel:* CARMENES VIS (orange) and HARPS-N (blue) RVs. The gray curve is the median best-fit *juliet* model, and the light and dark blue areas are its 68% and 95% credibility bands. *Bottom panel:* Phase-folded RVs for TOI-1235 without the GP component. Orange circles are CARMENES VIS data, blue circles are HARPS-N data, white points are binned data for reference. The gray curve is the median best-fit *juliet* model, and the light and dark blue areas are its 68% and 95% credibility bands.

2 Precise mass and radius of a transiting super-Earth planet orbiting the M dwarf TOI-1235: a planet in the radius gap?

| Parameter <sup>a</sup>                              | TOI-1235 b                         |
|-----------------------------------------------------|------------------------------------|
| Stellar parameters                                  |                                    |
| $\rho_{\star}$ ( $\text{g cm}^{-3}$ )               | $3.74^{+0.30}_{-0.31}$             |
| Planet parameters                                   |                                    |
| $P$ (d)                                             | $3.444717^{+0.000040}_{-0.000042}$ |
| $t_0$ (BJD)                                         | $2458683.6155^{+0.0017}_{-0.0015}$ |
| $a/R_{\star}$                                       | $13.29^{+0.34}_{-0.38}$            |
| $p = R_p/R_{\star}$                                 | $0.02508^{+0.00084}_{-0.00085}$    |
| $b = (a/R_{\star}) \cos i_p$                        | $0.25^{+0.12}_{-0.14}$             |
| $i_p$ (deg)                                         | $88.90^{+0.62}_{-0.57}$            |
| $r_1$                                               | $0.500^{+0.081}_{-0.097}$          |
| $r_2$                                               | $0.02506^{+0.00083}_{-0.00085}$    |
| $K$ ( $\text{ms}^{-1}$ )                            | $3.40^{+0.35}_{-0.34}$             |
| Photometry parameters                               |                                    |
| $M_{\text{TESS,S14}}$ ( $10^{-6}$ )                 | $-31.0^{+8.5}_{-8.3}$              |
| $M_{\text{TESS,S20}}$ ( $10^{-6}$ )                 | $-17.0^{+8.3}_{-8.2}$              |
| $M_{\text{TESS,S21}}$ ( $10^{-6}$ )                 | $-24.0^{+8.0}_{-8.0}$              |
| $\sigma_{\text{TESS,S14}}$ (ppm)                    | $1.9^{+10.5}_{-1.6}$               |
| $\sigma_{\text{TESS,S20}}$ (ppm)                    | $1.9^{+8.2}_{-1.6}$                |
| $\sigma_{\text{TESS,S21}}$ (ppm)                    | $1.5^{+7.8}_{-1.3}$                |
| $q_{1,\text{TESS}}$                                 | $0.42^{+0.32}_{-0.25}$             |
| $q_{2,\text{TESS}}$                                 | $0.31^{+0.30}_{-0.20}$             |
| $M_{\text{LCO}}$ ( $10^{-6}$ )                      | $-257^{+84}_{-86}$                 |
| $\sigma_{\text{LCO}}$ (ppm)                         | $970^{+82}_{-83}$                  |
| $q_{1,\text{LCO}}$                                  | $0.49^{+0.30}_{-0.30}$             |
| $\theta_{0,\text{LCO}}$ ( $10^{-6}$ )               | $-10^{+11}_{-11}$                  |
| $\theta_{1,\text{LCO}}$ ( $10^{-6}$ )               | $-49^{+11}_{-11}$                  |
| RV parameters                                       |                                    |
| $\gamma_{\text{CARMENES}}$ ( $\text{ms}^{-1}$ )     | $-3.0^{+4.6}_{-4.3}$               |
| $\sigma_{\text{CARMENES}}$ ( $\text{ms}^{-1}$ )     | $0.17^{+0.61}_{-0.14}$             |
| $\gamma_{\text{HARPS-N}}$ ( $\text{ms}^{-1}$ )      | $3.8^{+4.6}_{-4.2}$                |
| $\sigma_{\text{HARPS-N}}$ ( $\text{ms}^{-1}$ )      | $1.29^{+0.43}_{-0.37}$             |
| GP hyperparameters                                  |                                    |
| $\sigma_{\text{GP,RV}}$ ( $\text{ms}^{-1}$ )        | $12.3^{+17.9}_{-6.3}$              |
| $\alpha_{\text{GP,RV}}$ ( $10^{-6} \text{d}^{-2}$ ) | $74^{+127}_{-50}$                  |
| $\Gamma_{\text{GP,RV}}$                             | $0.084^{+0.251}_{-0.068}$          |
| $P_{\text{rot;GP,RV}}$ (d)                          | $20.93^{+0.56}_{-0.52}$            |

**Table 2.5:** Posterior parameters of the `juliet` joint fit for TOI-1235 b. <sup>(a)</sup> Priors and descriptions for each parameter are in Table 2.4. Error bars denote the 68% posterior credibility intervals.

| Parameter <sup>a</sup>             | TOI-1235 b                      |
|------------------------------------|---------------------------------|
| <i>Derived transit parameters</i>  |                                 |
| $u_1^b$                            | $0.38^{+0.30}_{-0.24}$          |
| $u_2^b$                            | $0.22^{+0.35}_{-0.32}$          |
| $t_T$ (h)                          | $2.094^{+0.126}_{-0.086}$       |
| <i>Derived physical parameters</i> |                                 |
| $M_p$ ( $M_\oplus$ )               | $5.90^{+0.62}_{-0.61}$          |
| $R_p$ ( $R_\oplus$ )               | $1.694^{+0.080}_{-0.077}$       |
| $\rho_p$ ( $\text{g cm}^{-3}$ )    | $6.7^{+1.3}_{-1.1}$             |
| $g_p$ ( $\text{m s}^{-2}$ )        | $20.1^{+3.0}_{-2.7}$            |
| $a_p$ (au)                         | $0.03826^{+0.00048}_{-0.00049}$ |
| $T_{\text{eq}}$ (K) <sup>c</sup>   | $775^{+13}_{-13}$               |
| $S$ ( $S_\oplus$ )                 | $60.3^{+1.6}_{-1.5}$            |

**Table 2.6:** Derived planetary parameters for TOI-1235 b. <sup>(a)</sup> Parameters obtained with the posterior values from Table 2.5,  $t_T$ =Transit duration, from first contact to fourth contact. Error bars denote the 68 % posterior credibility intervals. <sup>(b)</sup> Derived from the *TESS* light curve. <sup>(c)</sup> The equilibrium temperature was calculated assuming zero Bond albedo.

## 2.5 Discussion

Our 61 RV measurements yield a planetary mass for TOI-1235 b with an uncertainty of about 10 %, and the *TESS* and LCOGT light curves constrain the planetary radius at a level of about 5 % uncertainty. This means that TOI-1235 b belongs to the select group of terrestrial planets with a well-determined bulk density. The population with measurements better than 30 % is shown in the mass-radius diagram of Fig. 2.8. The comparison of TOI-1235 b with theoretical models of Zeng et al. (2016, 2019) is consistent with a rocky MgSiO<sub>3</sub>-dominated composition with a bulk density slightly higher than that of Earth. This classifies it as a super-Earth planet.

Based again on the mass and radius relationships from Zeng et al. (2016), the best fit results in an iron core mass fraction of  $\text{CRF} = 0.10^{+0.38}_{-0.10}$ , but the planet is also consistent with an Earth-like bulk composition ( $\text{CRF} \approx 0.4\text{--}0.6$ ). Furthermore, using Hardcore (Suissa et al., 2018) and our  $R$  and  $M$ , the marginal core ratio fraction,  $\text{CRF}_{\text{marg}}$ , is  $0.53 \pm 0.20$ , similar to the Earth’s true CRF value of 0.55.

Like many other transiting terrestrial and sub-Neptune planets, TOI-1235 b is on a fairly irradiated orbit and therefore may have been strongly sculpted by extreme atmospheric escape due to XUV-driven photoevaporation (e.g., López & Fortney, 2013; Owen & Wu, 2013a) or core-powered mass loss (e.g., Wu, 2019b; Gupta & Schlichting, 2020). Because of its expected low envelope mass fraction, the required binding energy makes this explanation difficult for TOI-1235 b, but using the escape scaling relations from López & Fortney (2013), we found that this planet lies right at the boundary of where escape evolution is likely to

## 2 Precise mass and radius of a transiting super-Earth planet orbiting the M dwarf TOI-1235: a planet in the radius gap?

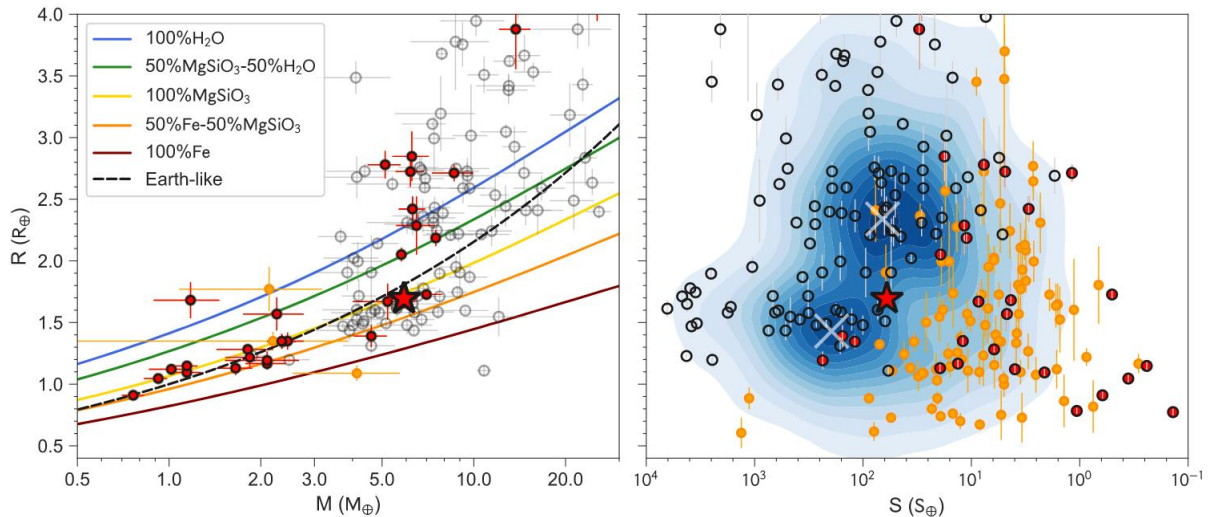


**Figure 2.8:** Mass-radius (*left*) and insolation-radius (*right*) diagrams in Earth units. In the two panels, open circles are transiting planets around F-, G-, and K-type stars with mass and radius measurement better than 30% from the TEPCat database of well-characterized planets (Southworth, 2011), filled red circles are planets around M dwarfs with mass and radius measurement, filled yellow circles are planets around M dwarfs with mass determinations lower than 30% or without mass constraints at all (*right* panel only), and the red star is TOI-1235 b, whose radius and mass are determined with accuracies of 5% and 10%, respectively. In the *left* panel, the color lines are the theoretical  $R$ - $M$  models of Zeng et al. (2016), and the three planets with mass determinations lower than 30% are K2-3 b, BD-17 588A b, and LHS 1815 b. In the *right* panel, we plot the  $R$ - $S$  point density of all the known confirmed transiting planets with contours, and mini-Neptunes and super-Earths density maxima with white crosses. The M dwarf without mass determination in the radius gap is K2-104 b (Mann et al., 2017), a planet around an active star in the Praesepe cluster that is fainter by 5 mag in  $V$  than TOI-1235.

play a significant role in removing primordial H/He gaseous envelopes.

As described in Sect. 3.1 and illustrated by the insolation-radius diagram in Fig. 2.8, the growing exoplanet statistics has revealed a gap in the radius distribution of planets slightly larger than Earth (Fulton et al., 2017). Rocky super-Earth planets of up to  $\sim 1.5 R_{\oplus}$  are relatively common, as are gaseous mini-Neptunes in the range of  $2$ – $4 R_{\oplus}$ , but only a few planets have been detected with a radius inside this gap (Gandolfi et al., 2019). Using the location of the radius valley as determined by Van Eylen et al. (2018), that is,  $\log R = m \log P + a$  with  $m = -0.09^{+0.02}_{-0.04}$  and  $a = 0.37^{+0.04}_{-0.02}$ , we determine the predicted location of the radius valley at the orbital period of TOI-1235 b. We find that for  $P = 3.44$  d, the radius valley is located at  $R = 2.1 \pm 0.2 R_{\oplus}$ . Therefore and according to this definition, TOI-1235 b, which has a radius  $R = 1.69^{+0.08}_{-0.07} R_{\oplus}$ , would be located near the lower edge of the radius valley. Its rocky composition is indeed consistent with the planet having lost its atmosphere, as expected for planets below the radius valley (e.g., Owen & Wu, 2013a).

However, the location of the radius gap as determined by Van Eylen et al. (2018) was based on F-, G-, and K-type stars, whereas TOI-1235 b orbits an M dwarf star. Whether these same boundaries apply to M dwarfs (and whether the gap actually exists for planets

around M dwarfs) has been the subject of several recent studies (Zeng et al., 2017; Fulton & Petigura, 2018; Hirano et al., 2018a). Following Zeng et al. (2017), for example, who used all of the *Kepler* planet candidates, the radius and stellar irradiation level of TOI-1235 b place it exactly in the gap for early-M dwarfs (located at about  $1.7 R_{\oplus}$  for an irradiation of  $60 S_{\oplus}$  in that work). On the other hand, when we extrapolate from the sample of Fulton & Petigura (2018), who focused on F-, G-, and K-type stars with precise stellar parameters and on stars that host validated *Kepler* exoplanets, we reach a similar conclusion. Finally, using the sample of Hirano et al. (2018a), who focused only on low-mass stars hosting validated small planets unveiled by K2 and *Kepler*, we would locate TOI-1235 b in the gap, but the data in that sample (arguably more suitable for a proper comparison with the stellar properties of TOI-1235) were unable to track a proper stellar irradiation versus radius dependence of the gap. Therefore our measurements of the bulk composition of TOI-1235 b, consistent with the planet having lost its atmosphere, place a strong constraint on any interpretation regarding the radius gap for M dwarfs at the irradiation levels received by TOI-1235 b. If atmospheric loss is indeed the correct physical interpretation for the radius gap, and if it applies to M dwarfs at the period or stellar irradiation level of TOI-1235 b, the gap for early-type M dwarfs has to be either at or above  $1.7 R_{\oplus}$ .

## 2.6 Conclusions

We confirmed that TOI-1235 b is a transiting super-Earth planet around an M0.5 V star, observed in sectors 14, 20, and 21 of the *TESS* mission. We collected CARMENES and HARPS-N spectroscopic data, from which we confirmed the planetary nature of the transit signal detected by *TESS*. Further support for the planetary interpretation came from our LCOGT photometric data during one transit, as well as from lucky and speckle imaging. From the joint analysis of all the data, we derived the following parameters for TOI-1235 b: mass of  $M_p = 5.9 \pm 0.6 M_{\oplus}$ , radius of  $R_p = 1.69 \pm 0.08 R_{\oplus}$ , and density of  $\rho_p = 6.7_{-1.1}^{+1.7} \text{ g cm}^{-3}$ .

A comparison of the physical properties of TOI-1235 b with compositional models reveals the planet to be a rocky super-Earth, with a bulk density only slightly higher than that of Earth. Although the location (and existence) of a radius gap for exoplanets around M-dwarfs is still debated, the radius and irradiation level of TOI-1235 b place it at the radius gap according to various suggestions of its location in the literature for these small low-mass stars. If the gap indeed exists for M-dwarfs, the bulk properties of TOI-1235 b, which make it consistent with having lost its atmosphere, constrain the gap to be at or above the planetary radius of TOI-1235 b, that is,  $\sim 1.7 R_{\oplus}$  at its irradiation level ( $\sim 60 S_{\oplus}$ ). These findings help to better constrain the dependence of the gap location on stellar type and irradiation, and thus to understand its origin. Finally, the brightness of TOI-1235 ( $V \approx 11.5$  mag) makes this planet an accessible and very interesting object for further studies of planet formation and atmospheric evolution.

2 Precise mass and radius of a transiting super-Earth planet orbiting the M dwarf  
TOI-1235: a planet in the radius gap?

| BJD<br>(-2450000) | RV<br>(m s <sup>-1</sup> ) | CRX<br>(m s <sup>-1</sup> Np <sup>-1</sup> ) | HARPS-N                                  |               | $S_{\text{MWO}}$ | $\log R'_{\text{HK}}$ |
|-------------------|----------------------------|----------------------------------------------|------------------------------------------|---------------|------------------|-----------------------|
|                   |                            |                                              | dLW<br>(m <sup>2</sup> s <sup>-2</sup> ) | H $\alpha$    |                  |                       |
| 8862.5810         | 6.6±2.0                    | 11±17                                        | -12.7±3.5                                | 0.7144±0.0026 | 0.967±0.043      | -4.748±0.045          |
| 8862.7100         | 2.0±1.0                    | -2.2±7.5                                     | -25.8±2.0                                | 0.7125±0.0013 | 0.991±0.014      | -4.735±0.038          |
| 8863.6284         | 0.24±0.60                  | 2.1±4.8                                      | -30.4±1.3                                | 0.7154±0.0010 | 1.015±0.008      | -4.722±0.037          |
| 8863.7378         | -1.32±0.72                 | 4.7±5.7                                      | -30.4±1.3                                | 0.7147±0.0009 | 1.005±0.009      | -4.727±0.037          |
| 8864.6070         | 5.2±1.0                    | 19.5±7.6                                     | -28.4±1.7                                | 0.7144±0.0013 | 1.000±0.012      | -4.730±0.038          |
| 8864.7169         | 5.91±0.99                  | 7.6±7.8                                      | -30.4±1.6                                | 0.7242±0.0013 | 1.040±0.014      | -4.709±0.038          |
| 8865.5889         | 8.28±0.70                  | -0.9±5.7                                     | -29.8±1.4                                | 0.7156±0.0012 | 1.027±0.010      | -4.716±0.037          |
| 8865.7198         | 4.97±0.76                  | 8.8±6.0                                      | -29.0±1.3                                | 0.7134±0.0011 | 1.009±0.008      | -4.725±0.037          |
| 8869.6175         | 10.75±0.98                 | 4.5±7.8                                      | -25.9±2.2                                | 0.7131±0.0015 | 0.986±0.021      | -4.738±0.039          |
| 8869.7536         | 10.22±0.89                 | -4.2±6.9                                     | -26.1±1.5                                | 0.7152±0.0009 | 1.073±0.011      | -4.692±0.037          |
| 8870.6093         | 6.0±1.6                    | -22±13                                       | -22.4±2.4                                | 0.7120±0.0018 | 1.031±0.030      | -4.713±0.040          |
| 8870.6978         | 6.0±1.6                    | -21±13                                       | -22.4±2.9                                | 0.7087±0.0020 | 1.017±0.033      | -4.721±0.041          |
| 8895.4528         | 11.9±1.9                   | 7±15                                         | -27.5±2.8                                | 0.7159±0.0024 | 0.999±0.042      | -4.731±0.044          |
| 8896.5214         | 11.37±0.95                 | -2.2±7.5                                     | -31.2±1.9                                | 0.7186±0.0013 | 0.985±0.016      | -4.738±0.038          |
| 8896.6331         | 12.1±1.2                   | -2.2±9.6                                     | -31.7±1.8                                | 0.7155±0.0012 | 1.021±0.014      | -4.719±0.038          |
| 8897.6418         | 4.6±1.1                    | -14.0±8.4                                    | -34.1±1.5                                | 0.7166±0.0012 | 0.978±0.012      | -4.742±0.038          |
| 8898.5249         | 6.64±0.87                  | -16.4±6.4                                    | -35.4±1.3                                | 0.7170±0.0010 | 1.009±0.010      | -4.725±0.037          |
| 8898.6937         | 2.4±1.0                    | -8.2±8.2                                     | -35.0±1.8                                | 0.7234±0.0015 | 0.980±0.019      | -4.741±0.039          |
| 8905.5116         | -0.8±1.4                   | 2±11                                         | -36.8±2.6                                | 0.7242±0.0018 | 0.989±0.025      | -4.736±0.040          |
| 8905.6346         | -0.5±1.6                   | -8±13                                        | -36.3±2.3                                | 0.7185±0.0020 | 0.942±0.026      | -4.763±0.041          |
| 8925.5936         | -5.1±1.5                   | 3±12                                         | -27.1±2.3                                | 0.7183±0.0020 | 1.033±0.031      | -4.712±0.040          |

**Table 2.7:** Radial velocity measurements and spectroscopic activity indicators for TOI-1235 from HARPS-N optical spectra.

| iSHELL            |                            |
|-------------------|----------------------------|
| BJD<br>(-2450000) | RV<br>(m s <sup>-1</sup> ) |
| 8874.1303         | -0.71 ± 9.1                |
| 8875.1161         | 6.61 ± 11.1                |
| 8895.0886         | 2.6 ± 4.0                  |
| 8899.0817         | 13.07 ± 5.2                |
| 8901.0644         | -4.16 ± 6.1                |

**Table 2.8:** Radial velocity measurements for TOI-1235 from iSHELL spectra.

| BJD<br>(-2450000) | CARMENES NIR                |                                             |                                       |
|-------------------|-----------------------------|---------------------------------------------|---------------------------------------|
|                   | RV<br>( $\text{m s}^{-1}$ ) | CRX<br>( $\text{m s}^{-1} \text{Np}^{-1}$ ) | dLW<br>( $\text{m}^2 \text{s}^{-2}$ ) |
| 8796.6534         | $-3.62 \pm 8.7$             | $-15.51 \pm 43$                             | $-9.56 \pm 16$                        |
| 8807.7242         | $2.7 \pm 11.5$              | $35.98 \pm 51$                              | $14.64 \pm 11$                        |
| 8815.7113         | $-5.57 \pm 7.0$             | $59.31 \pm 32$                              | $20.36 \pm 6.3$                       |
| 8816.6574         | $-12.1 \pm 4.3$             | $50.87 \pm 17$                              | $26.59 \pm 12$                        |
| 8817.7193         | $-28.31 \pm 12.5$           | $91.45 \pm 58$                              | $2.89 \pm 24$                         |
| 8831.5418         | $14.98 \pm 10.8$            | $25.22 \pm 51$                              | $20.13 \pm 16$                        |
| 8832.6942         | $-9.92 \pm 9.5$             | $102.59 \pm 39$                             | $32.11 \pm 11$                        |
| 8846.6695         | $16.88 \pm 14.2$            | $-169.25 \pm 98$                            | $-55.07 \pm 11$                       |
| 8848.7123         | $9.06 \pm 7.1$              | $21.37 \pm 37$                              | $19.54 \pm 5.2$                       |
| 8850.6443         | $-7.15 \pm 7.5$             | $41.75 \pm 37$                              | $10.7 \pm 6.1$                        |
| 8852.6275         | $-3.75 \pm 6.2$             | $-18.49 \pm 31$                             | $25.48 \pm 8.5$                       |
| 8854.6613         | $3.59 \pm 8.7$              | $-23.5 \pm 40$                              | $12.99 \pm 9.2$                       |
| 8855.6350         | $-25.78 \pm 14.4$           | $-127.78 \pm 99$                            | $-10.78 \pm 13$                       |
| 8856.6274         | $-16.5 \pm 5.1$             | $37.01 \pm 23$                              | $28.13 \pm 8.2$                       |
| 8857.6309         | $0.07 \pm 4.8$              | $12.28 \pm 22$                              | $9.51 \pm 7.9$                        |
| 8858.6034         | $-12.53 \pm 5.6$            | $-13.31 \pm 23$                             | $-8.3 \pm 10$                         |
| 8860.6337         | $-7.52 \pm 7.3$             | $95.19 \pm 27$                              | $24.34 \pm 11$                        |
| 8861.6289         | $-3.69 \pm 5.5$             | $28.43 \pm 26$                              | $19.61 \pm 9.8$                       |
| 8862.6275         | $10.29 \pm 8.1$             | $84.9 \pm 36$                               | $31.28 \pm 9.3$                       |
| 8863.6678         | $-27.79 \pm 25.7$           | $56.84 \pm 127$                             | $63.0 \pm 29$                         |
| 8863.6864         | $-10.75 \pm 13.1$           | $14.07 \pm 65$                              | $27.92 \pm 11$                        |
| 8864.6146         | $-9.35 \pm 8.6$             | $108.24 \pm 34$                             | $44.67 \pm 8.2$                       |
| 8865.6222         | $6.09 \pm 9.3$              | $82.43 \pm 42$                              | $0.45 \pm 8.3$                        |
| 8866.6361         | $-24.99 \pm 19.1$           | $46.87 \pm 108$                             | $-107.27 \pm 34$                      |
| 8877.5768         | $-11.17 \pm 5.6$            | $7.22 \pm 27$                               | $14.44 \pm 6.4$                       |
| 8881.5859         | $-7.27 \pm 5.8$             | $61.08 \pm 25$                              | $3.89 \pm 6.7$                        |
| 8882.5755         | $-5.17 \pm 5.0$             | $-12.44 \pm 24$                             | $-2.18 \pm 6.8$                       |
| 8883.5726         | $-6.14 \pm 6.6$             | $38.85 \pm 32$                              | $-3.2 \pm 6.8$                        |
| 8884.5719         | $-7.81 \pm 4.9$             | $24.28 \pm 23$                              | $-4.16 \pm 8.1$                       |
| 8885.5807         | $-12.04 \pm 7.0$            | $29.82 \pm 34$                              | $19.68 \pm 9.0$                       |
| 8887.5639         | $-5.08 \pm 10.8$            | $-104.73 \pm 46$                            | $-15.27 \pm 25$                       |
| 8888.7295         | $-12.98 \pm 17.3$           | $34.81 \pm 85$                              | $-27.62 \pm 28$                       |
| 8890.5100         | $1.13 \pm 15.4$             | $-5.12 \pm 113$                             | $-34.55 \pm 18$                       |
| 8890.5349         | $-8.16 \pm 7.1$             | $-20.73 \pm 38$                             | $18.13 \pm 10$                        |
| 8891.5421         | $-1.74 \pm 4.8$             | $-12.32 \pm 24$                             | $10.26 \pm 8.6$                       |
| 8893.5073         | $9.0 \pm 7.6$               | $47.15 \pm 45$                              | $38.66 \pm 14$                        |
| 8894.5324         | $-8.05 \pm 5.3$             | $55.52 \pm 24$                              | $5.35 \pm 6.9$                        |
| 8895.5593         | $4.62 \pm 6.1$              | $-33.6 \pm 30$                              | $3.3 \pm 7.3$                         |
| 8896.5263         | $0.14 \pm 5.1$              | $-11.55 \pm 27$                             | $32.04 \pm 6.6$                       |
| 8897.5325         | $5.19 \pm 13.7$             | $-22.3 \pm 100$                             | $-41.89 \pm 19$                       |
| 8903.4969         | $-4.6 \pm 10.7$             | $139.99 \pm 63$                             | $36.28 \pm 16$                        |
| 8904.4842         | $-11.51 \pm 6.1$            | $-19.26 \pm 29$                             | $6.46 \pm 10$                         |

**Table 2.9:** Radial velocity measurements and spectroscopic activity indicators for TOI-1235 from NIR spectra.

| BJD<br>(-2450000) | RV<br>(m s <sup>-1</sup> ) | CRX<br>(m/s Np) | dLW<br>(m <sup>2</sup> s <sup>-2</sup> ) | CARMENES VIS  |               |               |               |               |
|-------------------|----------------------------|-----------------|------------------------------------------|---------------|---------------|---------------|---------------|---------------|
|                   |                            |                 |                                          | H $\alpha$    | Ca IRTa       | TiO7050       | TiO8430       | TiO8860       |
| 8796.6533         | -1.2±2.2                   | 9±19            | -30.4±3.8                                | 0.6954±0.0021 | 0.5204±0.0022 | 0.8474±0.0015 | 0.8656±0.0027 | 0.9722±0.0028 |
| 8807.7240         | 0.4±2.4                    | -24±20          | -3.2±2.8                                 | 0.7004±0.0017 | 0.5221±0.0018 | 0.8487±0.0012 | 0.8694±0.0022 | 0.9684±0.0023 |
| 8811.6588         | 6.3±2.8                    | 37±25           | -22.0±4.1                                | 0.6859±0.0027 | 0.5194±0.0029 | 0.8515±0.0020 | 0.8640±0.0036 | 0.9746±0.0035 |
| 8815.7134         | -2.7±1.8                   | 8±15            | -0.8±2.0                                 | 0.6907±0.0014 | 0.5294±0.0016 | 0.8494±0.0011 | 0.8665±0.0019 | 0.9742±0.0020 |
| 8816.6576         | 3.0±1.6                    | -14±13          | 5.5±2.0                                  | 0.6916±0.0013 | 0.5299±0.0015 | 0.8859±0.0010 | 0.8650±0.0018 | 0.9768±0.0018 |
| 8817.7185         | 0.4±3.2                    | 64±29           | -19.3±3.4                                | 0.6973±0.0030 | 0.5223±0.0035 | 0.8379±0.0022 | 0.8542±0.0042 | 0.9759±0.0042 |
| 8831.5414         | 5.4±2.8                    | 0±23            | -4.6±3.3                                 | 0.6884±0.0020 | 0.5199±0.0022 | 0.8460±0.0015 | 0.8667±0.0027 | 0.9770±0.0027 |
| 8832.6949         | 2.5±2.2                    | -7±19           | 11.4±3.3                                 | 0.6893±0.0018 | 0.5223±0.0020 | 0.8486±0.0014 | 0.8629±0.0025 | 0.9782±0.0025 |
| 8846.6694         | -4.2±1.6                   | 16±14           | 6.3±1.6                                  | 0.6894±0.0011 | 0.5267±0.0013 | 0.8514±0.0009 | 0.8666±0.0016 | 0.9769±0.0017 |
| 8848.7121         | 5.8±1.6                    | 27±13           | 10.1±1.6                                 | 0.6963±0.0011 | 0.5200±0.0013 | 0.8489±0.0008 | 0.8640±0.0015 | 0.9765±0.0016 |
| 8850.6431         | 2.8±1.4                    | 12±13           | 1.5±1.9                                  | 0.6905±0.0012 | 0.5256±0.0014 | 0.8518±0.0009 | 0.8709±0.0017 | 0.9761±0.0017 |
| 8852.6259         | 4.5±1.4                    | 9±12            | 8.0±1.3                                  | 0.6989±0.0012 | 0.5191±0.0014 | 0.8502±0.0009 | 0.8687±0.0017 | 0.9812±0.0017 |
| 8854.6620         | 6.0±2.1                    | 27±14           | 5.5±1.8                                  | 0.6950±0.0011 | 0.5268±0.0013 | 0.8488±0.0009 | 0.8647±0.0016 | 0.9798±0.0016 |
| 8855.6361         | 4.7±2.0                    | -3±14           | 2.5±1.6                                  | 0.6864±0.0012 | 0.5254±0.0013 | 0.8499±0.0009 | 0.8678±0.0016 | 0.9754±0.0016 |
| 8856.6278         | 0.0±1.5                    | 13±11           | 6.6±1.7                                  | 0.6868±0.0011 | 0.5187±0.0013 | 0.8523±0.0009 | 0.8650±0.0015 | 0.9756±0.0016 |
| 8857.6312         | -1.5±1.9                   | 6±13            | 6.1±2.1                                  | 0.6952±0.0011 | 0.5283±0.0013 | 0.8491±0.0009 | 0.8666±0.0016 | 0.9832±0.0016 |
| 8858.6017         | 6.7±2.0                    | 15±16           | -2.3±2.5                                 | 0.6934±0.0017 | 0.5265±0.0018 | 0.8514±0.0013 | 0.8659±0.0022 | 0.9826±0.0023 |
| 8860.6327         | -3.8±1.8                   | -3±16           | 2.8±2.3                                  | 0.6859±0.0015 | 0.5227±0.0017 | 0.8538±0.0012 | 0.8665±0.0020 | 0.9769±0.0021 |
| 8861.6279         | -3.8±1.9                   | 26±15           | 3.2±2.3                                  | 0.6944±0.0014 | 0.5262±0.0015 | 0.8506±0.0010 | 0.8665±0.0019 | 0.9794±0.0019 |
| 8862.6304         | -0.2±1.8                   | 27±14           | -0.7±1.9                                 | 0.6947±0.0014 | 0.5285±0.0016 | 0.8509±0.0011 | 0.8693±0.0019 | 0.9768±0.0020 |
| 8863.6852         | -1.4±3.0                   | -48±27          | 2.7±3.5                                  | 0.6932±0.0021 | 0.5312±0.0023 | 0.8470±0.0016 | 0.8613±0.0028 | 0.9778±0.0029 |
| 8864.6148         | -3.8±2.1                   | -11±16          | -6.6±2.4                                 | 0.6862±0.0016 | 0.5217±0.0018 | 0.8507±0.0012 | 0.8662±0.0021 | 0.9758±0.0021 |
| 8865.6228         | 0.6±2.5                    | -33±23          | -5.5±2.6                                 | 0.6967±0.0019 | 0.5277±0.0021 | 0.8477±0.0014 | 0.8648±0.0025 | 0.9864±0.0026 |
| 8866.6362         | 2.0±3.4                    | -23±28          | -4.4±3.5                                 | 0.6948±0.0028 | 0.5287±0.0030 | 0.8479±0.0020 | 0.8626±0.0036 | 0.9867±0.0036 |
| 8877.5779         | -2.4 ±2.0                  | -10±13          | -4.4±2.2                                 | 0.6927±0.0011 | 0.5219±0.0012 | 0.8467±0.0008 | 0.8682±0.0015 | 0.9839±0.0015 |
| 8881.5843         | -0.6±1.6                   | 13±15           | -8.0±1.9                                 | 0.6875±0.0012 | 0.5185±0.0013 | 0.8471±0.0009 | 0.8670±0.0016 | 0.9821±0.0017 |
| 8882.5742         | 0.3±1.6                    | 2±14            | -19.2±2.2                                | 0.6948±0.0014 | 0.5208±0.0015 | 0.8493±0.0010 | 0.8687±0.0018 | 0.9793±0.0019 |
| 8883.5713         | -5.9±1.6                   | 1±13            | -9.5±1.7                                 | 0.6954±0.0012 | 0.5210±0.0014 | 0.8485±0.0009 | 0.8679±0.0017 | 0.9821±0.0017 |
| 8884.5713         | -5.5±1.2                   | 2.0±8.8         | -4.9±1.6                                 | 0.6912±0.0011 | 0.5151±0.0012 | 0.8473±0.0008 | 0.8675±0.0014 | 0.9756±0.0015 |
| 8885.5794         | 1.2±1.7                    | -8±13           | -5.9±1.8                                 | 0.6859±0.0013 | 0.5209±0.0014 | 0.8468±0.0010 | 0.8701±0.0017 | 0.9804±0.0018 |
| 8887.5650         | -9.7±3.2                   | 17±27           | -9.4±3.7                                 | 0.6919±0.0027 | 0.5260±0.0028 | 0.8484±0.0020 | 0.8684±0.0035 | 0.9772±0.0035 |
| 8888.7326         | 2.2±3.7                    | 12±34           | 11.0±4.6                                 | 0.6912±0.0032 | 0.5210±0.0034 | 0.8472±0.0024 | 0.8611±0.0043 | 0.9758±0.0041 |
| 8890.5100         | -0.1±2.8                   | -37±24          | 2.3±2.0                                  | 0.6939±0.0016 | 0.5295±0.0018 | 0.8487±0.0012 | 0.8651±0.0022 | 0.9798±0.0022 |
| 8890.5332         | -1.5±1.8                   | -19±13          | 2.2±1.8                                  | 0.6884±0.0014 | 0.5268±0.0016 | 0.8500±0.0011 | 0.8668±0.0019 | 0.9816±0.0020 |
| 8891.5446         | -2.6±1.5                   | 4±12            | 6.0±2.4                                  | 0.7054±0.0012 | 0.5305±0.0014 | 0.8525±0.0009 | 0.8677±0.0016 | 0.9872±0.0017 |
| 8893.5107         | 4.1±1.6                    | 4±13            | 7.9±2.2                                  | 0.6982±0.0013 | 0.5270±0.0014 | 0.8500±0.0010 | 0.8705±0.0017 | 0.9800±0.0018 |
| 8894.5328         | -1.0±1.9                   | -24±14          | 8.1±1.4                                  | 0.6911±0.0010 | 0.5297±0.0011 | 0.8522±0.0008 | 0.8678±0.0014 | 0.9802±0.0015 |
| 8895.5580         | 0.6±2.0                    | -52±14          | -4.9±2.2                                 | 0.6938±0.0013 | 0.5265±0.0014 | 0.8506±0.0010 | 0.8706±0.0018 | 0.9865±0.0018 |
| 8896.5272         | 3.0±1.4                    | -8±12           | 0.3±1.9                                  | 0.6989±0.0011 | 0.5233±0.0012 | 0.8510±0.0008 | 0.8682±0.0015 | 0.9784±0.0015 |
| 8897.5334         | -3.0±1.4                   | -15±11          | 1.5±1.5                                  | 0.6990±0.0012 | 0.5270±0.0013 | 0.8489±0.0009 | 0.8642±0.0016 | 0.9877±0.0017 |

**Table 2.10:** Radial velocity measurements and spectroscopic activity indicators for TOI-1235 from CARMENES optical spectra.





# 3

## An ultra-short-period transiting super-Earth orbiting the M3 dwarf TOI-1685

---

*“I believe in evidence. I believe in observation, measurement, and reasoning, confirmed by independent observers. I will believe anything, no matter how wild and ridiculous, if there is evidence for it. The wilder and more ridiculous something is, however, the firmer and more solid the evidence will have to be.”*

by Isaac Asimov

---

The content of this chapter is based in the published article “*An ultra-short-period transiting super-Earth orbiting the M3 dwarf*”, (Bluhm et al., 2021), for which I am the first author from a team effort of 53 co-authors. I have done the scientific work, analysis, and reached the conclusions. I was under the supervision of Prof. Andreas Quirrenbach with collaboration with Enric Pallé, Jonas Kemmer, Diana Kossakowski, and Stephan Stock. The stellar parameters were computed by Vera Passegger, Andreas Schweitzer, and Carlos Cifuentes. The Galactic velocities UVW were computed by Carlos Cardona. The text was written by me with the contributions of Karan Molaverdikhani, Artie Hatzes, and José Caballero.

### 3.1 Motivation

Currently, over one hundred planets with orbital periods of less than one day are known<sup>23</sup>. These exoplanets, normally referred to as ultra-short-period planets (USPs; Sahu et al., 2006; Winn et al., 2018), are frequently found around main-sequence stars. The majority of USPs are small and appear to have compositions similar to that of the Earth (Winn et al., 2018). Their origin is still uncertain. One possible scenario is that these planets were originally hot Jupiters that experienced a phase of intense erosion due to tidal activity and/or intense stellar irradiation (Owen & Wu, 2013b), while in another scenario the progenitors of USPs were the exposed remnants of so-called mini-Neptunes, which can still harbor external gaseous layers (Lundkvist et al., 2016; Lee & Chiang, 2017). Additional theories propose that these objects might have formed at more separated orbits before migrating to their current locations

---

<sup>23</sup><https://exoplanetarchive.ipac.caltech.edu/>,  
<http://exoplanet.eu/>

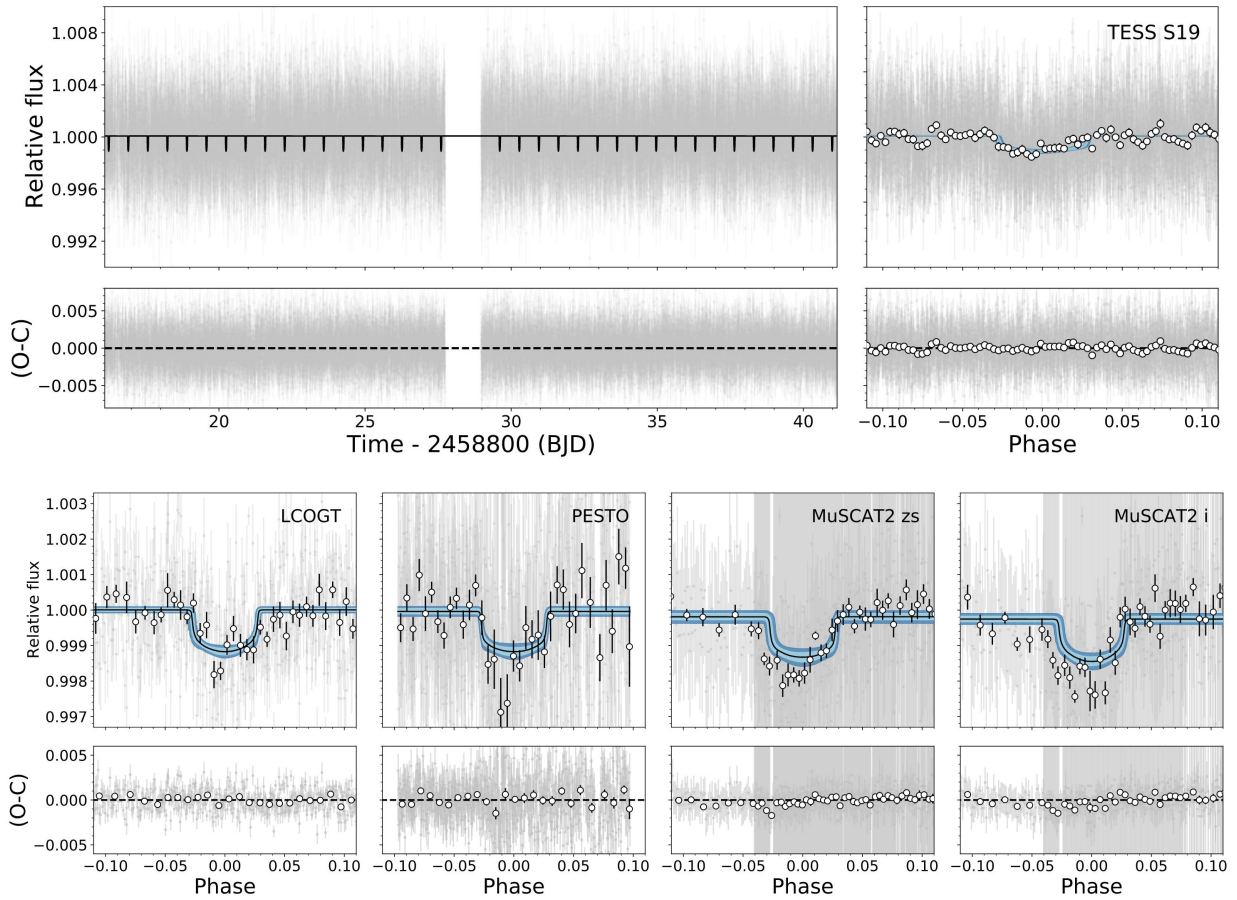


**Figure 3.1:** *TESS* and ground-based photometry light curves of TOI-1685. *Upper panels:* PDC simple aperture photometry (SAP) *TESS* light curve of TOI-1685 and the corresponding phase-folded light curve. *Lower panels:* Phase-folded light curves of LCOGT, PESTO, and MuSCAT2 in filters *i* and  $z_s$  of TOI-1685. For all phase-folded light curves the residuals are shown for the USP found in the system. White circles are binned data (shown only for reference; the data used to fit the model were the unbinned points). Black curves are the best-fit models, and light and dark blue areas are the 68% and 95% credibility bands, respectively. The different sizes of the MuSCAT2 error bars correspond to the two observing nights.

(Rice, 2015; Lee & Chiang, 2017) or even formed in situ (Chiang & Laughlin, 2013). For the moment, a clear picture of the origins of these objects remains elusive (Adams & Bloch, 2015), which makes them critical tracers of theories of planet formation and evolution.

Due to their proximity to their host stars, these planets can reach equilibrium temperatures of thousands of kelvins (Rouan et al., 2011; Demory et al., 2012; Sanchis-Ojeda et al., 2013), which also makes them ideal laboratories for studying atmospheric composition via thermal emission spectroscopy.

Several follow-up studies have suggested that USPs are usually formed in multi-planetary systems (Sanchis-Ojeda et al., 2014), where multi-body interactions could play an important role in tidal migration. Accurately measuring the masses and orbits of any additional planet in such systems would be helpful in discriminating between different USP origin scenarios.

Thus, in order to understand the processes involved in the formation and evolution of these planets, high cadence photometry and radial velocity (RV) campaigns, able to detect multi-planetary systems, are needed. Because of their short periods, it is relatively easy to precisely measure the parameters of USPs, but it is important to also explore and constrain additional planetary signals in systems that host USPs.

Theory and empirical data have shown that the occurrence rate of small planets tends to increase around late-type stars (Bonfils et al., 2013; Dressing & Charbonneau, 2015; Mulders et al., 2015; Gaidos et al., 2016). The *Kepler* (Borucki et al., 2010b; Borucki, 2016) and *K2* (Howell et al., 2014) space missions uncovered only a few USPs around M dwarfs ( $T_{\text{eff}} \lesssim 4000$  K), such as Kepler-42 c, Kepler-732 c, Kepler-32 b, K2-137 b, K2-22 b, and K2-147 b (Muirhead et al., 2012; Morton et al., 2016; Smith et al., 2018; Dressing et al., 2017; Hirano et al., 2018b). However, during the first years of the *Transiting Exoplanet Survey Satellite* (*TESS*; Ricker et al., 2015) mission, the number of discoveries nearly doubled (LP 791-18 b, LHS 3844 b, GJ 1252 b, LTT 3780 b, and TOI-1634 b; Crossfield et al., 2019; Vanderspek et al., 2019; Shporer et al., 2020; Nowak et al., 2020a; Hirano et al., 2021).

In this paper, we report a transiting USP and a potential non-transiting planet candidate around the nearby M3.0 dwarf TOI-1685. The USP, with a period of 0.669 d, was initially discovered as a transiting planet candidate in *TESS* data and is confirmed here using ground-based photometry and RV measurements. The outer non-transiting planet candidate has a longer period of about 9 d.

The paper is organized as follows. Section 3.2 presents the *TESS* and ground-based photometry, lucky imaging, and high-resolution spectroscopy of TOI-1685. Section 3.3 presents the properties of the host star, either newly derived or collected from the literature. In Sect. 3.4 we present our search for the rotational period of the star, RV modeling, and the joint analysis of all available data made to constrain the properties of the system. In Sect. 3.5 we discuss our results and in Sect. 3.6 present our conclusions.

## 3.2 Data

### 3.2.1 *TESS* photometry

TOI-1685 (TIC 28900646) was observed by *TESS* in 2 min short-cadence integrations during cycle 2 in sector 19 (see Table 3.1 for details) and was announced on 30 January 2020 as a *TESS* object of interest (TOI) through the dedicated *TESS* data public website from the Massachusetts Institute of Technology (MIT)<sup>24</sup>. We downloaded the data from the Mikulski Archive for Space Telescopes<sup>25</sup> (MAST) using the `lightkurve`<sup>26</sup> package (Lightkurve Collaboration et al., 2018). The photometric light curve was corrected for systematics (Pre-search Data Conditioning (PDC); Smith et al., 2012; Stumpe et al., 2012, 2014), which is optimized for *TESS* transit searches. The upper-left panel of Fig. 3.1 shows the PDC data for *TESS* sector 19 with our best-fit model (see Sect. 3.4.5 for details).

In order to search for any contaminant sources, we placed limits on the dilution factor of TOI-1685. We verified that the sources in the selection aperture in the *TESS* target

---

<sup>24</sup><https://tess.mit.edu/toi-releases/>

<sup>25</sup><https://mast.stsci.edu>

<sup>26</sup><https://github.com/KeplerGO/Lightkurve>

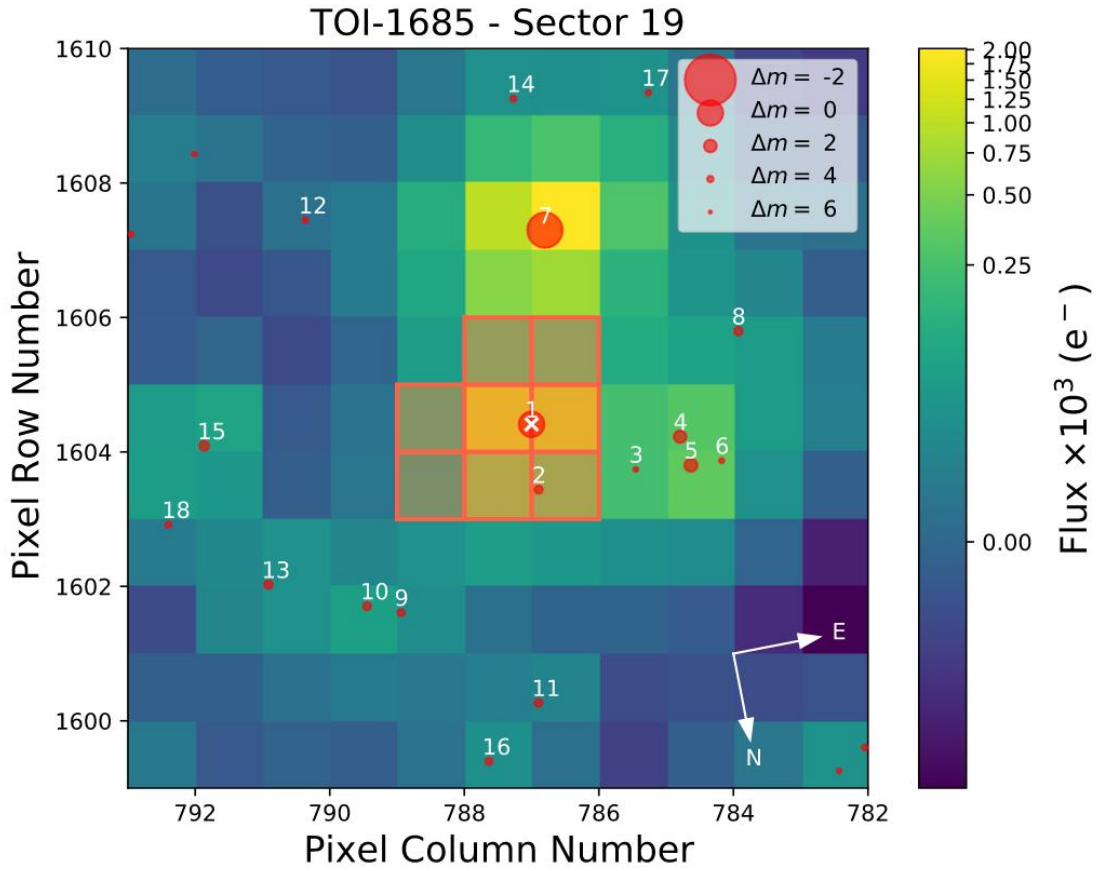


**Figure 3.2:** Target pixel files of TOI-1685 in *TESS* sector 19. The electron counts are color coded. The red bordered pixels are used in the SAP. The sizes of the red circles indicate the *Gaia* magnitudes of nearby sources down to  $G = 18$  mag and that of TOI-1685 (circle 1 marked with an  $\times$ ).

| Sector | Camera | CCD | Start date   | End date     |
|--------|--------|-----|--------------|--------------|
| 19     | 1      | 2   | 28 Nov. 2019 | 23 Dec. 2019 |

**Table 3.1:** *TESS* observations of TOI-1685.

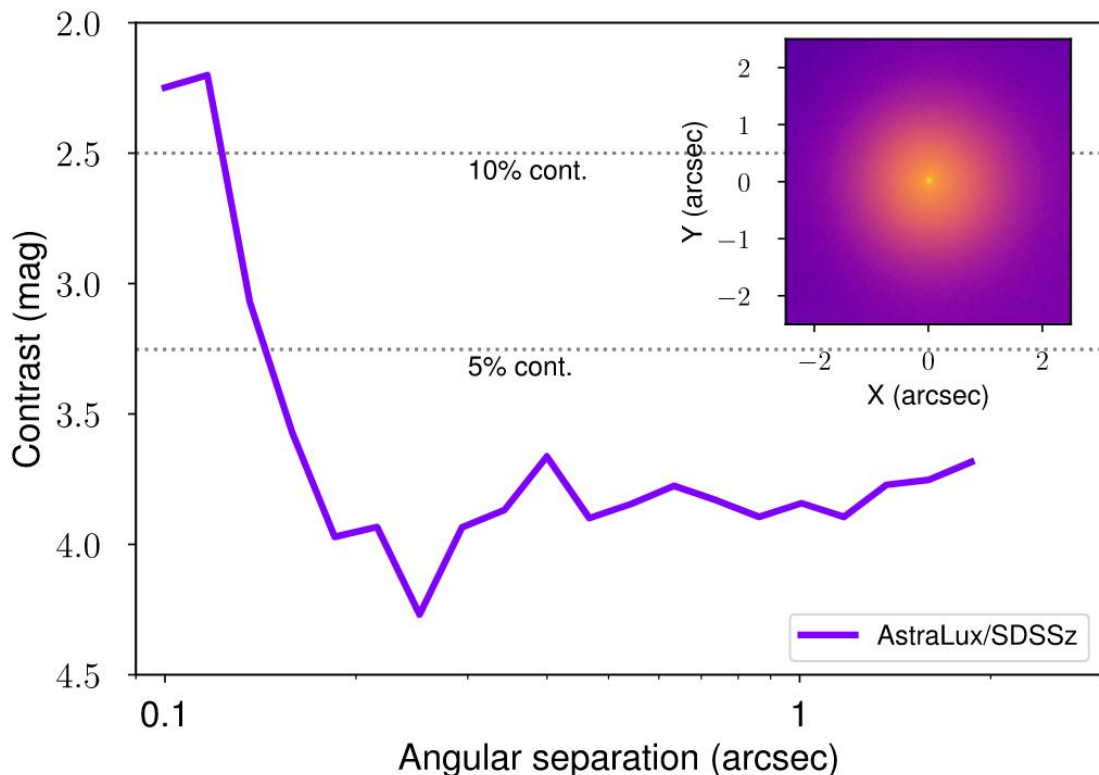


**Figure 3.3:** Sensitivity curve for the AstraLux high-spatial-resolution observation of TOI-1685 in the SDSS  $z'$  filter. The inset figure shows the AstraLux image when using the best 10% of frames from the whole data cube.

pixel file (TPF) did not significantly affect the depth of the transits. The TPF created with `tpfplotter`<sup>27</sup> (Aller et al., 2020) is shown in Fig. 3.2. Within the TPF aperture, we found only one extra source (TIC-28900668, *Gaia* EDR3 252366613254979328), which is separated by 15.6 arcsec from TOI-1685 and is 3.3 mag fainter. Further information comes from the TOI-1685 *Gaia* Early Data Release 3 (EDR3) renormalized unit weight error (RUWE) value (Lindgren et al., 2020) that is associated with each *Gaia* source. This is 1.18, below the critical value of 1.40 that indicates that the source may be non-single or otherwise problematic for the astrometric solution. We estimated the *TESS* minimum dilution factor at  $D \sim 0.97$  from Eq. 6 in Espinoza et al. (2019). Since the PDC light curves are already corrected for possible nearby flux contamination, we fixed this value to 1.0 for all of our model fits presented in the following sections.

### 3.2.2 High-resolution imaging

Given the intrinsic faintness of M dwarfs and the large photometric apertures of wide-field surveys ( $\sim 21$  arcsec for *TESS*), the presence of an unresolved companion must be excluded before a planet candidate is confirmed. In some cases, other bright stars in the aperture mask can directly affect the photometry. To confirm the identification of the host star and

<sup>27</sup><https://github.com/jlillo/tpfplotter>

to take nearby potential contaminants into account, we obtained seeing-limited and high-spatial-resolution imaging. We also needed to rule out the possibility that the transit in the light curve is due to an eclipsing binary. For this reason, we obtained ground-based photometry.

To search for companions at subarcsecond separations, we observed TOI-1685 with the lucky imaging instrument AstraLux (Hormuth et al., 2008) mounted on the 2.2 m telescope at the Observatorio de Calar Alto in Almería, Spain. We observed TOI-1685 on 25 February 2020 under good weather conditions with a mean seeing of 1.2 arcsec and at airmass 1.1. The instrument performs imaging with a fast readout (below the coherence time), creating data cubes of thousands of short-exposure frames. Those with the highest Strehl ratio (Strehl, 1902) are subsequently selected and combined into a final high-spatial-resolution image, which is done by the observatory pipeline (Hormuth et al., 2008). We observed in the Sloan Digital Sky Survey (SDSS)  $z'$  filter and obtained 87 600 frames with 20 ms exposure times and a field of view windowed to  $6 \times 6$  arcsec. Only the best 10 % of the frames were aligned and stacked. The final image is shown in the inset panel of Fig. 3.3. Based on this final image, we computed the sensitivity curve using the `astrasens` package<sup>28</sup> with the procedure described by Lillo-Box et al. (2012, 2014).

We found no evidence of additional sources within a  $2 \times 2$  arcsec<sup>2</sup> field of view and within the computed sensitivity limits, as shown in Fig. 3.3. This allowed us to set an upper limit to the contamination in the light curve of around 10 % down to 0.1 arcsec.

We further used this contrast curve to estimate the probability of contamination from blended sources in the *TESS* aperture that are undetectable in the public images. This probability is called blended source confidence (BSC), and the steps for estimating it were described by Lillo-Box et al. (2014). We used a python implementation of this approach (`bsc`) that uses the Trilegal<sup>29</sup> Galactic model (v1.6; Girardi et al., 2012) to retrieve a simulated source population of the region around the corresponding target. This is done in python with the `astrobase` implementation by (Bhatti et al., 2020). This simulation is used to compute the density of stars around a target position (within a radius of  $\rho = 1$  deg) and derive the probability of a chance alignment at a given contrast magnitude and separation. We used the default parameters for the bulge, halo, and disk (thin and thick), as well as the log-normal initial mass function from Chabrier (2001). We applied this technique to TOI-1685. Given the transit depth of planet TOI-1685 b, this signal could be mimicked by blended eclipsing binaries with magnitude contrasts of up to  $\Delta m_{b,max} = 7.5$  mag<sup>30</sup> in the SDSS  $z'$  bandpass. However, the high-spatial-resolution images provided a low probability of 1.5 % for an undetected source with such a magnitude contrast. The probability of this source being an appropriate eclipsing binary is well below 0.1 %. Given these numbers, we further assumed that the transit signal is not due to a blended binary star and that the probability of a contaminating source is very low.

| Instrument         | Country    | Date                | Filter | Exposure<br>[s] | Duration <sup>a</sup><br>[min] | $N_{obs}$ | rms <sup>b</sup><br>[ppt] |
|--------------------|------------|---------------------|--------|-----------------|--------------------------------|-----------|---------------------------|
| LCOGT              | USA        | 26 August 2020      | $I$    | 50              | 173                            | 123       | 1.29                      |
|                    |            | 07 November 2020    | $i_p$  | 25              | 266                            | 270       | 1.47                      |
|                    |            | 11 November 2020    | $i_p$  | 50              | 279                            | 199       | 1.01                      |
| PESTO              | Canada     | 08 March 2020       | $i'$   | 15              | 187                            | 724       | 2.63                      |
| MuSCAT2            | Spain      | 19 January 2020     | $z_s$  | 15              | 179                            | 328       | 1.24                      |
|                    |            |                     | $i'$   | 15              | 179                            | 238       | 1.18                      |
|                    |            | 29 January 2020     | $z_s$  | 15              | 331                            | 333       | 1.70                      |
|                    |            |                     | $i'$   | 15              | 331                            | 333       | 1.71                      |
| LCOGT <sup>c</sup> | Spain, USA | 22–31 December 2020 | $V$    | 100             | 39.83 [d]                      | 20        | 13.7                      |

**Table 3.2:** Ground-based transit follow-up observations of TOI-1685. **Notes.** <sup>(a)</sup> Time span of the observation. <sup>(b)</sup> Root mean square in parts-per-thousand. <sup>(c)</sup> Data used only in Sect. 3.4.2 for determining the stellar rotational period. The duration of the long-term monitoring is in days instead of minutes.

### 3.2.3 Ground-based seeing-limited photometry

One partial and one full transit of the red dwarf TOI-1685 were observed on 19 and 29 January 2021 with the MuSCAT2 instrument (Narita et al., 2019) at the 1.52 m Telescopio Carlos Sánchez at Observatorio del Teide, Spain. MuSCAT2 is a four-channel imager that performs simultaneous photometry in the  $g'$ ,  $r'$ ,  $i'$ , and  $z_s$  bands. However, the low-quality  $g'$  and  $r'$  data were discarded from the analysis. The exposure times of our observations were 15 s in each band, and the observations were repeated for at least three times the USP period. Data reduction and photometric analysis were carried out using the custom-built pipeline for MuSCAT2 (Parviainen et al., 2020). The pipeline provides aperture photometry for a set of comparison stars and different aperture sizes. From them, the final light curves are chosen after a global optimization that takes into account the transit model and several different sources of systematics from covariates. The data obtained on 19 January 2021 were significantly affected by poor weather.

Four additional transit observations of TOI-1685 were taken with the Las Cumbres Observatory Global Telescope (LCOGT), on the night of 26 August 2020 and the nights of 7, 9, and 11 November 2020. The night of 9 November was discarded due to the bad quality of the data. Observations were taken with the 1.0 m telescopes at McDonald Observatory, USA, which were equipped with  $4096 \times 4096$  pixel SINISTRO cameras, using the  $I$  filter on the night in August and the  $i_p$  filter on all the nights in November. Exposure times were set to 25, 50, and 50 s for the nights of 7 November, 11 November, and 26 August, respectively. Data reduction and photometric analysis were performed with the dedicated LCOGT Banzai pipeline and AstroImageJ, respectively (Collins et al., 2017b).

Finally, another full transit of TOI-1685 was observed at Observatoire du Mont-Mégantic,

<sup>28</sup><https://github.com/jlillo/astrasens>

<sup>29</sup><http://stev.oapd.inaf.it/cgi-bin/trilegal>

<sup>30</sup>Maximum contrast (with respect to the measured flux); see Sect. 4.4.1 and Eq. 2 of (Lillo-Box et al., 2014).

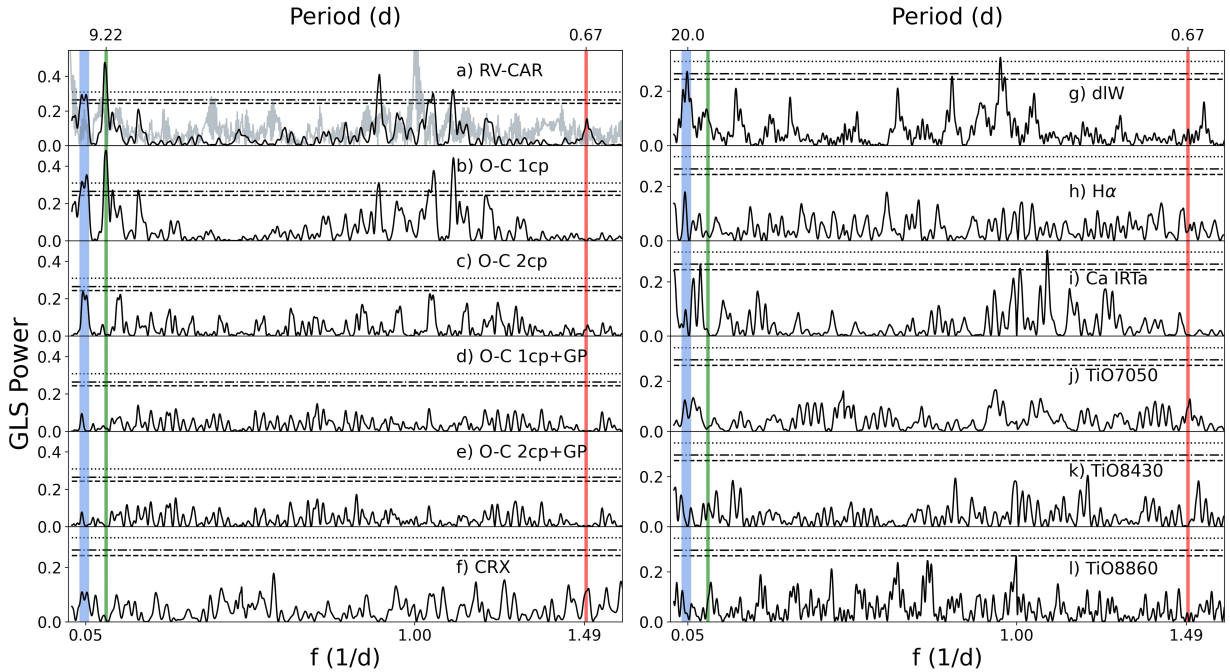


**Figure 3.4:** GLS periodograms of: (a) RVs from CARMENES VIS and the respective spectral window function (gray), (b) RV residuals after subtracting the one-planet signal, (c) RV residuals after subtracting the two-planet signal, (d) RV residuals after subtracting the one-planet signal plus GP, (e) RV residuals after subtracting the two-planet signal plus GP, (f-l) CRX, dLW, H $\alpha$ , Ca IRTa (“a” corresponds to the Ca ii  $\lambda$ 8498.0 Å line), TiO7050, TiO8430, and TiO8860 activity indices from CARMENES VIS data. The “cp” in the residual models (panels a-e) corresponds to circular orbits (for a detailed explanation, see Sect. 3.4.3). In all panels the vertical lines indicate the periods of 0.67 d (red, USP) and  $\sim$ 9 d (green, second planet candidate). The rotational period of the star (blue line) falls in the region between  $\sim$ 19 and 26 d. The horizontal lines mark the theoretical FAP levels of 1% (dotted), 5% (dash-dotted), and 10% (dashed).

Canada, on 8 March 2020. Using the 1.6 m telescope equipped with the PESTO camera, the data were obtained in the  $i'$  filter with a 15 s exposure time. The bias subtraction, flat field division, and light curve extraction were also carried out using AstroImageJ.

Table 3.2 summarizes the three data sets, including the root mean square (rms) of the light curve fluxes. The resulting transit light curves obtained with MuSCAT2 (in  $i$  and  $z_s$ ), LCOGT, and PESTO are shown in the bottom panels of Fig. 3.1.

### 3.2.4 CARMENES RV measurements

TOI-1685 was observed 55 times with CARMENES between 8 August 2020 and 9 November 2020. CARMENES (Quirrenbach et al., 2014, 2018) is a high-resolution spectrograph installed at the 3.5 m telescope at the Observatorio de Calar Alto, Spain. It splits the incoming light into two beams that feed the visual (VIS; 0.52–0.96  $\mu$ m,  $\mathcal{R} = 94\,600$ ) and near-infrared (NIR; 0.96–1.71  $\mu$ m,  $\mathcal{R} = 80\,400$ ) channels via optical fibers. Exposure times ranged between about 1300 s (limited to the time needed to achieve a signal-to-noise ratio

of 150, based on information from real-time exposure meters) and 1800 s (the maximum exposure time). We followed the standard data flow of the CARMENES guaranteed time observations (Caballero et al., 2016). In particular, we reduced the spectra with `caracal` (Zechmeister et al., 2014) and determined the corresponding RVs and spectral activity indices (see Sect. 3.4.3) with `serval` (Zechmeister et al., 2018). The RVs were corrected for barycentric motion, instrumental drift, secular acceleration, and nightly zero points (see Kaminski et al. 2018, Tal-Or et al. 2019, and, especially, Trifonov et al. 2020 for details).

The RVs, activity indices, and their corresponding uncertainties are listed in Table 3.8.

### 3.3 Stellar properties

The star TOI-1685 (2MASS J04342248+4302148,  $V \approx 13.3$  mag) is a nearby M3.0 V star at a distance of approximately 37.6 pc (Bailer-Jones et al., 2020). It has only been tabulated by a few proper-motion surveys (Lépine & Gaidos, 2011; Frith et al., 2013; Terrien et al., 2015). In this work, we recalculated all stellar parameters for this M dwarf. In particular, we measured  $T_{eff}$ , surface gravity  $\log g$ , and iron abundance [Fe/H] from the stacked CARMENES VIS spectra by fitting them with a grid of PHOENIX-SESAM models, as in Passegger et al. (2019), the rotational velocity  $v \sin i$  with the cross-correlation method, as in Reiners et al. (2018b), and the stellar luminosity,  $L_{\star}$ , as in Cifuentes et al. (2020). The stellar radius,  $R_{\star}$ , was determined through the Stefan Boltzmann law,  $L_{\star} = 4\pi R_{\star}^2 \sigma T_{eff}^4$ , and the stellar mass,  $M_{\star}$ , using the mass-radius relation derived from main-sequence eclipsing binaries by Schweitzer et al. (2019). In particular, we used astro-photometry from *Gaia* EDR3 and photometry from Fourth U.S. Naval Observatory CCD Astrograph Catalog (UCAC4), Two Micron All Sky Survey (2MASS), and All Wide-field Infrared (AllWISE) (Zacharias et al., 2012; Skrutskie et al., 2006; Cutri et al., 2021).

We measured the pseudo-equivalent width, pEW(H $\alpha$ ), a key indicator of stellar activity, on the CARMENES stacked spectrum following Schöfer et al. (2019). In Sect. 3.4.1 we report the search for periodic signals in this and other spectroscopic activity indicators. As described in Sect. 3.4.2, we found that TOI-1685 has a rotation period of around 19 d. Although the star is rotating moderately fast for an early M dwarf, and the Galactic velocities  $UVW$  indicate that it belongs to the relatively young thin disk (see Table 3.3), it is not associated with any particular young stellar kinematic group. The absence of X-ray emission in *ROSAT* observations (First *ROSAT* X-ray Survey (1RXS) ; Voges et al., 1999) and ultraviolet emission in the Galaxy Evolution Explorer (*GALEX*) images (Bianchi et al., 2017) is also an indication that the star is not very young. Using the gyrochronology relations from Barnes (2007) and Angus et al. (2015), and comparing the rotation period of the star with those of members in open clusters such as Praesepe (Rebull et al., 2017), we estimated an age of 0.6–2 Ga for the system.

Table 3.3 summarizes the stellar properties of TOI-1685, providing average values, uncertainties, and the corresponding references.

| Parameter                             | Value              | Reference | Parameter                                       | Value               | Reference |
|---------------------------------------|--------------------|-----------|-------------------------------------------------|---------------------|-----------|
| <i>Name/identifiers</i>               |                    |           | <i>Parallax/kinematics</i>                      |                     |           |
| Name                                  | J04342248+4302148  | 2MASS     | $\varpi$ [mas]                                  | $26.589 \pm 0.019$  | Gaia EDR3 |
| Karmin <sup>a</sup>                   | J04343+430         | AF15      | $d$ [pc]                                        | $37.609 \pm 0.027$  | Gaia EDR3 |
| TOI                                   | 1685               | ExoFOP    | $\mu_\alpha \cos \delta$ [mas a <sup>-1</sup> ] | $+37.762 \pm 0.022$ | Gaia EDR3 |
| TIC                                   | 28900646           | Sta18     | $\mu_\delta$ [mas a <sup>-1</sup> ]             | $-87.062 \pm 0.047$ | Gaia EDR3 |
| <i>Phot. parameters</i>               |                    |           | <i>Physical parameters</i>                      |                     |           |
| $T_{\text{eff}}$ [K]                  | $3434 \pm 51$      | This work | $\gamma$ [kms <sup>-1</sup> ]                   | $-27.512 \pm 0.018$ | This work |
| $\log g$                              | $4.85 \pm 0.04$    | This work | $U$ [kms <sup>-1</sup> ]                        | $+35.6 \pm 8.0$     | This work |
| [Fe/H]                                | $-0.13 \pm 0.16$   | This work | $V$ [kms <sup>-1</sup> ]                        | $-29.8 \pm 2.9$     | This work |
| $v \sin i_\star$ [kms <sup>-1</sup> ] | $< 2.0$            | This work | $W$ [kms <sup>-1</sup> ]                        | $-3.14 \pm 0.47$    | This work |
| <i>Coords/Spec. type</i>              |                    |           | $V_r$ [kms <sup>-1</sup> ]                      | $-43.4 \pm 8.5$     | Terr15    |
| $\alpha$ (J2000) <sup>b</sup>         | 04:34:22.55        | Gaia EDR3 | Gal. population                                 | Thin disk           | This work |
| $\delta$ (J2000) <sup>b</sup>         | +43:02:13.3        | Gaia EDR3 | <i>Activity and age</i>                         |                     |           |
| Sp. type                              | M3.0 V             | Terr15    | $L_\star$ [ $L_\odot$ ]                         | $0.0303 \pm 0.0005$ | This work |
| $G$ [mag]                             | $12.284 \pm 2.452$ | Gaia EDR3 | $M_\star$ [ $M_\odot$ ]                         | $0.495 \pm 0.019$   | This work |
| $T$ [mag]                             | $11.111 \pm 0.007$ | Sta19     | $R_\star$ [ $R_\odot$ ]                         | $0.492 \pm 0.015$   | This work |
| $J$ [mag]                             | $9.616 \pm 0.018$  | 2MASS     | pEW(H $\alpha$ ) [Å]                            | $+0.51 \pm 0.06$    | This work |
|                                       |                    |           | $\log R'_{\text{HK}}$                           | $-4.728 \pm 0.015$  | This work |
|                                       |                    |           | $S_{\text{MWO}}$                                | $1.005 \pm 0.029$   | This work |
|                                       |                    |           | Age (Ga)                                        | 0.6–2.0             | This work |

**Table 3.3:** Stellar parameters of TOI-1685.

**References.** 2MASS: [Skrutskie et al. \(2006\)](#); AF15: [Alonso-Floriano et al. \(2015\)](#);

ExoFOP-TESS: <https://exofop.ipac.caltech.edu/tess/>; Gaia EDR3: [Gaia Collaboration et al. \(2020\)](#); Sta18: [Stassun et al. \(2018\)](#); Terr15: [Terrien et al. \(2015\)](#); Sta19: [Stassun et al. \(2019\)](#). <sup>(a)</sup> Target acronym from the CARMENES input catalog of M dwarfs (see AF15). <sup>(b)</sup> Gaia EDR3 equatorial coordinates in equinox J2000 and at epoch J2016.

## 3.4 Analysis and results

### 3.4.1 Periodogram analysis of the RV data

We explored the generalized Lomb-Scargle (GLS) periodograms ([Zechmeister & Kürster, 2009b](#)) of the RVs of TOI-1685. The periodogram and window function are shown in panel *a* of Fig. 3.4. The strongest signal was found at about 9 d, with a nominal false alarm probability (FAP)  $< 1\%$ , and its aliases around periods of 1 d (due to the sampling of the data). A double peak is visible in the period range of about 19–26 d with FAP  $< 5\%$ , while a small isolated peak is discernible at the orbital frequency of TOI-1685 b. The formal FAP for this feature is  $\geq 10\%$ . However, we need to distinguish between an FAP for a peak anywhere in the frequency range of the periodogram and one at a known frequency in the data. Usually, the FAP is computed by finding the probability that noise creates a peak in the periodogram higher than what is observed over a wide frequency range, typically taken from near zero out to the Nyquist frequency. However, in this case there is a signal at the known orbital frequency of the planet,  $f_b$ . We need to assess the probability that random

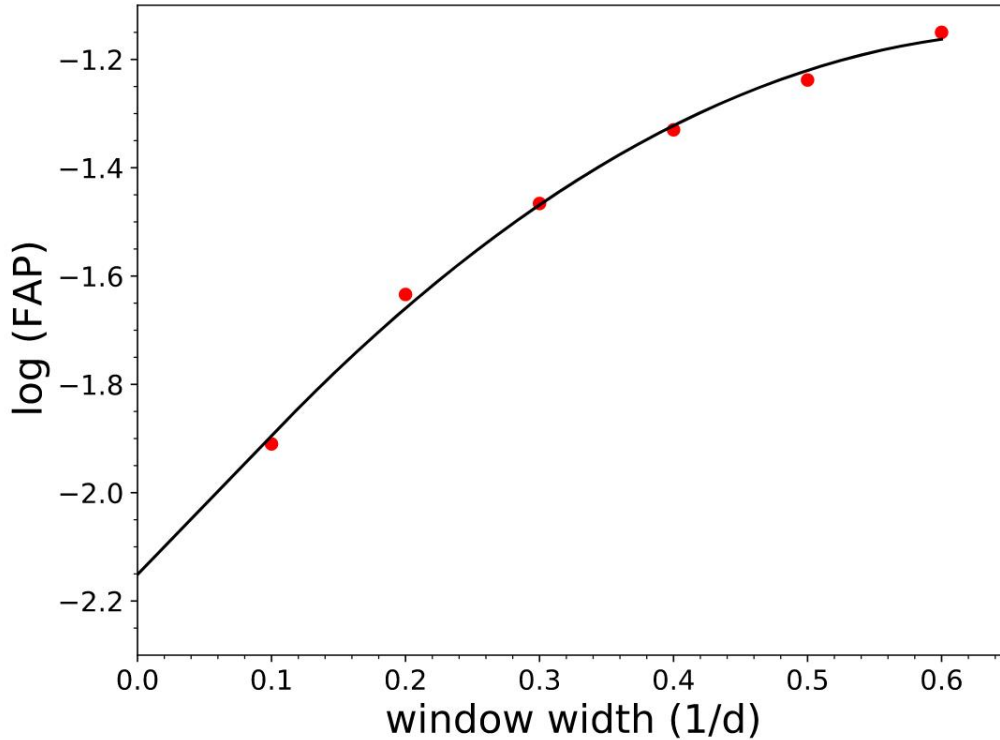


**Figure 3.5:** False alarm probability (FAP) versus window size using a bootstrap as described in Sect. 3.4.1. Red points are from the bootstrap, and the solid black line is the fit.

data produce more power than what is observed exactly at this frequency.

A better estimate of the FAP comes from using the bootstrap randomization method. Therefore, we randomly shuffled the RV values while keeping the time stamps fixed and noted how often a peak had a power higher than what was observed. However, this must be done over a narrow frequency range centered on  $f_b$ , which can be problematic. Too large a window and the FAP is over-estimated, too narrow and the results may not be statistically significant. As a result, we employed a "windowing" bootstrap method (Hatzes, 2019) to compute the FAP over a wide frequency window centered on  $f_b$  and then successively narrowed the window for additional bootstraps. The fit of the FAP versus window size, extrapolated to zero window length, yields the FAP at  $f_b$ . This method yielded an FAP  $\approx 0.007$ , based on 100 000 bootstraps, as shown in Fig. 3.5. This fit confirms that the FAP of the peak at the orbital frequency of the transiting planet is less than 1%.

### 3.4.2 Searching for the rotation period

In order to understand the origin of the  $\sim 9$  d and the double-peak ( $\sim 19$ – $26$  d) signals present in the RV data, we searched for additional information in the periodograms of the activity indicators that `serval` provides, which are shown in panels  $f$ – $i$  of Fig. 3.4. These indicators comprise the chromatic index (CRX), differential line width (dLW),  $H\alpha$  line emission, and Ca II infrared triplet (Ca IRT) emission. The titanium oxide indices that quantify the

strengths of the TiO  $\gamma$ ,  $\epsilon$ , and  $\delta$  absorption band heads at 7050 Å, 8430 Å, and 8860 Å were derived from the individual CARMENES spectra following (Zechmeister et al., 2018; Schöfer et al., 2019) and are shown in panels *j*, *k*, and *l*, respectively. The double-peak signal visible in the RV periodogram is also strong in dLW ( $\approx 20$  d; panel *g*), which may indicate that this signal is related to stellar activity (Zechmeister et al., 2018).

As expected for an early-type M dwarf, the TiO7050, TiO8430, and TiO8860 indices, usually used to measure the properties of cool starspots of magnetically active stars, do not show significant signals. A measured median pEW(H $\alpha$ ) of +0.51 Å classifies TOI-1685 as an H $\alpha$  inactive star (Jeffers et al., 2018a). This is consistent with its low  $v \sin i_*$  value of  $< 2.0 \text{ km s}^{-1}$ . The activity indices and their uncertainties are listed in Table 3.8.

In order to explore the stability of the double-peak signal, we computed the stacked-Bayesian GLS (s-BGLS) periodogram of the RV data with the normalization from Mortier & Collier Cameron (2017). The main idea was to stack the RV periodograms by subsequently adding observations and recalculating the periodogram. Figure 3.6 shows an s-BGLS periodogram between 0.5–40 d, after subtracting the USP signal. The signal at  $\sim 9$  d shows a first probability maximum after around 44 observations, after which the probability monotonically increases, as is expected for a Keplerian signal. On the other hand, the s-BGLS of the double-peak signal (centered around  $\sim 19$  d) shows a first probability maximum after around 44 measurements and then decreases for some time. This incoherence is characteristic for a non-planetary origin of the signal, and due to the evidence from the dLW we attributed it to the stellar rotation.

Additionally, we observed TOI-1685 in the *V* band with the 40 cm telescopes of LCOGT at the Teide and Haleakalā observatories. The 40 cm telescopes are equipped with  $3\text{k} \times 2\text{k}$  Santa Barbara Instrument Group Charge-coupled device (SBIG CCD) cameras, with identical pixel scales of 0.571 arcsec and fields of view of  $29.2 \times 19.5$  arcmin. Weather conditions at both observatories were mostly clear, and the average seeing varied from 2.0 arcsec to 4.0 arcsec (for observation details, see Table 3.2). Raw data were processed with the *banzai* pipeline, which includes bad pixel, bias, dark, and flat-field corrections for each individual night. We performed aperture photometry for TOI-1685 and three reference stars of the field and obtained the relative differential photometry between the target and reference stars. We adopted an aperture of 16 pixels (9.1 arcsec), which minimizes the dispersion of the differential light curve. Figure 3.7 shows the GLS periodogram of the joint LCOGT Teide and Haleakalā photometric data. The highest peak close to the 10% FAP level has a period of  $26.0 \pm 2.5$  d, which supports the notion that this signal is related to stellar activity and is consistent with the double peak at  $\sim 19$ – $26$  d found in the spectroscopic data.

Finally, we searched for available photometric data for TOI-1685. We found some data in the All-Sky Automated Survey for SuperNovae light curves (ASAS-SN; Shappee et al., 2014; Kochanek et al., 2017), but unfortunately they were not useful for confirming the rotational period of TOI-1685.

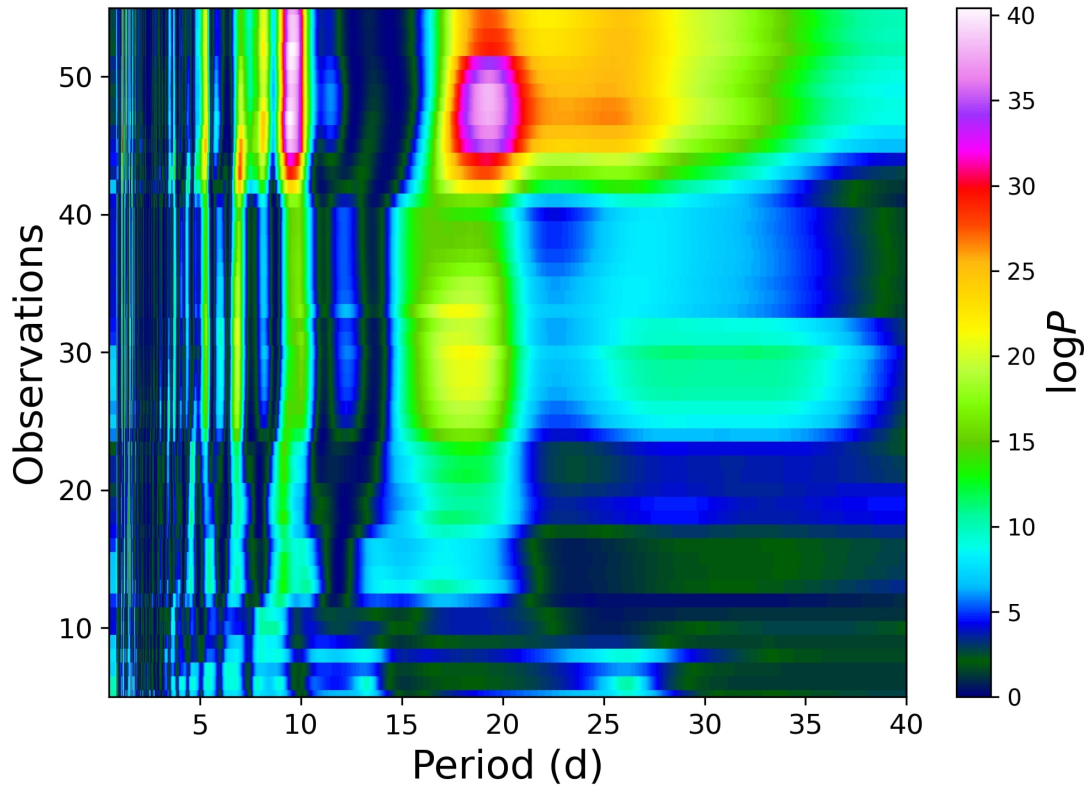


**Figure 3.6:** Evolution of the s-BGLS periodogram of the RV data between 0.5 d and 40 d, after subtracting the USP signal. The planet candidate is at  $\sim 9$  d, and the activity signal related to the rotational period is visible around 19 d. The number of data points included in the computation of the periodogram increases from bottom to top.

### 3.4.3 Modeling results

To model the RV data, we used `juliet`<sup>31</sup> (Espinoza et al., 2019), which allows fitting the data at a given prior volume. `juliet` searches the global posterior maximum based on the evaluation of the Bayesian log-evidence ( $\ln \mathcal{Z}$ ), with which one can perform formal model comparisons given the differences in  $\Delta \ln \mathcal{Z}$ . To select our final model we used the criteria described in Trotta (2008), which consider a difference of  $\Delta \ln \mathcal{Z} > 5.0$  between models as "significant" and of  $\Delta \ln \mathcal{Z} > 2.5$  at "moderate," favoring the former over the latter. Models with  $\Delta \ln \mathcal{Z} < 2$  are indistinguishable, which means none of them are preferred over the others.

`juliet` calculates the log-evidence via nested sampling algorithms. For the joint fit (see Sect. 3.4.5 for details) we used `dynesty` (Speagle, 2019)<sup>32</sup>, and for the RV modeling we used `MultiNest` (Feroz et al., 2009), which employs the `PyMultiNest` package (Buchner et al., 2014). To model Keplerian RV signals we used `radvel`<sup>33</sup> (Fulton et al., 2018), and for the Gaussian process (GP) modeling we used `george`<sup>34</sup> (Ambikasaran et al., 2015). For the GP,

<sup>31</sup><https://juliet.readthedocs.io/en/latest/>

<sup>32</sup><https://github.com/joshspeagle/dynesty>

<sup>33</sup><https://radvel.readthedocs.io/en/latest/>

<sup>34</sup><https://george.readthedocs.io/en/latest/>

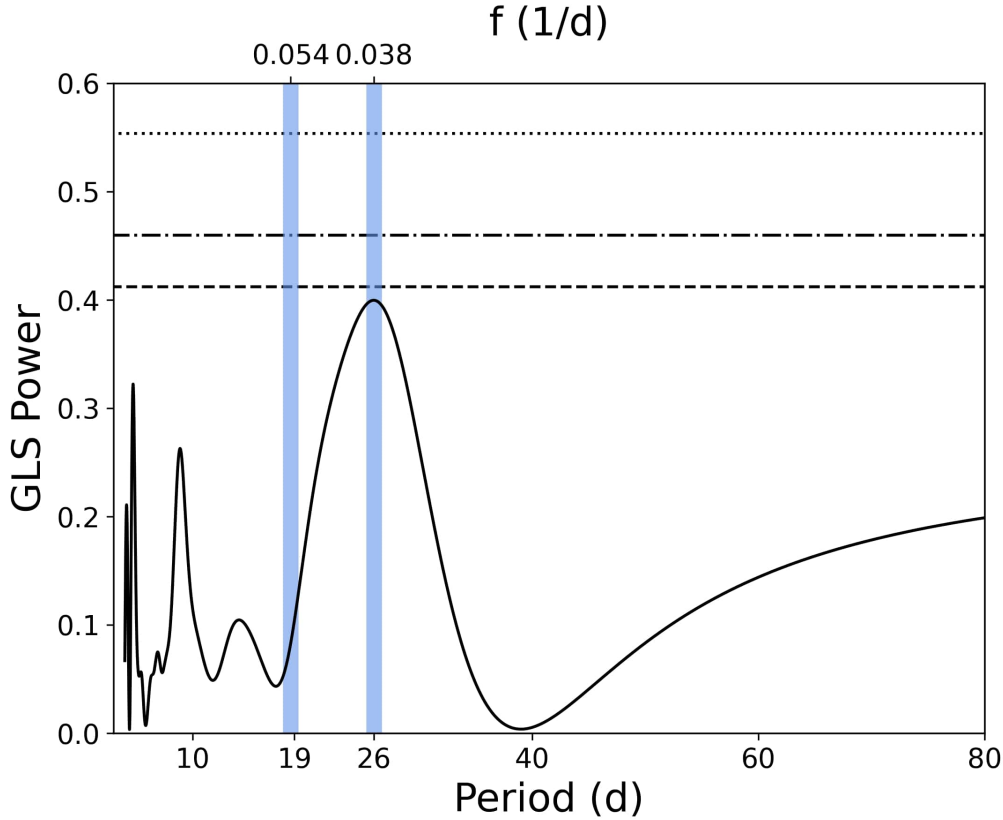


**Figure 3.7:** GLS periodogram of the joint V-band LCOGT Teide and Haleakalā light curve. The horizontal lines mark the theoretical FAP levels of 1% (dotted), 5% (dash-dotted), and 10% (dashed). The highest peak, near the 10% FAP level, which is related to the rotational period and has a period of  $26.0 \pm 2.5$  d, and the signal found in the RV data at  $\sim 19$  d are marked with blue vertical bands.

we selected an exp-sin-squared kernel multiplied by a squared-exponential kernel, also known as the quasi-periodic (QP) kernel, which has the following form:

$$k(\tau) = \sigma_{GP}^2 \exp\left(-\alpha_{GP}\tau^2 - \Gamma \sin^2(\pi\tau P_{rot})\right) \quad , \quad (3.1)$$

where  $\sigma_{GP}$  is the amplitude of the GP given in  $\text{ms}^{-1}$ ,  $\Gamma$  is the amplitude of the GP sine-squared component,  $\alpha$  is the square of the inverse length scale of the exponential component of the GP given in  $\text{d}^{-2}$ ,  $\tau$  is the time lag in days, and  $P_{rot}$  is the period of the GP-QP component given in days. The GP-QP is a kernel that is widely used to model stellar activity signatures (see, e.g., [Faria, 2017](#); [Nava et al., 2020](#); [Stock et al., 2020b](#); [Kemmer et al., 2020](#); [Bluhm et al., 2020](#), and references therein). The advantage of using a multiplied kernel is due to its exp-sine-squared factor, which enables the modeling of complex periodic signals. At the same time, the square-exponential factor allows changes in the periodic function over time, that is, either decreasing or increasing its amplitude. This combination is suitable for describing stochastic physical processes occurring in stars, such as the exponential growth or decay of active regions.

| Models      | Periods           | $\ln \mathcal{Z}$    | $\Delta \ln \mathcal{Z}$ |
|-------------|-------------------|----------------------|--------------------------|
| 1cp         | 0.67              | $-186.609 \pm 0.107$ | 0.0                      |
| 1cp+GP      | 0.67              | $-177.843 \pm 0.014$ | 8.77                     |
| 2cp         | 0.67, 9.22        | $-177.872 \pm 0.073$ | 8.74                     |
| 1cp+1kp     | 0.67, 9.31        | $-178.501 \pm 0.076$ | 8.11                     |
| 2cp+GP      | 0.67, 9.03        | $-176.609 \pm 0.062$ | 10.00                    |
| 1cp+1kp+GP  | 0.67, 9.02        | $-175.149 \pm 0.015$ | 11.47                    |
| 3cp         | 0.67, 9.12, 19.83 | $-175.464 \pm 0.032$ | 11.15                    |
| 1cp+1kp+1cp | 0.67, 9.01, 19.94 | $-174.369 \pm 0.042$ | 12.24                    |
| 1cp+1kp+1kp | 0.67, 9.00, 20.27 | $-174.791 \pm 0.011$ | 11.82                    |

**Table 3.4:** RV model selection. Bayesian log-evidence for the different models used for the RV data. In the model names, "cp" corresponds to circular models, "kp" to Keplerian orbits with non-fixed eccentricity, and "GP" to the QP kernel GP described in Sect. 3.4.3

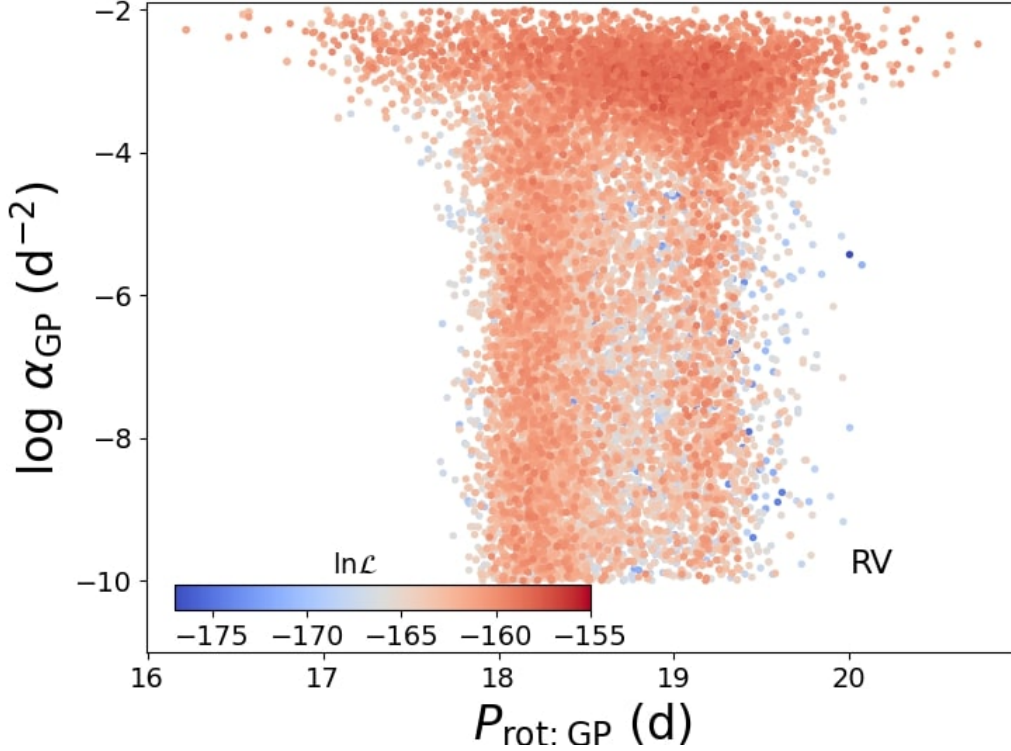


**Figure 3.8:** Posterior distribution of the GP fit to the RV data in the  $\alpha$  versus  $P_{\text{rot}}$  plane for TOI-1685. The color coding shows the log-likelihood normalized to the highest value in the posterior sample.

### 3.4.4 Only RV data

We performed an extensive model comparison on the RV data to find the model that accounts best for all three signals described in Sect. 3.4.2. As we discussed, the  $\sim 9$  d signal does not seem to be related to the  $\sim 19$  d rotational period of TOI-1685; it could be due to a second (non-transiting) planet in the system. An overview of the different models and their Bayesian evidence is shown in Table 3.4. The residual periodograms for the best log-evidence are shown in Fig. 3.4.

Since the USP signal was statistically significant (see Sect. 3.4.1 for details), we started fitting the RVs with a one-planet circular model around the USP period using uniform priors between 0.6 d and 0.7 d. The residual periodogram is shown in panel *b* of Fig. 3.4. Here, the strongest periodicity is at 9.22 d (FAP  $< 1\%$ ). After subtracting the USP period and the 9.22 d signal (using uniform priors between 8 d and 10 d) with a circular two-planet fit, only the double-peak signal at  $P \approx 19$ –26 d with FAP  $\sim 10\%$  remained (panel *c*). The double-peak structure and the activity indicators described in Sect. 3.4.2 show that the  $\sim 19$ –26 signal could be related to the stellar rotation period. Therefore, we next investigated whether including a GP to account for this signal improved the log-evidence of the fit.

We did our GP prior selection and final prior volume definition as described by Stock et al. (2020a). We started by using a wide prior for the GP period and GP  $\alpha$  values. We constructed a GP  $\alpha$ -period diagram, which is useful for identifying whether stronger correlated noise (small  $\alpha$ ) favors a certain periodicity (see, e.g., Stock et al., 2020b, and references therein). With this first approach, the diagram showed a plateau along with all periods in the range  $\log \alpha \gtrsim -2$  as well as a structure around the  $\sim 19$  d signal. The origin of the plateau is that the GP is essentially modeling white noise at that  $\alpha$  range. As we were mostly interested in fitting the spectral region around the suspected stellar rotational period with the GP, we set narrow uniform priors for the signal centered at  $\sim 19$  d, and we cut off the plateau by constraining the  $\alpha$  values. Figure 3.8 shows a scatter plot of the sampled  $\alpha$  values of the QP kernel over the sampled rotational periods using the priors presented in Table 3.5. Considering this plane, we inferred that the likelihood and number of posterior samples around  $\sim 19$  d are consistent with a periodic signal present over the entire time of observations.

Once the parameters of our GP-QP were chosen, we performed a simultaneous fit to a one-planet circular model together with a GP (1cp+GP). As we expected, including a GP significantly improved the log-evidence compared to the one-planet circular fit alone ( $\Delta \ln \mathcal{Z} \sim 8.8$ ). To account for the signal at  $\sim 9$  d, we further performed a two-planet plus GP model, where we either fixed the eccentricity (2cp+GP) or kept it free (1cp+1kp+GP). In these cases, the differences between these models with the 1cp+GP fit were  $\Delta \ln \mathcal{Z} \sim 1.2$  for 2cp+GP and  $\Delta \ln \mathcal{Z} \sim 2.7$  for 1cp+1kp+GP. In the first case, the difference made these two models indistinguishable from each other, while in the second the difference made the 1cp+1kp+GP fit moderately favored. On the other hand, the difference between them was  $\Delta \ln \mathcal{Z} \sim 1.5$ , which made the models indistinguishable if they were equally likely a priori, so the simplest model should be chosen in this case.

Additionally, we performed a three-planet model fit and compared the  $\Delta \ln \mathcal{Z}$  with the 1cp+GP fit. In this case, we used uniform priors between 15 and 30 d, the suspected region for the stellar rotational period (Sect. 3.4.2). In all cases, the differences were  $\Delta \ln \mathcal{Z} < 5$ , which implied that none of them were significantly favored. However, we noticed that most

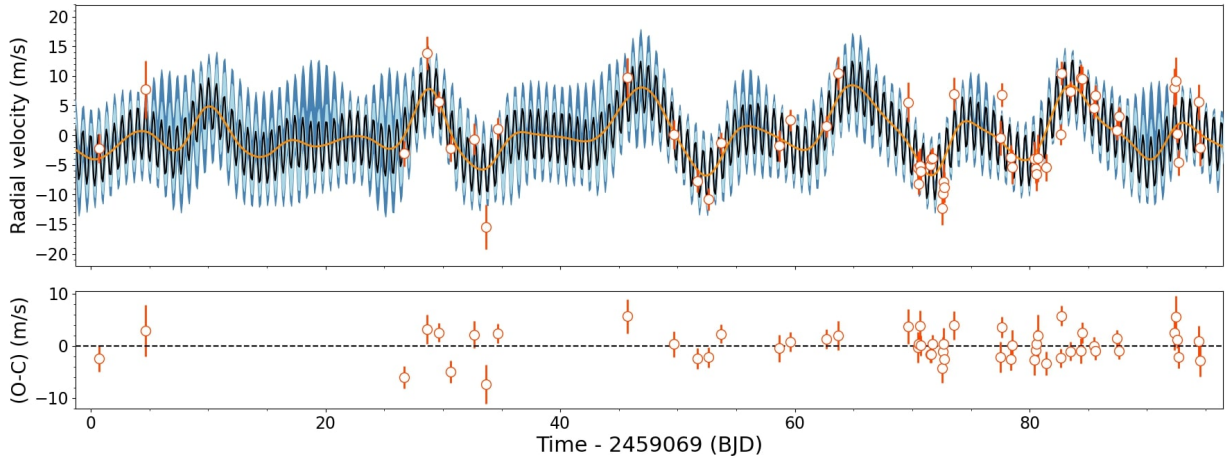


**Figure 3.9:** RV data from CARMENES (red). The gray curve is the median best-fit Keplerian juliet model, the light and dark blue areas are its 68 % and 95 % credibility bands, and the orange curve is the QP kernel (GP-QP).

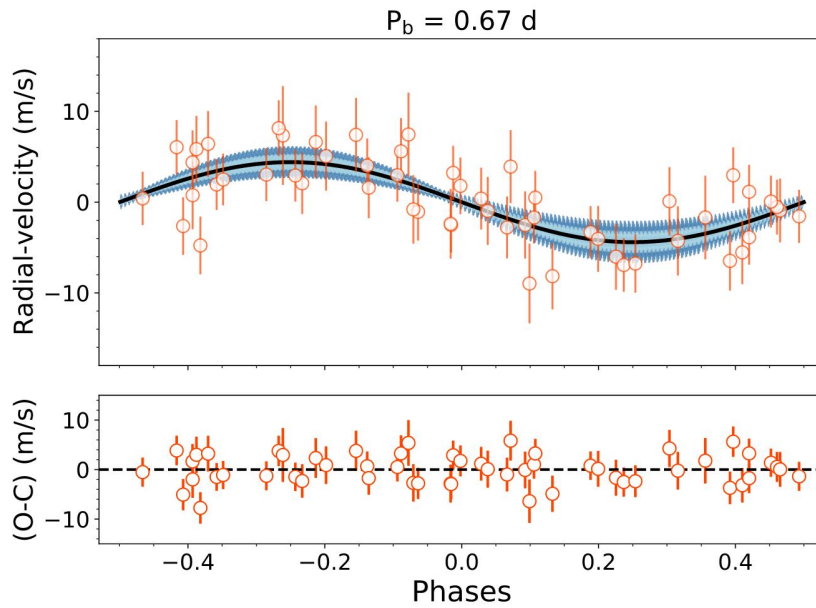


**Figure 3.10:** Phase-folded RV curves and their residuals of the USP. Black curves are the best-fit models, and blue areas are the 68 % and 95 % credibility bands.

of the models that include three signals show a  $\Delta \ln \mathcal{Z} \gtrsim 2.5$  compared to the 1cp+GP, which makes them moderately favored; hence, we cannot immediately rule out an additional signal in the system.

We decided to choose the 1cp+GP as our fiducial model, and in Sect. 3.5.2 we explore the possibility of include the  $\sim 9$  d signal with a 2cp+GP model. The residuals of these two fits are shown in panels *d* and *e* of Fig. 3.4, respectively, where no additional significant peaks are detectable.

| Parameter <sup>a</sup>                                                       | Prior                               | Unit               | Description                                   |
|------------------------------------------------------------------------------|-------------------------------------|--------------------|-----------------------------------------------|
| Stellar parameters                                                           |                                     |                    |                                               |
| $\rho_\star$                                                                 | $\mathcal{U}(5.7, 5.9)$             | $\text{g cm}^{-3}$ | Stellar density                               |
| Planet b parameters                                                          |                                     |                    |                                               |
| $P_b$                                                                        | $\mathcal{N}(0.66, 0.01)$           | d                  | Period of planet b                            |
| $t_{0,b}$                                                                    | $\mathcal{U}(2458816.0, 2458816.7)$ | d                  | Time of transit center of planet b            |
| $r_{1,b}$                                                                    | $\mathcal{U}(0, 1)$                 | ...                | Parameterization for $p$ and $b$              |
| $r_{2,b}$                                                                    | $\mathcal{U}(0, 1)$                 | ...                | Parameterization for $p$ and $b$              |
| $K_b$                                                                        | $\mathcal{U}(0, 10)$                | $\text{ms}^{-1}$   | RV semi-amplitude of planet b                 |
| $e_b$                                                                        | 0.0 (fixed)                         | ...                | Orbital eccentricity of planet b              |
| $\omega_b$                                                                   | 90.0 (fixed)                        | deg                | Periastron angle of planet b                  |
| Planet candidate [c] parameters $\rightarrow$ only used for 2cp+GP model fit |                                     |                    |                                               |
| $P_c$                                                                        | $\mathcal{U}(8.5, 9.5)$             | d                  | Period of candidate [c]                       |
| $t_{0,c}$                                                                    | $\mathcal{U}(2458816, 2458826)$     | d                  | Time of transit center of candidate [c]       |
| $K_c$                                                                        | $\mathcal{U}(0, 10)$                | $\text{ms}^{-1}$   | RV semi-amplitude of candidate [c]            |
| $e_c$                                                                        | 0.0 (fixed)                         | ...                | Orbital eccentricity of candidate [c]         |
| $\omega_c$                                                                   | 90.0 (fixed)                        | deg                | Periastron angle of candidate [c]             |
| Phot. param. for TESS Sector 19                                              |                                     |                    |                                               |
| $D_{\text{TESS}}$                                                            | 1.0 (fixed)                         | ...                | Dilution factor for <i>TESS</i>               |
| $M_{\text{TESS}}$                                                            | $\mathcal{N}(0, 0.1)$               | ...                | Relative flux offset for <i>TESS</i>          |
| $\sigma_{\text{TESS}}$                                                       | $\mathcal{J}(0.1, 1000)$            | ppm                | Extra jitter term for <i>TESS</i>             |
| $q_{1,\text{TESS}}$                                                          | $\mathcal{U}(0, 1)$                 | ...                | Limb-dark. param. for <i>TESS</i>             |
| $q_{2,\text{TESS}}$                                                          | $\mathcal{U}(0, 1)$                 | ...                | Limb-dark. param. for <i>TESS</i>             |
| Phot. param. for LCOGT nights, 2020-08-26, and 2020-11-07,11                 |                                     |                    |                                               |
| $D_{\text{LCOGT}}$                                                           | 1.0 (fixed)                         | ...                | Dilution factor for LCOGT                     |
| $M_{\text{LCOGT}}$                                                           | $\mathcal{N}(0, 0.1)$               | ...                | Relative flux offset for LCOGT                |
| $\sigma_{\text{LCOGT}}$                                                      | $\mathcal{J}(0.1, 1000)$            | ppm                | Extra jitter term for LCOGT                   |
| $q_{1,\text{LCOGT}}$                                                         | $\mathcal{U}(0, 1)$                 | ...                | Limb-dark. param. for LCOGT                   |
| Phot. param. for PESTO, night 2020-03-08                                     |                                     |                    |                                               |
| $D_{\text{PESTO}}$                                                           | 1.0 (fixed)                         | ...                | Dilution factor for PESTO                     |
| $M_{\text{PESTO}}$                                                           | $\mathcal{N}(0, 0.1)$               | ...                | Relative flux offset for PESTO                |
| $\sigma_{\text{PESTO}}$                                                      | $\mathcal{J}(0.1, 1000)$            | ppm                | Extra jitter term for PESTO                   |
| $q_{1,\text{PESTO}}$                                                         | $\mathcal{U}(0, 1)$                 | ...                | Limb-dark. param. for PESTO                   |
| Phot. param. for MuSCATS2 i, and z <sub>s</sub> bands, nights 2021-01-19,29  |                                     |                    |                                               |
| $D_{\text{MuSCAT2}}(i, z_s)$                                                 | 1.0 (fixed)                         | ...                | Dilution factor for MuSCAT2                   |
| $M_{\text{MuSCAT2}}(i, z_s)$                                                 | $\mathcal{N}(0, 0.1)$               | ...                | Relative flux offset for MuSCAT2              |
| $\sigma_{\text{MuSCAT2}}(i, z_s)$                                            | $\mathcal{J}(0.1, 1000)$            | ppm                | Extra jitter term for MuSCAT2                 |
| $q_{1,\text{LCOGT}}(i, z_s)$                                                 | $\mathcal{U}(0, 1)$                 | ...                | Limb-dark. param.                             |
| RV parameters                                                                |                                     |                    |                                               |
| $\gamma_{\text{CARMENES}}$                                                   | $\mathcal{U}(-10, 10)$              | $\text{ms}^{-1}$   | RV zero point for CARMENES                    |
| $\sigma_{\text{CARMENES}}$                                                   | $\mathcal{J}(0.01, 10)$             | $\text{ms}^{-1}$   | Extra jitter term for CARMENES                |
| GP hyperparameters                                                           |                                     |                    |                                               |
| $\sigma_{\text{GP,RV}}$                                                      | $\mathcal{U}(0, 80)$                | $\text{ms}^{-1}$   | Amp. of GP comp. for the RVs                  |
| $\alpha_{\text{GP,RV}}$                                                      | $\mathcal{J}(10^{-10}, 0.01)$       | $\text{d}^{-2}$    | Inv.length-scale of GP exp. comp. for the RVs |
| $\Gamma_{\text{GP,RV}}$                                                      | $\mathcal{J}(0.1, 10)$              | ...                | Amp. of GP sine-squared comp. for the RVs     |
| $P_{\text{Tot;GP,RV}}$                                                       | $\mathcal{U}(15, 30)$               | d                  | Period of the GP-QP comp. for the RVs         |

**Table 3.5:** Priors used for TOI-1235 b and TOI-1685 [c] in the joint fit with *juliet*.

**Notes.** <sup>(a)</sup> The parameterization for  $(p, b)$  was made with  $(r_1, r_2)$  as in [Espinoza \(2018\)](#).

 The prior labels of  $\mathcal{N}$ ,  $\mathcal{U}$ , and  $\mathcal{J}$  represent normal, uniform, and Jeffreys distributions, respectively;  $\mathcal{N}(\mu, \sigma^2)$  is a normal distribution of the mean,  $\mu$ , and variance,  $\sigma^2$ ;  $\mathcal{U}(a, b)$  and

 $\mathcal{J}(a, b)$  are uniform; and Jeffreys (log-uniform) distributions are between  $a$  and  $b$ .

### 3.4.5 Joint fit

In order to obtain precise parameters of the TOI-1685 system, we performed a joint analysis with `juliet`. For the joint fit we used *TESS*, LCOGT, PESTO, MuSCAT2, and CARMENES VIS data. For the transit modeling, `juliet` makes use of the `batman` package (Kreidberg, 2015). To parameterize the quadratic limb-darkening effect in the *TESS* photometry, we employed the efficient, uninformative sampling scheme of Kipping (2013) and a quadratic law. For LCOGT, PESTO, and MuSCAT2 photometry, we used a linear law to parameterize the limb-darkening effect. We followed the Espinoza (2018) parameterization to explore the full physically plausible parameter space for the planet-to-star radius ratio,  $p = R_p/R_\star$ , and the impact parameter,  $b$ . The model selection was performed based on the analyses on the photometric data plus the highest peaks in the RV periodogram. As discussed in Sect. 3.4.3, we selected as our fiducial model one planet with a circular orbit and a QP GP for the stellar rotation (1cp+GP).

The selected priors for our joint fit are presented in Table 3.5. The posterior distributions of our joint fit are presented in Tables 3.6 and 3.7, while the resulting photometry and RV models are presented in Figs. 3.1, 3.9, and 3.10, respectively. The obtained posterior probabilities are presented in Fig. 3.11. The maximum posterior of the rotational period of the GP periodic component was around 19 d, in agreement with the region at  $\approx 19\text{--}26$  d observed in the GLS RV periodogram (Fig. 3.4 and Sect. 3.4.2).

3 An ultra-short-period transiting super-Earth orbiting the M3 dwarf TOI-1685

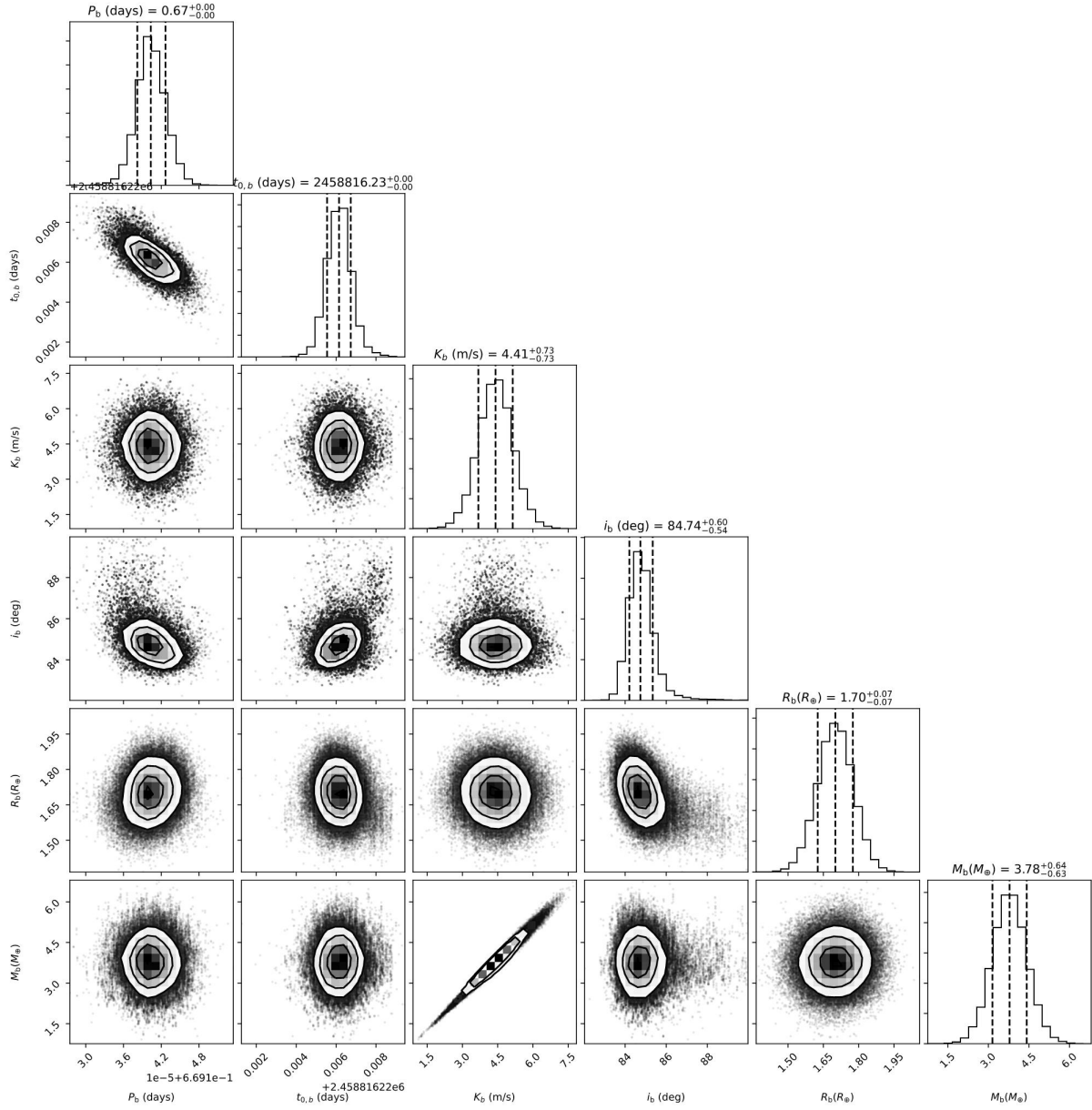


**Figure 3.11:** Posterior distribution for the joint model parameters (1cp+GP) derived with juliet.

| Parameter <sup>a</sup>                               | TOI-1685                   |
|------------------------------------------------------|----------------------------|
| <i>Stellar parameters</i>                            |                            |
| $\rho_{\star}$ ( $\text{g cm}^{-3}$ )                | $5.797^{+0.064}_{-0.060}$  |
| <i>Photometry parameters</i>                         |                            |
| $M_{\text{TESS,S19}}$ ( $10^{-5}$ )                  | $-7.63^{+1.60}_{-1.60}$    |
| $\sigma_{\text{TESS,S19}}$ (ppm)                     | $2.63^{+15.44}_{-2.26}$    |
| $q_{1,\text{TESS}}$                                  | $0.37^{+0.27}_{-0.20}$     |
| $q_{2,\text{TESS}}$                                  | $0.54^{+0.29}_{-0.32}$     |
| $M_{\text{LCOGT}}$ ( $10^{-5}$ )                     | $-0.46^{+4.31}_{-4.30}$    |
| $\sigma_{\text{LCOGT}}$ (ppm)                        | $826.79^{+44.54}_{-42.89}$ |
| $q_{1,\text{LCOGT}}$                                 | $0.63^{+0.22}_{-0.29}$     |
| $M_{\text{PESTO}}$ ( $10^{-5}$ )                     | $3.41^{+7.36}_{-7.42}$     |
| $\sigma_{\text{PESTO}}$ (ppm)                        | $967.07^{+22.71}_{-40.25}$ |
| $q_{1,\text{PESTO}}$                                 | $0.49^{+0.29}_{-0.29}$     |
| $M_{\text{MuSCAT2 i}}$ ( $10^{-5}$ )                 | $24.92^{+7.97}_{-7.97}$    |
| $\sigma_{\text{MuSCAT2 i}}$ (ppm)                    | $7.06^{+63.95}_{-6.49}$    |
| $q_{1,\text{MuSCAT2 i}}$                             | $0.71^{+0.20}_{-0.30}$     |
| $M_{\text{MuSCAT2 } z_s}$ ( $10^{-5}$ )              | $18.75^{+8.84}_{-8.88}$    |
| $\sigma_{\text{MuSCAT2 } z_s}$ (ppm)                 | $5.17^{+48.83}_{-4.69}$    |
| $q_{1,\text{MuSCAT2 } z_s}$                          | $0.54^{+0.29}_{-0.32}$     |
| <i>RV parameters</i>                                 |                            |
| $\gamma_{\text{CARMENES}}$ ( $\text{m s}^{-1}$ )     | $0.34^{+2.69}_{-2.78}$     |
| $\sigma_{\text{CARMENES}}$ ( $\text{m s}^{-1}$ )     | $2.35^{+0.79}_{-0.93}$     |
| <i>GP hyperparameters</i>                            |                            |
| $\sigma_{\text{GP,RV}}$ ( $\text{m s}^{-1}$ )        | $6.46^{+3.17}_{-1.68}$     |
| $\alpha_{\text{GP,RV}}$ ( $10^{-3} \text{ d}^{-2}$ ) | $0.25^{+1.70}_{-0.25}$     |
| $\Gamma_{\text{GP,RV}}$                              | $5.76^{+2.75}_{-3.35}$     |
| $P_{\text{rot;GP,RV}}$ (d)                           | $18.66^{+0.71}_{-0.56}$    |

**Table 3.6:** Posterior distributions of the *juliet* joint fit for the instrumental parameters.  
<sup>(a)</sup> The priors and descriptions for each parameter are given in Table 3.5. Error bars denote the 68 % posterior credibility intervals.

| Parameter <sup>a</sup>             | TOI-1685 b                            |
|------------------------------------|---------------------------------------|
| <i>Planet parameters</i>           |                                       |
| $P_b$ (d)                          | $0.6691403^{+0.0000023}_{-0.0000021}$ |
| $t_{0,b}$ (BJD)                    | $2458816.22615^{+0.00059}_{-0.00060}$ |
| $a_b/R_\star$                      | $5.158^{+0.019}_{-0.018}$             |
| $p = R_b/R_\star$                  | $0.0317^{+0.0009}_{-0.0010}$          |
| $b = (a_b/R_\star) \cos i_b$       | $0.473^{+0.048}_{-0.054}$             |
| $i_b$ (deg)                        | $84.74^{+0.60}_{-0.54}$               |
| $r_1$                              | $0.65^{+0.03}_{-0.04}$                |
| $r_2$                              | $0.0317^{+0.0009}_{-0.0010}$          |
| $K_b$ (ms <sup>-1</sup> )          | $4.41^{+0.73}_{-0.73}$                |
| <i>Derived physical parameters</i> |                                       |
| $M_b$ ( $M_\oplus$ )               | $3.78^{+0.63}_{-0.63}$                |
| $R_b$ ( $R_\oplus$ )               | $1.70^{+0.07}_{-0.07}$                |
| $\rho_b$ (g cm <sup>-3</sup> )     | $4.21^{+0.95}_{-0.82}$                |
| $g_b$ (m s <sup>-2</sup> )         | $12.79^{+2.49}_{-2.28}$               |
| $T_{\text{eq},b}$ (K) <sup>b</sup> | $1069^{+16}_{-16}$                    |
| $S_b$ ( $S_\oplus$ )               | $217^{+13}_{-13}$                     |
| Parameter <sup>b</sup>             | TOI-1685 [c] <sup>c</sup>             |
| $P_c$ (d)                          | $9.025^{+0.104}_{-0.119}$             |
| $t_{0,c}$ (BJD)                    | $2458820.4^{+2.9}_{-2.6}$             |
| $a_c/R_\star$                      | $29.23^{+0.23}_{-0.24}$               |
| $K_c$ (ms <sup>-1</sup> )          | $4.53^{+1.01}_{-1.02}$                |
| $T_{\text{eq},c}$ (K) <sup>c</sup> | $449.1^{+6.9}_{-6.9}$                 |
| $S_c$ ( $S_\oplus$ )               | $6.76^{+0.42}_{-0.41}$                |
| $M_c \text{ sini}$ ( $M_\oplus$ )  | $9.21^{+2.06}_{-2.07}$                |

**Table 3.7:** Derived planetary parameters for TOI-1685 b and TOI-1685 [c]. <sup>(a)</sup> Parameters obtained with the posterior values from Table 3.6. <sup>(b)</sup> Parameters obtained with the posterior values of the 2cp+GP model fit. <sup>(c)</sup> We use square brackets to denote the tentative second planet as there is no agreed-upon nomenclature for unconfirmed planet candidates. It is understood that the values tabulated here have been computed under the assumption that the RV signal is indeed of a planetary origin. Error bars denote the 68% posterior credibility intervals. <sup>(c)</sup> The equilibrium temperature was calculated assuming zero Bond albedo.

## 3.5 Discussion

### 3.5.1 Ultra-short-period planet: TOI-1685 b

We present the discovery of the USP TOI-1685 b, which orbits its host star with a period of 0.669 d. To confirm the planetary nature of the TESS transiting candidate, we obtained high-resolution spectra using the CARMENES spectrograph. We derived a mass of  $M_b = 3.78_{-0.63}^{+0.63} M_\oplus$ , a radius of  $R_b = 1.70_{-0.07}^{+0.07} R_\oplus$ , and a bulk density of  $\rho_b = 4.21_{-0.82}^{+0.95} \text{ g cm}^{-3}$  (see Table 3.7).

Figure 3.12 shows TOI-1685 b in the context of all known exoplanets from NASA’s exoplanet archive<sup>35</sup>, with  $R \leq 4 R_\oplus$  and a planet bulk density of  $\rho \leq 15 \text{ g cm}^{-3}$ . Here, the USPs with orbital periods ranging from less than 10 hours to about one day tend to be smaller than  $2 R_\oplus$  (Winn et al., 2018) and are believed to have lost their atmospheres due to X-ray and ultraviolet (XUV) photo-evaporation from their host stars (e.g., Owen & Wu, 2013a; López & Fortney, 2013; Jin et al., 2014; Chen & Rogers, 2016; Owen & Wu, 2017). With an equilibrium temperature of  $T_{\text{eq}} = 1069 \pm 16 \text{ K}$ , it is likely that TOI-1685 b has gone through a similar process. In terms of separation from its host star, TOI-1685 b is one of the closest known planets with a mass determination. An insolation flux of  $S = 217 \pm 13 S_\oplus$  also makes TOI-1685 b one of the hottest transiting super-Earth discovered to date. TOI-1685 b is the third known USP to be found orbiting an M star, and the least dense of the three.

A comparison of the physical properties of TOI-1685 b with compositional models from Zeng et al. (2016, 2019) is shown in Fig. 3.13. The diagram reveals that TOI-1685 b is consistent with a bulk composition of 50 % H<sub>2</sub>O and 50 % silicate.

Finally, the proximity of TOI-1685 b to its host star, and assuming that the planet has not lost its atmosphere, makes TOI-1685 b an attractive target for atmospheric characterization. In order to estimate the suitability of TOI-1685 b for such characterization, we calculated the spectroscopic metrics from Kempton et al. (2018). The transmission spectroscopy metric (TSM) and the emission spectroscopy metric (ESM) are analytic metrics for the expected S/N of transmission and emission spectroscopy observations by James Webb Space Telescope (*JWST*).

The TSM is estimated based on the strength of spectral features and the brightness of the host star, assuming a cloud-free atmosphere. The ESM is an approximation of the expected S/N for a single secondary eclipse observation integrated over the full 5–10  $\mu\text{m}$  bandpass of the low-resolution spectroscopy (LRS) mode of the *JWST* Mid-Infrared Instrument (MIRI). We estimated the ESM of TOI-1685 b to be about 13.9. This is larger than that of Gl 1132 b, which is considered a benchmark rocky planet for emission spectroscopy (Kempton et al., 2018). The top panel of Fig. 3.14 shows the ESMs of exoplanets with measured masses, either through RVs or transit-timing variations (TTVs), with a radius from the NASA exoplanet archive<sup>36</sup> of less than  $3 R_\oplus$ . We chose this radius cutoff in order to keep only the most likely terrestrial planets, and we excluded potential small sub-Neptunes (Kempton et al., 2018). Planets with ESMs on the order of or above the value of Gl 1132 b are separated from the

---

<sup>35</sup><https://exoplanetarchive.ipac.caltech.edu/>,  
<http://exoplanet.eu/>

<sup>36</sup><https://exoplanetarchive.ipac.caltech.edu/>,  
<http://exoplanet.eu/>

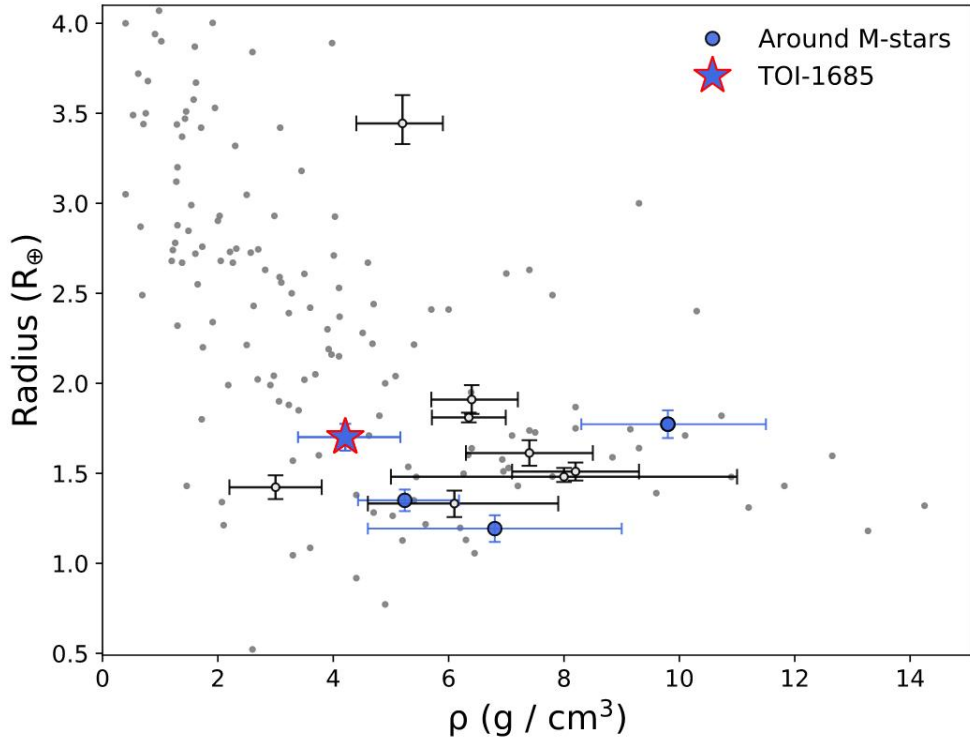


**Figure 3.12:** Density-radius diagram for all known exoplanets with planet bulk densities  $\rho \leq 15 \text{ g cm}^{-3}$  and radii  $R \leq 4 R_{\oplus}$  (gray) from the NASA exoplanet archive. USPs are drawn in black and are shown with the error bars of the measurements. Blue-filled circles mark USPs around M dwarfs, and the filled star symbol is TOI-1685 b.

others by a horizontal dotted line. TOI-1685 b is one of the hottest members of this family of small rocky planets suitable for emission spectroscopy.

We calculated a TSM value of  $86 \pm 18$  for TOI-1685 b. The TSMs of small exoplanets ( $1.5 R_{\oplus} < R_p < 3 R_{\oplus}$ ) are shown in the bottom panel of Fig. 3.14. We excluded planets with radii smaller than  $1.5 R_{\oplus}$  from this panel to make the TSMs comparable, as defined in (Kempton et al., 2018). A favorable TSM value for this class of planets is around 90 or higher (Table 1 in Kempton et al., 2018). This implies that TOI-1685 b would be a suitable target for atmospheric characterization through transmission spectroscopy as well. The suitability of TOI-1685 b for both transmission and emission spectroscopy makes this planet a worthy target for atmospheric characterization over a wide orbital phase.

The equilibrium temperature of TOI-1685 b is estimated to be about 1070 K. This is larger than the 880 K temperature threshold above which planets are expected to have molten surfaces, such as 55 Cnc e (McArthur et al., 2004). No thick  $\text{H}_2$ -dominated primary atmosphere is expected at these high temperatures, except possibly an exosphere maintained by vaporized rocks (Mansfield et al., 2019) or a secondary outgassing atmosphere due to volcanic activity. If such a substantial exosphere exists, it could provide critical observable tracers to shed light on the planet formation and evolution of USPs as it would directly trace the surface or near-surface composition of these planets.

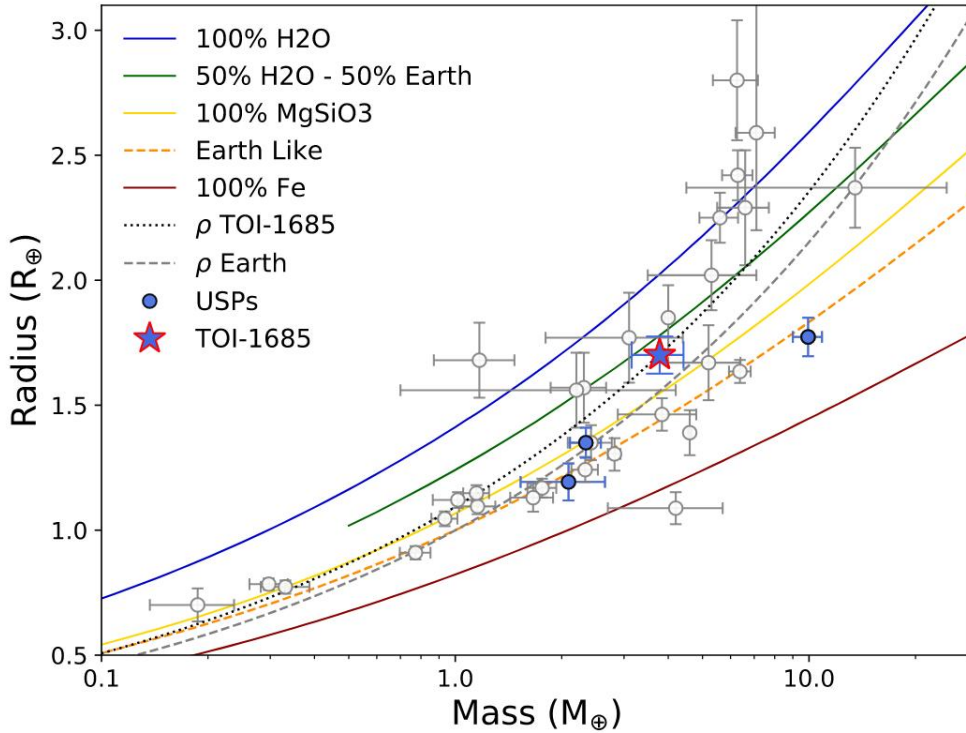


**Figure 3.13:** Mass-radius diagram in Earth units. Open circles are transiting planets around M-dwarf stars from the Transiting Extrasolar Planets Catalogue (TEPCat) database (Southworth 2011 and Martínez-Rodríguez et al. 2019), blue-filled circles are USPs, and the filled star symbol is TOI-1685 b.

Following such a scenario, it is expected that small exoplanets at higher temperatures have higher bulk densities. This is indeed what has been observed so far, as shown by the red shaded region in Fig. 3.15. However, TOI-1685 b does not follow such a prediction. This may suggest that TOI-1685 b maintains a substantial atmosphere, unlike other hot small planets. In such a scenario, water, carbon dioxide, or methane features could be observable in its atmosphere (Molaverdikhani et al., 2019b,a) or such atmospheric features might be obscured by clouds (Molaverdikhani et al., 2020). Nevertheless, future emission and transmission spectroscopy of TOI-1685 b is needed to answer the question of whether the entire atmosphere has escaped or a substantial atmosphere has been maintained on TOI-1685 b, making this USP a rather unusual and interesting planet discovery.

### 3.5.2 The planet candidate TOI-1685 [c]

Our RV modeling shows moderate evidence for a second potentially planetary signal in the system. As discussed in Sect. 3.4.2, the observed period of  $\sim 9$  d is not obviously linked to the stellar rotation period of  $\sim 26$  d, and the analysis of a comprehensive set of activity indicators revealed no signs of stellar activity at the period in question. However, the fact that the  $\sim 9$  d signal is close to the first harmonic of the likely rotational period derived from

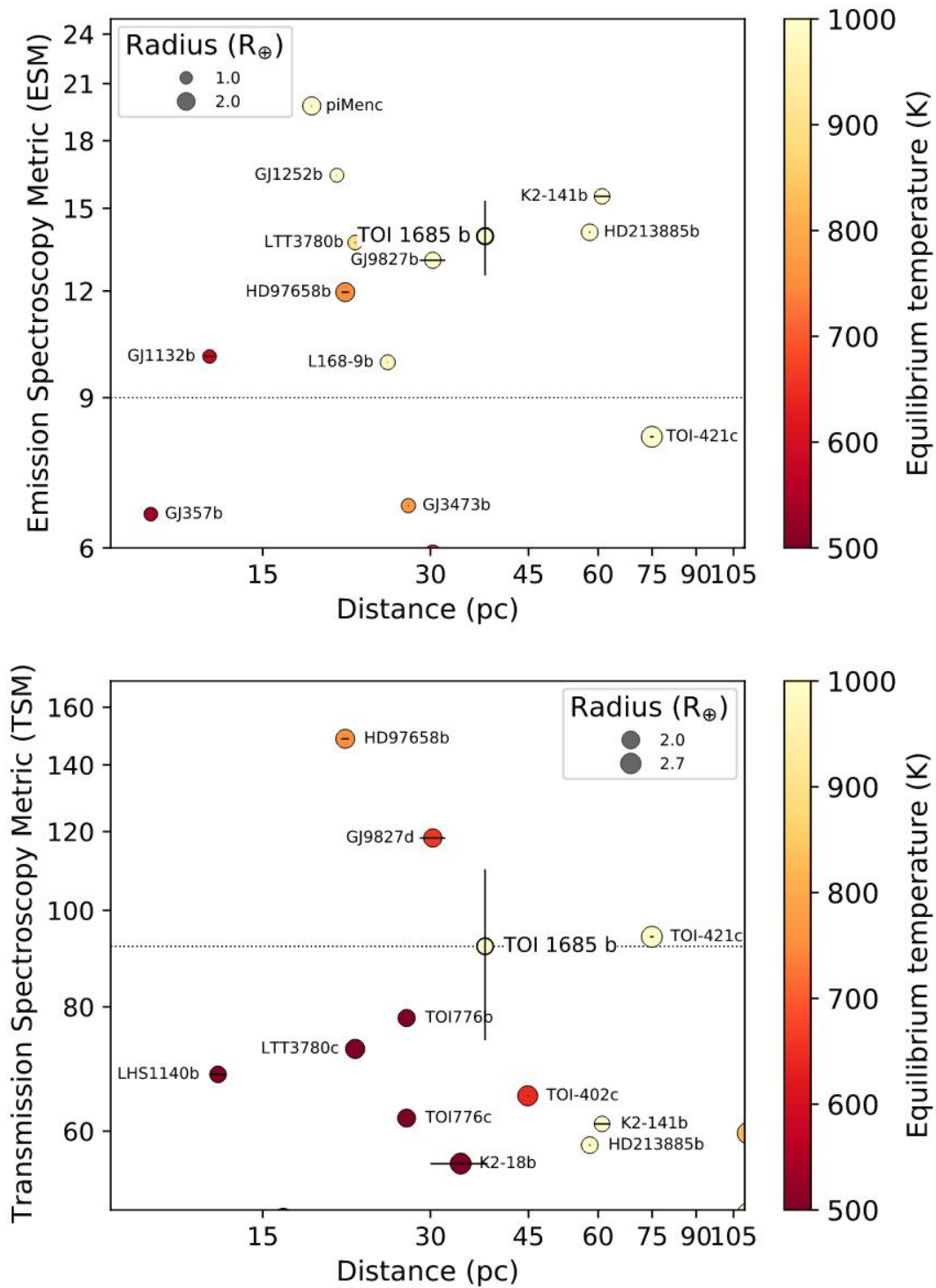


**Figure 3.14:** ESM and TSM metrics for TOI-1685 b. *Top:* ESM for exoplanets with a radius of less than  $3 R_{\oplus}$ . *Bottom:* TSM for exoplanets with a radius of less than  $3 R_{\oplus}$  but larger than  $1.5 R_{\oplus}$ . All planets have mass determination by either RVs or TTVs. TOI-1685 b is labeled and marked with a thicker black borderline in both panels. For most exoplanets, the error bars, in distance, are smaller than the symbol size. The uncertainties in the ESM and TSM are only plotted for TOI-1685 b.

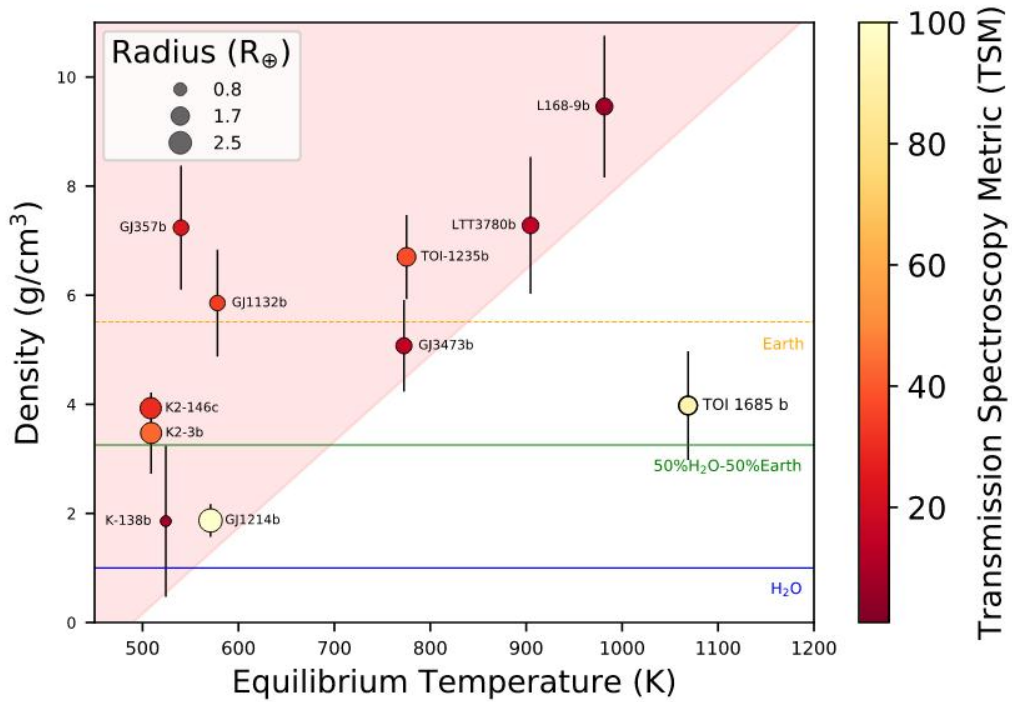


**Figure 3.15:** Density-equilibrium temperature diagram of warm-hot exoplanets with a radius of less than  $3 R_{\oplus}$  around M dwarfs. All planets have mass determination by either RVs or TTVs. TOI-1685 b is labeled and marked with a thicker black border. Some densities are marked as reference by horizontal lines, including Earth (dashed orange),  $H_2O$  (blue), and 50 %  $H_2O$ , 50% silicate (green). The observed  $\rho$ - $T_{eq}$  space before the discovery of TOI-1685 b is shaded in red to illustrate the dissimilarity of TOI-1685 b with previous discoveries.

the RVs implies that we cannot be completely certain about its origin.

A comparison of the log-evidence values of the different models considered does not settle the issue as the differences between them are not highly significant. The situation is further complicated by the fact that sinusoidal or Keplerian models may also represent stellar activity well, especially over a relatively short time span.

Nevertheless, the significance and the coherence of the 9 d signal compared to the presumed stellar activity signal at 19 d does lend some support to a planetary origin. After all, it represents the highest peak in the RV periodogram (Fig. 3.4), and it seems to be the most persistent (Fig. 3.6). Under the assumption that the signal is indeed due to a planet, we performed a 2cp+GP model fit. We used the same distribution prior as that presented in Table 3.5, and for the signal at  $\sim 9$  d we used a uniform distribution between 8.5 and 9.5 d.

From our joint fit, we derived for the planet candidate a period of  $P_c = 9.03^{+0.10}_{-0.12}$  d and a minimum mass of  $M_c = 9.2^{+2.1}_{-2.1} M_{\oplus}$ ; additional planet parameters are reported in Table 3.7. The obtained parameters with the 2cp+GP model were consistent within one sigma with those derived from the 1cp+GP model.

As a further test, we investigated whether the two-planet system would be dynamically stable. We used *Exo-Striker*<sup>37</sup> (Trifonov, 2019) to check the long-term stability of planetary

<sup>37</sup><https://github.com/3fon3fonov/exostriker>

systems via the angular momentum deficit key parameter (Laskar & Petit, 2017). The best joint fit resulted in a stable solution for the TOI-1685 system.

### 3.6 Conclusion

We present the discovery of a possible multi-planetary system around the M3.0 V star TOI-1685. The system has one transiting planet with an ultra-short orbital period plus another planet candidate at a wider orbit found only in RV data. The USP TOI-1685 b was first detected in the photometric time series of sector 19 of the *TESS* mission. We collected CARMENES RV data, as well as photometric transit follow-up observations from LCOGT, PESTO, and MuSCAT2, with which we confirmed its planetary nature. From the joint analysis, we derived a mass of  $M_b = 3.78^{+0.63}_{-0.63} M_\oplus$  and a radius of  $R_b = 1.70^{+0.07}_{-0.07} R_\oplus$ . The derived bulk density of  $\rho_b = 4.21^{+0.95}_{-0.82} \text{ g cm}^{-3}$  makes TOI-1685 b the least dense USP around an M dwarf known to date.

A comparison of the physical properties of TOI-1685 b with compositional models revealed a bulk composition of 50 % H<sub>2</sub>O and 50 % silicate. With a mass and radius precision better than 18 % and 5 %, respectively, TOI-1685 b complements the sample of well-characterized small planets orbiting nearby M dwarfs. Its proximity to its host star and the measured values for the TSM and the ESM metrics qualify this planet for atmospheric characterization through emission and transmission spectroscopy, as well as make it an interesting planet for studying atmospheric evolution and escape processes.

In the exploration of the RV data, a significant signal at  $\sim 9$  d was also found. To explore the origin of this signal, we analyzed the periodogram for RV activity indicators as well as the s-BGLS periodogram, and the signal was found to be persistent.

To model the stellar activity we used a GP-QP model based on a QP kernel plus two circular orbits (2cp+GP). However, due to the proximity of the  $\sim 9$  d planet candidate period to half of the stellar rotation period, we cannot rule out that it is related to stellar activity. Nevertheless, the strength and coherence of the signal make it a promising planet candidate. However, based on the currently available RV data, it is not possible to confidently claim the detection of a second planet in the system. To reach a solid conclusion, more data will be needed.

| BJD<br>(-2450000) | RV<br>( $\text{m s}^{-1}$ ) | CRX<br>( $\text{m/s Np}$ ) | dLW<br>( $\text{m}^2 \text{s}^{-2}$ ) | H $\alpha$    | Ca IRTa       | TiO7050     | TiO8430     | TiO8860     |
|-------------------|-----------------------------|----------------------------|---------------------------------------|---------------|---------------|-------------|-------------|-------------|
| 9069.6744         | -1.87±2.43                  | 9.17±24.55                 | 23.23±3.44                            | 0.8715±0.0043 | 0.6121±0.0031 | 0.616±0.002 | 0.836±0.004 | 0.004±0.003 |
| 9073.6703         | 8.05±4.91                   | 30.68±50.73                | 23.22±5.48                            | 0.8531±0.0095 | 0.6132±0.0067 | 0.620±0.004 | 0.822±0.008 | 0.008±0.006 |
| 9095.6713         | -2.74±2.14                  | -3.32±19.66                | 4.05±2.91                             | 0.8605±0.0037 | 0.6124±0.0029 | 0.616±0.002 | 0.831±0.003 | 0.003±0.003 |
| 9097.6749         | 14.20±2.81                  | 12.22±28.42                | -7.50±3.14                            | 0.8794±0.0059 | 0.6111±0.0044 | 0.612±0.003 | 0.834±0.005 | 0.005±0.004 |
| 9098.6754         | 5.97±1.78                   | 21.89±14.47                | -1.50±2.17                            | 0.8591±0.0029 | 0.6054±0.0023 | 0.619±0.001 | 0.838±0.003 | 0.003±0.002 |
| 9099.6693         | -1.93±2.13                  | -23.05±20.72               | 0.91±2.25                             | 0.8480±0.0031 | 0.6069±0.0025 | 0.616±0.001 | 0.840±0.003 | 0.003±0.002 |
| 9101.6859         | -0.34±2.63                  | -20.53±24.23               | 1.27±3.41                             | 0.8539±0.0050 | 0.6010±0.0037 | 0.616±0.002 | 0.835±0.004 | 0.004±0.004 |
| 9102.6845         | -15.14±3.71                 | 45.34±26.79                | 0.25±2.40                             | 0.8520±0.0047 | 0.6002±0.0035 | 0.616±0.002 | 0.829±0.004 | 0.004±0.004 |
| 9103.6777         | 1.44±1.84                   | 11.14±14.56                | -2.91±1.79                            | 0.8635±0.0030 | 0.6062±0.0024 | 0.619±0.001 | 0.840±0.003 | 0.003±0.002 |
| 9114.7106         | 10.09±3.26                  | -20.69±33.19               | -10.15±3.45                           | 0.8709±0.0058 | 0.6069±0.0042 | 0.618±0.002 | 0.841±0.005 | 0.005±0.004 |
| 9118.6966         | 0.46±2.46                   | 83.69±15.50                | 0.61±2.41                             | 0.8573±0.0040 | 0.6134±0.0031 | 0.617±0.002 | 0.832±0.003 | 0.003±0.003 |
| 9120.6746         | -7.34±1.95                  | 32.41±17.54                | -4.17±1.82                            | 0.8422±0.0030 | 0.6135±0.0024 | 0.617±0.001 | 0.834±0.003 | 0.003±0.002 |
| 9121.6352         | -10.46±1.90                 | -24.59±17.06               | -0.05±1.94                            | 0.8777±0.0033 | 0.6192±0.0025 | 0.618±0.001 | 0.833±0.003 | 0.003±0.003 |
| 9122.6841         | -0.98±1.82                  | 25.19±17.66                | -1.04±2.68                            | 0.8602±0.0046 | 0.6126±0.0035 | 0.617±0.002 | 0.838±0.004 | 0.004±0.003 |
| 9127.6877         | -1.46±2.61                  | -28.39±22.25               | 0.54±2.89                             | 0.8678±0.0041 | 0.6235±0.0032 | 0.616±0.002 | 0.835±0.004 | 0.004±0.003 |
| 9128.6223         | 2.87±1.83                   | -41.62±14.62               | 1.58±1.89                             | 0.8685±0.0033 | 0.6157±0.0026 | 0.617±0.001 | 0.836±0.003 | 0.003±0.003 |
| 9131.6723         | 1.86±1.81                   | -15.46±16.06               | -0.81±1.89                            | 0.8874±0.0031 | 0.6121±0.0024 | 0.616±0.001 | 0.837±0.003 | 0.003±0.002 |
| 9132.6702         | 10.82±2.8                   | 7.56±28.28                 | 4.81±3.04                             | 0.9270±0.0050 | 0.6233±0.0037 | 0.617±0.002 | 0.838±0.004 | 0.004±0.004 |
| 9138.6485         | 5.90±3.33                   | -21.62±34.82               | -10.22±4.55                           | 0.9023±0.0079 | 0.6240±0.0058 | 0.613±0.003 | 0.832±0.006 | 0.006±0.006 |
| 9139.4464         | -5.21±2.91                  | 62.16±29.17                | -9.47±3.24                            | 0.9378±0.0053 | 0.6143±0.0038 | 0.623±0.002 | 0.827±0.004 | 0.004±0.004 |
| 9139.5469         | -7.91±1.66                  | -13.62±16.14               | -3.51±2.18                            | 0.8794±0.0038 | 0.6089±0.0029 | 0.614±0.002 | 0.835±0.003 | 0.003±0.003 |
| 9139.6241         | -4.77±2.93                  | -34.23±29.98               | 2.84±3.54                             | 0.8765±0.0047 | 0.6088±0.0035 | 0.610±0.002 | 0.826±0.004 | 0.004±0.003 |
| 9139.7292         | -5.76±1.91                  | 16.39±18.42                | 20.24±3.11                            | 0.8773±0.0038 | 0.6246±0.0032 | 0.620±0.002 | 0.836±0.004 | 0.004±0.003 |
| 9140.5196         | -4.64±1.54                  | -13.22±12.95               | 0.0±1.71                              | 0.8837±0.0029 | 0.6159±0.0023 | 0.612±0.001 | 0.829±0.002 | 0.002±0.002 |
| 9140.5965         | -3.62±1.65                  | -0.46±14.53                | -6.21±1.79                            | 0.8840±0.0029 | 0.6201±0.0023 | 0.613±0.001 | 0.832±0.003 | 0.003±0.002 |
| 9140.6963         | -3.50±1.72                  | 16.93±14.90                | -4.29±1.97                            | 0.9025±0.0034 | 0.6230±0.0027 | 0.616±0.002 | 0.825±0.003 | 0.003±0.003 |
| 9141.5171         | -11.99±2.8                  | 20.14±25.05                | -8.89±2.51                            | 0.8737±0.0042 | 0.6242±0.0032 | 0.613±0.002 | 0.828±0.003 | 0.003±0.003 |
| 9141.5792         | -9.55±2.78                  | -30.48±24.65               | -7.91±2.73                            | 0.8732±0.0048 | 0.6133±0.0036 | 0.618±0.002 | 0.831±0.004 | 0.004±0.004 |
| 9141.6397         | -7.51±3.00                  | 47.54±26.84                | -7.12±2.60                            | 0.8755±0.0047 | 0.6164±0.0035 | 0.618±0.002 | 0.832±0.004 | 0.004±0.004 |
| 9141.7027         | -8.45±2.59                  | -1.09±22.58                | -9.26±2.69                            | 0.8756±0.0044 | 0.6143±0.0037 | 0.615±0.002 | 0.837±0.004 | 0.004±0.004 |
| 9142.5187         | 7.29±2.74                   | 11.59±27.32                | 0.14±3.83                             | 0.8788±0.0055 | 0.6051±0.0039 | 0.611±0.002 | 0.844±0.005 | 0.005±0.004 |
| 9146.5184         | -0.12±2.91                  | 24.29±30.27                | -9.94±3.42                            | 0.8472±0.0060 | 0.5986±0.0044 | 0.622±0.003 | 0.815±0.005 | 0.005±0.004 |
| 9146.6025         | 7.18±1.98                   | -5.05±19.81                | -2.67±3.28                            | 0.8671±0.0051 | 0.6118±0.0039 | 0.620±0.002 | 0.831±0.004 | 0.004±0.004 |
| 9147.4080         | -3.36±2.12                  | 11.37±21.39                | 12.64±3.18                            | 0.8812±0.0058 | 0.6122±0.0041 | 0.621±0.002 | 0.816±0.005 | 0.005±0.004 |
| 9147.5126         | -5.02±2.86                  | 12.22±29.49                | -3.44±3.67                            | 0.8605±0.0062 | 0.6149±0.0043 | 0.614±0.003 | 0.827±0.005 | 0.005±0.004 |
| 9149.4108         | -3.6±2.95                   | 41.15±30.27                | -2.14±3.11                            | 0.8765±0.0054 | 0.6174±0.0039 | 0.618±0.002 | 0.834±0.003 | 0.003±0.003 |
| 9149.5024         | -5.31±2.48                  | -15.23±24.06               | 7.44±3.84                             | 0.8563±0.0048 | 0.6117±0.0036 | 0.621±0.002 | 0.822±0.004 | 0.004±0.004 |
| 9149.5915         | -6.27±2.76                  | 10.11±28.16                | -1.92±3.67                            | 0.8749±0.0051 | 0.6117±0.0039 | 0.629±0.002 | 0.841±0.004 | 0.004±0.004 |
| 9149.6962         | -3.53±3.95                  | -20.06±41.52               | -38.04±5.54                           | 0.8493±0.0073 | 0.6071±0.0058 | 0.616±0.002 | 0.833±0.004 | 0.004±0.004 |
| 9150.3895         | -5.06±2.30                  | -16.21±23.57               | 3.44±2.26                             | 0.8578±0.0041 | 0.6025±0.0032 | 0.610±0.003 | 0.839±0.007 | 0.007±0.006 |
| 9151.6239         | 0.51±1.78                   | 3.03±16.67                 | -2.03±2.00                            | 0.8627±0.0033 | 0.6118±0.0026 | 0.611±0.002 | 0.830±0.004 | 0.004±0.003 |
| 9151.7309         | 10.76±1.97                  | -26.45±18.18               | -2.60±2.27                            | 0.8928±0.0040 | 0.6265±0.0032 | 0.617±0.001 | 0.830±0.003 | 0.003±0.003 |
| 9152.4645         | 7.73±1.74                   | -10.62±16.92               | 1.94±1.92                             | 0.8654±0.0029 | 0.6183±0.0023 | 0.619±0.002 | 0.837±0.004 | 0.004±0.003 |
| 9153.3820         | 9.91±2.40                   | -26.93±23.87               | 10.93±2.72                            | 0.8557±0.0037 | 0.6090±0.0029 | 0.617±0.001 | 0.832±0.003 | 0.003±0.002 |
| 9153.4717         | 9.87±2.05                   | -13.32±18.68               | 20.78±1.97                            | 0.9707±0.0032 | 0.6261±0.0024 | 0.616±0.002 | 0.833±0.003 | 0.003±0.003 |
| 9154.4992         | 4.88±1.76                   | 5.60±17.37                 | 8.33±1.60                             | 0.8606±0.0029 | 0.6142±0.0023 | 0.618±0.001 | 0.838±0.003 | 0.003±0.002 |
| 9154.6201         | 7.08±1.73                   | 7.89±16.85                 | 11.88±2.64                            | 0.8660±0.0034 | 0.6192±0.0028 | 0.614±0.001 | 0.83±0.003  | 0.003±0.002 |
| 9156.4518         | 1.17±1.60                   | -10.93±14.04               | 1.14±2.04                             | 0.8961±0.0038 | 0.6187±0.0030 | 0.617±0.002 | 0.833±0.003 | 0.003±0.003 |
| 9156.5853         | 3.51±1.61                   | 8.04±14.35                 | 3.97±1.66                             | 0.8785±0.0027 | 0.6094±0.0022 | 0.615±0.002 | 0.822±0.003 | 0.003±0.003 |
| 9161.3599         | 8.37±3.26                   | -29.20±35.50               | -47.90±7.13                           | 0.8561±0.0067 | 0.6055±0.0047 | 0.615±0.001 | 0.833±0.002 | 0.002±0.002 |
| 9161.4505         | 9.47±3.97                   | 34.02±42.22                | -12.87±4.06                           | 0.8620±0.0076 | 0.6142±0.0055 | ....        | ....        | ....        |
| 9161.5732         | 0.63±1.63                   | 13.21±15.68                | -5.77±2.58                            | 0.8814±0.0042 | 0.6113±0.0032 | ....        | ....        | ....        |
| 9161.6724         | -4.24±2.18                  | -25.79±21.32               | -8.84±2.16                            | 0.8623±0.0039 | 0.6153±0.0032 | ....        | ....        | ....        |
| 9163.3774         | 5.92±2.99                   | -42.62±31.26               | -8.72±3.81                            | 0.9328±0.0069 | 0.6167±0.0049 | ....        | ....        | ....        |
| 9163.4992         | -1.73±3.03                  | -76.62±29.37               | -14.60±3.82                           | 0.8851±0.0062 | 0.6183±0.0045 | ....        | ....        | ....        |

**Table 3.8:** RV measurements and spectroscopic activity indicators for TOI-1685 from CARMENES VIS spectra.



# 4

## Gliese 617 an M-dwarf binary system in TESS Continuous View Zone

---

*“Measure what can be measured, and make measurable what cannot be measured.”*

*by Galileo Galilei*

---

This chapter summarizes my analysis in the TESS Continuous View Zone (CVZ) using CARMENES spectroscopic and TESS photometry data for the binary system Gliese 617. Additionally, in this chapter I included a comprehensive guide in how to remove instrumental systematics from TESS data while keeping intrinsic stellar variability.

Gliese 617 A was previously studied by [Reiners et al. \(2018a\)](#) who discovered a low-mass planet which is located inside of the temperate habitable zone of its host star. Here I re-analyzed, the previous data incorporating new CARMENES radial velocities.

For Gliese 617 A and Gliese 617 B, I have done the scientific work, analysis, and discussion. I was under the supervision of Prof. Andreas Quirrenbach with collaboration with Víctor Bejar. The stellar parameters were computed by Vera Passegger, Andreas Schweitzer, and Carlos Cifuentes.

### 4.1 Gliese 617 system

GJ 617 is a binary system located at  $\sim 35.11$  [ly] (EDR3; [Gaia Collaboration et al., 2020](#)). A projected separation of 1.07 [arcmin], or  $\sim 690$  [AU] ([Lépine & Bongiorno, 2007](#)) separate the two components of the system.

**GJ 617 A** (HD 147379) is the brightest star in the system ( $V = 8.6$  [mag];  $J = 5.8$  [mag]), and is cataloged as a M0.0 V star ([Alonso-Floriano et al., 2015](#)). The star has a mass of  $M_{A\star} = 0.628 \pm 0.025 M_{\odot}$ , a radius of  $R_{A\star} = 0.62 R_{\odot}$  equilibrium temperature off  $T_{\text{eff},A} = 4090$ [K]. In 2017, [Reiners et al. \(2018a\)](#) discovered a low-mass planet at  $\sim 86.5$  days. The planet was found by analyzing the generalized Lomb-Scargle periodograms (GLS; [Zechmeister & Kürster, 2009b](#)) of the combined spectroscopic data from CARMENES and HIRES/Keck spectrographs. The planet has a minimum mas of  $M_p = 24.7^{+1.8}_{-2.0} M_{\oplus}$ , which is

$\sim 1.5$  times the mass of Neptune and is located inside of the temperate habitable zone of its host star.

Additionally, from the CARMENES data and following (Reiners et al., 2018b) the authors detected a marginal Doppler broadening caused by stellar rotation, with  $v \sin i = 2.7 \text{ [km s}^{-1}\text{]}$ . The value of  $v \sin i$  would indicate a high magnetic activity, that could be interpreted as a short rotational period. As we discussed in the stellar activity section (Sec. 1.4.1), a high magnetic activity can be induce additional signals in the radial-velocity curve and even can mimic a planetary signal.

As additional information, Pepper (2018) published a pre-print with the analysis for the photometric observations on GJ 617A taken by KELT. The authors through a GLS analysis searched for periodicities in the KELT light curve finding a strong peak about of  $\sim 22$  days, which would be related to the rotational period of the star.

The companion **GJ 617 B**, currently known as EW Dra, is cataloged as a M3.0 V star, is the fainter companion of the system ( $V = 10.6 \text{ [mag]}$ ;  $J = 6.9 \text{ [mag]}$ ). The star has a mass of  $M_{B\star} = 0.483 \pm 0.0216 M_{\odot}$ , a radius of  $R_{B\star} = 0.47 R_{\odot}$ , and a equilibrium temperature off  $T_{\text{eff},B} = 3488 \text{ [K]}$ . In this case, no known exoplanets have been currently discovered.

### 4.1.1 New available CARMENES and TESS data

Gliese 617 system was observed in 12 of the 13 TESS sectors of the northern continuous viewing zone (CVZ) during the second year of the TESS mission (July 2019-July 2020). The CVZ covers a 12 degree circle around the north ecliptic pole, which will overlaps with the continuous viewing zone of the next JWST (Gardner et al., 2009).

Due to Gliese 617 system has a photometric time coverage of about 324 days, and more than 100 radial velocities measurements were taken with CARMENES between 2016 to 2021, this large amount of data, will provide a unique opportunity to search additional exoplanets, analyzing long orbital period baselines, and also investigate the rotational period for both stars.

## 4.2 Preliminary photometric analysis – How to work with TESS data?

Within the second year of the primary mission (Cycle 2), TESS imaged 13 individual sectors in the northern hemisphere, where each sector was observed for two orbits with a total of 27.4 days. The mission provides photometric data at two different cadences (2 and 30 minutes). While the entire CCDs, also known as full-frame images (**FFIs**) was taken every 30-minute cadence data, and are available for all TESS targets, the 2-minute cadence data, are known as the Target Pixel file (**TPFs**), are available for and only a subset of targets an even smaller number of targets taken every 30 minutes. After Cycle 2, FFIs will be taken with a cadence of 10 minutes, and the TPF every 20 seconds. All the mentioned data are available online and can be downloaded through the Mikulski Archive for Space Telescope (MAST) portal.

To create a TESS light curves (**LC**) from a TPF, an optimal aperture is selected as a set of pixels around a selected star, the pixels are stored as arrays, where flux collected is

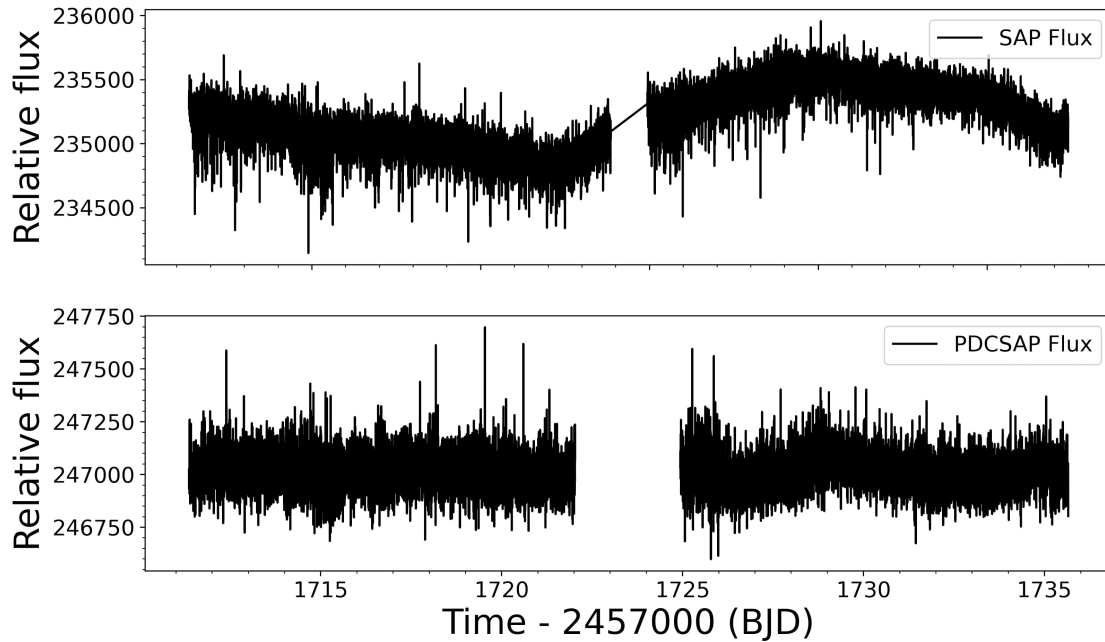


**Figure 4.1:** Upper and lower panels shows SAP and PDCSAP light curves for GJ 617 A from sector 15 taken by *TESS* mission.

summed creating the raw flux (**SAP**) which combined with the time, the raw light curves are created. For these files the background subtraction is already included, and most of the common instrumental systematics are preserved.

Due to *TESS* is an exoplanet finding mission, TPFs also provides, the corrected light curves or Pre-search Data Conditioning SAP flux (**PDCSAP**). In this case the PDCSAP is subject to more treatment than the raw light curve and is derived using the information from the simple aperture photometry (SAP) plus the Co-trending Basis Vectors (**CBVs**), which will be explained in the next Sec. 4.2.2. Here the most of the systematics has been removed by keeping planetary transits (if there are) intact.

In order to better isolate transits and eclipses, the PDCSAP data show a somewhat lower scatter level than SAP data. As direct consequence, PDCSAP often removes astrophysical features and long term trends from the data. So using the PDCSAP light curve would be not the optimal option for to search stellar rotational periods. A comparison between SAP and PDCSAP light curves for GJ 617 A from sector 15, are shown in upper and bottom panel of Fig. 4.1, respectively.

To explore the variability of the stars we used the SAP light curves. However, important systematic needs be considered. *TESS* orbits the Earth in half the time it takes the Moons to orbit once. During this 13.7 days period the telescope is mostly observing the sky, and as it approaches Earth, *TESS* rotates and transmits all the accumulated data. During this time, the telescope is subject to background variations mostly from reflected sunlight causing a periodic contamination which is difficult to remove. These creates artificial trends in the

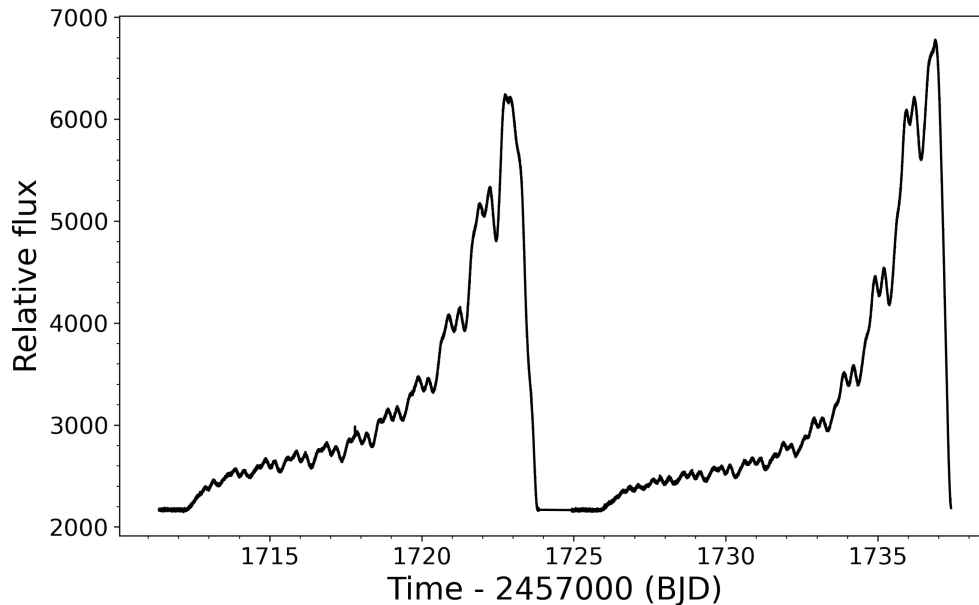


**Figure 4.2:** Background variation of *TESS* Sector 15

data that must be carefully removed. As a direct result, some studies have found unreliable measuring rotational periods shorter than about 13 days (see, e.g., Howard et al., 2021; Clayton et al., 2021, and references therein). Figure 4.2 shows the typical photometric background variations for the individual *TESS* sectors.

Additional systematics such as the focus changes, spacecraft pointing jitter, long-term pointing drifts (due to differential velocity aberration), and other stochastic errors can also introduce trends in the data. Finally, and due to the *TESS* pixels are large (21 arcsec), is important to consider that the photometry for many targets will be contaminated by nearby objects.

### 4.2.1 Creating a Design Matrix

*TESS* FFI cutouts do not have aperture masks created by the pipeline. Instead, users must make their own apertures, sum the flux contained in pixels inside the aperture as a function of time, and select a background region to subtract the possible contamination due to scattered light. To select the aperture and subtract the background a few tools are available e.g. `eleanor`<sup>38</sup> (Feinstein et al., 2019) and `tesseract`<sup>39</sup>, both tools are specifically made for extract light curves from FFIs.

To select the background region, `eleanor` and `tesseract` uses the pixels outside the aperture as vectors that are highly predictive of the systematic noise, i.e. making the assumption that these pixels do not contain any flux from our target, and are mostly dominated by background stars and instrumental noise. Thus, to remove these sources of noise, a **Design Matrix**

<sup>38</sup><https://adina.feinste.in/eleanor/>

<sup>39</sup><https://github.com/astrofelipe/tesseract>

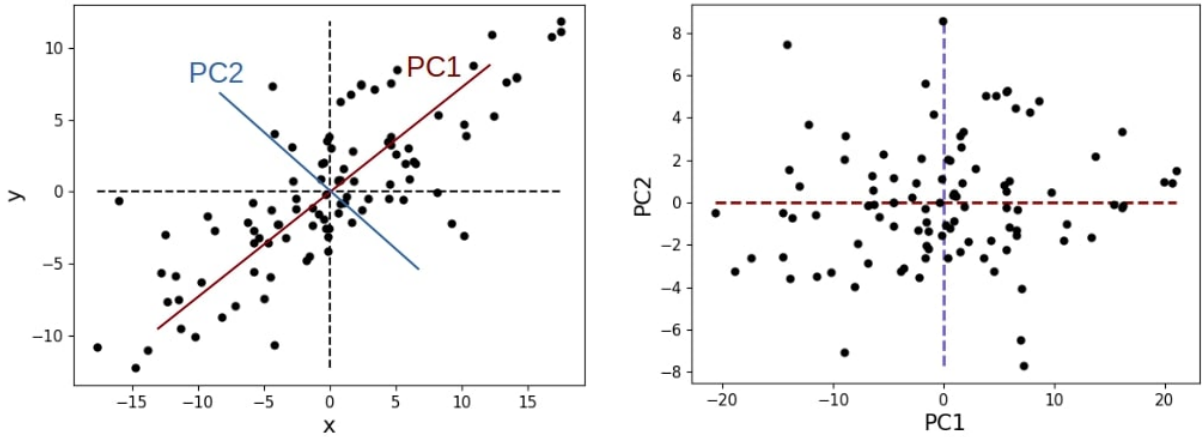


**Figure 4.3:** Principal component analysis (PCA) for a given dataset. Left: Show the PC1, and PC2 axis. The first one corresponds to the principal direction along the samples shows the largest variation and the PC2 corresponds to the second direction. Right: show the corresponding Design Matrix on which the dimensionality has been reduced from two-dimensional data to a single dimension by projecting each sample onto the first principal component.

(DM) is created by applying a principal component analysis (PCA), to the flux of the pixels outside the selected aperture.

The Principal Component Analysis (PCA) is a method of decomposing data into uncorrelated components by identifying correlated variables. This is achieved by transforming the initial variables into a new small set of variables without losing the most important information in the original data set. This new set of variables, are uncorrelated, and are ordered so that the first few retain most of the variation present in all of the original variables. In a few words, the central idea of the PCA is to reduce the dimensionality of data that contains a large set of variables.

To make it simple, for a certain data-set as is shown in Fig. 4.3, the black filled circles represented the data in the X-Y coordinate system, where the dimension reduction is achieved by identifying the principal directions, called principal components, in which the data varies. The PCA assumes that the directions with the largest variances are the most “important” (i.e, the most principal).

In the left panel of Fig. 4.3, the PC1 axis, marked with a red line, is the first principal direction along which the samples show the largest variation. While the second most important direction, marked in blue, corresponds to the PC2 axis which is orthogonal to the PC1 axis. By identifying the main components it is possible to construct a projection matrix or a DM. These new variables, allow us to reduce the dimensionality for the two-dimensional data to a single dimension by projecting each sample onto the first principal component as is shown in the left panel of Fig. 4.3.

For our purposes, we can remove the background and other systematic trends from the raw light curves, by creating a light curve Design Matrix, using as predictive vectors, the pixels outside from the aperture (Pixel-DM, hereafter).

As we mentioned, in contrast to the FFI, a few TPF observed by 30-minute cadence

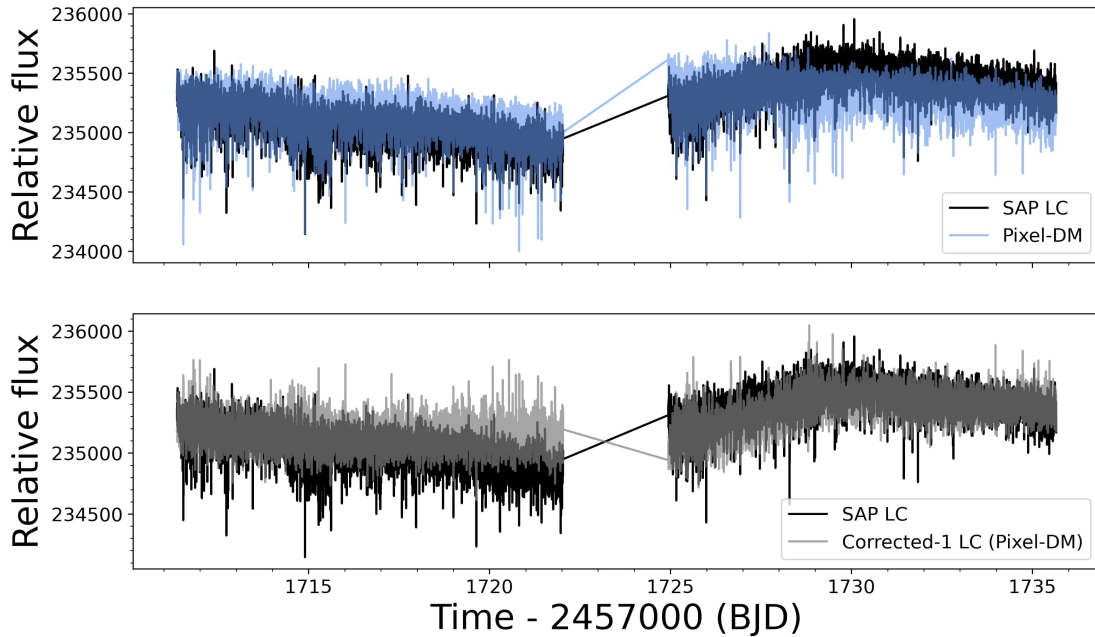


**Figure 4.4:** Top panel shows the SAP light curve of GJ 617 A (black), and the Pixel-DM light curve is over-plotted (blue). Lower panel shows, the corrected light curve (gray) and the SAP light curve in black as reference.

contains a light curve derived using simple aperture photometry. However, there are still common trends in the SAP light curves are not due to scattered light, but could be from, for example, spacecraft motion. In this case, instead of directly using the SAP light curve, we use the information contained in the Pixel-DM to remove these common trends, similarly to the FFI. Here the aperture selection is a straight-forward step due to the aperture is created by SPOC pipeline (default apertures are not available for FFI).

Also, the TESS pipeline populates a series of quality flags<sup>40</sup> to indicate when a cadence may have been taken during an anomalous event. These flags are available in the TESS light curves, TPFs, and a subset are available for the FFIs. In order to consider the “good” data points we only used the flags without events (quality=0).

Figure 4.4 shows an example of how much can vary the final light curve applying the pixel-DM method to the TPF. The top panel shows the SAP light curve of GJ 617 A (black), and the pixel-DM light curve is over-plotted (blue). The lower panel shows, the corrected light curve (gray) and the SAP light curve in black as reference.

To calculate if the corrected light curve has improved, we can estimate the noise level using the Combined Differential Photometric Precision (CDPP) metric (Jenkins et al., 2010). This metric characterizes the noise in a light curve as the scatter that remains after all long term trends have been removed. For the SAP light curve the  $CDPP-SAP \sim 126$  ppm, and for the corrected light curve is  $CDPP-CORR1 \sim 103$  ppm. As the corrected light curve has a lower CDPP, it means that this light curve is less noisy.

<sup>40</sup><https://outerspace.stsci.edu/display/TESS/2.0+-+Data+Product+Overview>

## 4.2.2 Cotrending Basis Vectors (CBVs)

Cotrending Basis Vectors (CBVs) are generated in the PDC component of the TESS products. They are built from the most common systematic trends found in each TESS sector, and are used to account for systematic present in the light curves. The CBVs are ranked by order of the relative amplitude or their contribution in the systematic trends across the CCD. This characterization, is stored as a maximum of 16 best fit vectors, and they can be accessed through the `lightkurve` package.

An important decision to take is how many CBVs to use, in order to optimize the reduction of the SAP data. Fitting just a few CBVs will capture instrumental artifacts less effectively. However, using too many can over-fit the data, removing real astrophysical features. A further consideration is that no basis vector is perfect, so the inclusion of each additional CBV to the fit adds a noise component to the data. The choice of CBV number is a balance between maximizing the removal of systematics, and minimizing the removal of real astrophysics components.

**There are three basic types of CBVs:**

1. **Single-Scale:** Contains all systematic trends combined in a single set of basis vectors. This type of CBVs is better at preserving longer period signals. A total of 16 Single-Scale CBVs are available per sector.
2. **Multi-Scale:** Contains systematic trends in specific wavelet-based band passes. There are usually three sets of multi-scale basis vectors in three bands. In this case, Multi-Scale is optimal for periods close to transiting planet duration. A total of 8 Multi-Scale CBVs are available per sector for each band.
3. **Spike:** Contains only short impulsive spike systematics. A total of 6 Spike CBVs are available per sector.

An example of the first 8 Single Scale, and 6 Spike CVBs vectors for the star GJ617A (TIC - 230073581) is shown in the top and bottom panels of Fig. 4.5, respectively. Due to the first 8 CBVs contains most of the systematics, the *TESS* pipeline uses them by default. The latter CBVs pose a greater risk of injecting additional noise, rather than removing systematics.

## 4.2.3 Optimizing the fit

For *TESS* time series, we can optimize the data reduction using both, the Pixel-DM, and a selected group of CBVs. In this case, we include the information provided by the CBVs to that encoded in the Design Matrix (Pixel\_CBV-DM, hereafter), in order to account for both set of signals simultaneously.

However, when we fit a model to a data set, there exists the possibility of over-fitting or under-fitting the data. While in the case of over-fitting, the model has too many degrees of freedom, and the fit is forced to adjust all possible variations in the data. Furthermore, over-fitting can also introduce broad-band noise to the data, as the vectors used to remove systematic trends have their own level of noise. Consequently, over-fitting can remove important intrinsic signals, such as stellar variability instead of non-physical systematics, or dilute astrophysical signals due to the addition of noise.

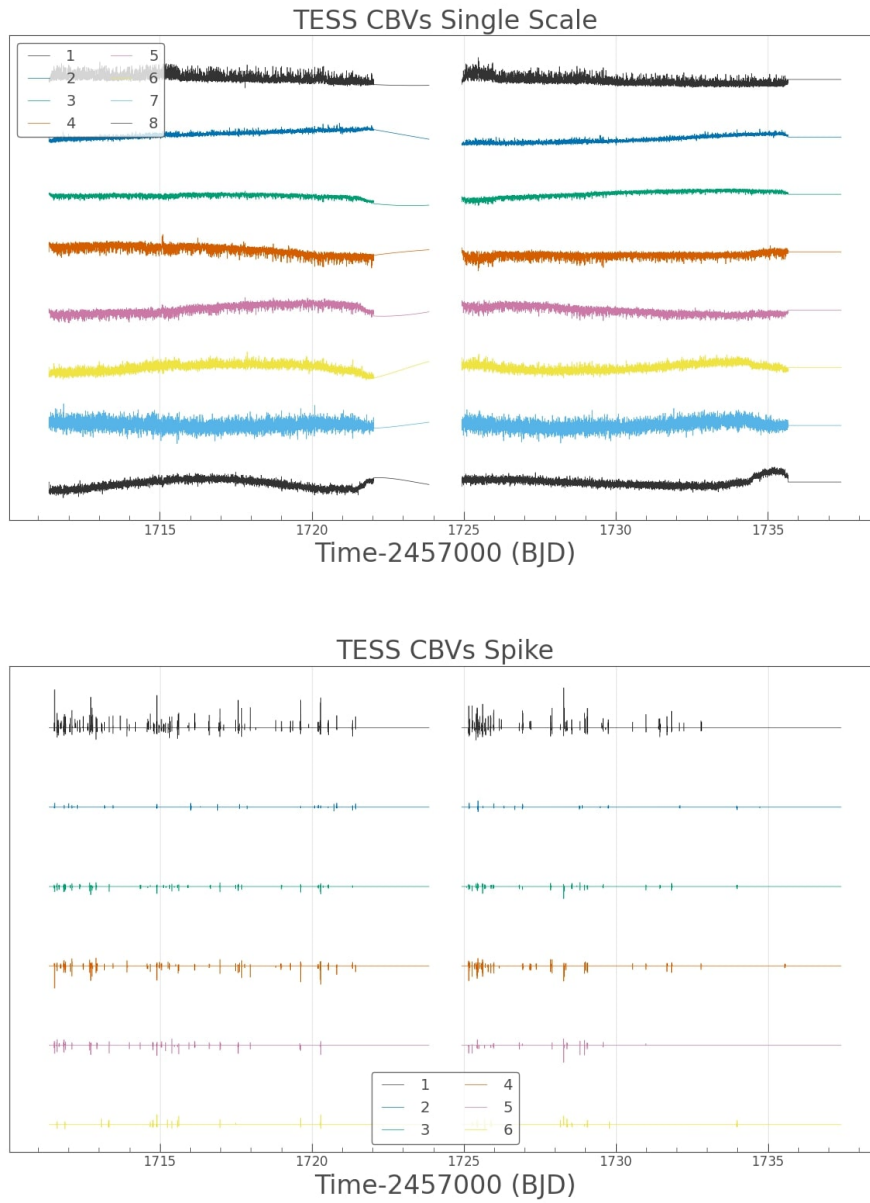


**Figure 4.5:** (8 first Single Scale CBVs, and the 6 Spike CBVs of the star GJ617 A, are shown in top and bottom panels, respectively.

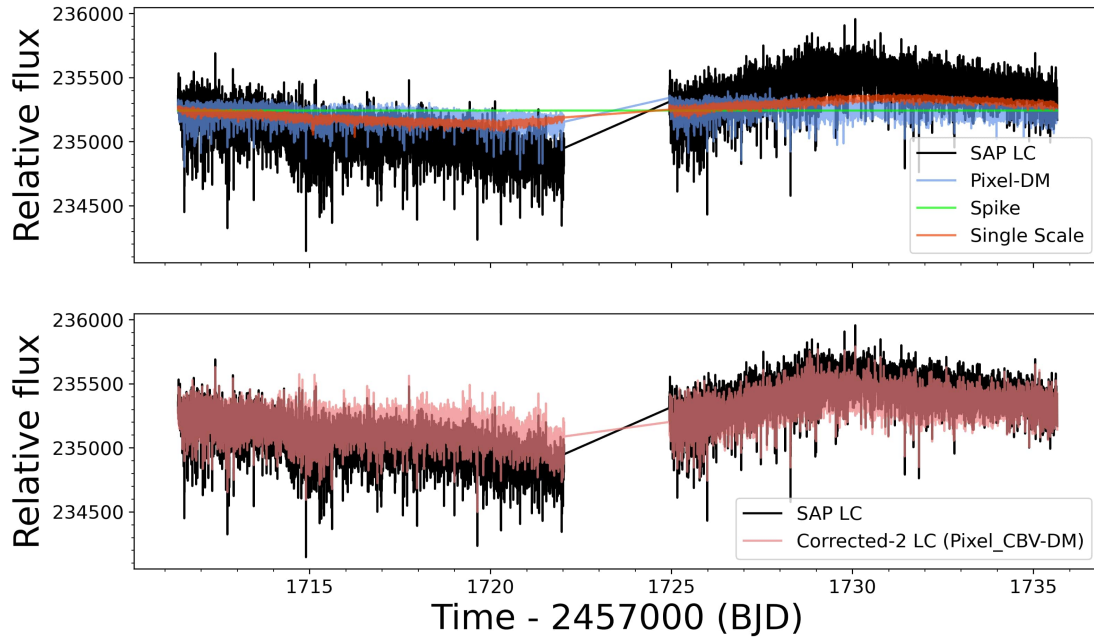


**Figure 4.6:** Top panel shows the SAP light curve of GJ 617 A (black), where Pixel-DM (blue), Single Scale (orange), and the Spike are over-plotted (green). Lower panel shows, the corrected light curve by using a regularization  $\alpha$  (pink) and the SAP light curve in black as reference

Under-fitting occurs when the model has too few degrees of freedom and fails to adequately describe the physical process it is attempting to model, resulting in systematic trends on the residuals.

To find a balance between these two regimes, we can add a regularization factor ( $\alpha$ ) to fine-tune the reduction. This factor favors models in which the contribution of different components is smooth, and the strength of this additional constraint is parametrized by  $\alpha$ . Higher  $\alpha$  values lead to a more homogeneous choice of the available components and vice-versa. Thus, low  $\alpha$  values can lead to an over-fitting regime, whereas high  $\alpha$  values can cause an under-fitting of the data.

The optimal reduction is shown in the lower panel of Fig. 4.6, we can notice that the combination of the Pixel-DM plus CBV, with a regularization term, removes the thermal settling systematic, while the stellar variability is preserved.

We can scan the over-fit and under-fit **goodness metrics** as a function of the regularization term,  $\alpha$ . The over-fit metric measures the introduced noise in the light curve after the correction, where the under-fitting metric measures the mean residual target to target Pearson correlation between the target under study and a selection of neighboring targets. The latter metric is calibrated such that a value of 0.95 means the residual correlations in the target are equivalent to chance correlations of white gaussian noise.

Usually, a goodness metric of 0.8 or above is generally considered good. However, the goodness metrics are not perfect and need to be used only as a guideline to assess the

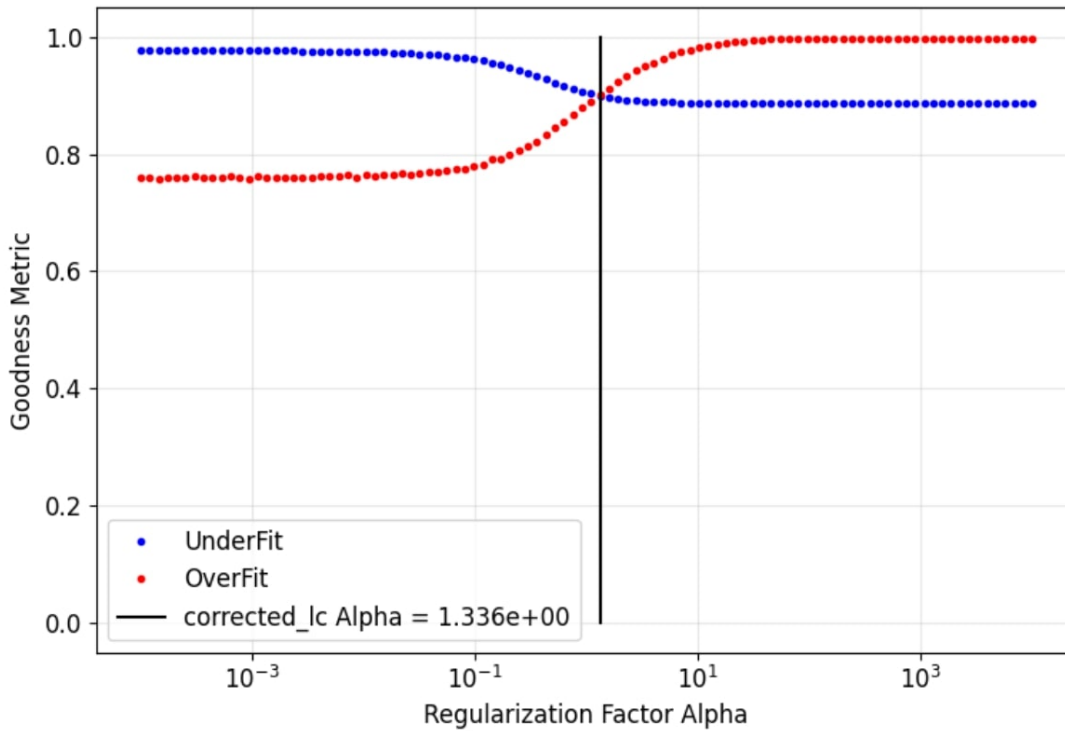


**Figure 4.7:** Goodness Metrics

quality of the final light curve. Figure 4.7 shows the goodness metrics for the fit performed in Fig. 4.6

Comparing the CDPP metric value for the regularized modeling (considering both, Pixel-DM and CBV vectors) of  $\text{CDPP-CORR2} \sim 92$  ppm with the CDPP value obtained for the unregularized one of  $\text{CORR1} \sim 106$  ppm, indicate that the regularized model is less noisy. However, we need to keep in mind that the stars studied during this chapter are observed by several TESS sectors, so using a single  $\alpha$  value to balance under- and over-fitting metrics is not possible since  $\alpha$  varies from one sector to another. Consequently, using a varying regularization term for each TESS sector can introduce additional systematics in the final reduction light curve adding more difficulties for further analysis.

Finally, as can be seen in Fig. 4.8, the addition of the information provided by the CBV vectors does not produce significant differences in the reduction of the data. This is not surprising, as the instrumental trends described by the CBV vectors are likely captured as well by the flux of the pixels outside the aperture used to build the Design Matrix. Therefore, we adopt the Pixel-DM reduction as our fiducial methodology for the further analysis presented in this chapter. This has the additional advantage of reducing the number of parameters in our model, which is desirable to avoid over-fitting our data since we do not include a regularization parameter.

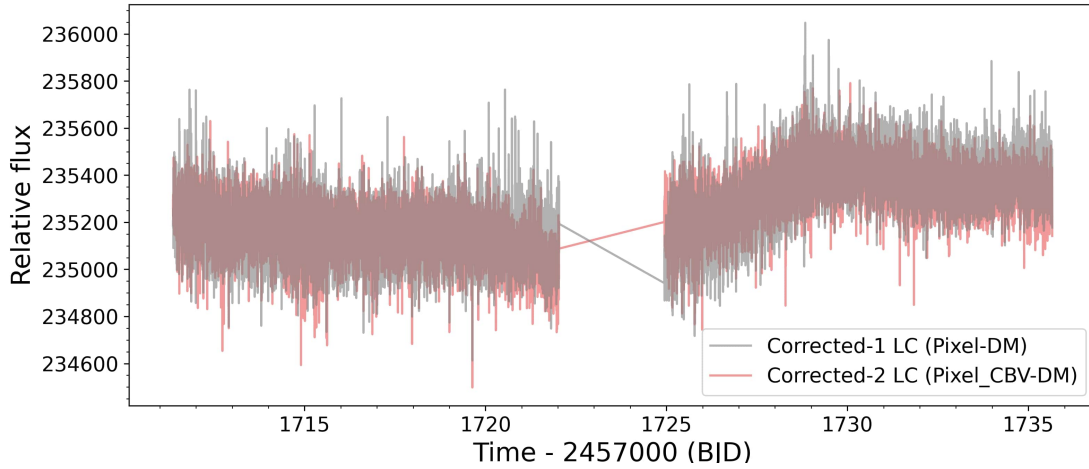


**Figure 4.8:** Comparison between corrected light curve Pixel\_CBV-DM by using a regularization  $\alpha$  (pink) and light curve corrected by Pixel-DM (gray)

### 4.3 Photometric analysis of GJ 617 A

GJ 617 A (TIC-230073581) was observed at 2 min short-cadence integrations during almost all cycle 2 of the northern continuous viewing zone of *TESS* mission (Sectors 14 to 26) only in Sector 22, the target was not observed. To search for a possible transiting exoplanet, we first downloaded the photometric light curve, corrected for systematics (PDC; Smith et al., 2012), from the Mikulski Archive for Space Telescopes (MAST) using the lightkurve<sup>41</sup> package (Lightkurve Collaboration et al., 2018). The data are shown in the top panel of Fig. 4.9. We performed a period search using the Box-Fitting Least Squares (BLS; Kovács et al., 2002) and the Transit Least Squares (TLS; Hippke & Heller, 2019) algorithms. However, we did not detect any interesting signal that could be related to a transiting planet on GJ 617 A.

As next step, we proceeded to download the TESS target pixel files (TPF). In order to exclude the presence of contaminants close to our target, we verified if the sources in the selection aperture in the each of TPFs did not significantly contaminate the flux of GJ 617 A. Figure 4.10 shows the TPFs for the sectors in which GJ 617 A was observed. The TPFs were generated with tpfplotter<sup>42</sup> (Aller et al., 2020). Within the TPFs apertures, we found two extra sources *Gaia* DR2 1642642884107003648, and *Gaia* DR2 1642641475357729920, which are separated 40.30 arcsec, and 48.09 arcsec from GJ 617 A, respectively, and both sources are 9.7 mag fainter. The binary companion GJ 617 B is also visible in the TPFs, it is 1.70 mag fainter than their companion, and their separation is  $\sim 65$  arcsec. We placed limits on the dilution factor of  $D = 0.998 \sim 1$  for GJ 617 A by following the Eq. 2 described in Espinoza et al. (2019). We fixed this value for the next model analysis.

<sup>41</sup><https://github.com/lightkurve/lightkurve>

<sup>42</sup><https://github.com/jlillo/tpfplotter>

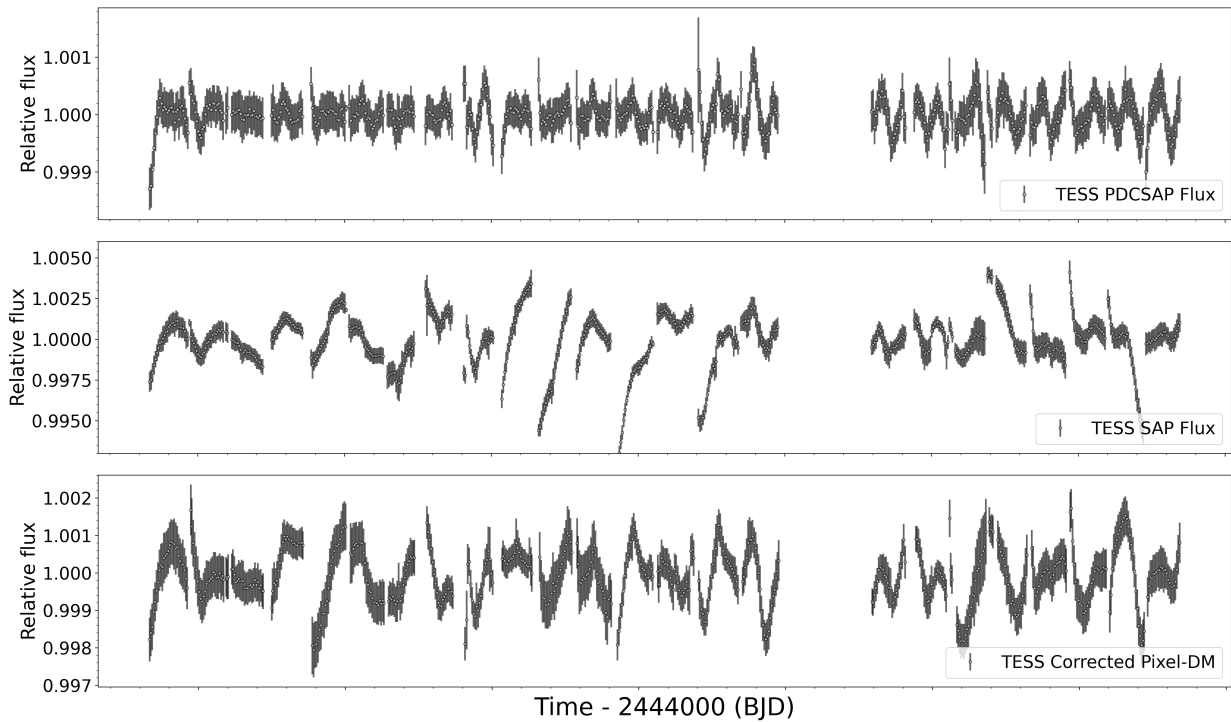


**Figure 4.9:** GJ 617 A *TESS* light curve for sectors between 14–26 (gray), sector 22 was not observed. *Top panel:* shows the PDCSAP light curve. *Middle panel:* shows the SAP light curve. *Bottom panel:* shows our corrected light curve (Pixel-DM). All light curves were binned to 0.5 d.

### 4.3.1 Stellar rotational period from TESS data

To determine the photometric rotational period of GJ 617 A, we carried out different analyses of the available photometric data. We decided to download the TPFs and corrected for systematic as was described in Sec. 4.2. We use the information contained in the Pixel-DM to remove common trends, and to create our final corrected light curve. For that, we used only the “good” data e.i., data without reported events during the acquisition times (for details see Sec. 4.2.1).

Figure 4.9 shows a comparison between the PDCSAP, SAP, and our corrected light curve (Pixel-DM). For visualization, the three light curves were binned to 0.5 d. Here is easy to notice that the PDCSAP light curve (Top panel) shows a lower scattering level than the SAP light curve (middle panel), which is dominated by numerous systematic trends. However, neither the PDCSAP light curve nor the SAP one are suitable for variability searching because in the case of the PDCSAP most of the astrophysical features are removed, and for the SAP the drastic trends between sectors complicate the correct extraction of any information related to the stellar rotation period. In the case of our corrected light curve (bottom panel), most of the systematic trends have been taken out with the care to preserve the astrophysical features.

To search for periodicities in our binned corrected *TESS* light curve, we employed the traditional GLS periodogram analysis (Zechmeister & Kürster, 2009a). The resulting GLS,

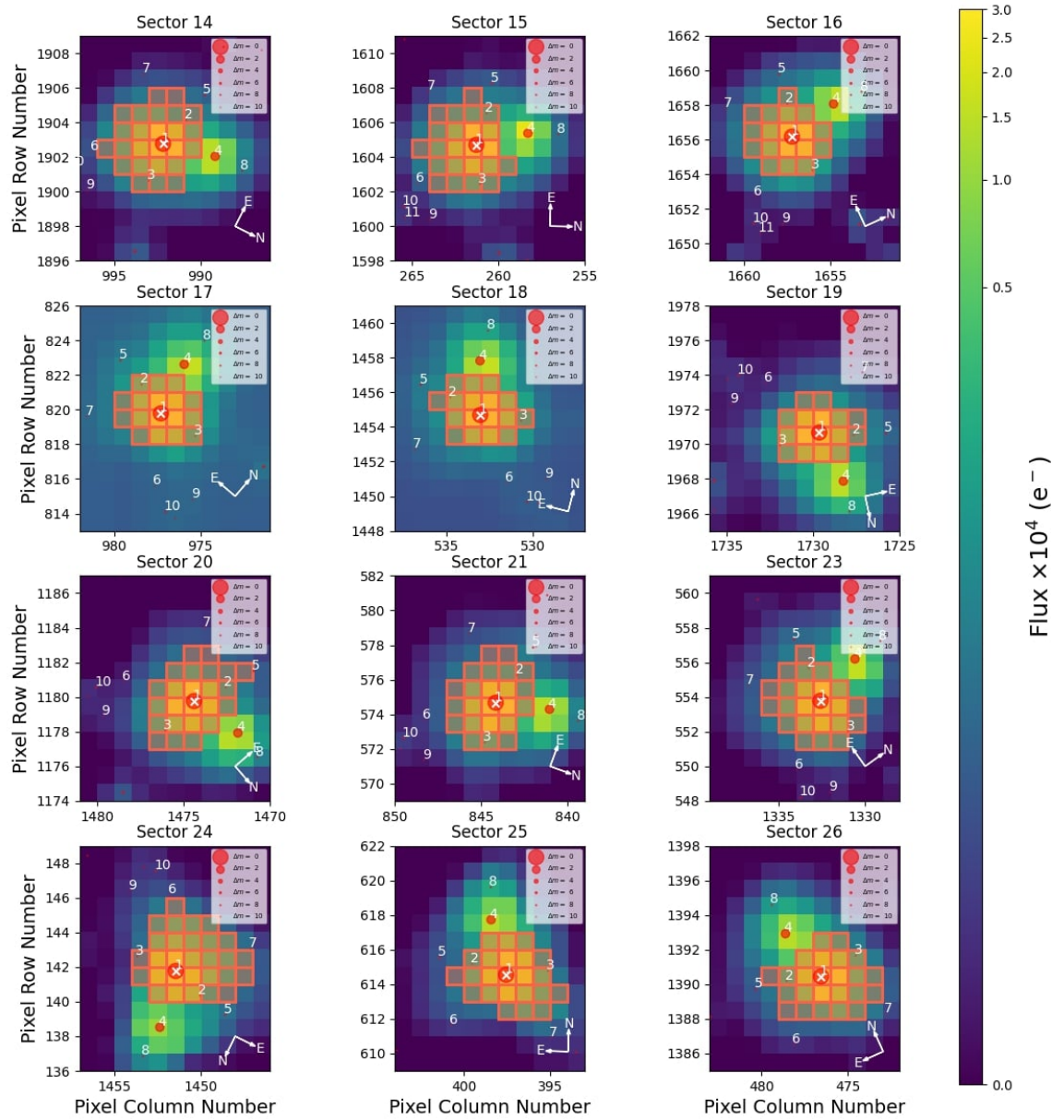


**Figure 4.10:** TPF for GJ 617 A for sectors 14, 15, 16, 17, 18, 19, 20, 21, 23, 24, 25, and 26. The corrected light curve was computed using the flux counts coming in the pixels mask (red). The red circles represent neighboring sources listed in Gaia DR2, where the size corresponds to the brightness difference with respect to GJ 617 A (circle 1 marked with an ×)

shown in Fig. 4.11, which reveals that highest peak is found at  $\sim 23.6$  d with a FAP  $< 0.1\%$ . Next, we used a more sophisticated model and fit the corrected light curve with a GP. In this case, we selected the double SHO (dSHO) to model the stellar rotational period, which is the sum of two stochastically driven, damped harmonic oscillator (SHO) terms. We decided to use this kernel due to their flexibility, and its computational speed, which allow us to model two active longitudes at the same time, so makes them suitable for accounting for the effects of rotating spots on the data and therefore a better way to model the stellar activity (e.g., see [Kossakowski et al., 2021](#), and references therein).

The power spectrum of each SHO term was given by [Anderson et al. \(1990\)](#) and follows the form:

$$\text{SHO}_1(\omega_{\text{GP}}) = \sqrt{\frac{2}{\pi}} \frac{S_0 \omega_1^4}{(\omega_{\text{GP}}^2 - \omega_1^2)^2 + \omega_1^2 \omega_{\text{GP}}^2 / Q_1^2} \quad (4.1a)$$

and,

$$\text{SHO}_2(\omega_{\text{GP}}) = \sqrt{\frac{2}{\pi}} \frac{S_0 \omega_2^4}{(\omega_{\text{GP}}^2 - \omega_2^2)^2 + \omega_2^2 \omega_{\text{GP}}^2 / Q_2^2} \quad (4.1b)$$

for which we applied the reparametrization using the hyperparameters,

$$Q_1 = 0.5 + Q_0 + \delta Q, \quad \omega_1 = \frac{4\pi Q_1}{P_{\text{rot}} \sqrt{4Q_1^2 - 1}}, \quad S_1 = \frac{\sigma_{\text{GP}}^2}{(1+f)\omega_1 Q_1} \quad (4.1c)$$

$$Q_2 = 0.5 + Q_0, \quad \omega_2 = 2\omega_1 = \frac{8\pi Q_1}{P_{\text{rot}} \sqrt{4Q_1^2 - 1}}, \quad S_2 = \frac{f\sigma_{\text{GP}}^2}{(1+f)\omega_2 Q_2} \quad (4.1d)$$

where  $\sigma_{\text{GP}}$  is the amplitude of the GP,  $P_{\text{rot}}$  is the primary period of the variability,  $Q_0$  is the quality factor for the secondary oscillation,  $\delta Q$  is the difference between the quality factors, and  $f$  represents the fractional amplitude of the secondary oscillation with respect to the primary one.

For our modeling we used `juliet`, we considered wide uninformative priors for  $\sigma_{\text{GP}}$  (log-uniform between  $1e-4$  to  $1e6$ ),  $Q_0$  and  $\delta Q$  (both with a log-uniform between  $1.0$  to  $1000$ ),  $f$  (uniform between  $0.1$  to  $1.0$ ), and  $P_{\text{rot(GP-dSHO, phot)}}$  (uniform between  $1$  d and  $100$  d). The binned *TESS* light curve and the resulting GP fit is shown in orange in Fig. 4.12. In this case, the rotational period from the dSHO-GP analysis was found to be  $P_{\text{rot(GP-dSHO, phot)}} = 21.17^{+0.86}_{-0.78}$ . The obtained posterior probabilities are presented in Fig. 4.13.

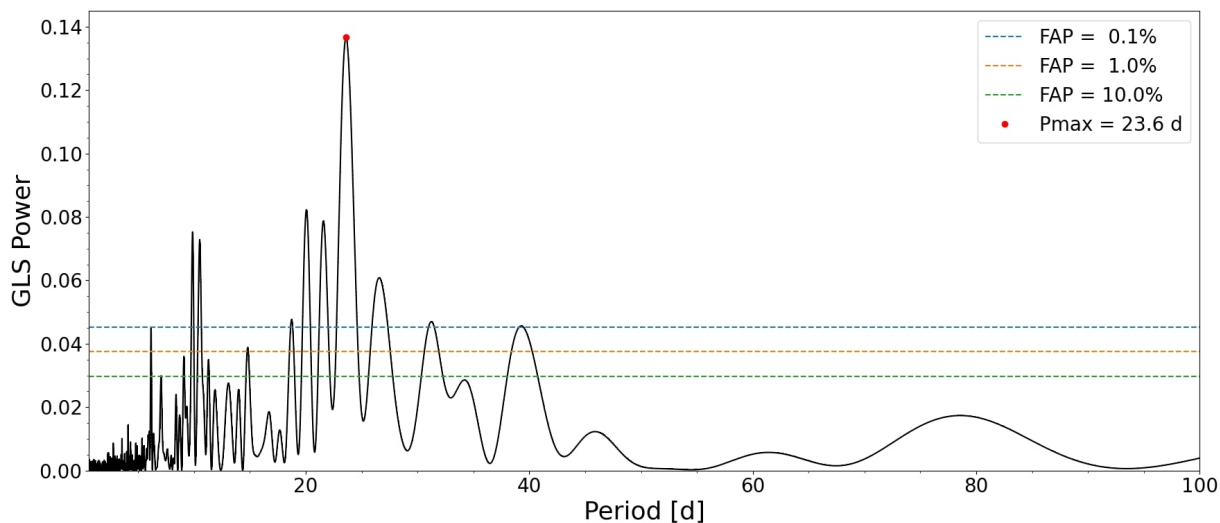


**Figure 4.11:** *TESS* photometric GLS periodogram of GJ 617 A. The highest GLS periodicity was found at  $\sim 23$  d and is marked with a red dot. The horizontal lines mark the theoretical FAP levels of 0.1% (dotted blue), 1% (dotted orange), and 10% (dotted green). The highest peak at  $\sim 23.6$  d, is related to the rotational period.

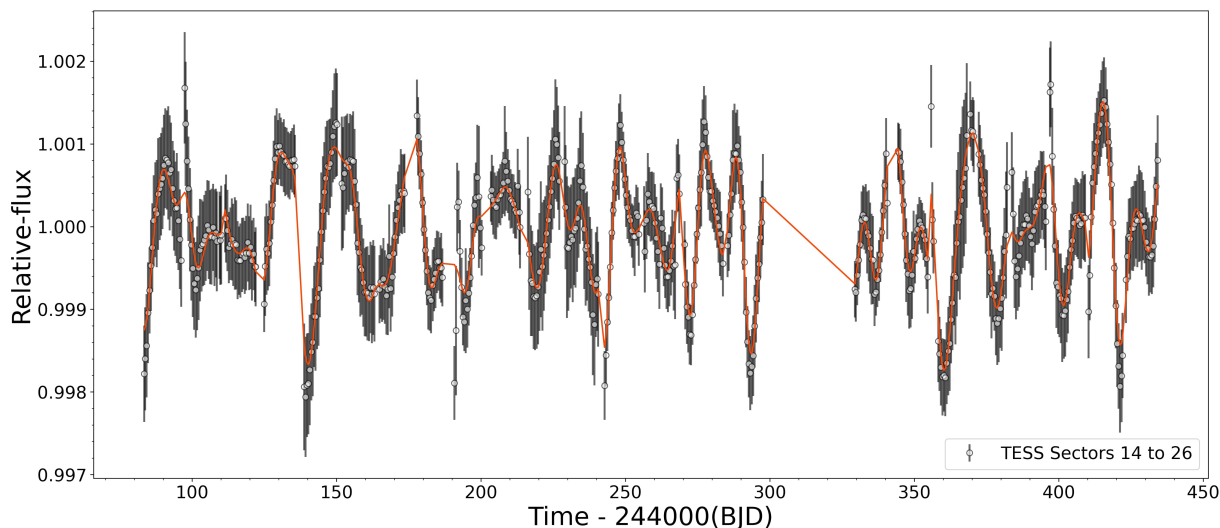


**Figure 4.12:** Binned *TESS* light curve (black) for sectors between 14–26, sector 22 was not observed. The the best *juliet* dSHO-GP fit is shown with a solid orange curve.

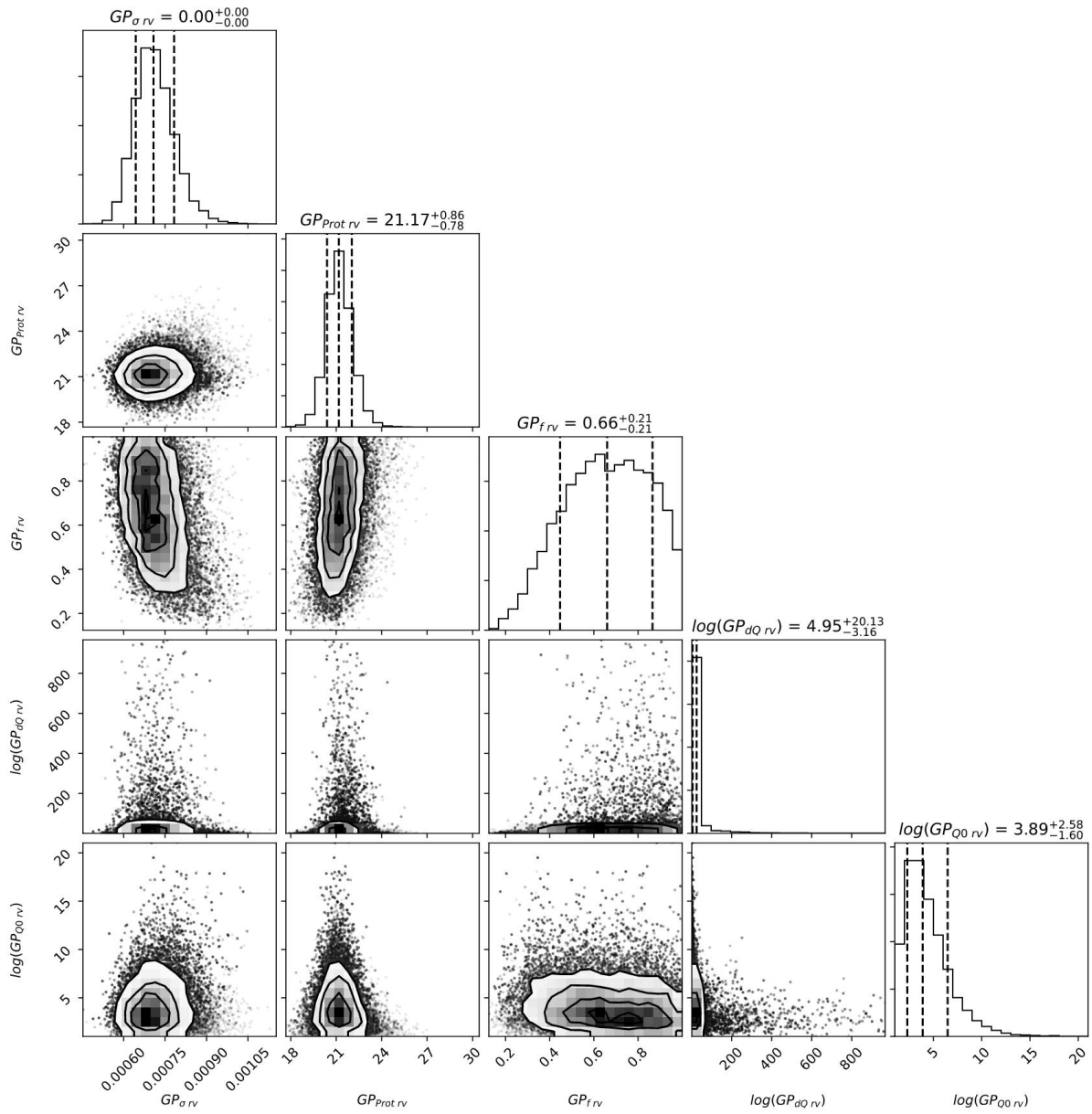


**Figure 4.13:** Posterior distribution for the dSHO GP model parameter derived with *juliet*.

## 4.4 Spectroscopic analysis of GJ 617 A

As was mentioned in Sec. 4.1, In 2017, the CARMENES radial velocities observations of GJ617A revealed a  $24.7 M_{\oplus}$  planet in the temperate zone around this early-M star. At that time, the authors were collected 114 RVs covering a span of time of about two years. However, CARMENES we have continued the observations of GJ617A, collecting a total of 186 RVs covering a total span of time of more than four years. In this section, we have re-reduced the previous data, re-determined the activity indices, and re-analyzed all the available RVs.

### 4.4.1 Radial velocity exploration and modeling

We searched for periodic signals in the all the available CARMENES data, by computing a generalized Lomb-Scargle periodogram (GLS; Zechmeister & Kürster, 2009a). We initially employed the `Exo-Striker`<sup>43</sup> (Trifonov, 2019) tool to identify potential combinations of the signals present in the data. We used this information to select the priors for the RV-only modeling. To model the RV data, we used `juliet`<sup>44</sup> (Espinoza et al., 2019), a python fitting package for modeling transits and RV that uses nested samplers to explore the prior volume in order to efficiently compute the Bayesian model log evidence,  $\ln \mathcal{Z}$ .

For model comparison, we followed the general rule described in Trotta (2008), that if  $\Delta \ln \mathcal{Z} \lesssim 2.5$ , then the two models are indistinguishable and neither is preferred so the simpler model would then be chosen.

Figure 4.14 shows a sequence of GLS periodograms from the RV data after subtracting an increasing the number of signals. The signal corresponding to the planet reported by Reiners et al. (2018a) was significantly detected in the RVs at  $\sim 86.8$  d with a false alarm probability (FAP)  $< 0.1\%$ ; (panel a), additional signals at periods around one year  $\sim 365$  d and a set of peaks around  $\sim 21$  d are also visible in the periodogram.

To justify if the origin of the forest of signals around  $\sim 21$  d would be related to the stellar rotation period, we searched for additional information in activity indicators that `serval` provides (Zechmeister et al., 2018). Figure 4.15 shows the GLS periodograms of the CRX, dLW,  $H_{\alpha}$ , NaD, Ca II-IRT triplet, and TiO bands at 7050Å, 8430Å, and 8860Å. Notably, the chromospheric indicators  $H_{\alpha}$  index, Ca II-IRT triplet and the photospheric titanium oxide band at 7050Å have the tendency to show a set of similar periods around  $\sim 20$ -23 d (orange region) which all of them reaches or exceeds the power of 1% FAP suggesting that this forest of signals could be related to stellar activity being in good agreement with the  $P_{\text{rot(phot)}}$  found in the photometric analysis. Thus, we can attribute it to the range where would be the true stellar rotation period (see Lafarga et al., 2021, for details).

For the RV modeling, we started fitting the RVs with a “flat” model where we assumed there is no planetary signal present in the radial-velocity data. Our second model explores the RVs by fitting the data with a “one-Keplerian-signal” (1 Kep). For this fit, we using uniform priors between 80 d and 90 d. After removing the planetary signal at  $\sim 86$  d, the power for the peak around  $\sim 21$  d remains, and its harmonic at 10.5 d shows up reaching a

---

<sup>43</sup><https://github.com/3fon3fonov/exostriker>

<sup>44</sup><https://juliet.readthedocs.io/en/latest/>

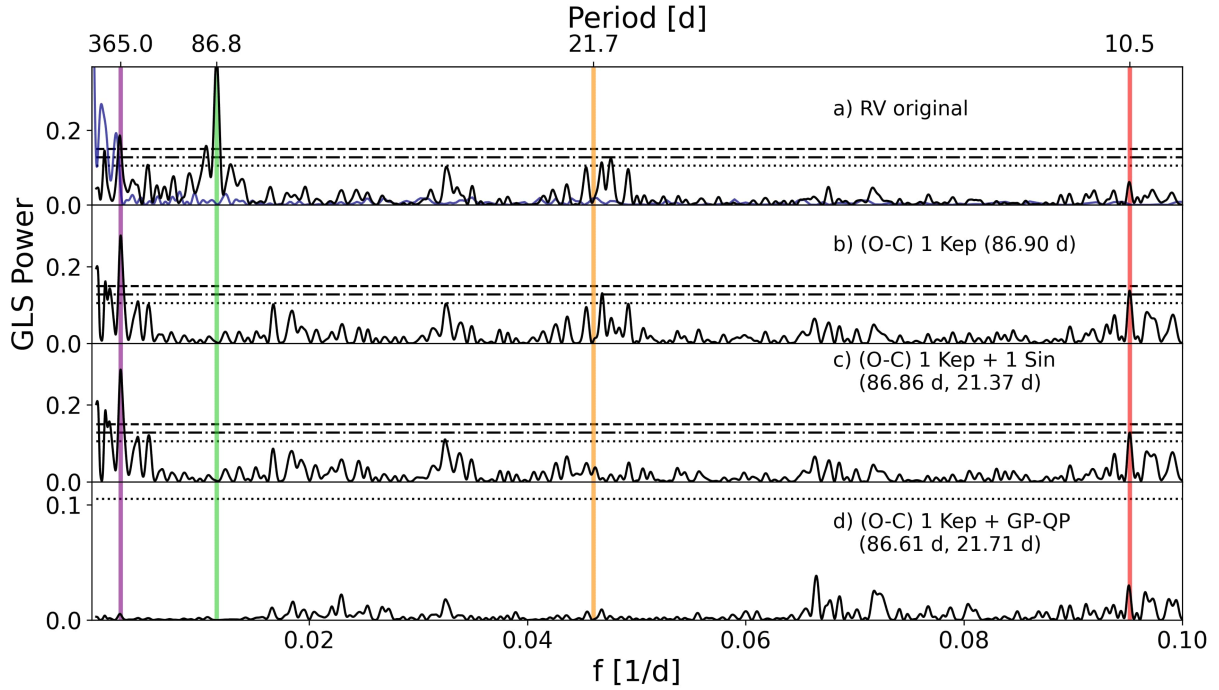


**Figure 4.14:** GLS periodograms of the RV data and the residuals after subtracting different models for GJ 617 A. The vertical solid green, and purple lines corresponds to the planet ( $\sim 86$  d), and the one year alias, respectively. The vertical orange and red lines corresponds to the rotational period picked up in the RVs ( $\sim 21.7$  d), and approximately  $P_{\text{rot}}/2$ , respectively. Panel (a): Original RVs with the window function of the data set (blue). Panel (b): Residuals after subtracting the planet signal at  $\sim 86$  d. Panel (c): Residuals after subtracting a simultaneous model fit of two signals at  $\sim 86$  d and  $\sim 21$  d. Panel (d): Residuals after subtracting a simultaneous model fit of the planet signal and a QP-GP. The horizontal lines mark the theoretical FAP levels of 0.1 % (dashed), 1 % (dash-dotted), and 10 % (dotted).

FAP  $\sim 1$  % (panel b). Hence, we decided to investigate if including two signals could improve the fit. We considered a “one-Keplerian plus one-sinusoidal-signal” (1 Kep + 1 Sin) one for the planet found at  $\sim 86$  d and the second for the signal around  $\sim 21$  d. Also, we investigated whether including a GP to the “one-Keplerian” model (1 Kep + GP-QP) would improve the log-evidence of the fit.

For the GP, we selected the so-called quasi-periodic (QP) kernel, which has the following form:

$$k(\tau) = \sigma_{GP}^2 \exp\left(-\alpha_{GP}\tau^2 - \Gamma \sin^2(\pi\tau P_{\text{rot}})\right) \quad , \quad (4.2)$$

where  $\tau$  is the time lag in days,  $\sigma_{GP}$  is the amplitude of the GP given in  $\text{ms}^{-1}$ ,  $\Gamma$  is the amplitude of the GP sine-squared component,  $\alpha$  is the square of the inverse length scale of the exponential component of the GP given in  $\text{d}^{-2}$ , and  $P_{\text{rot}}$  is the period of the GP-QP component given in days. We set uniform priors for  $\sigma_{GP}$ , and  $P_{\text{rot}}$ , with lower and upper limits of  $(0,10) \text{ ms}^{-1}$ , and  $(18, 28) \text{ d}$ , respectively. For  $\alpha$ , and  $\Gamma$  we used Jeffreys priors between  $(10^{-8}, 1) \text{ d}^{-2}$ , and  $(0.01, 10)$ , respectively. We set this priors based on the experiments performed with this kernel in [Stock et al. \(2020b\)](#) and [Stock et al. \(2020b\)](#) (for

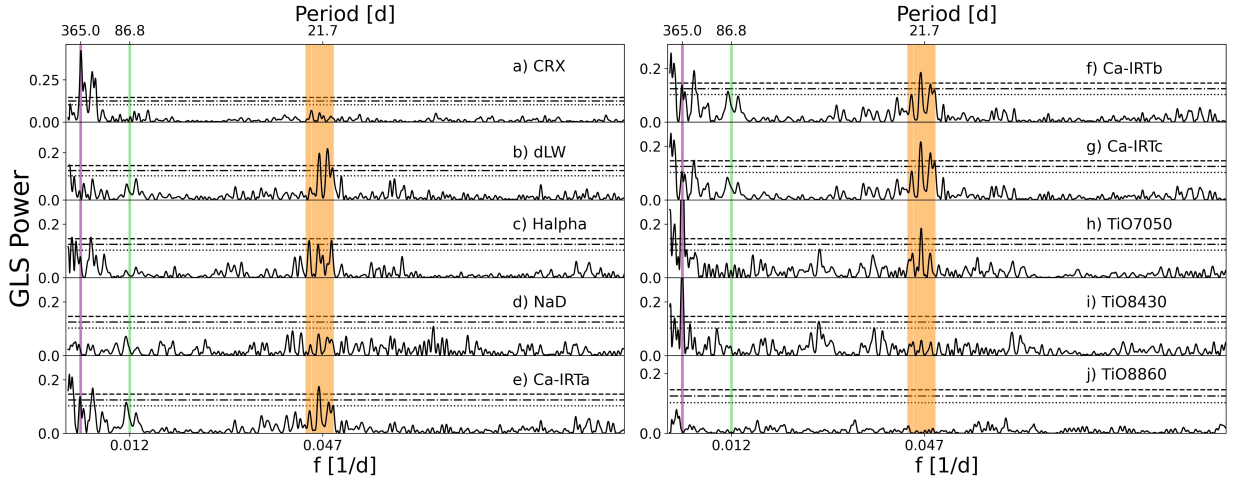


**Figure 4.15:** GLS periodograms of set of activity indicators (a–j) CRX, dLW,  $H_{\alpha}$ , nad, Ca II-IRT triplet (a, b, c), and TiO activity indices at  $7050\text{\AA}$ ,  $8430\text{\AA}$ , and  $8860\text{\AA}$ . In all panels the vertical lines indicate the periods of  $\sim 86$  d (green, planet),  $\sim 20$ – $23$  d (orange band related to the  $P_{\text{rot}}$ ), and the year alias at  $365$  d (purple). The horizontal lines mark the theoretical FAP levels of  $0.1\%$  (dashed),  $1\%$  (dash-dotted), and  $10\%$  (dotted).

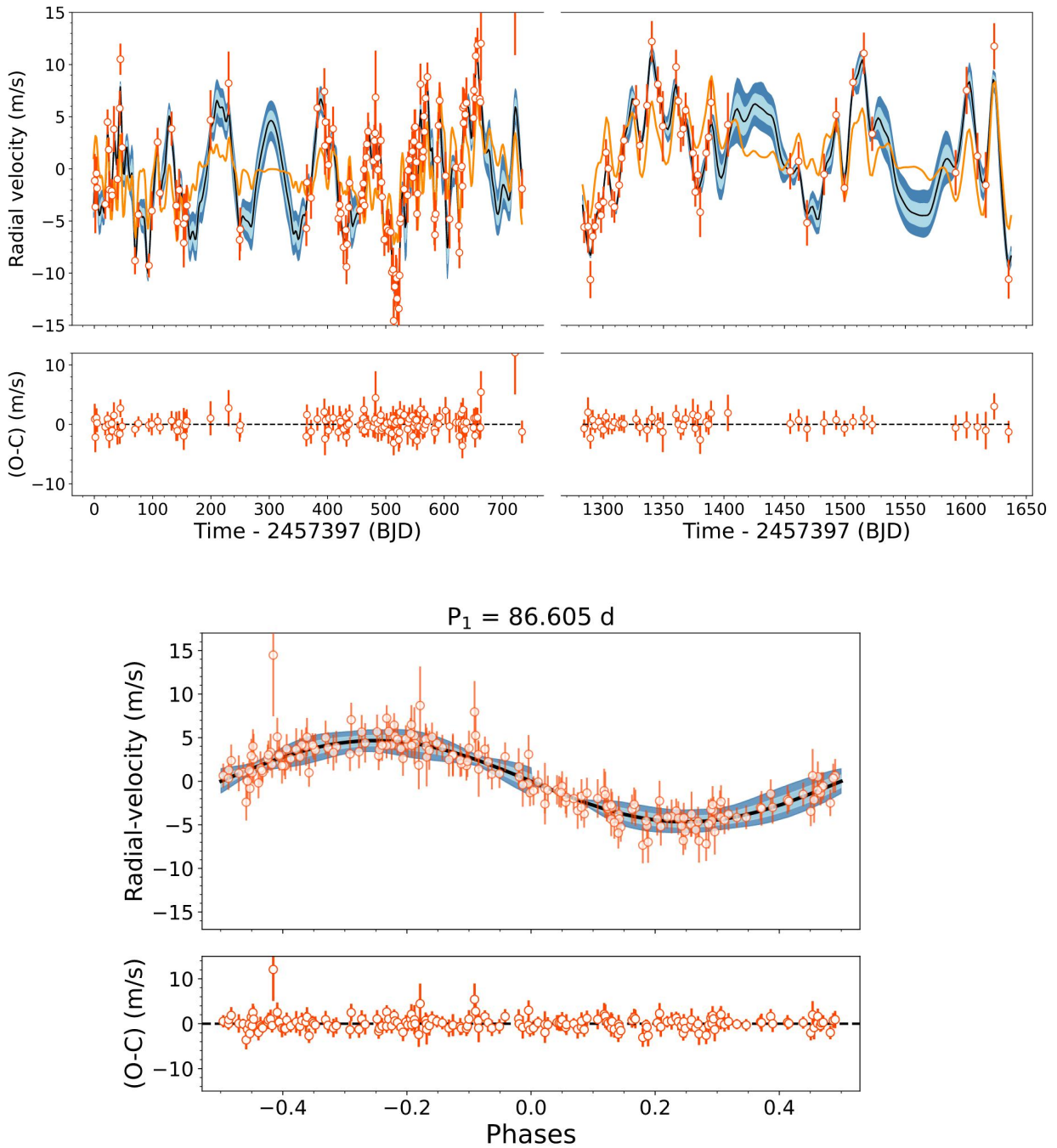
| Models                     | Periods             | $\ln \mathcal{Z}$                     | $ \Delta \ln \mathcal{Z} $ |
|----------------------------|---------------------|---------------------------------------|----------------------------|
| flat                       | ...                 | $-590.974 \pm 0.081$                  | 0.0                        |
| QP-GP                      | 21.20               | $-511.294 \pm 0.0536$                 | 79.68                      |
| 1 Kep                      | 86.90               | $-549.507 \pm 0.30$                   | 41.46                      |
| 1 Sin + 1 Kep              | 21.37, 86.86        | $-547.520 \pm 0.335$                  | 43.45                      |
| 2 Sin + 1 Kep              | 10.51, 21.96, 86.86 | $-546.026 \pm 0.467$                  | 44.95                      |
| <b>1 Kep + GP-QP</b>       | <b>86.61, 21.71</b> | <b><math>-498.435 \pm 0.04</math></b> | <b>92.54</b>               |
| 1 Kep <sub>e</sub> + GP-QP | 86.84, 21.62        | $-497.323 \pm 0.086$                  | 93.65                      |

**Table 4.1:** Bayesian log-evidence for the different models used for the RV data. In the model names, “Kep” corresponds a keplerian orbit, “Sin” corresponds a sinusoidal signal, “GP-QP” to the quasi periodic GP kernel, and “e” refers to an model on which an eccentric orbit was used. The model selected for the final was the 1 Kep ( $86.61$  d) + GP-QP, indicated by the bold-faced row.

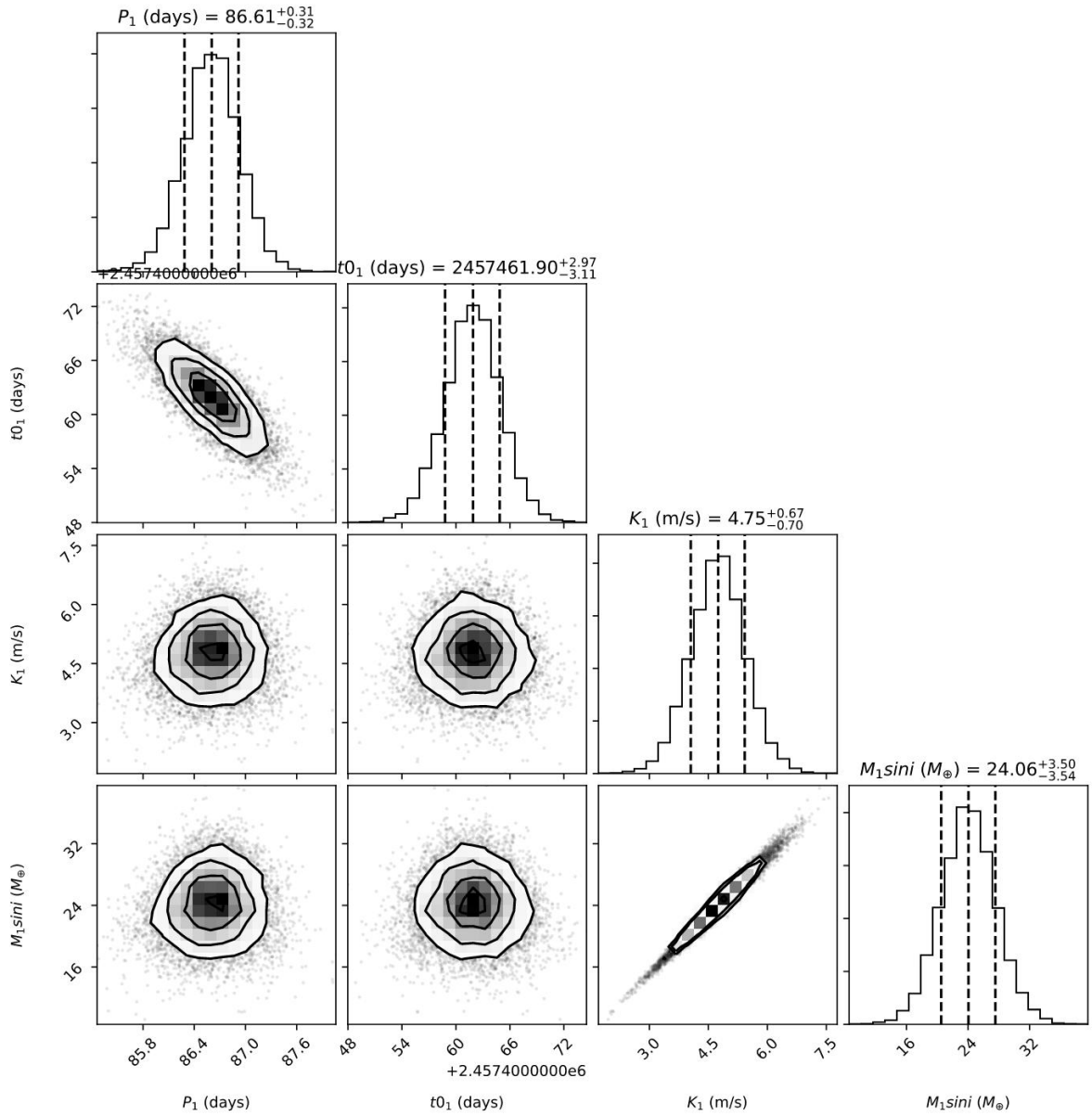
more details about this kernel see Chapter 2 and Chapter 3).

Table ?? shows an overview of the different models whit their corresponding Bayesian evidence. From the RV model comparison, the best-fit model, judged by their log-evidence ( $|\Delta \ln \mathcal{Z}| \approx 93$ ), was a one-Keplerian signal model plus a QP-GP (1 Kep + GP-QP). The selected priors and posteriors for our fit are presented in Table 4.2. The resulting RV model are presented in Fig. 4.16. The obtained posterior probabilities for the planet and QP-GP are presented in Fig. 4.17 and Fig. 4.18, respectively.

To assess the coherence of the significant RV signals, we used the Stacked-Bayesian GLS periodogram (s-BGLS; Mortier et al., 2015) with the normalization of Mortier & Collier Cameron (2017). We show the resulting s-BGLS diagram in left panel of Fig. 4.19. We



**Figure 4.16:** CARMENES RV data for GJ617 A with the best-fit model from the RV fit overplotted (black), and the GP-QP component (orange). Top panel: RV time series. The blue and light-blue band represents the 68% and 98% credibility intervals, respectively. Bottom panel: RVs phase-folded to the periods of the planet (left). Top and bottom panels shows the residuals after the model is subtracted.



**Figure 4.17:** Posterior distribution for the RV model parameters (1 Kep + QP-GP) derived with juliet

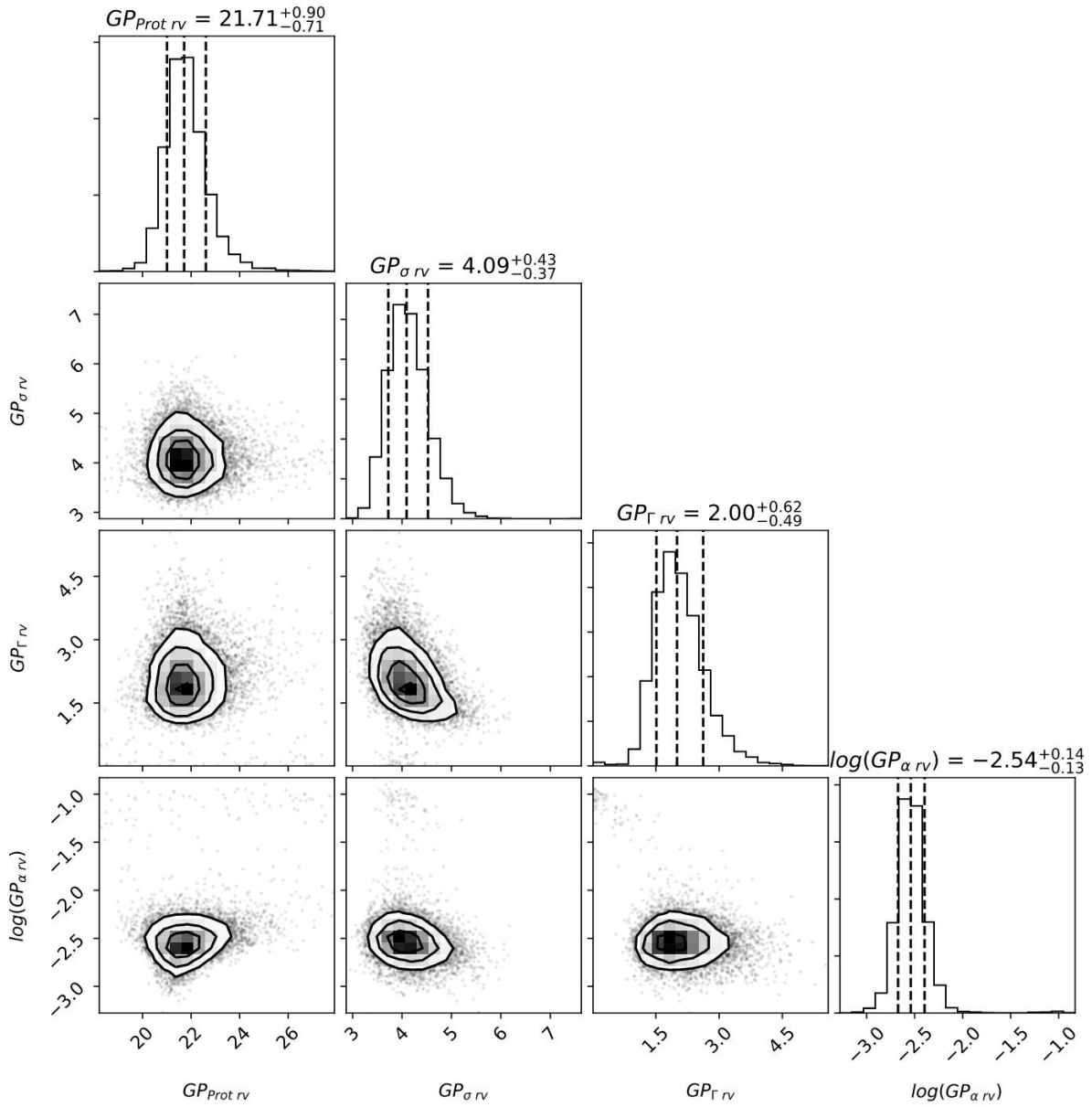


**Figure 4.18:** Posterior distribution for the QP-GP RV model parameters (1 Kep + QP-GP) derived with juliet of GJ 617 A

| Parameter                                         | Prior                       | Posterior                    | Description                           |
|---------------------------------------------------|-----------------------------|------------------------------|---------------------------------------|
| <i>Planet parameters GJ 617 A b</i>               |                             |                              |                                       |
| $P$ (d)                                           | $\mathcal{U}(80.0, 90.0)$   | $86.605^{+0.314}_{-0.319}$   | Period of planet b                    |
| $K_b$ (m s <sup>-1</sup> )                        | $\mathcal{U}(0, 10)$        | $4.749^{+0.674}_{-0.697}$    | RV semi-amplitude of planet b         |
| $e_b$                                             | 0.0 (fixed)                 | ...                          | Orbital eccentricity of planet b      |
| $\omega_b$ (deg)                                  | 90.0 (fixed)                | ...                          | Periastron angle of planet b          |
| $M_p \sin i$ ( $M_\oplus$ )                       | ...                         | $24.056^{+3.498}_{-3.545}$   | Derived mass of planet b              |
| <i>RV parameters</i>                              |                             |                              |                                       |
| $\gamma_{\text{CARMENES}}$ (m s <sup>-1</sup> )   | $\mathcal{U}(-10, 10)$      | $0.196^{+0.681}_{-0.661}$    | RV zero point for CARMENES            |
| $\sigma_{\text{CARMENES}}$ (m s <sup>-1</sup> )   | $\mathcal{LU}(0.01, 10)$    | $0.07^{+0.254}_{-0.055}$     | Extra jitter term for CARMENES        |
| <i>GP hyperparameters</i>                         |                             |                              |                                       |
| $\sigma_{(\text{QP-GP,RV})}$ (m s <sup>-1</sup> ) | $\mathcal{U}(0.0, 10)$      | $4.092^{+0.434}_{-0.369}$    | Amp. of GP component                  |
| $\alpha_{(\text{QP-GP,RV})}$ (d <sup>-2</sup> )   | $\mathcal{J}(10^{-8}, 100)$ | $0.0029^{+0.0011}_{-0.0008}$ | Inv.length-scale of GP exp. component |
| $\Gamma_{(\text{QP-GP,RV})}$                      | $\mathcal{J}(0.01, 10)$     | $2.001^{+0.6212}_{-0.4871}$  | Amp. of GP sine-squared component     |
| $P_{\text{rot}(\text{QP-GP,RV})}$ (d)             | $\mathcal{U}(18, 28)$       | $21.71^{+0.90}_{-0.71}$      | Period of the GP-QP component         |

**Table 4.2:** Prior and Posterior parameters of the `juliet` RV fit for GJ 617 A b. Error bars denote the 68 % posterior credibility intervals. The prior labels of  $\mathcal{N}$ ,  $\mathcal{U}$ ,  $\mathcal{J}$ , and  $\mathcal{LU}$  represent normal, uniform, and Jeffreys distributions, respectively, where  $\mathcal{N}(\mu, \sigma^2)$  is a normal distribution of the mean  $\mu$  and variance  $\sigma^2$  and  $\mathcal{U}(a, b)$ ,  $\mathcal{J}(a, b)$ , and  $\mathcal{LU}(a, b)$  are uniform, and Jeffreys is a log-uniform distribution between  $a$  and  $b$

identified that neither the signals around 10.5 d nor the forest of signals between 20–23 d were stable over the observational time baseline. These results together with the analysis of the activity indicators means that these signals would be related with the stellar rotation.

Additionally, we performed a GP  $\alpha$ -period diagram, colored by likelihood (right panel of Fig. 4.19). Trough this diagram, we can infer that a rotational period close to 21.7 d is preferred towards lower values of  $\log \alpha_{\text{GP}}$ . This is consistent with a periodic signal present over the entire time of observations and also with the stellar rotation period found through photometric data.

As a further investigation, we decided to compare our RV modeling results changing the QP-GP for a dSHO-GP kernel. We used a wide prior for the dSHO-GP period between 1.0–150, for  $\sigma_{\text{GP}}$  we used a uniform between 0–10, for  $f$  a uniform between 0.1–1.0, and for  $Q_0$  and  $\delta Q$  we used a log-uniform between 1.0–10<sup>5</sup> and 1.0–100, respectively. In this case, the planet was found at period  $86.71 \pm 0.3$  d and the resulting  $P_{\text{rot}(\text{GP-dSHO,RV})}$  period was  $26.05^{+4.65}_{-2.45}$  d being consistent inside of  $1\sigma$ , and  $2\sigma$  with the values found with the QP-GP, respectively.

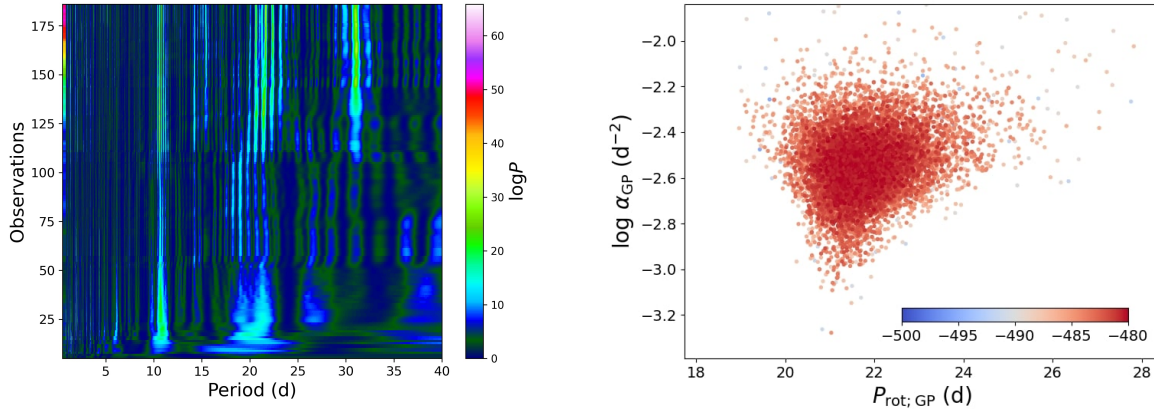


**Figure 4.19:** *Left:* s-BGLS periodogram of the RV data between 0.5 d and 40 d, after subtracting the planet at  $\sim 86$  d. The forest of signals between 20 d and 23 d corresponding to the stellar activity related to the rotational period. The signal close to  $\sim 10.5$  d is roughly half of the rotation period at  $\sim 21$  d. The number of data points included in the computation of the periodogram increases from bottom to top. *Right:* Posterior distribution of the GP fit to the RV data in the  $\log_{\alpha}$  versus  $P_{\text{rot}}$ , including a QP-GP centered on the rotational period  $\sim 21$  d. The color coding shows the log-likelihood normalized to the highest value in the posterior sample.

#### 4.4.2 Conclusions

From a number of 186 radial velocities covering a span of time of 1634 days, we have analyzed the early-M star GJ 617 A. This star was previously studied by [Reiners et al. \(2018a\)](#) which reported a planet companion with a mass of  $M_p \sin i \approx 25 M_{\oplus}$  with an orbital semi-major axis of  $\sim 0.32$  AU, which locates the planet inside of the temperate zone of its host star.

From our new RV analysis, we have confirmed the planet candidate and derived a planet minimum mass of  $24 \pm 3.5 M_{\oplus}$ , in an orbit of  $\sim 86$  d, being consistent with the previous findings. Additionally, from almost one year of *TESS* photometric data, we don't have to detect any transiting companion. However, from our reduced light curve, we have determined a stellar rotational period of  $\sim 21.2$  d. This result was in good agreement with previous studies from KELT data.

From the RV model comparison, the best-fit model was a one-Keplerian signal model plus a QP-GP (1 Kep + GP-QP). In this case, the rotational component of the QP-GP shows a posterior maximum at  $\sim 21.7$  d.

Finally, our results confirm that the rotational period of GJ 617 A should be  $\sim 21$  d.

## 4.5 Photometric analysis of GJ 617 B

Similarly to its brighter companion, GJ 617 B (TIC-230073588) was observed in 12 of the 13 of the *TESS* sectors belonging to the CVZ. In this case, the photometric data was taken with 30-minute cadence as full-frame images (FFIs) but also has available TPF. Since the FFI have important systematics and further processing is needed to remove instrumental and observational systematics, and due to the TPF has available an optimal aperture that ensures that the stellar signal has a high signal-to-noise-ratio, with minimal contamination from the background, we decided to use the TPF instead of FFI.

We downloaded the TPFs from the Mikulski Archive for Space Telescopes (MAST) and corrected the dominant systematic effects as same as we did for GJ 617 A and is described in detail in Sec. 4.2. The SAP and our corrected light curves (Pixel-DM) are shown in Fig. 4.20. As same as for GJ 617 A, here also the SAP flux are strongly dominated for systematics, while our corrected light curve seems to remove most of the systematics trends and preserve the stellar variability. In this case the SAP light curves is 10 times more noisy than our corrected light curve.

Next, we proceed to verified if the sources in the selection aperture in the each of TPFs did not significantly contaminate the flux of GJ 617 B. In this case, we found three sources inside of the TPF apertures *Gaia* DR2 1642642952827749504, *Gaia* DR2 1642642987186220032, and *Gaia* DR2 1642642957122494080, which are separated 11.42 arcsec, 34.24 arcsec, and 37.00 arcsec, and are 9.83 mag, 8.45 mag, and 6.39 mag fainter, respectively. In this case,

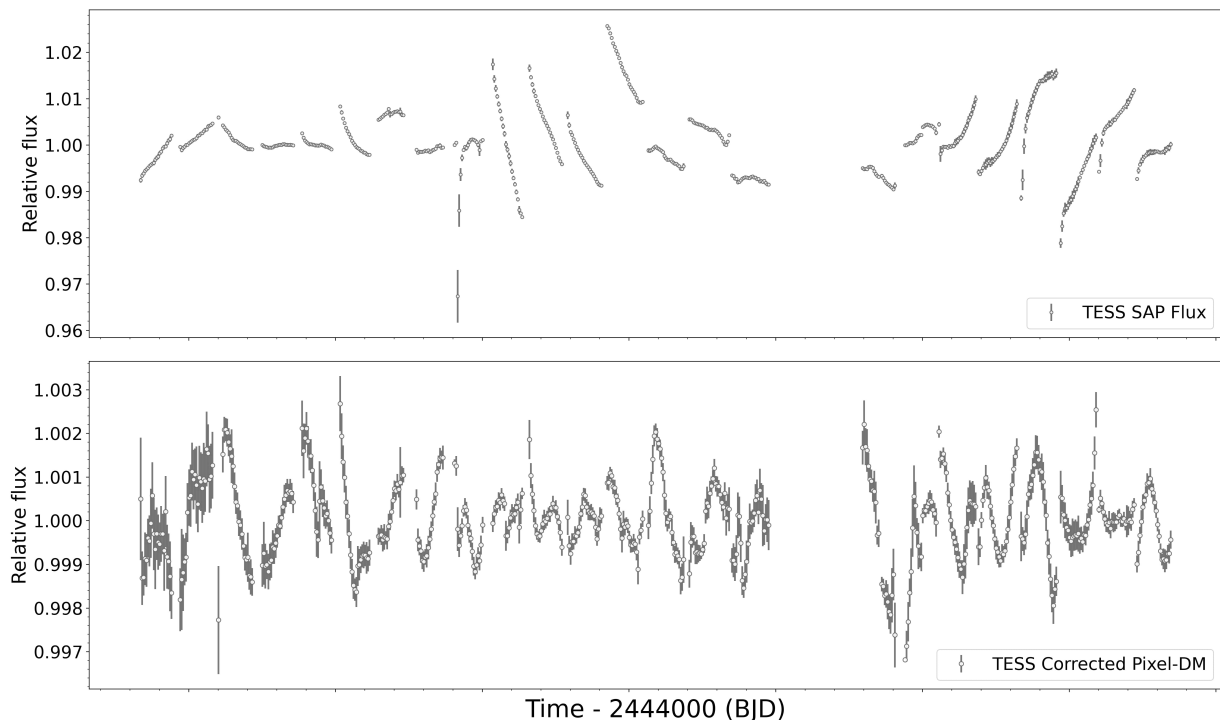


**Figure 4.20:** GJ 617 B *TESS* light curves for sectors between 14–26 (gray), sector 22 was not observed. *Top panel:* shows the SAP light curve. *Bottom panel:* shows our corrected light curve (Pixel-DM). All light curves were binned to 0.5 d.

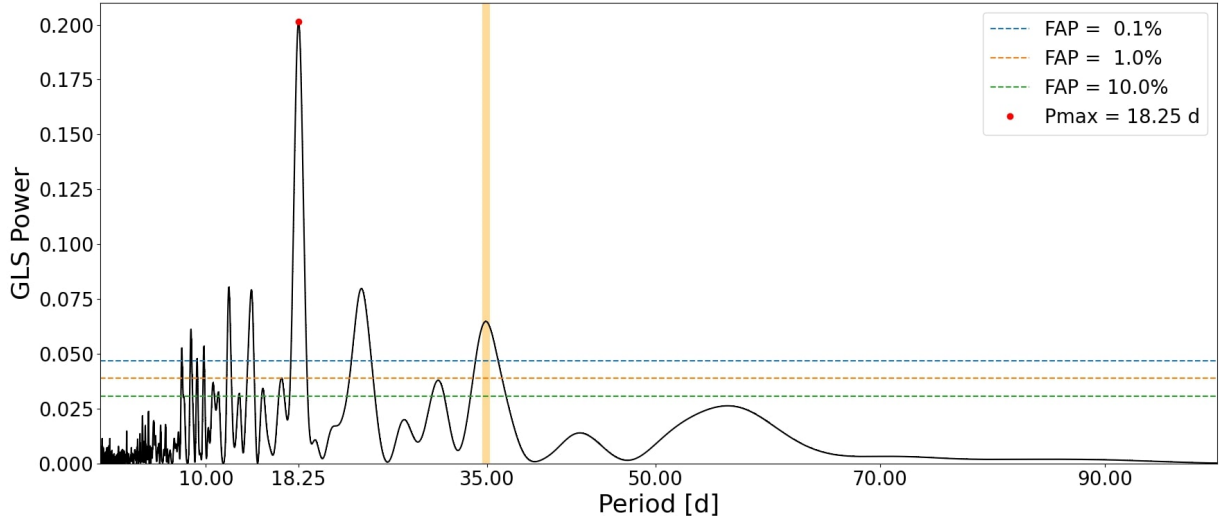


**Figure 4.21:** GLS periodogram of the binned *TESS* light curve. The highest GLS periodicity was found at 18 d and is marked with a red dot. The tick-orange line marks the approximately the double of the derived photometric stellar rotational period which is close to the highest periodicity found in the GLS of the RV activity indicators. The horizontal lines mark the theoretical FAP levels of 0.1% (dotted blue), 1% (dotted orange), and 10% (dotted green). The highest peak at  $\sim 18$  d, is related to the rotational period.

the dilution factor for GJ 617 B was calculated of  $D = 0.97$  and we fixed this value for the next model analysis. Figure 4.22 shows a set of TPFs in which GJ 617 B was observed.

#### 4.5.1 Identifying the stellar rotational period from TESS data

To determine the stellar rotational period of GJ 617 B, we carried out the same procedures as described in Sec. 4.3.1. For the corrected binned light curve (0.5 d), first we performed a GLS periodogram following Zechmeister & Kürster (2009b) and searched for significant peaks in the data. Then, we used the dSHO-GP kernel introduced in Eq. 4.1 for modelling our corrected photometric data. For our modeling, we used *juliet* and we selected the same priors as for for GJ 617 A.

Figure 4.21 and the top panel of Fig. 4.23, shows the GLS photometric periodogram and the binned corrected light curve with the resulting dSHO-GP fit overplotted in red, respectively. The highest GLS periodicity was found at 18 d, and from the maximum likelihood posterior parameters, we derive a photometric rotation period of  $P_{\text{rot(GP-dSHO,phot)}} = 18.79^{+1.44}_{-1.72}$  d. The obtained posterior probabilities distributions are presented in bottom panel of Fig. 4.23.

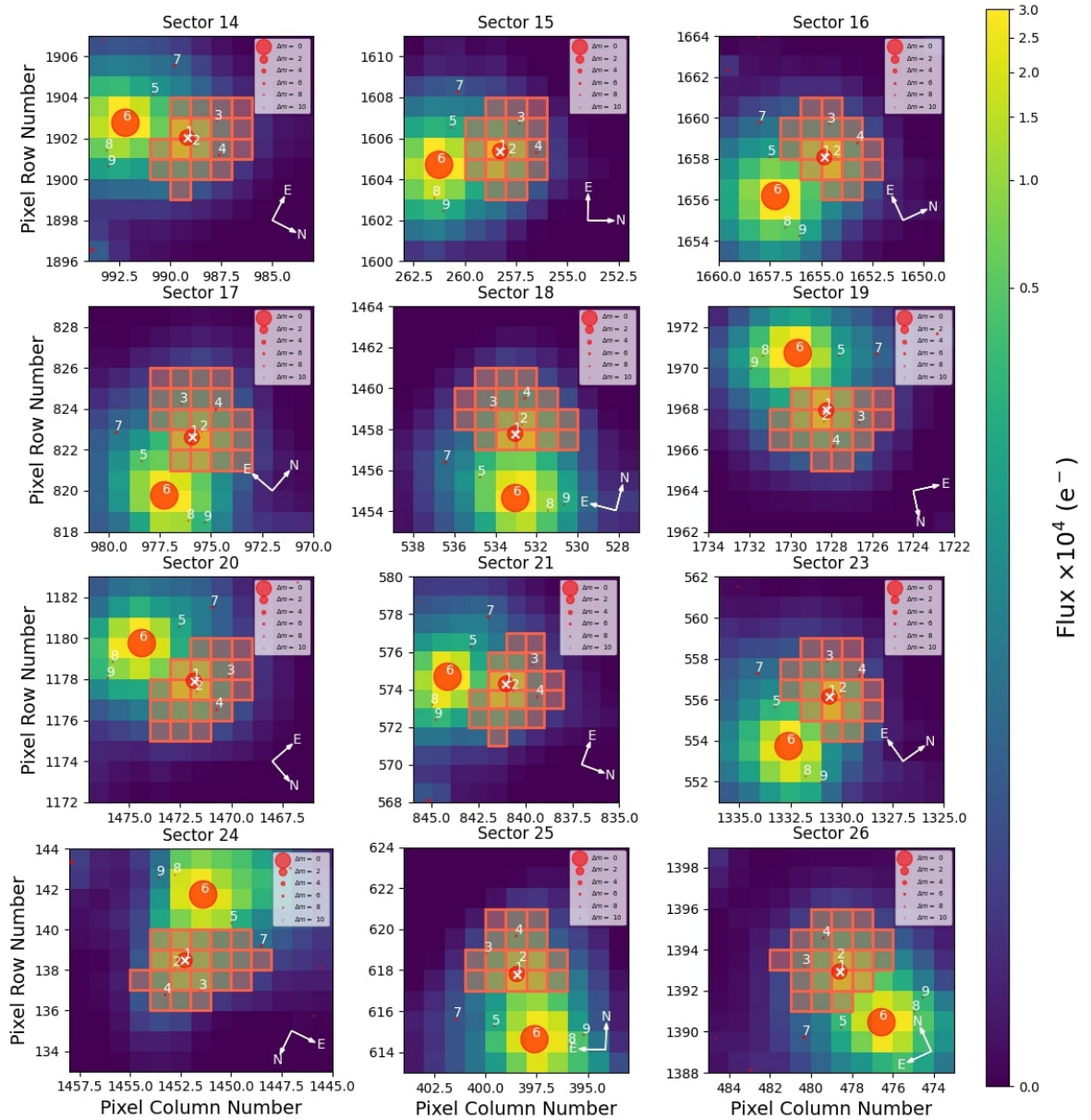


**Figure 4.22:** TESS TPF plots for GJ 617 B for sectors 14, 15, 16, 17, 18, 19, 20, 21, 23, 24, 25, and 26. The corrected light curve was computed using the flux counts coming in the pixels mask (red). The red circles represent neighboring sources listed in Gaia DR2, where the size corresponds to the brightness difference with respect to GJ 617 B (circle 1 marked with an  $\times$ )

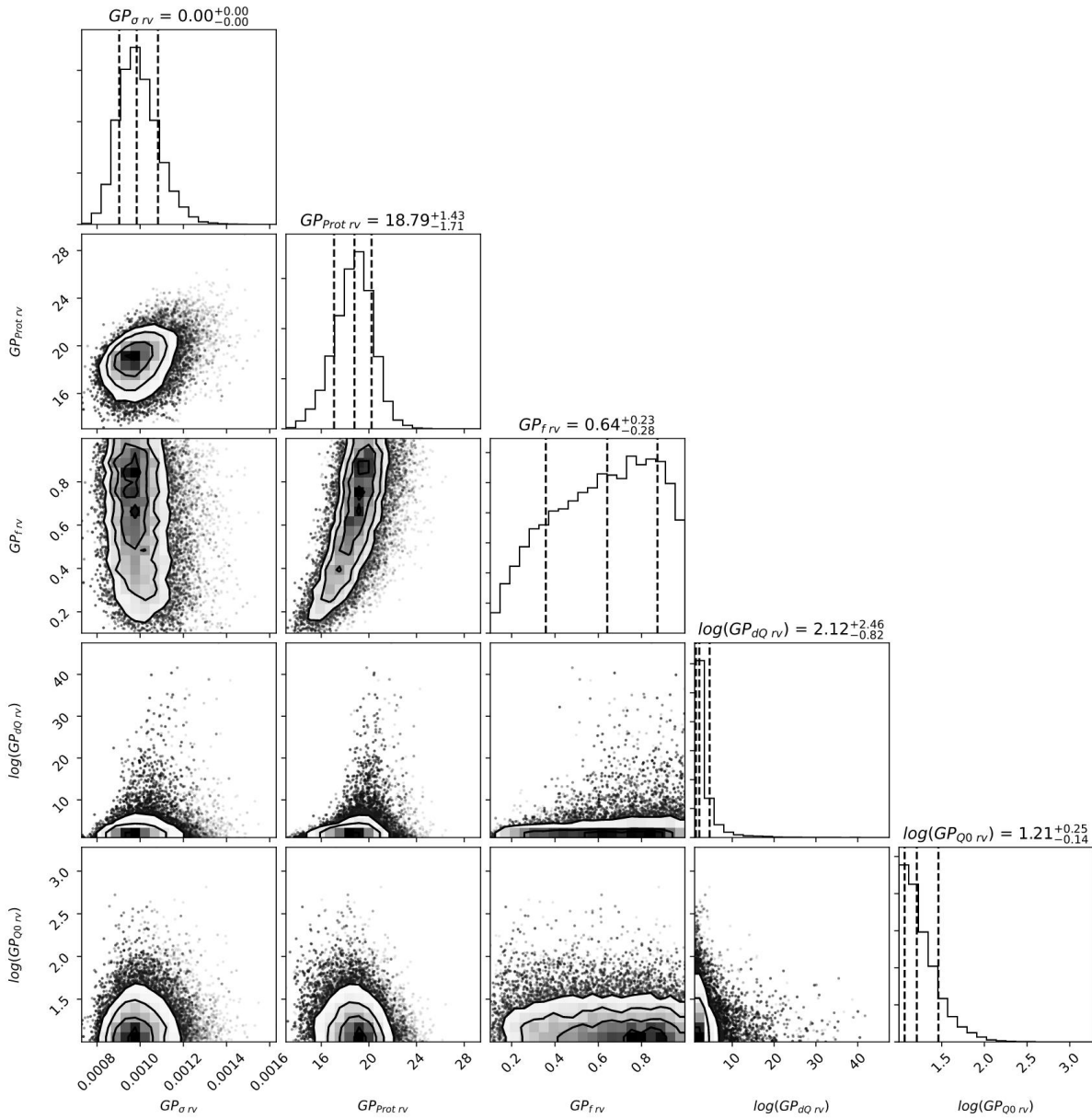
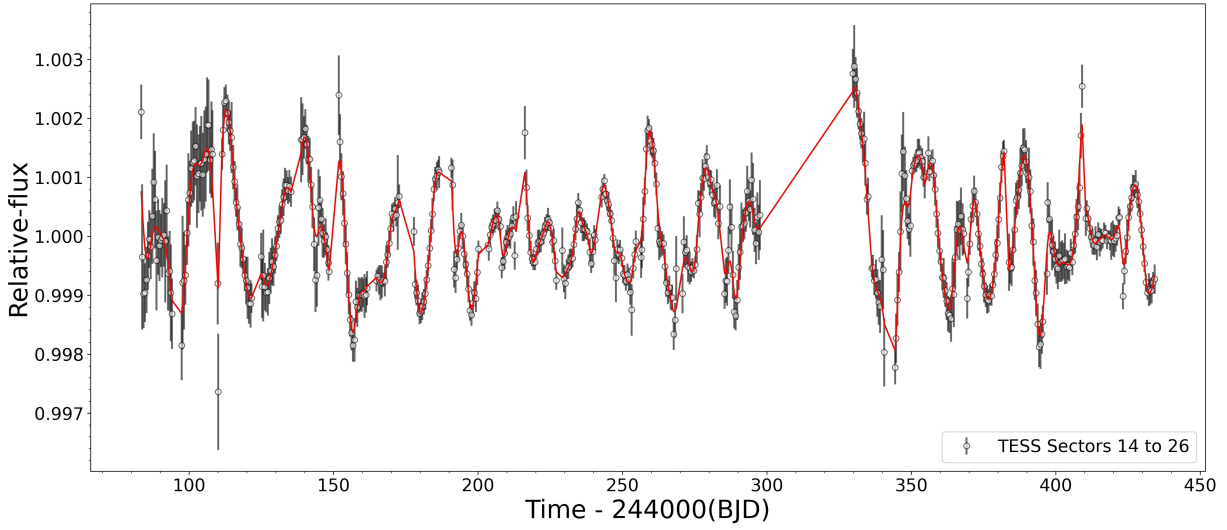


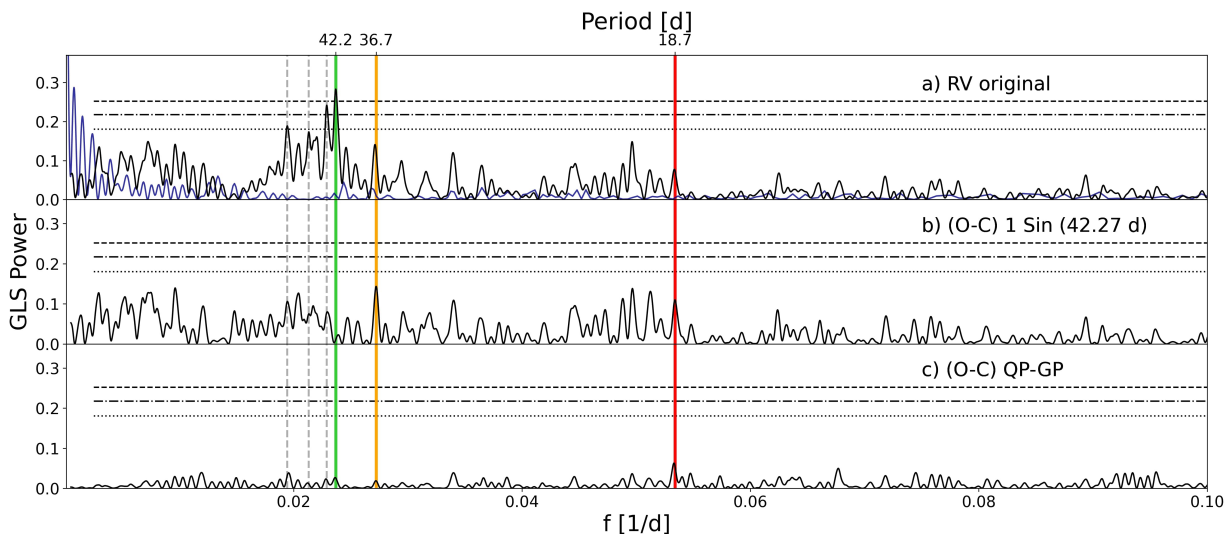
**Figure 4.23:** *Top:* Binned TESS light curve (gray) for sectors between 14–26, sector 22 was not observed. The red curve is the best `juliet` fit model found with the dSHO-GP. *Bottom:* Posterior distribution for the dSHO GP model parameter derived with `juliet`.

## 4.6 Radial velocity analysis of GJ 617 B

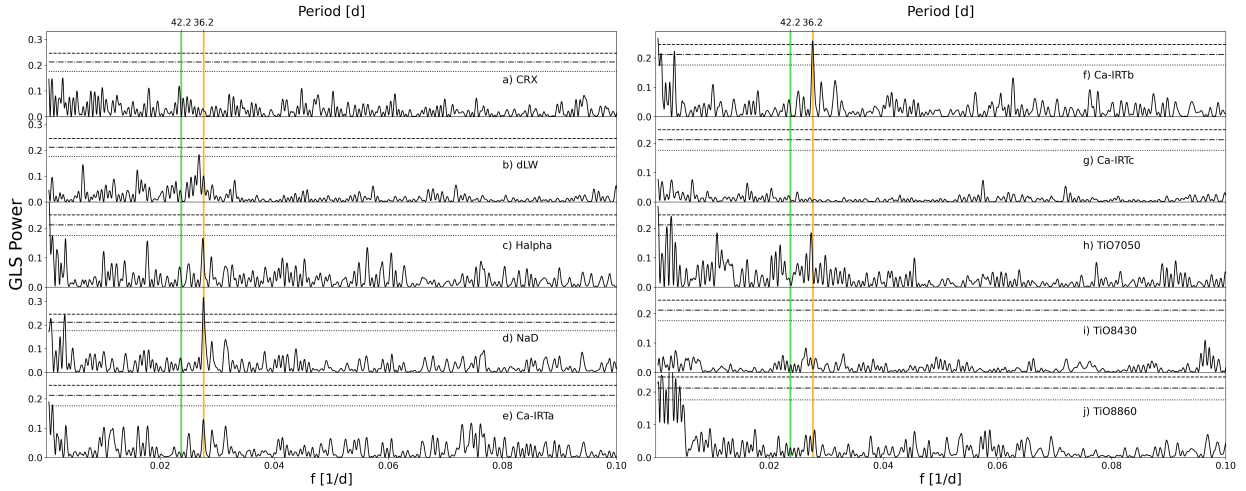
GJ 617 B correspond to the faintest star of the binary system GJ 617. Was observed between 2016 to 2021 by the CARMENES spectrograph collecting a total of 103 radial velocities measurements. To search for periodic signals, we computed the generalised Lomb-Scargle periodogram (GLS [Zechmeister & Kürster, 2009b](#)) and determined the false alarm probabilities (FAP). We followed the same procedures as we did for GJ 617 A (see Sec. 4.4.1 for details).

Figure 4.24 shows a sequence of GLS periodograms from the RV data after subtracting an increasing the number of signals. Panel (a) shows the periodogram of the original CARMENES RV measurements with their window function. Here, the strongest peak is found a period of 42.2 d (green-solid line) with a false alarm probability (FAP) < 0.1%. Their aliases at  $\sim 43.6$ ,  $\sim 46.8$ , and  $\sim 51.52$  d are marked with dashed-gray lines. Before continuing with model Bayesian model comparison, we decide to explore the GLS periodograms of a set of activity indicators derived from the CARMENES spectra.

Figure 4.25 shows the GLS periodograms of the CRX, dLW,  $H_\alpha$ , NaD, Ca II-IRT triplet, and TiO bands (panels from a to j). An interesting signal close to  $\sim 36$ – $37$  d is present with many of the activity indicators (dLW,  $H_\alpha$ , NaD, Ca IRT b, and TIO7015) which in all of them the signal reaches a power of 10% FAP. Interestingly, these signal are close to the double of the rotational period found in the *TESS* photometric data at  $P_{\text{rot(phot)}} = 18.8$  d, suggesting that would be related to the stellar rotation period.



**Figure 4.24:** GLS periodograms of the RV data and the residuals after subtracting different models for GJ 617 B. The vertical solid green line corresponds to the highest signal ( $\sim 42.2$  d). The vertical orange and red lines corresponds to the prominent signal shown in a set of activity indicators ( $\sim 36$  d), and approximately  $P_{\text{rot(phot)}}$ , respectively. Panel (a): Original RVs with the window function of the data set (blue). Panel (b): Residuals after subtracting one-sinusoidal-signal at  $\sim 42.2$  d. Panel (c): Residuals after subtracting a QP-GP model fit. The horizontal lines mark the theoretical FAP levels of 0.1 % (dashed), 1 % (dash-dotted), and 10 % (dotted).



**Figure 4.25:** GLS periodograms of set of activity indicators (a–j) CRX, dLW,  $H_{\alpha}$ , NaD, Ca II-IRT triplet (a, b, c), and TiO activity indices at  $7050\text{\AA}$ ,  $8430\text{\AA}$ , and  $8860\text{\AA}$ . In the panels the vertical solid-green and solid-orange lines indicate the highest peak found at 42.2 d and the prominent signal shown in a set of activity indicators ( $\sim 36$  d). The horizontal black lines mark the theoretical FAP levels of 0.1 % (dashed), 1 % (dash-dotted), and 10 % (dotted).

To inspect the coherence of the signal at  $\sim 42.2$  d over the whole observational time, we performed the Stacked-Bayesian GLS periodogram (s-BGLS). The resulting diagram is shown in left panel of Fig. 4.26. Additionally, in the middle and right panels, we display s-BGLS periodograms, after subtracting a sinusoid at  $\sim 42.2$  d, for the range of periods around 36 d and nearby to the forest of signals between  $\sim 20$ –23 d.

We identified from the left panel that the signal at  $\sim 42.2$  d monotonically increased their probability after 70 observations, as we would expect for a signal coming from a planetary origin. However, from the remaining panels, neither the signals around 36 d nor the forest of signals between 20–23 d was stable over the observational time baseline. Together with the analysis of the activity indicators, these results would be associated with an intrinsic stellar phenomenon.

For modeling the RV data, we used `juliet` and we follow the same rule for model comparison if  $\Delta \ln \mathcal{Z} \lesssim 2.5$  the models are indistinguishable. We started modeling the data with a “flat” model, a red noise model using a QP-GP<sub>wide</sub>, a “one-sinusoidal-signal” model around the highest peak with a uniform priors between 41 to 43 d ( $1 \text{ Sin}_{42}$ ). Also, we investigated whether including a GP to the one-sinusoidal-signal model ( $1 \text{ Sin}_{42} + \text{GP-QP}$ ) would improve the log-evidence of the fit. We used a different prior combinations for the rotational component of the QP-GP. First we used a “wide” prior between 1 to 150 d, and then we tried a GP<sub>36</sub> with a uniform priors between 34 to 38 d, aiming to capture the prominent signal detected in many activity indicators. For the remaining GP priors parameters we used uniform distributions between 0 and 10 [ $\text{ms}^{-1}$ ] for GP $_{\sigma}$ , and a log-uniform priors for GP $_{\alpha}$  and GP $_{\Gamma}$  between  $10^{-8}$  to 1 [ $\text{d}^{-2}$ ], and 0.01 to 10, respectively. Table ?? presents the log-evidences for each model. The best fits were those in which a GP was applied. However, the  $|\Delta \ln \mathcal{Z}|$  between them was lower than 2, and thus none of them is preferred over the other. Hereafter, we decided to select as our fiducial fit the QP-GP<sub>wide</sub> model only. For this

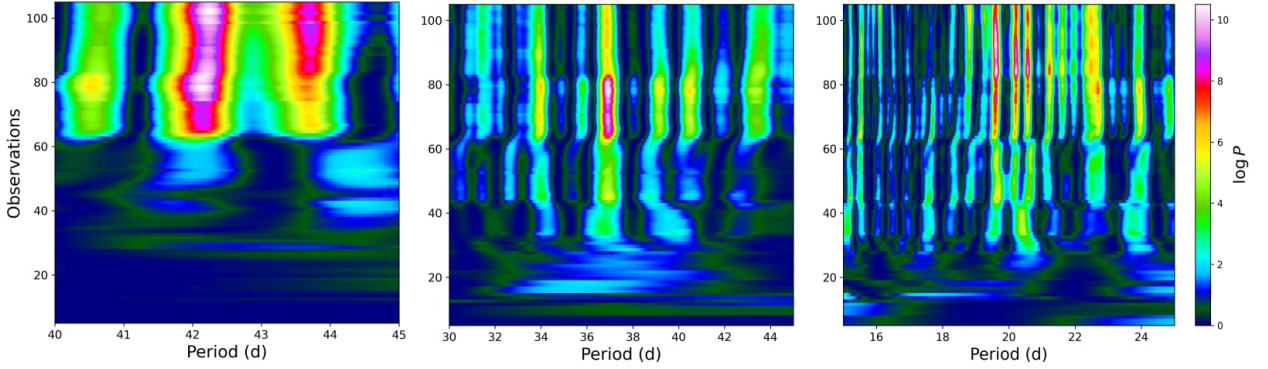


**Figure 4.26:** Evolution of the s-BGLS periodogram of the RV data for GJ 617 B. *Left panel:* shows the original data centered at  $\sim 42$  d. *Middle and right panels:* shows the activity signals between 20 d to 44 d, and 15 d to 25 d after subtracting the  $\sim 42$  d with a sinusoidal fit. The number of data points included in the computation of the periodogram increases from bottom to top.

| Models                                      | Periods      | $\ln \mathcal{Z}$                      | $ \Delta \ln \mathcal{Z} $ |
|---------------------------------------------|--------------|----------------------------------------|----------------------------|
| flat                                        | ...          | $-259.694 \pm 0.127$                   | 0.0                        |
| <b>QP-GP<sub>wide</sub></b>                 | <b>40.32</b> | <b><math>-247.200 \pm 0.058</math></b> | <b>12.49</b>               |
| 1 Sin <sub>42</sub>                         | 42.27        | $-253.475 \pm 0.122$                   | 6.22                       |
| 1 Sin <sub>42</sub> + QP-GP <sub>36</sub>   | 42.30, 37.10 | $-246.254 \pm 0.125$                   | 13.44                      |
| 1 Sin <sub>42</sub> + QP-GP <sub>wide</sub> | 42.29, 39.59 | $-246.840 \pm 0.194$                   | 12.85                      |

**Table 4.3:** Bayesian log-evidence for the different models used for the RV data. In the model names, “Sin” corresponds a sinusoidal-fit around the highest peak, the sub labels correspond to different priors for the  $\text{GP}_{P_{\text{rot(RV)}}}$  parameter.

case the  $\text{GP}_{P_{\text{rot(RV)}}}$  was found at  $\sim 40$  d. The obtained posterior distributions are presented in Fig. 4.27.

### 4.6.1 Discussion

As presented in Sec. 4.6 we found from the GLS of CARMENES RVs data that the strongest signal was located at  $\sim 42$  d within a forest of additional signals. Also, from the GLS analysis of set of activity indicators we don’t found any signal related to this peak. Instead, NaD and Ca II-IRT b index shows a prominent periodicity at  $\sim 36$ -37 d. On the other hand, from the s-BGLS periodgram, the  $\sim 42$  d signal monotonically increase its coherence towards larger number of observations, which would give hints of a planetary origin.

We decided to subtract this signal and proceed to analyze the residuals. In this case, two peaks are visible around  $\sim 36$  d and close to  $\sim 19$  d, supporting the findings made in Sec. 4.5 from the photometric analyses, and also in agreement with the information came from the activity indices. Furthermore, the s-BGLS of the residual shows that the forest of signals around these two values are not coherent with an increasing number of observations, hinting that the origin of these signals could be related to stellar activity. However these two signals

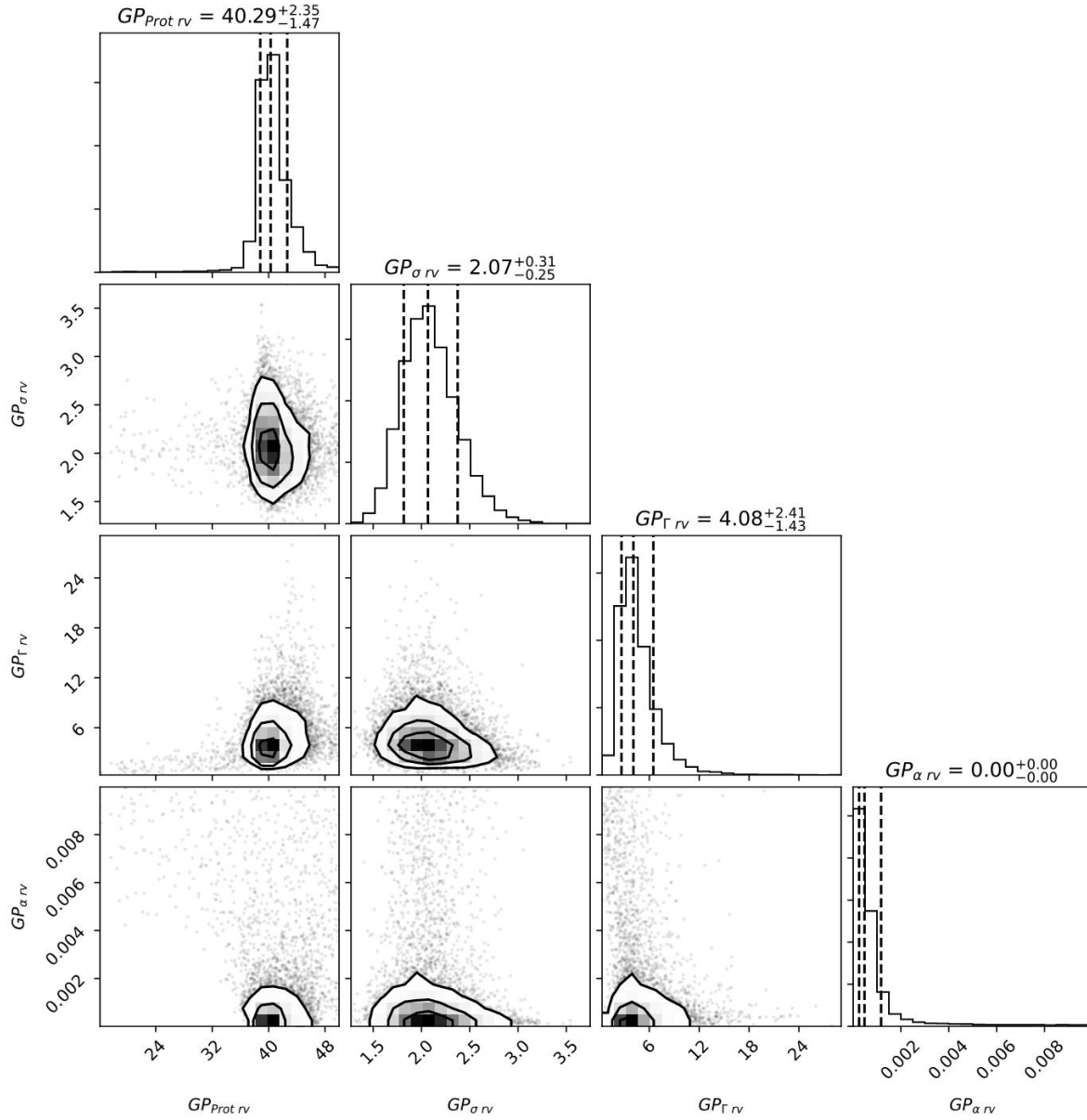


**Figure 4.27:** Posterior distribution for the QP-GP model parameter derived for the RVs with juliet for GJ 617B.

seems to be one double the other complicating the determination of a single value for a possible stellar rotational period.

Thereafter, we decided to fit the data adjusting a sinusoidal model to the signal at  $\sim 42$  d ( $1 \text{ Sin}_{42}$ ) and make a model comparison with a “flat” and a “red noise model” (only QP-GP). However, the difference between their log-evidence  $\Delta \ln \mathcal{Z}$  with the latter models doesn’t satisfy the criteria to select this model over the others. So, we decided to fit the data with a combination of  $1 \text{ Sin}_{42}$  with a the stellar activity model using a QP-GP with wide priors. In this case the model has the same log-evidence that the ‘red noise model’. As a further exploration, we decided to constrain the region of the supposed stellar rotational period obtained from the activity indices. For this fit we selecting a narrow prior for the rotational GP component. A result, the model was slightly improved the log-evidence compared with the only QP-GP model, but one more time, their differences was not significant, so we decided to select as our fiducial the model only using a QP-GP. In this case, the posterior distribution for the rotational QP-GP component preferred a rotational period about 40 d.

One possible explanation of this result could be a consequence of the proximity in the period range between these two signals makes it difficult for the GP to disentangle them. Alternatively, a differential rotation in the star could be the source of the broad-band forest of signals around 42 d complicating the determination of a single value for the rotation period. Consequently, the real origin of these signals remains unclear.



# 5

## Conclusions and future work

---

*“If I have seen further it is by standing on the shoulders of Giants.”*

*by Isaac Newton*

---

Without doubts, the search for small exoplanets has become a prominent research field, on which M dwarfs have proven to be optimal targets for the detection of rocky planets in the habitable zones of their parent star. The RV technique has been one of the most successful methods applied to detect a large number of exoplanets. However, only with the development of extremely precise instruments it has been possible to detect these small worlds.

Despite the high potential that M dwarfs have for finding Earth-like planets, these stars pose various observational difficulties. Usually, they are one of the most active kind of stars in the Universe, on which their activity cycles and their chromosphere variability can produce changes in the spectral line profiles, which can mimic a Doppler shift. This makes it challenging to detect low-signal companions since stellar jitter can reach amplitudes of a few metres per second, having similar amplitudes that small exoplanets. So, it is crucial to understand the impact of stellar variability on the data, by correctly identifying and modeling all the presented signals, because an incorrect diagnosis of these variations could be interpreted as an orbiting exoplanet.

The main objective of this thesis has been the discovery and characterization of exoplanets around M dwarfs, using RV data from CARMENES survey, and transit method from space and ground-based telescopes. The methods applied to reduce and analyze the data were based in state-of-the-art techniques.

Throughout the three chapters of this thesis, the comparison of the Bayesian evidence method was applied to select the fiducial models to fit the data, where the power of this technique over other numerical methods has been proved to be a robust approach to model selection. Additionally, a careful exploration of the GLS of the RVs and as many as possible activity indicators is mandatory to recognize and correctly account for the stellar variability in the model.

For the first scan of the data, we used *Exo-Striker* (Trifonov, 2019). This tool allows to identify potential combinations of the signals existing in the data. Then, we proceeded to model the identified signals using *juliet* (Espinoza et al., 2019). This versatile tool allow us to model all the data simultaneously, combining large data sets of photometry and RVs, considerably improving the fitted parameters and their uncertainties. Additionally, *juliet* allows to model correlated noise using GP, determining not only the planet parameters, but also the stellar rotation period and long-term signals.

As part of the CARMENES consortium, I have been heavily involved in combining the high-resolution spectroscopic data provided by CARMENES and photometric data from the currently ongoing TESS mission to perform an exhaustive analysis of the periodic signals that M dwarf can exhibit. I outlined some of these exciting discoveries in Section 1.4.3.

**Chapter 2:** In this chapter, we report the confirmation of a transiting planet around the bright weakly active M0.5 V star TOI-1235, whose transit signal was detected in the photometric time series of sectors 14, 20, and 21 of the *TESS* space mission. We confirm the planetary nature of the transit signal, which has a period of 3.44 d, by using precise RV measurements with the CARMENES, HARPS-N, and iSHELL spectrographs, supplemented by high-resolution imaging and ground-based photometry. A comparison of the properties derived for TOI-1235 b with theoretical models reveals that the planet has a rocky composition, with a bulk density slightly higher than that of Earth. In particular, we measure a mass of  $M_p = 5.9 \pm 0.6 M_\oplus$  and a radius of  $R_p = 1.69 \pm 0.08 R_\oplus$ , which together result in a density of  $\rho_p = 6.7^{+1.3}_{-1.1} \text{ g cm}^{-3}$ .

When compared with other well-characterized exoplanetary systems, the particular combination of planetary radius and mass places our discovery in the radius gap, which is a transition region between rocky planets and planets with significant atmospheric envelopes. A few examples of planets occupying the radius gap are known to date. While the exact location of the radius gap for M dwarfs is still a matter of debate, our results constrain it to be located at around  $1.7 R_\oplus$  or larger at the insolation levels received by TOI-1235 b ( $\sim 60 S_\oplus$ ). This makes it an extremely interesting object for further studies of planet formation and atmospheric evolution.

**Chapter 3:** In this chapter, we report a transiting ultra-short-period planet (USP) detected in the *TESS* sector 19 photometric time series, and a potential non-transiting planet candidate around the nearby M3.0 V star TOI-1685. We confirm the planetary nature of the transit signal, which has a period of  $P_b = 0.6691403^{+0.0000023}_{-0.0000021}$  d, using precise radial velocity measurements taken with the CARMENES spectrograph. From the joint photometry and radial velocity analysis, we estimate the following parameters for TOI-1685 b: a mass of  $M_b = 3.78^{+0.63}_{-0.63} M_\oplus$ , a radius of  $R_b = 1.70^{+0.07}_{-0.07} R_\oplus$ , which together result in a bulk density of  $\rho_b = 4.21^{+0.95}_{-0.82} \text{ g cm}^{-3}$ , and an equilibrium temperature of  $T_{\text{eq}} = 1069^{+16}_{-16}$  K.

TOI-1685 b is the least dense ultra-short-period planet around an M dwarf known to date. TOI-1685 b is also one of the hottest transiting super-Earth planets with accurate dynamical mass measurements, which makes it a particularly attractive target for thermal emission spectroscopy. Additionally, we report with moderate evidence an additional non-transiting planet candidate in the system, TOI-1685 [c], which has an orbital period of  $P_c = 9.02^{+0.10}_{-0.12}$  d.

**Chapter 4:** The study of stars with long-term baselines allows us not only to detect in wide orbit planets, but also allows to search for long-term modulation in the data that could be related with the stellar rotation period.

In this chapter we study the binary GJ 617 which its brighter companion was a previously study by [Reiners et al. \(2018a\)](#), which through an RV analysis reveal a planetary companion of about  $25 M_{\oplus}$  which locates it in the temperate zone around this early-M star. In their article they discussed if the planet transits, the expected transit depth would be of 5-10 mmag, but by keeping in mind that geometric transit probability is only 0.8%. Furthermore, this star belongs to selected targets with 2-minutes cadence data, and due to being located only 10 deg away from the ecliptic pole, *TESS* could be able to determine whether transits occur.

Our first step was to search for transits in the 2-minutes-cadence light curves of *TESS*. We performed a period search using the Box-Fitting Least Squares, and the Transit Least Squares algorithms. However, we not detect any transiting signal in the data.

Due to the long-term photometric baseline we proceed to analyze the raw light curve by using a reduction method that optimizes the balance between remove systematic trends by preserving the stellar variability on the data. We also inspect the GLS periodograms for the RV activity indicators, which are good tracers of stellar activity. We apply a QP-GP model for both, the photometric data and for the RV to which we also added a Keplerian model for to account the planet companion. As result, in both cases, we get the same value for the rotational GP component. So we conclude that GJ 617 A has a rotational period of  $\sim 21$  d.

Also, we study the fainter component of this binary system, named GJ 617 B. We follow the same procedures as we did for GJ 617 A. In this case, the available *TESS* data doesn't include the PDCSAP light curve due to this target was observed with 30-minutes cadence. We download the available data from MAST, reduce the SAP light curve with our reduction method, and ran a QP-GP model to determine the photometric rotational period of the star. In this case, we found a value of about  $\sim 18$  d. However, from the GLS analysis of the activity indicators we don't find any periodicity related to this value, instead, we found that the prominent peaks were around the double of this value  $\sim 36-37$  d. Additionally we found a very interesting signal in the GLS of the RV data close to  $\sim 42$  days surrounded by a forest of signals, where many of them, was identified as aliases of the data sampling.

We performed a model comparison to search for the best fit for our data. The results suggested that the data is good represented only by a QP-GP. However, a GP model that also includes a sinusoidal around the  $\sim 42$  d was slightly more significant. In both cases, the rotational GP component darts a rotation period around  $\sim 40$  d. As we discussed in [Sec. 4.6.1](#) one possible explication of this results that hindering the determination of a single value for the stellar rotational period could be caused by a differential rotation on the star, or maybe the GP component is not flexible enough to disentangle these signals, absorbing part of the  $\sim 42$  d signal.

## 5.1 Future work

*“The universe is a pretty big place. If it’s just us, seems like an awful waste of space.”*

*by Carl Sagan*

---

Today is a very exciting time for exoplanet research, where bright, nearby, low-mass stars have shown to be optimal hosts for planet search. The study of thousands of planetary systems has revealed that the exoplanet “zoo” comes in a diversity of planet configurations, and today we know that exoplanets are a common phenomena in our Galaxy.

Future ground-based and space telescopes, such as the next *ELT* combined with *PLATO* and *JWST* missions, will allow us to not only increase this large amount of exoplanets but also will allow to accurately characterize their atmospheres, revealing the fingerprints of their compositions. Furthermore, with a sizable sample of the well-characterized exoplanet population, the evaluation of habitability and a search for biosignatures would help to determine which exoplanetary systems could be able to harbor life. A large sample would also permit the study of architecture and time evolution of exoplanets, providing insights on how the conditions for habitability evolve, and potentially revealing the future of planetary systems such as our own.

Finally, if life is prevalent in our neighborhood, it is within our reach to be the first generation in human history to finally cross this threshold and finally find an “Earth 2.0”.

As a result of the work done in this thesis, a number of projects and ideas come ahead:

- **Increase the sample of well-characterized exoplanets around M stars:** Super-Earth characterization continues to be a particular focus of the exoplanet field given that it is the interface between terrestrial and gas-dominated planets. The implications of this division reverberate in planet formation, planetary interiors, and the origins and evolution of planetary atmospheres. As mentioned in Sec 1.3.3, studies of the *Kepler* planet population shows that planets at small orbital separations exhibited a bimodal radius distribution, the so-called the radius gap. There are two alternative scenarios that could explain the existence of this gap: photoevaporation and core-powered mass loss. In the former scenario, the radius valley would move towards planets of smaller radii for stars of lower masses. In the latter scenario, the position of the radius gap will be no not affected by the mass of the host star. The radius gap represents the transition radii range between sub-Neptunes, that still retain a substantial amount of their atmosphere, and rocky planets, whose envelope has been significantly removed. Thus, accurate measurements of planetary masses and radii are required in order to estimate their density, infer their composition using theoretical models, and determine to which extend their atmosphere has been retained or removed. To understand which mechanism is responsible for this bimodal behavior, a higher number of planets within this radius-transition regime towards low-mass stars is required. This will enable a comparison of the gap location around M-dwarfs with that for planets orbiting brighter

stars, to finally clarify if the location of the radius gap depends on the spectral type of the host star.

In chapter 2, I presented the interesting planet TOI-1235 b which places this planet in the lower-edge of the radius gap, helping to constrain its location. Unfortunately, only a few systems with these conditions have been discovered around M dwarfs. However, thousands of well-characterized small planets around low-mass stars are needed in order to robustly state if the radius gap is the result of the photoevaporation or the core-powered mass loss mechanism.

- **Atmosphere characterization with HST–JWST:** One key aspect for any realistic assessment of habitability in a system, is the atmospheric mass loss of the exoplanet due to the high-energy environment and stellar wind of its host star. Exoplanets with periods less than a day, orbiting small stars are extremely attractive as extended atmosphere candidates. The small host star makes the atmospheric absorption signature larger, and the short period makes mass loss more likely and provides many opportunities to obtain a transmission spectrum.

In chapter 3, I presented TOI-1685 b, which is the lowest density super-Earth to orbit a small, low-mass star. Its low density and small host star, make it an ideal candidate for extended atmosphere characterization and a measurement of super-Earth mass loss. The signature of this loss could be observed in the ultraviolet spectrum, when the planet and its escaping atmosphere transit the star, giving rise to deeper and longer transit signatures than in the optical spectrum. Due to the relatively hot atmosphere and its close orbit, TOI-1685 b, is an excellent target for measuring atmospheric hydrogen escape. Currently, the *Hubble Space Telescope* (HST) is the only observatory capable of measuring high spectral resolution line profiles of Lyman- $\alpha$ , the critical atomic transition for detecting the exospheres of hot planets. During this year we have sent a proposal to observe TOI-1685 b with the *HST*, and in June of 2021, we have received the approval to observe this interesting target during the ongoing Cycle 29. These observations, will provide a vital characterization of the stellar inputs into the planetary atmospheres on this system. Furthermore, in case of having success with the *HST* observations, additional observations with the upcoming *JWST* will shed light on their atmospheric composition, due to its extended wavelength range towards the mid-IR, enables the observation of a number of molecular bands.

- **Investigation of the effects of stellar activity in exoplanet detections:** Intrinsic stellar activity behavior can occur on different timescales, where the star spots are the most common manifestation of the activity in the stellar photosphere. One of the current problems is how to mitigate the effects of stellar co-rotating spots on the stellar surface.

In chapter 4 I presented the binary system GJ 617 A+B, on which their fainter component GJ 617 B, is an excellent case to study the performance of the GP when two different signals with similar periods are present in the data. In the hypothetical case that one of these signals is an orbiting exoplanet and the other is related to stellar rotation period, the GP does not have the flexibility to disentangle between them, hindering a correct interpretation of their origins. As the GP is based on the modeling of signals, rather than the modeling of intrinsic stellar phenomena, if in a given system,

the rotational period of the star matches closely the orbital period of a existing planet, the separation of the signals would not possible. An alternative approach to model stellar activity is by simulating the spectral imprints of a rotating spotted photosphere in the RV signal. Tools such as **StarSim** (Herrero et al., 2016) can reproduce the effects on the flux intensities and spectral features induced by active regions, by finding the causal factors that drive the observed variability in the photometric and spectroscopic observations. The aim is to obtain a dynamical spot configuration that fulfills the photometric time series allowing us to characterize the stellar activity patterns beyond parametric models and based on physical mechanisms. This permits the subtraction of stellar signals from the RV time series, allowing the detection of small exoplanets, and also provides a more physically-based perspective for future studies of stellar activity.

## List of publications

These scientific publications have been submitted and published during my studies, or are in preparation for publication within this year.

### 1st AUTHOR PUBLICATIONS

1. **Bluhm P.**, Luque, R., Espinoza, N., Pallé, E., et al. 2020, [A&A](#), **639**, [A132](#);  
“Precise mass and radius of a transiting super-Earth planet orbiting the M dwarf TOI-1235: a planet in the radius gap? ”  
[Chapter 2 in this PhD Thesis]
2. **Bluhm, P.**, Pallé, E., Molaverdikhani, K, Kemmer, J., Hatzes, A. P., et al. 2021, [A&A](#) **650**, [A78](#);  
“A An ultra-short-period transiting super-Earth orbiting the M3 dwarf TOI-1685”  
[Chapter 3, in this PhD Thesis]
3. **Bluhm P.**, Jones, M. I., Vanzì, L., Soto, M. G., et al. 2016, [A&A](#), **593**, [A133](#);  
“New spectroscopic binary companions of giant stars and updated metallicity distribution for binary systems ”  
[Not including in this PhD Thesis]

### CONTRIBUTIONS TO PUBLICATIONS INCLUDED IN THIS THESIS

1. Chaturverdi, P., Nagel, E., **Bluhm, P** et al. 2021, to be submitted;  
“TOI-1468 : A system of two transiting planets, a Super-Earth and a mini-Neptune, one on each side of the radius valley”
2. Kossakowski, D., Kemmer, J., **Bluhm, P.**, Stock, S., et al. 2021, [eprint arXiv:2109.09346](#);  
“TOI-1201 b: A mini-Neptune transiting a bright and moderately young M dwarf ”
3. Trifonov, T., Caballero, J. A., Morales, J. C.,..., **Bluhm, P.**, et al. 2021, [Science](#), **371**, [6533](#);  
“A nearby transiting rocky exoplanet that is suitable for atmospheric investigation”

[Parts summarized in Section 1.5 of Chapter 1]

## CONTRIBUTIONS TO PUBLICATIONS NOT INCLUDED IN THIS THESIS

1. Kemmer, J., Dreizler, S., Kossakowski, D., ..., **Bluhm, P.** et al. 2022 [eprint arXiv:2202.00970](#);  
“Discovery and mass measurement of the hot, transiting, Earth-sized planet GJ 3929 b”
2. Espinoza, N., Pallé, E., Kemmer, J., ..., **Bluhm, P.** et al. 2021, to be submitted;  
TOI-1759 b: “A transiting, temperate mini-Neptune orbiting the M dwarf TOI-1759 unveiled by *TESS*”.
3. Soto, M., Anglada-Escudé, G., Dreizler, S., ..., **Bluhm, P.**, et al. 2021, [A&A, 649, A144](#);  
“Mass and density of the transiting hot and rocky super-Earth LHS 1478 b (TOI-1640 b)”.
4. Stock, S., Kemmer, J., Reffert, S., ..., **Bluhm, P.** et al. 2020, [A&A, 636, A119](#);  
“The CARMENES search for exoplanets around M dwarfs. Characterization of the nearby ultra-compact multiplanetary system YZ Ceti”
5. Kemmer, J., Stock, S., Kossakowski, D., ..., **Bluhm, P.** et al. 2020, [A&A, 642, A236](#);  
“Discovery of a hot, transiting, Earth-sized planet and a second temperate, non-transiting planet around the M4 dwarf GJ 3473 (TOI-488)”
6. Luque, R., Pallé, E., Kossakowski, D., ..., **Bluhm, P.** et al. 2019, [A&A, 628, A39](#);  
“Planetary system around the nearby M dwarf GJ 357 including a transiting, hot, Earth-sized planet optimal for atmospheric characterization”
7. Zechmeister, M., Dreizler, S., Ribas, I., ..., **Bluhm, P.** et al. 2019, [A&A, 627, A49](#);  
“The CARMENES search for exoplanets around M dwarfs. Two temperate Earth-mass planet candidates around Teegarden’s Star”
8. Izzo, L., Della Valle, M., Mason, E., ..., **Bluhm, P.** et al. 2015, [ApJ, 808, 1, L14](#);  
“Early Optical Spectra of Nova V1369 Cen Show the Presence of Lithium”
9. Jones, M. I., Jenkins, J. S., Rojo, P., Melo, C. H. F., **Bluhm, P.** 2015, [A&A, 573, A3](#);  
“A planetary system and a highly eccentric brown dwarf around the giant stars HIP 67851 and HIP 97233”
10. Jones, M. I., Jenkins, J. S., **Bluhm, P.**, Rojo, P., Melo, C. H. F., 2015, [A&A, 566, A113](#);  
“The properties of planets around giant stars”
11. Jones, M. I., Jenkins, J. S., Rojo, P., Melo, C. H. F., **Bluhm, P.**, 2013, [A&A, 556, A78](#);  
“Study of the impact of the post-MS evolution of the host star on the orbits of close-in planets. II. A giant planet in a close-in orbit around the RGB star HIP 63242”

## Bibliography

---

- Adams, F. C., & Bloch, A. M. 2015, *MNRAS*, 446, 3676 [72](#)
- Adams, F. C., & Laughlin, G. 1997, *Reviews of Modern Physics*, 69, 337 [28](#)
- Agol, E., Steffen, J., Sari, R., & Clarkson, W. 2005, *MNRAS*, 359, 567 [14](#)
- Allen, C. W., & Youse, S. 1973, *MNRAS*, 161, 181 [30](#)
- Aller, A., Lillo-Box, J., Jones, D., Miranda, L. F., & Barceló Forteza, S. 2020, *A&A*, 635, A128 [50](#), [75](#), [111](#)
- Alonso-Floriano, F. J., Morales, J. C., Caballero, J. A., et al. 2015, *A&A*, 577, A128 [50](#), [80](#), [101](#)
- Ambikasaran, S., Foreman-Mackey, D., Greengard, L., Hogg, D. W., & O’Neil, M. 2015, *IEEE Transactions on Pattern Analysis and Machine Intelligence*, 38, arXiv:1403.6015 [83](#)
- Anderson, E. R., Duvall, Thomas L., J., & Jefferies, S. M. 1990, *ApJ*, 364, 699 [114](#)
- Anglada-Escudé, G., & Butler, R. P. 2012, *ApJS*, 200, 15 [32](#)
- Angus, R., Aigrain, S., Foreman-Mackey, D., & McQuillan, A. 2015, *MNRAS*, 450, 1787 [79](#)
- Arenou, F., Luri, X., Babusiaux, C., et al. 2018, *A&A*, 616, A17 [52](#)
- Astudillo-Defru, N., Delfosse, X., Bonfils, X., et al. 2017, *A&A*, 600, A13 [49](#), [52](#)
- Astudillo-Defru, N., Cloutier, R., Wang, S. X., et al. 2020, *A&A*, 636, A58 [42](#)
- Bailer-Jones, C. A. L., Rybizki, J., Fouesneau, M., Demleitner, M., & Andrae, R. 2020, *arXiv e-prints*, arXiv:2012.05220 [79](#)
- Bakos, G., Noyes, R. W., Kovács, G., et al. 2004, *PASP*, 116, 266 [48](#)
- Barge, P., Baglin, A., Auvergne, M., & CoRoT Team. 2008, in *Exoplanets: Detection, Formation and Dynamics*, ed. Y.-S. Sun, S. Ferraz-Mello, & J.-L. Zhou, Vol. 249, 3–16 [15](#)
- Barnes, R. 2017, *Celestial Mechanics and Dynamical Astronomy*, 129, 509 [58](#)
- Barnes, S. A. 2007, *ApJ*, 669, 1167 [79](#)

- Baruteau, C., Crida, A., Paardekooper, S. J., et al. 2014, in *Protostars and Planets VI*, ed. H. Beuther, R. S. Klessen, C. P. Dullemond, & T. Henning, 667 [21](#)
- Batalha, N. M., Rowe, J. F., Bryson, S. T., et al. 2013, *ApJS*, 204, 24 [23](#), [41](#)
- Bauer, F. F., Zechmeister, M., & Reiners, A. 2015, *A&A*, 581, A117 [12](#)
- Bauer, F. F., Zechmeister, M., Kaminski, A., et al. 2020, arXiv e-prints, arXiv:2006.01684 [46](#)
- Bayo, A., Rodrigo, C., Barrado Y Navascués, D., et al. 2008, *A&A*, 492, 277 [48](#)
- Bedding, T. R., & Kjeldsen, H. 2003, *Journal of Geophysical Research*, 108, 203 [29](#)
- . 2007, *Communications in Asteroseismology*, 150, 106 [29](#)
- Benz, W., Broeg, C., Fortier, A., et al. 2021, *Experimental Astronomy*, 51, 109 [16](#)
- Berdyugina, S. V. 2005, *Living Reviews in Solar Physics*, 2, 8 [30](#)
- Berger, T. A., Huber, D., Gaidos, E., & van Saders, J. L. 2018, *ApJ*, 866, 99 [23](#), [42](#)
- Bhatti, W., Bouma, L., Joshua, John, & Price-Whelan, A. 2020, waqasbhatti/astrobase: astrobase v0.5.0, doi:10.5281/zenodo.3723832 [76](#)
- Bianchi, L., Shiao, B., & Thilker, D. 2017, *ApJS*, 230, 24 [79](#)
- Bitsch, B., Raymond, S. N., & Izidoro, A. 2019, *A&A*, 624, A109 [22](#)
- Bluhm, P., Luque, R., Espinoza, N., et al. 2020, *A&A*, 639, A132 [16](#), [41](#), [84](#)
- Bluhm, P., Pallé, E., Molaverdikhani, K., et al. 2021, *A&A*, 650, A78 [16](#), [71](#)
- Bonfils, X., Delfosse, X., Udry, S., et al. 2013, *A&A*, 549, A109 [41](#), [73](#)
- Boro Saikia, S., Marvin, C. J., Jeffers, S. V., et al. 2018, *A&A*, 616, A108 [49](#)
- Borsa, F., Scandariato, G., Rainer, M., et al. 2015, *A&A*, 578, A64 [49](#)
- Borucki, W. J. 2016, *Reports on Progress in Physics*, 79, 036901 [41](#), [73](#)
- Borucki, W. J., Koch, D., Basri, G., et al. 2010a, *Science*, 327, 977 [15](#), [41](#)
- . 2010b, *Science*, 327, 977 [73](#)
- Boss, A. P. 1997, *ApJ*, 483, 309 [19](#)
- Brown, T. M., Baliber, N., Bianco, F. B., et al. 2013, *Publications of the Astronomical Society of the Pacific*, 125, 1031 [47](#)
- Buchhave, L. A., Latham, D. W., Johansen, A., et al. 2012, *Nature*, 486, 375 [17](#)
- Buchner, J., Georgakakis, A., Nandra, K., et al. 2014, *A&A*, 564, A125 [83](#)

- Caballero, J. A., Guàrdia, J., López del Fresno, M., et al. 2016, Society of Photo-Optical Instrumentation Engineers (SPIE) Conference Series, Vol. 9910, CARMENES: data flow, 99100E [45](#), [79](#)
- Cale, B., Plavchan, P., LeBrun, D., et al. 2019, *AJ*, 158, 170 [46](#)
- Casasayas-Barris, N., Orell-Miquel, J., Stangret, M., et al. 2021, *A&A*, 654, A163 [33](#)
- Ceillier, T., Tayar, J., Mathur, S., et al. 2017, *A&A*, 605, A111 [54](#)
- Chabrier, G. 2001, *ApJ*, 554, 1274 [76](#)
- . 2003, *PASP*, 115, 763 [35](#), [41](#)
- Chabrier, G., & Baraffe, I. 2000, *ARA&A*, 38, 337 [28](#)
- Chabrier, G., Johansen, A., Janson, M., & Rafikov, R. 2014, in *Protostars and Planets VI*, ed. H. Beuther, R. S. Klessen, C. P. Dullemond, & T. Henning, 619 [18](#)
- Chang, S. H., Gu, P. G., & Bodenheimer, P. H. 2010, *ApJ*, 708, 1692 [22](#)
- Charbonneau, D., Brown, T. M., Latham, D. W., & Mayor, M. 2000, *ApJ*, 529, L45 [8](#)
- Chaturvedi, P. in prep. [38](#)
- Chen, H., & Rogers, L. A. 2016, *ApJ*, 831, 180 [23](#), [42](#), [93](#)
- Chiang, E., & Laughlin, G. 2013, *MNRAS*, 431, 3444 [72](#)
- Cifuentes, C., Caballero, J. A., Cortés-Contreras, M., & et al. 2020, *A&A*, *subm.* [28](#), [48](#), [79](#)
- Cincunegui, C., Díaz, R. F., & Mauas, P. J. D. 2007, *A&A*, 469, 309 [29](#)
- Claytor, Z. R., van Saders, J. L., Llama, J., et al. 2021, arXiv e-prints, arXiv:2104.14566 [104](#)
- Cloutier, R., Eastman, J. D., Rodriguez, J. E., et al. 2020a, *AJ*, 160, 3 [26](#), [42](#)
- Cloutier, R., Rodriguez, J. E., Irwin, J., et al. 2020b, *AJ*, 160, 22 [27](#), [42](#)
- Collins, K. A., Kielkopf, J. F., Stassun, K. G., & Hessman, F. V. 2017a, *AJ*, 153, 77 [47](#)
- . 2017b, *AJ*, 153, 77 [77](#)
- Cortés-Contreras, M., Béjar, V. J. S., Caballero, J. A., et al. 2017, *A&A*, 597, A47 [37](#)
- Cosentino, R., Lovis, C., Pepe, F., et al. 2012, in *Society of Photo-Optical Instrumentation Engineers (SPIE) Conference Series*, Vol. 8446, Proceedings of SPIE, 84461V [46](#)
- Crossfield, I. J. M., Waalkes, W., Newton, E. R., et al. 2019, *ApJ*, 883, L16 [42](#), [73](#)
- Cutri, R. M., & et al. 2014, *VizieR Online Data Catalog*, II/328 [48](#)

Cutri, R. M., Wright, E. L., Conrow, T., et al. 2021, *VizieR Online Data Catalog*, II/328 [79](#)

Dai, F., Masuda, K., & Winn, J. N. 2018, *ApJ*, 864, L38 [27](#)

Demory, B.-O., Gillon, M., Seager, S., et al. 2012, *ApJ*, 751, L28 [72](#)

Díez Alonso, E., Caballero, J. A., Montes, D., et al. 2019, *A&A*, 621, A126 [48](#)

Dorren, J. D., & Guinan, E. F. 1994, *ApJ*, 428, 805 [29](#)

Drake, A. J., Djorgovski, S. G., Mahabal, A., et al. 2009, *ApJ*, 696, 870 [48](#)

Dressing, C. D., & Charbonneau, D. 2015, *ApJ*, 807, 45 [41](#), [73](#)

Dressing, C. D., Vanderburg, A., Schlieder, J. E., et al. 2017, *AJ*, 154, 207 [73](#)

Dumusque, X. 2010, in *Astronomy of Exoplanets with Precise Radial Velocities*, 11 [29](#)

Dumusque, X., Santos, N. C., Udry, S., Lovis, C., & Bonfils, X. 2011, *A&A*, 527, A82 [29](#)

Dumusque, X., Turner, O., Dorn, C., et al. 2019, *A&A*, 627, A43 [26](#)

Durisen, R. H., Boss, A. P., Mayer, L., et al. 2007, in *Protostars and Planets V*, ed. B. Reipurth, D. Jewitt, & K. Keil, 607 [19](#)

Espinoza, N. 2018, *Research Notes of the American Astronomical Society*, 2, 209 [58](#), [59](#), [88](#), [89](#)

Espinoza, N., & Jordán, A. 2016, *MNRAS*, 457, 3573 [58](#)

Espinoza, N., Kossakowski, D., & Brahm, R. 2019, *MNRAS*, 490, 2262 [52](#), [54](#), [75](#), [83](#), [111](#), [117](#), [136](#)

Faria, J. 2017, in *CHEOPS Fifth Science Workshop*, 18 [84](#)

Feinstein, A. D., Montet, B. T., Foreman-Mackey, D., et al. 2019, *PASP*, 131, 094502 [104](#)

Feroz, F., Hobson, M. P., & Bridges, M. 2009, *MNRAS*, 398, 1601 [83](#)

Fischer, D. A., & Marcy, G. W. 1992, *ApJ*, 396, 178 [35](#)

Fischer, D. A., & Valenti, J. 2005, *ApJ*, 622, 1102 [17](#)

Follert, R., Dorn, R. J., Oliva, E., et al. 2014, in *Society of Photo-Optical Instrumentation Engineers (SPIE) Conference Series*, Vol. 9147, *Ground-based and Airborne Instrumentation for Astronomy V*, ed. S. K. Ramsay, I. S. McLean, & H. Takami, 914719 [12](#)

Foreman-Mackey, D., Agol, E., Ambikasaran, S., & Angus, R. 2017, *celerite: Scalable 1D Gaussian Processes in C++, Python, and Julia*, ascl:1709.008 [54](#), [55](#)

Foreman-Mackey, D., Hogg, D. W., Lang, D., & Goodman, J. 2013, *PASP*, 125, 306 [60](#)

Foreman-Mackey, D., Hogg, D. W., & Morton, T. D. 2014, *ApJ*, 795, 64 [23](#)

- Frith, J., Pinfield, D. J., Jones, H. R. A., et al. 2013, MNRAS, 435, 2161 [48](#), [79](#)
- Fukui, A., Korth, J., Livingston, J. H., et al. 2021, AJ, 162, 167 [37](#)
- Fulton, B. J., & Petigura, E. A. 2018, AJ, 156, 264 [23](#), [42](#), [65](#)
- Fulton, B. J., Petigura, E. A., Blunt, S., & Sinukoff, E. 2018, Publications of the Astronomical Society of the Pacific, 130, 044504 [83](#)
- Fulton, B. J., Petigura, E. A., Howard, A. W., et al. 2017, AJ, 154, 109 [23](#), [25](#), [26](#), [42](#), [64](#)
- Gagné, J., Mamajek, E. E., Malo, L., et al. 2018, ApJ, 856, 23 [49](#)
- Gaia Collaboration, Brown, A. G. A., Vallenari, A., et al. 2020, Gaia Early Data Release 3: Summary of the contents and survey properties, arXiv:2012.01533 [16](#), [80](#), [101](#)
- Gaia Collaboration, Brown, A. G. A., Vallenari, A., et al. 2018, A&A, 616, A1 [42](#), [48](#), [50](#)
- . 2021, A&A, 649, A1 [8](#)
- Gaidos, E., Mann, A. W., Kraus, A. L., & Ireland, M. 2016, MNRAS, 457, 2877 [42](#), [73](#)
- Gaidos, E., Mann, A. W., Lépine, S., et al. 2014, MNRAS, 443, 2561 [48](#), [49](#)
- Galilei, G., Welser, M., & de Filiis, A. 1613, *Istoria E dimostrazioni intorno alle macchie solari E loro accidenti comprese in tre lettere scritte all'illvstrissimo signor Marco Velseri ...* [31](#)
- Gan, T., Shporer, A., Livingston, J. H., et al. 2020, AJ, 159, 160 [57](#)
- Gandolfi, D., Fossati, L., Livingston, J. H., et al. 2019, ApJ, 876, L24 [64](#)
- García, R. A., & Ballot, J. 2019, Living Reviews in Solar Physics, 16, 4 [42](#)
- García, R. A., Hekker, S., Stello, D., et al. 2011, MNRAS, 414, L6 [54](#)
- García, R. A., Mathur, S., Pires, S., et al. 2014a, A&A, 568, A10 [54](#)
- García, R. A., Ceillier, T., Salabert, D., et al. 2014b, A&A, 572, A34 [54](#)
- Gardner, J. P., Mather, J. C., Clampin, M., et al. 2006, Space Sci.Rev., 123, 485 [17](#)
- . 2009, Astrophysics and Space Science Proceedings, 10, 1 [102](#)
- Gershberg, R. E. 1972, Ap&SS, 19, 75 [30](#)
- Gilbert, E. A., Barclay, T., Schlieder, J. E., et al. 2020, arXiv e-prints, arXiv:2001.00952 [42](#)
- Gillon, M., Triaud, A. H. M. J., Demory, B.-O., et al. 2017, Nature, 542, 456 [22](#)
- Ginzburg, S., Schlichting, H. E., & Sari, R. 2016, ApJ, 825, 29 [24](#), [26](#), [42](#)
- . 2018, MNRAS, 476, 759 [24](#), [42](#)

- Girardi, L., Barbieri, M., Groenewegen, M. A. T., et al. 2012, *Astrophysics and Space Science Proceedings*, 26, 165 [76](#)
- Goodwin, S. P., Kroupa, P., Goodman, A., & Burkert, A. 2007, in *Protostars and Planets V*, ed. B. Reipurth, D. Jewitt, & K. Keil, 133 [37](#)
- Goodwin, S. P., Nutter, D., Kroupa, P., Ward-Thompson, D., & Whitworth, A. P. 2008, *A&A*, 477, 823 [37](#)
- Günther, M. N., Pozuelos, F. J., Dittmann, J. A., et al. 2019, *Nature Astronomy*, 3, 1099 [42](#)
- Günther, M. N., Zhan, Z., Seager, S., et al. 2020, *AJ*, 159, 60 [8](#), [30](#)
- Gupta, A., & Schlichting, H. E. 2019, *MNRAS*, 487, 24 [24](#), [42](#)
- . 2020, *MNRAS*, 493, 792 [24](#), [42](#), [63](#)
- Hathaway, D. H. 2015, *Living Reviews in Solar Physics*, 12, 4 [31](#)
- Hatzes, A. P. 2019, *The Doppler Method for the Detection of Exoplanets*, doi:10.1088/2514-3433/ab46a3 [81](#)
- Heinze, A. N., Tonry, J. L., Denneau, L., et al. 2018, *AJ*, 156, 241 [48](#)
- Henry, T. J., Jao, W.-C., Subasavage, J. P., et al. 2006, *AJ*, 132, 2360 [28](#), [41](#)
- Henry, T. J., Jao, W.-C., Winters, J. G., et al. 2018, *AJ*, 155, 265 [28](#)
- Herrero, E., Ribas, I., Jordi, C., et al. 2016, *A&A*, 586, A131 [140](#)
- Hippke, M., & Heller, R. 2019, *A&A*, 623, A39 [111](#)
- Hirano, T., Dai, F., Gandolfi, D., et al. 2018a, *AJ*, 155, 127 [42](#), [65](#)
- . 2018b, *AJ*, 155, 127 [73](#)
- Hirano, T., Livingston, J. H., Fukui, A., et al. 2021, arXiv e-prints, arXiv:2103.12760 [73](#)
- Hirayama, T. 1978, *PASJ*, 30, 337 [31](#)
- Høg, E., Fabricius, C., Makarov, V. V., et al. 2000, *A&A*, 355, L27 [48](#), [50](#)
- Holman, M. J., & Murray, N. W. 2005, *Science*, 307, 1288 [14](#), [60](#)
- Hormuth, F., Brandner, W., Hippler, S., & Henning, T. 2008, *Journal of Physics Conference Series*, 131, 012051 [46](#), [76](#)
- Howard, A. W., Marcy, G. W., Bryson, S. T., et al. 2012, *ApJS*, 201, 15 [17](#)
- Howard, W. S., Teske, J., Corbett, H., et al. 2021, arXiv e-prints, arXiv:2106.15638 [104](#)
- Howell, S. B., Everett, M. E., Sherry, W., Horch, E., & Ciardi, D. R. 2011, *AJ*, 142, 19 [47](#)

- Howell, S. B., Sobek, C., Haas, M., et al. 2014, *PASP*, 126, 398 [73](#)
- Hsu, D. C., Ford, E. B., Ragozzine, D., & Morehead, R. C. 2018, *AJ*, 155, 205 [23](#)
- Hunter, A., Macgregor, A., Szabo, T., Wellington, C., & Bellgard, M. 2012, *Source code for biology and medicine*, 7, 1 [49](#)
- Hussain, G. A. J. 2002, *Astronomische Nachrichten*, 323, 349 [30](#)
- Ida, S., & Lin, D. N. C. 2004, *ApJ*, 616, 567 [18](#)
- . 2010, *ApJ*, 719, 810 [37](#)
- Irwin, J., Berta, Z. K., Burke, C. J., et al. 2011, *ApJ*, 727, 56 [48](#)
- Jeffers, S. V., Schöfer, P., Lamert, A., et al. 2018a, *A&A*, 614, A76 [33](#), [82](#)
- . 2018b, *A&A*, 614, A76 [52](#)
- Jenkins, J. M. 2002, *ApJ*, 575, 493 [45](#)
- Jenkins, J. M., Tenenbaum, P., Seader, S., et al. 2017, *Kepler Data Processing Handbook: Transiting Planet Search* [45](#)
- Jenkins, J. M., Caldwell, D. A., Chandrasekaran, H., et al. 2010, *ApJ*, 713, L87 [106](#)
- Jenkins, J. M., Twicken, J. D., McCauliff, S., et al. 2016, in *Proceedings of SPIE, Vol. 9913, Software and Cyberinfrastructure for Astronomy IV*, 99133E [45](#)
- Jensen, E. 2013, *Tapir: A web interface for transit/eclipse observability*, *Astrophysics Source Code Library*, ascl:1306.007 [47](#)
- Jin, S., Mordasini, C., Parmentier, V., et al. 2014, *ApJ*, 795, 65 [42](#), [93](#)
- Johnson, D. R. H., & Soderblom, D. R. 1987, *AJ*, 93, 864 [49](#)
- Kaminski, A., Trifonov, T., Caballero, J. A., et al. 2018, *A&A*, 618, A115 [32](#), [45](#), [79](#)
- Kasting, J. F., Whitmire, D. P., & Reynolds, R. T. 1993, *Icarus*, 101, 108 [28](#)
- Kemmer, J., Stock, S., Kossakowski, D., et al. 2020, *A&A*, 642, A236 [84](#)
- Kempton, E. M. R., Bean, J. L., Louie, D. R., et al. 2018, *PASP*, 130, 114401 [35](#), [93](#), [94](#)
- Khalafinejad, S., Molaverdikhani, K., Blecic, J., et al. 2021, *arXiv e-prints*, arXiv:2109.06335 [33](#)
- Kipping, D. M. 2013, *MNRAS*, 435, 2152 [58](#), [89](#)
- Kirkpatrick, J. D., Kellogg, K., Schneider, A. C., et al. 2016, *ApJS*, 224, 36 [48](#)
- Knutson, H. A., Fulton, B. J., Montet, B. T., et al. 2014, *ApJ*, 785, 126 [27](#)

- Kochanek, C. S., Shappee, B. J., Stanek, K. Z., et al. 2017, *PASP*, 129, 104502 [31](#), [48](#), [82](#)
- Kossakowski, D. in prep. [32](#)
- Kossakowski, D., Kemmer, J., Bluhm, P., et al. 2021, arXiv e-prints, arXiv:2109.09346 [37](#), [114](#)
- Kovács, G., Zucker, S., & Mazeh, T. 2002, *A&A*, 391, 369 [111](#)
- Kowalski, A. F., Hawley, S. L., Wisniewski, J. P., et al. 2013, *ApJS*, 207, 15 [30](#)
- Kreidberg, L. 2015, *Publications of the Astronomical Society of the Pacific*, 127, 1161 [58](#), [89](#)
- . 2018, *Exoplanet Atmosphere Measurements from Transmission Spectroscopy and Other Planet Star Combined Light Observations*, ed. H. J. Deeg & J. A. Belmonte, 100 [14](#)
- Kreidberg, L., Bean, J. L., Désert, J.-M., et al. 2014, *Nature*, 505, 69 [28](#)
- Lafarga, M., Ribas, I., Lovis, C., et al. 2020a, *A&A*, 636, A36 [33](#)
- . 2020b, arXiv e-prints, arXiv:2003.07471 [49](#)
- Lafarga, M., Ribas, I., Reiners, A., et al. 2021, *A&A*, 652, A28 [33](#), [117](#)
- Lagrange, A. M., Meunier, N., Desort, M., & Malbet, F. 2011, *A&A*, 528, L9 [31](#)
- Lambrechts, M., Morbidelli, A., Jacobson, S. A., et al. 2019, *A&A*, 627, A83 [22](#)
- Laskar, J., & Petit, A. C. 2017, *A&A*, 605, A72 [98](#)
- Lee, E. J., & Chiang, E. 2017, *ApJ*, 842, 40 [27](#), [71](#), [72](#)
- Lee, E. J., Chiang, E., & Ormel, C. W. 2014, *ApJ*, 797, 95 [19](#)
- Léger, A., Rouan, D., Schneider, J., et al. 2009, *A&A*, 506, 287 [15](#)
- Lépine, S., & Bongiorno, B. 2007, *AJ*, 133, 889 [101](#)
- Lépine, S., & Gaidos, E. 2011, *AJ*, 142, 138 [48](#), [79](#)
- Lépine, S., Hilton, E. J., Mann, A. W., et al. 2013, *AJ*, 145, 102 [48](#), [50](#)
- Lépine, S., & Shara, M. M. 2005, *AJ*, 129, 1483 [48](#)
- Li, J., Tenenbaum, P., Twicken, J. D., et al. 2019, *PASP*, 131, 024506 [45](#)
- Lightkurve Collaboration, Cardoso, J. V. d. M., Hedges, C., et al. 2018, *Lightkurve: Kepler and TESS time series analysis in Python*, *Astrophysics Source Code Library*, ascl:1812.013 [73](#), [111](#)
- Lillo-Box, J., Barrado, D., & Bouy, H. 2012, *A&A*, 546, A10 [52](#), [76](#)

- . 2014, *A&A*, 566, A103 [76](#), [77](#)
- Lin, D. N. C., & Papaloizou, J. 1986, *ApJ*, 307, 395 [21](#)
- Lindegren, L., Hernández, J., Bombrun, A., et al. 2018, *A&A*, 616, A2 [52](#)
- Lindegren, L., Klioner, S. A., Hernández, J., et al. 2020, arXiv e-prints, arXiv:2012.03380 [75](#)
- Livingston, J. H., Endl, M., Dai, F., et al. 2018, *AJ*, 156, 78 [52](#)
- López, E. D., & Fortney, J. J. 2013, *ApJ*, 776, 2 [23](#), [37](#), [42](#), [63](#), [93](#)
- López, E. D., & Fortney, J. J. 2014, *ApJ*, 792, 1 [42](#)
- Lopez, E. D., & Rice, K. 2018, *MNRAS*, 479, 5303 [24](#)
- Lovis, C., & Fischer, D. 2010, *Radial Velocity Techniques for Exoplanets*, ed. S. Seager, 27–53 [12](#), [28](#)
- Lovis, C., Dumusque, X., Santos, N. C., et al. 2011, arXiv e-prints, arXiv:1107.5325 [31](#)
- Lundkvist, M. S., Kjeldsen, H., Albrecht, S., et al. 2016, *Nature Communications*, 7, 11201 [27](#), [71](#)
- Luque, R., Pallé, E., Kossakowski, D., et al. 2019, *A&A*, 628, A39 [42](#)
- Makarov, V. V., Beichman, C. A., Catanzarite, J. H., et al. 2009, *ApJ*, 707, L73 [31](#)
- Mann, A. W., Gaidos, E., Vanderburg, A., et al. 2017, *AJ*, 153, 64 [64](#)
- Mansfield, M., Kite, E. S., Hu, R., et al. 2019, *ApJ*, 886, 141 [94](#)
- Marchwinski, R. C., Mahadevan, S., Robertson, P., Ramsey, L., & Harder, J. 2015, *ApJ*, 798, 63 [32](#)
- Marcy, G. W., & Butler, R. P. 1992, *PASP*, 104, 270 [12](#)
- Martín, E. L., Guenther, E., Zapatero Osorio, M. R., Bouy, H., & Wainscoat, R. 2006, *ApJ*, 644, L75 [32](#)
- Martínez-Rodríguez, H., Caballero, J. A., Cifuentes, C., Piro, A. L., & Barnes, R. 2019, *ApJ*, 887, 261 [33](#), [58](#), [95](#)
- Mathur, S., García, R. A., Régulo, C., et al. 2010, *A&A*, 511, A46 [54](#)
- Mayor, M., & Queloz, D. 1995, *Nature*, 378, 355 [8](#)
- Mazeh, T., Holczer, T., & Faigler, S. 2016, *A&A*, 589, A75 [21](#)
- McArthur, B. E., Endl, M., Cochran, W. D., et al. 2004, *ApJ*, 614, L81 [94](#)

- McCully, C., Volgenau, N. H., Harbeck, D.-R., et al. 2018, in Society of Photo-Optical Instrumentation Engineers (SPIE) Conference Series, Vol. 10707, Proceedings of SPIE, 107070K [47](#)
- McLaughlin, D. B. 1924, *ApJ*, 60, 22 [14](#)
- McQuillan, A., Mazeh, T., & Aigrain, S. 2014, *ApJS*, 211, 24 [54](#)
- Meunier, N., Desort, M., & Lagrange, A. M. 2010, *A&A*, 512, A39 [31](#)
- Moffett, T. J. 1974, *ApJS*, 29, 1 [30](#)
- Molaverdikhani, K., Henning, T., & Mollière, P. 2019a, *ApJ*, 883, 194 [95](#)
- . 2019b, *ApJ*, 873, 32 [95](#)
- . 2020, *ApJ*, 899, 53 [95](#)
- Montes, D., González-Peinado, R., Taberner, H. M., et al. 2018, *MNRAS*, 479, 1332 [52](#)
- Morbidelli, A. 2018, arXiv e-prints, arXiv:1803.06708 [42](#)
- Morbidelli, A., & Crida, A. 2007, *Icarus*, 191, 158 [21](#)
- Mortier, A., & Collier Cameron, A. 2017, *A&A*, 601, A110 [55](#), [57](#), [82](#), [119](#)
- Mortier, A., Faria, J. P., Correia, C. M., Santerne, A., & Santos, N. C. 2015, *A&A*, 573, A101 [55](#), [119](#)
- Morton, T. D., Bryson, S. T., Coughlin, J. L., et al. 2016, *ApJ*, 822, 86 [73](#)
- Muirhead, P. S., Johnson, J. A., Apps, K., et al. 2012, *ApJ*, 747, 144 [73](#)
- Mulders, G. D. 2018, Planet Populations as a Function of Stellar Properties, ed. H. J. Deeg & J. A. Belmonte, 153 [18](#)
- Mulders, G. D., Pascucci, I., & Apai, D. 2015, *ApJ*, 798, 112 [17](#), [42](#), [73](#)
- Murphy, M. T., Udem, T., Holzwarth, R., et al. 2007, *MNRAS*, 380, 839 [12](#)
- Narita, N., Fukui, A., Kusakabe, N., et al. 2019, *J. Astron. Telesc. Instruments, Syst.*, 5, 015001 [77](#)
- Nava, C., López-Morales, M., Haywood, R. D., & Giles, H. A. C. 2020, *AJ*, 159, 23 [58](#), [84](#)
- Nortmann, L., Pallé, E., Salz, M., et al. 2018, *Science*, 362, 1388 [33](#)
- Nowak, G., Luque, R., Parviainen, H., et al. 2020a, *A&A*, 642, A173 [26](#), [37](#), [73](#)
- . 2020b, arXiv e-prints, arXiv:2003.01140 [42](#)
- Oshagh, M., Santos, N. C., Boisse, I., et al. 2013, *A&A*, 556, A19 [60](#)

- Owen, J. E., & Murray-Clay, R. 2018, *MNRAS*, 480, 2206 [23](#)
- Owen, J. E., & Wu, Y. 2013a, *ApJ*, 775, 105 [23](#), [24](#), [26](#), [42](#), [63](#), [64](#), [93](#)
- . 2013b, *ApJ*, 775, 105 [71](#)
- . 2017, *ApJ*, 847, 29 [24](#), [42](#), [93](#)
- Parviainen, H., Palle, E., Zapatero-Osorio, M. R., et al. 2020, *A&A*, 633, A28 [77](#)
- Passegger, V. M., Reiners, A., Jeffers, S. V., et al. 2018, *A&A*, 615, A6 [28](#)
- Passegger, V. M., Schweitzer, A., Shulyak, D., et al. 2019, *A&A*, 627, A161 [48](#), [79](#)
- Pepe, F., Cristiani, S., Rebolo, R., et al. 2021, *A&A*, 645, A96 [12](#)
- Pepe, F. A., Cristiani, S., Rebolo Lopez, R., et al. 2010, in *Society of Photo-Optical Instrumentation Engineers (SPIE) Conference Series*, Vol. 7735, *Ground-based and Airborne Instrumentation for Astronomy III*, ed. I. S. McLean, S. K. Ramsay, & H. Takami, 77350F [12](#)
- Pepper, J. 2018, *Research Notes of the American Astronomical Society*, 2, 14 [102](#)
- Perger, M., Scandariato, G., Ribas, I., et al. 2019, *A&A*, 624, A123 [46](#)
- Petrovich, C., Deibert, E., & Wu, Y. 2019, *AJ*, 157, 180 [27](#), [28](#)
- Pojmanski, G. 1997, , 47, 467 [31](#), [48](#)
- Pollacco, D. L., Skillen, I., Collier Cameron, A., et al. 2006, *PASP*, 118, 1407 [31](#), [48](#)
- Pollack, J. B., Hubickyj, O., Bodenheimer, P., et al. 1996, *Icarus*, 124, 62 [18](#)
- Pu, B., & Lai, D. 2019, *MNRAS*, 488, 3568 [28](#)
- Queloz, D., Mayor, M., Udry, S., et al. 2001, *The Messenger*, 105, 1 [12](#)
- Quirrenbach, A., Amado, P. J., Caballero, J. A., et al. 2014, in *Proceedings of SPIE*, Vol. 9147, *Ground-based and Airborne Instrumentation for Astronomy V*, 91471F [12](#), [45](#), [78](#)
- Quirrenbach, A., Amado, P. J., Ribas, I., et al. 2018, in *Society of Photo-Optical Instrumentation Engineers (SPIE) Conference Series*, Vol. 10702, *Ground-based and Airborne Instrumentation for Astronomy VII*, 107020W [32](#), [45](#), [78](#)
- Rauer, H., Catala, C., Aerts, C., et al. 2014, *Experimental Astronomy*, 38, 249 [8](#), [17](#)
- Rayner, J., Tokunaga, A., Jaffe, D., et al. 2016, in *Society of Photo-Optical Instrumentation Engineers (SPIE) Conference Series*, Vol. 9908, *Proceedings of SPIE*, 990884 [46](#)
- Rebull, L. M., Stauffer, J. R., Hillenbrand, L. A., et al. 2017, *ApJ*, 839, 92 [79](#)
- Reiners, A., Bean, J. L., Huber, K. F., et al. 2010, *ApJ*, 710, 432 [32](#)

- Reiners, A., Ribas, I., Zechmeister, M., et al. 2018a, *A&A*, 609, L5 [101](#), [117](#), [124](#), [137](#)
- Reiners, A., Zechmeister, M., Caballero, J. A., et al. 2018b, *A&A*, 612, A49 [32](#), [48](#), [79](#), [102](#)
- Rice, K. 2015, *MNRAS*, 448, 1729 [72](#)
- Ricker, G. R., Winn, J. N., Vanderspek, R., et al. 2014, in *Proceedings of SPIE, Vol. 9143, Space Telescopes and Instrumentation 2014: Optical, Infrared, and Millimeter Wave*, 914320 [16](#)
- Ricker, G. R., Winn, J. N., Vanderspek, R., et al. 2015, *Journal of Astronomical Telescopes, Instruments, and Systems*, 1, 014003 [42](#), [73](#)
- Rodríguez-López, C. 2019, *Frontiers in Astronomy and Space Sciences*, 6, 76 [30](#)
- Rogers, J. G., Gupta, A., Owen, J. E., & Schlichting, H. E. 2021, *MNRAS*, 508, 5886 [25](#), [26](#)
- Rossiter, R. A. 1924, *ApJ*, 60, 15 [14](#)
- Rouan, D., Deeg, H. J., Demangeon, O., et al. 2011, *ApJ*, 741, L30 [72](#)
- Sahu, K. C., Casertano, S., Bond, H. E., et al. 2006, *Nature*, 443, 534 [71](#)
- Sánchez-Menguiano, L., Sánchez, S. F., Pérez, I., et al. 2020, *MNRAS*, 492, 4149 [17](#)
- Sanchis-Ojeda, R., Rappaport, S., Winn, J. N., et al. 2014, *ApJ*, 787, 47 [27](#), [72](#)
- . 2013, *ApJ*, 774, 54 [72](#)
- Santerne, A., Moutou, C., Tsantaki, M., et al. 2016, *A&A*, 587, A64 [21](#)
- Santos, A. R. G., García, R. A., Mathur, S., et al. 2019, *ApJS*, 244, 21 [54](#)
- Schlaufman, K. C., Lin, D. N. C., & Ida, S. 2010, *ApJ*, 724, L53 [28](#)
- Schlichting, H. E. 2014, *ApJ*, 795, L15 [21](#)
- Schöfer, P., Jeffers, S. V., Reiners, A., et al. 2019, *A&A*, 623, A44 [33](#), [49](#), [55](#), [79](#), [82](#)
- Schrijver, C. J. 2002, *Astronomische Nachrichten*, 323, 157 [30](#)
- Schrijver, C. J., & Zwaan, C. 2000, *Solar and Stellar Magnetic Activity* [29](#)
- Schweitzer, A., Passegger, V. M., Cifuentes, C., et al. 2019, *A&A*, 625, A68 [42](#), [48](#), [79](#)
- Scott, N. J., & Howell, S. B. 2018, in *Society of Photo-Optical Instrumentation Engineers (SPIE) Conference Series, Vol. 10701, Proceedings of SPIE, 107010G* [47](#)
- Scott, N. J., Howell, S. B., Horch, E. P., & Everett, M. E. 2018, *PASP*, 130, 054502 [47](#)
- Seager, S., & Deming, D. 2010, *ARA&A*, 48, 631 [8](#)
- Seager, S., & Mallén-Ornelas, G. 2003, *ApJ*, 585, 1038 [13](#)

- Seager, S., & Sasselov, D. D. 2000, *ApJ*, 537, 916 [14](#)
- Seifahrt, A., Stürmer, J., Bean, J. L., & Schwab, C. 2018, in *Society of Photo-Optical Instrumentation Engineers (SPIE) Conference Series*, Vol. 10702, *Ground-based and Airborne Instrumentation for Astronomy VII*, ed. C. J. Evans, L. Simard, & H. Takami, 107026D [12](#)
- Shappee, B. J., Prieto, J. L., Grupe, D., et al. 2014, *ApJ*, 788, 48 [48](#), [82](#)
- Shporer, A., Collins, K. A., Astudillo-Defru, N., et al. 2020, *ApJ*, 890, L7 [73](#)
- Skrutskie, M. F., Cutri, R. M., Stiening, R., et al. 2006, *AJ*, 131, 1163 [50](#), [79](#), [80](#)
- Smith, A. M. S., Cabrera, J., Csizmadia, S., et al. 2018, *MNRAS*, 474, 5523 [73](#)
- Smith, J. C., Stumpe, M. C., Van Cleve, J. E., et al. 2012, *PASP*, 124, 1000 [45](#), [73](#), [111](#)
- Solanki, S. K. 2003, *A&A Rev.*, 11, 153 [30](#)
- Sousa, S. G., Santos, N. C., Mayor, M., et al. 2008, *A&A*, 487, 373 [17](#)
- Southworth, J. 2011, *MNRAS*, 417, 2166 [33](#), [64](#), [95](#)
- Speagle, J. S. 2019, arXiv e-prints, arXiv:1904.02180 [83](#)
- Stassun, K. G., Oelkers, R. J., Pepper, J., et al. 2018, *AJ*, 156, 102 [45](#), [80](#)
- Stassun, K. G., Oelkers, R. J., Paegert, M., et al. 2019, *AJ*, 158, 138 [50](#), [80](#)
- Steffen, J. H., & Coughlin, J. L. 2016, *Proceedings of the National Academy of Science*, 113, 12023 [27](#)
- Stock, S., Kemmer, J., Reffert, S., et al. 2020a, *A&A*, 636, A119 [86](#)
- Stock, S., Nagel, E., Kemmer, J., et al. 2020b, *A&A*, 643, A112 [84](#), [86](#), [118](#)
- Strehl, K. 1902, *Astronomische Nachrichten*, 158, 89 [47](#), [76](#)
- Stumpe, M. C., Smith, J. C., Catanzarite, J. H., et al. 2014, *PASP*, 126, 100 [45](#), [73](#)
- Stumpe, M. C., Smith, J. C., Van Cleve, J. E., et al. 2012, *PASP*, 124, 985 [45](#), [73](#)
- Suárez Mascareño, A., Rebolo, R., & González Hernández, J. I. 2016, *A&A*, 595, A12 [31](#)
- Suissa, G., Chen, J., & Kipping, D. 2018, *MNRAS*, 476, 2613 [63](#)
- Tal-Or, L., Trifonov, T., Zucker, S., Mazeh, T., & Zechmeister, M. 2019, *MNRAS*, 484, L8 [32](#), [45](#), [79](#)
- Tal-Or, L., Zechmeister, M., Reiners, A., et al. 2018, *A&A*, 614, A122 [32](#)
- Terrien, R. C., Mahadevan, S., Deshpande, R., & Bender, C. F. 2015, *ApJS*, 220, 16 [79](#), [80](#)

- Tinetti, G., Eccleston, P., Haswell, C., et al. 2021, arXiv e-prints, arXiv:2104.04824 8
- Torrence, C., & Compo, G. P. 1998, *Bulletin of the American Meteorological Society*, 79, 61 54
- Triaud, A. H. M. J. 2018, *The Rossiter-McLaughlin Effect in Exoplanet Research*, ed. H. J. Deeg & J. A. Belmonte, 2 15
- Trifonov, T. 2019, *The Exo-Striker: Transit and radial velocity interactive fitting tool for orbital analysis and N-body simulations*, ascl:1906.004 97, 117, 136
- Trifonov, T., Tal-Or, L., Zechmeister, M., et al. 2020, *A&A*, 636, A74 32, 45, 79
- Trifonov, T., Kürster, M., Zechmeister, M., et al. 2018, *A&A*, 609, A117 46
- Trifonov, T., Caballero, J. A., Morales, J. C., et al. 2021, *Science*, 371, 1038 35
- Trotta, R. 2008, *Contemporary Physics*, 49, 71 83, 117
- Twicken, J. D., Catanzarite, J. H., Clarke, B. D., et al. 2018, *PASP*, 130, 064502 45
- Udry, S., Mayor, M., & Santos, N. C. 2003, *A&A*, 407, 369 21
- Udry, S., Mayor, M., Benz, W., et al. 2006, *A&A*, 447, 361 17
- Van Eylen, V., Agentoft, C., Lundkvist, M. S., et al. 2018, *MNRAS*, 479, 4786 23, 26, 42, 64
- Van Eylen, V., Astudillo-Defru, N., Bonfils, X., et al. 2021, *MNRAS*, 507, 2154 26, 37
- Vanderspek, R., Huang, C. X., Vanderburg, A., et al. 2019, *ApJ*, 871, L24 73
- Voges, W., Aschenbach, B., Boller, T., et al. 1999, *A&A*, 349, 389 79
- Winn, J. N., Sanchis-Ojeda, R., & Rappaport, S. 2018, , 83, 37 27, 71, 93
- Winn, J. N., Petigura, E. A., Morton, T. D., et al. 2017, *AJ*, 154, 270 52
- Winters, J. G., Henry, T. J., Lurie, J. C., et al. 2015, *AJ*, 149, 5 28
- Wolszczan, A., & Frail, D. A. 1992, *Nature*, 355, 145 8
- Woźniak, P. R., Vestrand, W. T., Akerlof, C. W., et al. 2004, *AJ*, 127, 2436 48
- Wright, J. T., Marcy, G. W., Butler, R. P., & Vogt, S. S. 2004, *ApJS*, 152, 261 49
- Wu, Y. 2019a, *ApJ*, 874, 91 24
- . 2019b, *ApJ*, 874, 91 42, 63
- Zacharias, N., Finch, C. T., Girard, T. M., et al. 2012, *VizieR Online Data Catalog*, I/322A 79

- Zechmeister, M., Anglada-Escudé, G., & Reiners, A. 2014, *A&A*, 561, A59 [32](#), [45](#), [79](#)
- Zechmeister, M., & Kürster, M. 2009a, *A&A*, 496, 577 [52](#), [112](#), [117](#)
- . 2009b, *A&A*, 496, 577 [80](#), [101](#), [126](#), [129](#)
- Zechmeister, M., Reiners, A., Amado, P. J., et al. 2018, *A&A*, 609, A12 [32](#), [45](#), [55](#), [79](#), [82](#), [117](#)
- Zeng, L., Jacobsen, S. B., & Sasselov, D. D. 2017, *Research Notes of the American Astronomical Society*, 1, 32 [42](#), [65](#)
- Zeng, L., Sasselov, D. D., & Jacobsen, S. B. 2016, *ApJ*, 819, 127 [63](#), [64](#), [93](#)
- Zeng, L., Jacobsen, S. B., Sasselov, D. D., et al. 2019, *Proceedings of the National Academy of Science*, 116, 9723 [36](#), [63](#), [93](#)
- Zhu, W., & Dong, S. 2021, *arXiv e-prints*, arXiv:2103.02127 [27](#)



## Acknowledgements

---

*“No llores cuando el sol se ha ido porque las lágrimas no te dejarán ver las estrellas”  
by Violeta Parra – Esta tesis está dedicada a la estrellita más brillante, mi madre.*

---

I want to start by thanking the IMPRS program to allow me to do my Ph.D. in the beautiful city of Heidelberg, a place where I meet incredible people, which made these three years and a half of studies a pleasant journey.

The first person that I would like to thank is my supervisor, Prof. Dr. Andreas Quirrenbach, and the people of my thesis committee group, Dr. Sabine Reffert and Dr. Martin Krüster. Thanks to all those who, with your expertise, discussions, and advice that I had during our meetings, always were constructive, supportive, and helpful. Inspiring and guiding me through my academic journey, which is not easy at all.

An overall thank you to the CARMENES consortium, a group where I met amazing people. Particularly, I would like to say thanks to José Caballero, with their commitment and infinite patience helped me get my two first exoplanets publications. Without his help, I could never have submitted these works within the deadlines. Also, thank you to Néstor E., Rafael L., Karan M., and Enric P. to be the best co-authors team ever, and of course, I would like to thank to Florian R. and Adrian K., who have always been available to answer hard and simple questions, also for being friendly colleagues which I always felt comfortable talking about simple life things. Thank you so much Adrian for helping me with the translation of the abstract to german.

Without a doubt, I would like to thank the “phdheidelbergers” team, composed of Diana K. Jonas K. and Stephan S., which was the team that gave me the most meaningful feedback during my Ph.D., not only with science but also helping me to solve everyday life questions, such as How to survive to the german bureaucracy?. Thank you so much, guys.

Many thanks to the Latinos-Chilenos group (Samantha B., Marcelo B., Nicolás K., Lizxandra F., Gustavo M., Raúl D, and others) for being not only my fellow students mates but also being excellent friends, with which I feel 100% identified and supported. Thank you all for the laughs and good moments, for caring for my cats during my travels, and always being available to share a beer. Also, thank you very much to my good and old chileans friends Matías J. and Marcelo T., who encouraged me to apply to the LSW. Los quiero mucho amigos!

Apart from my friends and colleagues, I want to thank my family. First, my dad by constantly be fascinated with my career and results, he was my number one fan during all these years. To my brother, for being always there, he better than anyone knows everything that I had to go through to reach, today, to this moment. I love you with all my heart, my little Dito. Also, I would want to thank my life brothers and sisters Eduardo C., Daniela R. Muriel F., and Valeria T., for helping me stay sane in times of madness. Friends are the family one chooses.

Of course, I would like to thank Pessa-Gutiérrez family, in special to my future parents-in-law for always being aware of me, for all your love and support, and finally, I would like to thank my future husband, Ismael Pessa, that during these years, has been the most important person in my life, who has supported me in my most challenging moments, and of course, has always been available to help me with random programming stuff. You know, I know, we know, for all the things we had to go through together, and if today I am finishing this big step, it was because you have supported me every time.

*Ich bin Fertig!*

---

*“Master has given Dobby a sock. Master has presented Dobby with clothes! Dobby is free!”  
Harry Potter and the Chamber of Secrets.*

# Declaration of Originality

---

## **Declaration of Originality**

I hereby declare that this thesis is my own work and that I have used no other than the stated sources and aids.

## **Declaration**

Ich versichere, dass ich diese Arbeit selbstständig verfasst habe und keine anderen als die angegebenen Quellen und Hilfsmittel benutzt habe.

Heidelberg, der 06. December 2021

(Paz Bluhm)

